Electrochemical hydrogen storage in lightweight electrode materials

Electrochemical hydrogen storage in lightweight electrode materials

Rogier A.H. Niessen

Samenstelling van de promotiecommissie:

prof.dr. J.W. Niemantsverdriet	Technische Universiteit Eindhoven, *voorzitter*
prof.dr. P.H.L. Notten	Philips Research Laboratories Eindhoven Technische Universiteit Eindhoven, *eerste promotor*
prof.dr. M.T.M. Koper	Universiteit Leiden, *tweede promotor*
prof.dr. R.P. Griessen	Vrije Universiteit Amsterdam
prof.dr. J. Schoonman	Technische Universiteit Delft
prof.dr. G. de With	Technische Universiteit Eindhoven
prof.dr. R.A. van Santen	Technische Universiteit Eindhoven
dr. B.A. Boukamp	Technische Universiteit Twente

CIP-DATA LIBRARY TECHNISCHE UNIVERSITEIT EINDHOVEN

Niessen, Rogier A.H.

Electrochemical hydrogen storage in lightweight electrode materials / by
Rogier A.H. Niessen. – Eindhoven : Technische Universiteit Eindhoven, 2006.

Proefschrift. – ISBN 90-386-2917-6
NUR 913

Subject headings: electrochemistry ; batteries / hydrogen storage / electrode materials
/ thin films / magnesium alloys / nanotubes / thermodynamics / electric impedance ; EIS

Trefwoorden: elektrochemie ; batterijen / waterstofopslag / elektrodematerialen / dunne lagen
/ magnesium legeringen / nanobuizen / thermodynamica / elektrochemische impedantie ; EIS

Cover design: R.A.H. Niessen

Printed by Eindhoven University Press

This research has been financially supported by the Dutch Government within the framework of the Economy Ecologie and Technology (EET) program.

Electrochemical hydrogen storage in lightweight electrode materials

PROEFSCHRIFT

ter verkrijging van de graad van doctor aan de
Technische Universiteit Eindhoven, op gezag van de
Rector Magnificus, prof.dr.ir. C.J. van Duijn, voor een
Commissie aangewezen door het College voor
Promoties in het openbaar te verdedigen op
woensdag 18 januari 2006 om 16.00 uur

door

Rogier Adrianus Henrica Niessen

geboren te Weert

Dit proefschrift is goedgekeurd door de promotoren:

prof.dr. P.H.L. Notten
en
prof.dr. M.T.M. Koper

In honor of my father

"Education is the ability to listen to almost anything without losing your temper or your self-confidence."

(Robert Frost)

Acknowledgements

Having finished this dissertation thesis, I wish to express my deep gratitude to several people who supported me during the recent years.

First of all, prof.dr. Peter H.L. Notten, who offered me the opportunity to perform my Ph.D. research under his supervision. He always encouraged creativity on a scientific level and working conscientiously towards mutual goals in the fields of hydrogen storage materials and electrochemistry. His greatest asset is being able to combine a high degree of professionalism with genuine personal interest. I hope that some of these qualities have been marginally transferred to me during the last four years. Thanks to his flexibility my work was mainly conducted within Philips Research Laboratories Eindhoven. Thank you, prof.dr. J.W. Niemantsverdriet, prof.dr. R.P. Griessen, prof.dr. J. Schoonman, prof.dr. G. de With, prof.dr. M.T.M. Koper, prof.dr. R.A. van Santen and dr. B.A. Boukamp for finding the time to be part of my promotion committee.

The basic idea of this Ph.D. project was to investigate the hydrogen storage behavior of carbon nanotubes. After performing backbreaking research for two years, this quest was abandoned and an alternative route, hydrogen storage in magnesium-based alloys, was chosen. During all this time I had fruitful and stimulating discussions with many scientists both from the academic and industrial fields, among whom I would like to explicitly mention in alphabetical order; Afifa Belfadhel-Ayeb, René van Beek, Tom Housmans, Zhou Jiang, Peter Kalisvaart, dr. Alexander Ledovskikh, Martin Otten, dr. Martin Ouwerkerk, Bert Op het Veld, Paul Vermeulen and dr. Martine Wehrens-Dijksma. Thanks, everyone. Additionally, I would like to express my gratitude to all the people from the analysis department, whose results continuously raised new issues and luckily solved some as well.

During my work at Eindhoven University of Technology and Philips Research Laboratories Eindhoven, I have always enjoyed the spirit of teamwork, which ties together scientists, technicians, and undergraduate students. Many colleagues readily provided advice and hands-on expertise, always leading to a sound solution. The following students contributed with their theses or practical work to the research described in this thesis; R. van der Poel, J. Franse, M. Daenen, R. de Fouw, B. Hamers, P. Janssen, K. Schouteden, and M. Veld. Special thanks to J. de Jonge, for the enormous amount of work done on and time invested in those irksome carbon nanotubes.

My parents, Leo and Mia, who enabled my education and who were always there if support was needed. They showed me that everything is possible and taught me to make the most of every single opportunity. Regrettably, my father passed away during the final year of my Ph.D. and would thus never see the final result. I dedicate this work to him, knowing he would be most proud. My sister, Leonne, who has always been a pioneer throughout our upbringing, making life a lot easier for me. My brother-in-law, Ivar, who is a perfect interlocutor in the field of technical matters and, like me, an advocate of good whiskey and cigars. Roel, Martin and Stijn (in no particular order), friends of mine for a long time, I have shared with them on many occasions the things we like; cool sports, lengthy discussions, tender spare-ribs, Cuban cigars and peated single-malts. I would like to thank my (future) parents-in-law, Rieks and Clary, whose humor always brought out the best in me and who provided me with a second home during many weekends. Finally, my girlfriend, Elke, who gave me an immeasurable amount of love and patience for the last six and a half years.

Eindhoven, September 2005 Rogier Niessen

Contents

1
Introduction

1.1. Energy density & hydrogen storage materials

In an age where mobile technology plays an ever more dominant role in our daily life, energy storage has become an extremely important issue. Mobile equipment is being scaled down, while energy consumption, on the other hand, is generally not reduced. Nowadays, the demanding consumer puts a high standard on the operating time of the equipment, requiring strong and powerful energy sources.

Another important issue is the availability of energy. Traditional energy sources such as fossil fuels and natural gas are not infinitely available and if even they were, their combustion or end products are not always environmentally friendly. Sustainable alternatives like wind, hydro and solar energy are becoming more popular, but are at present not particularly suited for mobile applications. One of the alternatives is the use of hydrogen as an energy source.[1] Stored hydrogen can be used as fuel in various applications ranging from PEM fuel cells[2], to rechargeable Nickel Metal Hydride (NiMH) batteries for mobile phones, laptops or Hybrid Electrical Vehicles (HEVs)[3]. It has been shown that battery technology can be used in a broad field of applications and is therefore still subject to major and continuous research efforts.

Presently different technologies exist which enable the storage of hydrogen as a fuel. It can be stored under high pressure in metal containers, as a liquid at low temperatures, physisorbed on high surface area materials or in the form of a metal hydride (MH). If one of the previously mentioned hydrogen storage technologies is to be viable in the future it should at least meet the requirements of the U.S. Department of Energy (DoE) target for the year 2010, implying that at least 6 % of hydrogen should be stored by weight.[4]

Fundamental research on, especially, interstitial MHs has already been done for some 140 years, ever since Graham reported on the absorption of hydrogen by palladium in 1866.[5] MHs can generally be classified into three main groups depending on their bond character and structure[6]; interstitial hydrides (*e.g.* PdH_x and $LaNi_5$), covalent hydrides (*e.g.* SnH_4) or ionic hydrides (*e.g.* MgH_2 and $Na(AlH_4)_2$). Nowadays, energy densities approaching, or even exceeding, the DoE target can be realized using the appropriate MH. The excellent hydrogen storage properties of the interstitial MHs, especially when considering their volumetric storage capacities and high reversibility, has led to the fact that these materials are currently often used as electrodes in commercially available rechargeable batteries.

However, as their gravimetric storage capacity is limited to about 1.2 wt.%, their applicability in large mobile applications, such as HEVs, can prove problematic. This has led to the development of new lightweight hydrogen storage materials, which are often Mg-based. The reason behind this is the high gravimetrical storage capacity of pure Mg (7.66 wt.%).[7] If present issues regarding the slow sorption kinetics, poor stability and high desorption temperatures are solved, these materials can be advantageously used in many future applications.

Aside from MHs, it was already shown that high surface area materials, such as activated carbons and other highly porous materials, could physisorb up to 2 wt.% of hydrogen at cryogenic temperatures close to 70 K.[8,9] Recently, the existing activated carbons were modified which has resulted in a slight increase in storage capacity.[10] Apart from the activated carbons, some other classes of materials also have very large surface areas. Among these are, for example; zeolites, Metal-Organic-Frameworks (MOFs)[11] and Carbon Nanotubes (CNTs). It was at the very end of the previous millennium that research done by Rodriguez *et al.* and Dillon *et al.* showed that carbon nanofibers (CNFs) and CNTs could supposedly store up to 25 and 10 wt.% of hydrogen, respectively.[12,13] This immediately triggered a massive and worldwide research effort towards the hydrogen storage properties of various types of CNTs. However, up until now no researchers were able to duplicate these findings and work done on the hydrogen storage properties of CNTs since then showed significant spread in the results. On average, storage capacities of about 0.3 wt.% of hydrogen were reported, much lower than believed possible a few years ago.

1.2. Hydrogen-based rechargeable batteries

The key application in which hydrogen is currently used as a 'fuel' is the rechargeable NiMH battery. Commercial NiMH batteries are employed worldwide in portable electronic equipment like mobile telephones, laptops, shavers, power tools, *etc.*. Nowadays, these batteries, along with Li-ion secondary batteries, have become a serious alternative for the widespread use of rechargeable NiCd batteries. The NiMH battery has an energy capacity increase of up to 30 - 50 % as compared to the standard NiCd battery. Moreover, the electrode materials used are more environmentally friendly and the battery does not suffer from memory effects.[14,15] However, on a chemical level the NiMH battery is still quite similar to the traditional NiCd battery. A schematic representation of the chemistry in a sealed NiMH battery is shown in Fig. 1.

A separator electrically insulates the nickel and MH electrodes. Ionic conductivity between the two electrodes is achieved by the impregnation of both the electrodes and the separator with an alkaline electrolyte. Commonly, the electrolyte consists of a mixture of concentrated potassium hydroxide (KOH) and lithium hydroxide (LiOH) solutions. The overall electrochemical reactions, playing a role during charging (*ch*) and discharging (*d*) of this system, can be represented by

$$Ni(OH)_2 + OH^- \underset{d}{\overset{ch}{\rightleftarrows}} NiOOH + H_2O + e^- \quad , \tag{1}$$

and

$$M + xH_2O + xe^- \underset{d}{\overset{ch}{\rightleftarrows}} MH_x + xOH^- \quad . \tag{2}$$

Upon charging the battery, water is reduced at the MH electrode, forming OH^- and adsorbed hydrogen at its surface. This adsorbed hydrogen is subsequently absorbed by the metal, forming the MH. Simultaneously, divalent nickel is oxidized to the trivalent state, at the nickel electrode. Discharging the battery reverses the processes, resulting in the fact that the MH is oxidized, water is formed and one electron is released. The released electron is transported through an external circuit (*e.g.* a mobile phone) to the nickel electrode where it reduces water, forming nickelhydroxide and an hydroxyl ion. Of course, more complicated processes due to overcharging and overdischarging can occur, as also indicated in this figure.[16,17]

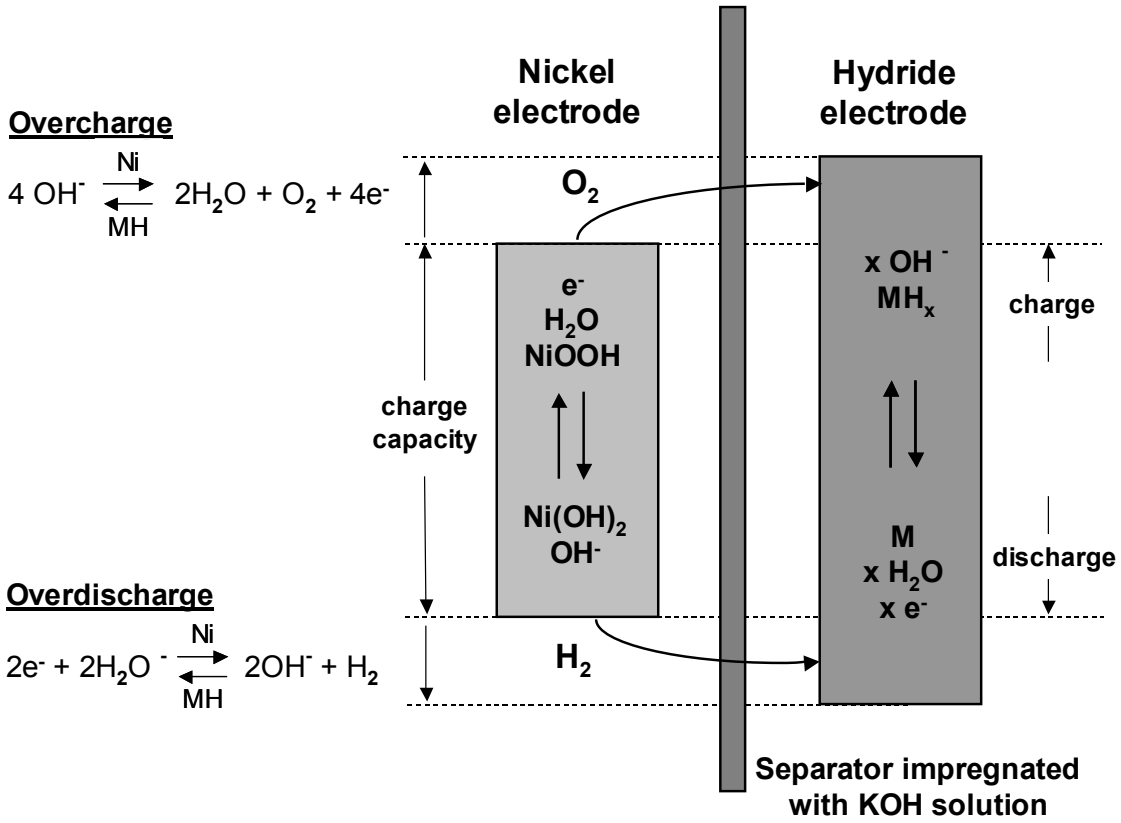

Fig. 1: Schematic representation of the chemistry in a rechargeable NiMH battery.

Due to the fact that the energy demand of portable and handheld equipment is steadily increasing, commercial NiMH batteries, of which the fundamental research was conducted in the late 70s, need to be improved continuously. The main focus nowadays lies on safety and increased energy density. The energy density of a NiMH battery can be increased by replacing the existing electrode materials with lighter ones with equal, or improved, hydrogen storage capacities (wt.% hydrogen). Two very different classes of materials, Mg-based MHs and CNTs, can possibly fulfill these requirements. Both have very low densities indeed and research aimed at the hydrogen storage characteristics has been most promising.

At *Philips Research Laboratories Eindhoven* (the Netherlands) a new Mg-based alloy comprised of magnesium and scandium has been investigated, revealing very high energy densities. Energy densities were reached close to 1500 mAh/g, equaling 5.6 wt.% of hydrogen stored.[18] These storage capacities are almost five times that of commercial

AB_5-type electrodes (300 mAh/g). The fact that for single-wall carbon nanotubes hydrogen storage capacities of up to 800 mAh/g have been reported, would also suggest that CNTs are suitable candidates for electrode materials in lightweight rechargeable batteries.[19]

1.3. This thesis

In Chapter 2, a theoretical consideration will be given concerning the two types of high energy density materials investigated during this Ph.D. research; metal hydrides (MHs) and carbon nanotubes (CNTs). Additionally, the theory linked to the electrochemistry, used as the main tool in the material characterization, will be treated. The main goal of this research project is to perform fundamental materials research on promising new high energy density materials using electrochemistry. The focus will be on the electrochemical storage of energy (hydrogen) in an alkaline environment. The reason why measurements were performed in an alkaline solution is related to the fact that, at present, the main application of these materials is that of battery electrode material in rechargeable NiMH batteries, which is based on an alkaline system.

The experimental details are outlined in Chapter 3. Aside from the basic electrochemical set-up and measurement methods, the detrimental effects of parasitic influences on the electrochemical response are treated. Two main parasitic effects are explained in detail in this chapter. Firstly, it will be shown that oxygen dissolved in the electrolyte has a profound impact on the measured electrochemical response of the materials under investigation. Secondly, the effect of surface poisoning on the electrochemical behavior will be discussed.

Chapters 4 and 5 deal with the electrochemical hydrogen storage in MHs, the first class of high energy density materials treated in this thesis. The research described is limited to the highly promising thin film Mg-based alloys, in which alongside Mg a second element is present. The research on MgSc alloys (Chapter 4) and MgX (X = Ti, V, Cr) alloys (Chapter 5) will be divided in several sections focusing on key material properties. These include; structural analysis, the hydrogen storage capacity, thermodynamic properties, surface kinetics and hydrogen transport in these materials.

The second class of high energy density materials, CNTs, will be presented in Chapter 6. The electrochemical energy storage characteristics of bulk CNT electrodes are treated in detail. The research presented in this chapter is focused primarily on elucidating which processes/mechanisms can account for the energy storage characteristics of CNT materials. Evidence will be presented showing that, depending on the nanotube morphology, charge (energy) stored in these high-surface materials is related to a combination of electrostatic and (electro)chemical processes.

At the end of this thesis, all research described in this work will be recapitulated in the summary. Here, the line of research followed, observations made and conclusions drawn will be addressed in a point-to-point manner.

2
Theory

Abstract

A general overview is presented of two types of promising lightweight hydrogen storage materials; metal hydrides (MHs) and carbon nanotubes (CNTs). For each class basic information is given regarding the different types of materials that exist, their structural properties, as well as in which applications they can be used. The remainder of the chapter deals with the subject of electrochemical hydrogen storage. Firstly, the (electro)chemical reactions of interest when electrochemically (de)hydrogenating a MH electrode will be presented. Secondly, the kinetic equations decribing the charge transfer reaction will be derived. Finally, some words will be devoted to how the thermodynamic properties of the system under investigation is linked to electrochemical parameters.

2.1. Introduction

In order to be able to fathom the discussions to be given in Chapters 3 to 5 more easily, some basic theory will be presented first. Sections 2.2 and 2.3 are devoted to a general overview of the different types of energy storage materials that have been investigated; MHs and CNTs, respectively. For each class basic information is presented regarding the different types of materials that exist, their structural properties, as well as in which applications they are most likely to be used. The remainder of the chapter deals with the electrochemical aspect of hydrogen storage. As this entire thesis is based on electrochemistry a detailed description is presented about; (i) the (electro)chemical reactions of interest when electrochemically (de)hydrogenating a MH electrode; (ii) the derivation of the kinetic equations of the charge transfer reaction; (iii) how electrochemical parameters can be used to deduce thermodynamic properties of the system under investigation.

2.2. Metal Hydrides

2.2.1. Types of metal hydrides

A hydride is a chemical compound of hydrogen with other elements. Originally, the term hydride was reserved strictly for compounds containing hydride ions, usually in combination with metals, but the definition has been broadened to compounds involving hydrogen in direct bond with another elements.

Hydrides can be roughly classified into three main types depending on the nature of bonding and structure:

- Ionic hydrides,
- Covalent hydrides,
- Interstitial hydrides.

In 'main group element' hydrides, the electronegativity of an element with respect to hydrogen determines whether the compound will be either ionic or covalent. For example, an electropositive metal from the left side of the Periodic Table of Elements, forms ionic hydrides whereas an electronegative element (usually from the Table's right side) forms covalent hydrides.

2.2.1.1. Ionic hydrides

In ionic hydrides the hydrogen behaves as a halogen and obtains an electron from the metal to form a hydride ion (H^-), thereby obtaining the stable electron configuration of helium by filling up the s-orbital. The other element is a metal more electropositive than hydrogen, usually one of the alkali metals or alkaline earth metals. The hydrides are called binary hydrides if they only involve two elements including hydrogen. Chemical formulae for binary ionic hydrides are either MH such as LiH or MH_2 like MgH_2. Gallium, indium, thallium and lanthanide hydrides are also ionic.

A special class of ionic hydrides is the so-called complex metal hydride, the most famous example being sodium alanate ($NaAlH_4$). Complex metal hydrides potentially have, at the temperatures and pressures where they are likely to be used, higher gravimetric hydrogen capacities than most interstitial metal hydrides commercially used to date (*e.g.* AB_5- and AB_2-type compounds). Alanates can reversibly store and release hydrogen when catalyzed with titanium dopants. For $NaAlH_4$ the following 2-step reaction is proposed:[20,21]

$$6\ NaAlH_4 \rightleftarrows 2\ Na_3AlH_6 + 4\ Al + 6\ H_2\ , \tag{3}$$

$$2\ Na_3AlH_6 \rightleftarrows 6\ NaH + 2\ Al + 3\ H_2\ . \tag{4}$$

At a pressure of 1 bar, the first reaction becomes thermodynamically favorable at temperatures above 33 ºC and can release 3.7 wt.% hydrogen, while the second reaction takes place above 110 ºC and can release an additional 1.8 wt.% hydrogen. Fig. 2 shows the crystal structure of $NaAlH_4$, which clearly shows that the hydrogen exists as AlH_4^- tetrahedra in an Na^+ ion lattice.

Issues with complex metal hydrides include the slow hydrogen uptake and release, irreversibility without a proper catalyst (*e.g.* Ti) and high cost. The maximum material gravimetric capacity of 5.5 wt.% hydrogen for $NaAlH_4$ is even below the 2010 DOE target of 6 wt.%.[4] Thus far, only 4 wt.% reversible hydrogen content has been experimentally demonstrated with alanate materials. Additional problems that need to be overcome before alanates can be used commercially are the low packing density of these powders (roughly 50 %) and the low volumetric capacity. Although $NaAlH_4$ will, in all likelihood, not evolve further than the research stage, it is envisioned that continued study will lead to more fundamental understanding of the complex processes taking place. Subsequently, this knowledge can be applied in the design and development of improved types of complex metal hydrides.

Some researchers recently found that selected metal nitrides also show large hydrogen storage capacities. These novel complex hydrides exhibit promising characteristics, like relatively moderate absorption and desorption temperatures and pressures. Chen *et al.* demonstrated in 2002 that the reversible hydrogen storage capacity of Li_3N was about 9.3 wt.%.[22] However, the fully hydrogenated form of Li_3N, the amide $LiNH_2$, is not able to release all this hydrogen in a single step. The overall desorption mechanism can be described by the following 2 steps, in which first lithium amide is converted into an Li_2NH (see Fig. 3) via

$$LiNH_2 + 2\ LiH \rightleftarrows Li_2NH + LiH + H_2\ , \tag{5}$$

and subsequently this imide is further oxidized to the lithium nitride according to

$$Li_2NH + LiH \rightleftarrows Li_3N + H_2\ . \tag{6}$$

Up until now the temperature required to release all hydrogen at usable pressures is too high for practical application of this material. This triggered research towards enhancing the catalytic activity as well as lowering the stability of these compounds.

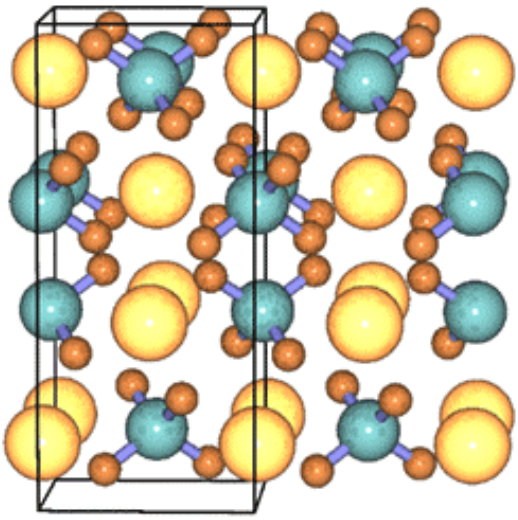

Fig. 2: Crystal structure of $NaAlH_4$. The Al and H atoms are represented by the medium-sized turquoise and small amber spheres, respectively. The large yellow spheres are the Na^+ ions.[20,21]

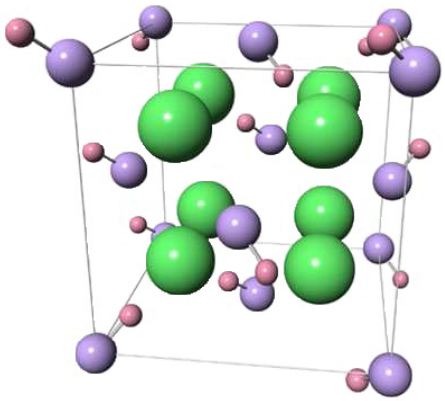

Fig. 3: Crystal structure of Li_2NH according to Ohoyama *et al.* (fcc-structure).[23] The large green, medium-sized purple and small pink spheres are Li^+ ions, nitrogen atoms and hydrogen atoms, respectively. One unit cell includes four Li_2NH molecules. Only one of the four hydrogen positions around the nitrogen atom is randomly occupied.

Ichikawa *et al.* examined the hydrogenation/dehydrogenation properties of a 1:1 mixture of $LiNH_2$ and LiH catalyzed by 1 mol.% of $TiCl_3$ prepared by ball milling.[24] They found that the product, upon heating (5 °C/min), desorbed a large amount of hydrogen (≤ 5.5 wt.%) in the temperature range from 150 - 250 °C without emission of ammonia. Xiong *et al.* investigated the properties of ternary Li-alkali earth metal imides.[25] They synthesized imides of Li-Mg and Li-Ca. It was found that a dramatic drop in hydrogen desorption temperatures, increased desorption pressures, and high storage capacities has successfully achieved. Partial substitution of Li by Mg in the nitride/imide/hydride system introduced by Chen *et al.*, was also investigated by Luo *et al.*[26] and resulted in improved hydrogen sorption characteristics of the material. This new system could release 5.2 wt.% of hydrogen at 200 °C with a pressure of 30 bar, thus showing very attractive properties for 'on-board' vehicular hydrogen storage applications.

2.2.1.2. Covalent hydrides

As the name suggests, the hydrogen in these compounds is covalently bonded. Generally, the element(s) to which hydrogen is bonded belongs to more electronegative elements like boron, aluminum or Group 4-7 elements. Common compounds including hydrocarbons, ammonia and hydrazine can be considered as hydrides of carbon and nitrogen but the term is generally used for collectively naming all hydrogen compounds of an element. Other examples of covalent hydrides are stanane (SnH_4), plumbane (PbH_4), selenium hydride (SeH_2) and polonium hydride (PoH_2).

Covalent hydrides behave as molecules with weak London forces and hence are generally volatile at room temperature and atmospheric pressure. However, aluminum and beryllium hydrides (AlH_3 and BeH_2, respectively) are solids at room temperature.[27] The crystal structure of AlH_3 is shown in Fig. 4. Properties of covalent hydrides can vary dramatically per species.

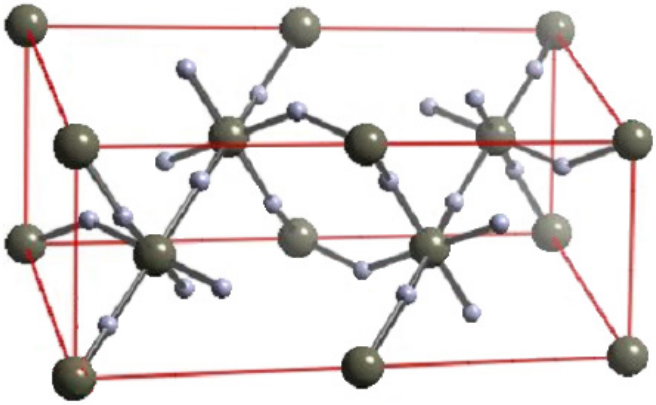

Fig. 4: Crystal structure of the AlH_3 compound. The large and small spheres represent the Al and H atoms, respectively.[27]

2.2.1.3. Transitional and interstitial hydrides

This class of MHs is the most fascinating among the three as their bonding nature vastly differs from element to element and can change according to external criteria such as temperature, pressure and electric current. Many of the transitional MHs are interstitial in nature. In these, molecules of hydrogen dissociate and hydrogen atoms settle in the octahedral or tetrahedral holes in the metal lattice called the interstitial sites. Notably, interstitial hydrides often have a non-stoichiometric nature. From these compounds hydrogen gas can be liberated proportional to the applied temperature and pressure, not to chemical composition. Interstitial hydrides show certain promise as a way for safe hydrogen storage and during the last 25 years many interstitial hydrides were developed that readily absorb and desorb hydrogen at room temperature and atmospherical pressure. They are usually based on intermetallic compounds and solid solution alloys. However, their application is still limited, as they are capable of storing only about 2 wt.% of hydrogen, which is, for example, not enough for automotive applications.

Among the most well-known interstitial metal hydrides are the so-called AB_5-type materials. These compounds can, on average, store up to 1.2 wt.% of hydrogen and are able

to absorb/desorb this hydrogen in a highly reversible manner under mild conditions. The AB_5-type materials currently used as electrode material in rechargeable NiMH batteries, are all based on $LaNi_5$ for which the exceptional hydriding properties were first reported by van Vught *et al.* in 1970.[28] However, it was soon recognized that the hydrogen absorption properties could be changed dramatically when nickel was partially substituted by other transition metals.[29] In the quest for optimizing the AB_5 compound with regard to, for example, plateau pressure, corrosion resistance and/or limitation of volume expansion studies were performed on more exotic compositions. These included without giving a complete list, $LaNi_{5-x}M_x$ (where M = Cr, Fe, Co, Cu, Pd and Ag) and $La_{1-x}R_xNi_5$ (where R = Ce, Misch metal, Ca, Y, Gd, Zr, Yb, Pr, Nd and Sm).[30,31,32]

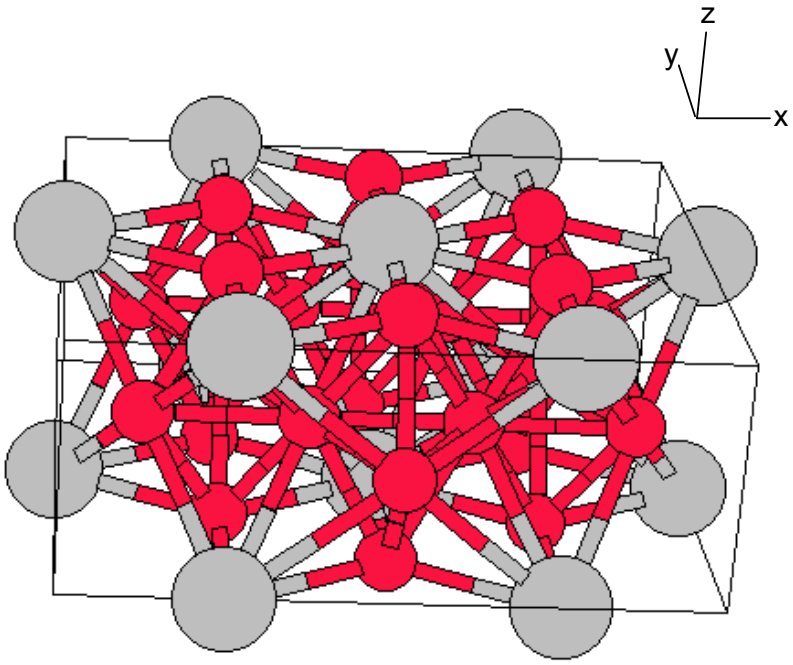

Fig. 5: Crystal structure of $LaNi_5$. The La atoms are depicted as the large gray spheres, whereas the small red spheres represent the Ni atoms.

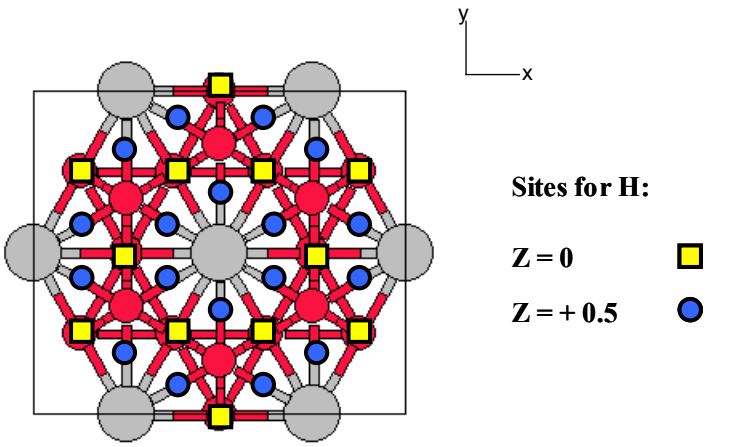

Fig. 6: Cross-sectional view of the $LaNi_5$ unit cell along the z-axis. The yellow squares and blue circles indicate where the interstitials in the lattice are located at z = 0 and z = + 0.5, respectively.

The crystal structure of the $LaNi_5$ compound is shown in Fig. 5. Upon hydrogenation, hydrogen atoms are able to occupy interstitial sites in the metal lattice. The positions of these interstitial sites are depicted in Fig. 6. When all these sites are filled, the composition of the hydride attained is $LaNi_5H_{6.7}$ and a total of 1.1 wt.% of hydrogen has been stored in the host compound. During this hydrogenation a phase transition occurs from the hydrogen-poor α-phase to the hydrogen-rich β-phase, resulting in a total volume expansion close to 23 %.

Although this phase transition induces stress in the material, eventually leading to severe embrittlement of the material, it is also the fundamental reason why AB_5-type compounds can both store and release the bulk of their hydrogen within a very narrow pressure window. Without going into detail, when a phase transition occurs the chemical potential of the total system does not alter, therefore the pressure cannot change. This is schematically illustrated in Fig. 7, where the pressure-composition isotherm for an ideal hydride-forming material is shown. It is evident that the equilibrium pressure gradually increases when more hydrogen is being absorbed by the α-phase. However, when a critical composition is reached (x_α), a second phase (β-phase) is formed and the equilibrium pressure remains constant until a second critical composition is reached at x_β. At this point only β-phase exists and once again a gradual increase in pressure can be observed with increasing hydrogen content.

If the temperature of the system is changed, the equilibrium plateau pressure changes rapidly, following the *Van 't Hoff rule*. With increasing temperature the plateau pressure increases and becomes narrower. Effectively, this is a direct result of the enhanced hydrogen solubility in the α- and β-phases. Ultimately, above the critical temperature, T_c, there is a disappearance of the two-phase coexistence region.

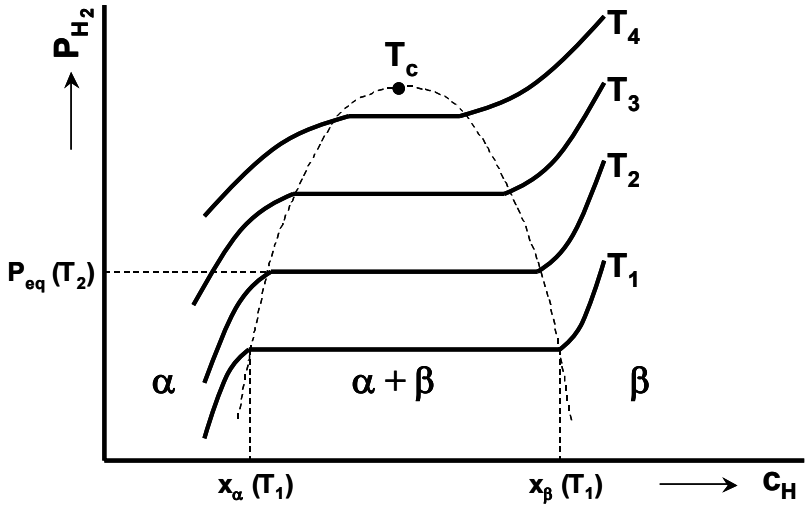

Fig. 7: Pressure-composition isotherms at different temperatures ($T_4 > T_3 > T_2 > T_1$) for the solid solution of hydrogen, the metal α- and β-phases. The two-phase coexistence region corresponds to a particular equilibrium plateau pressure. Above the critical temperature, T_c, instantaneous conversion from α- to β-phase occurs.

2.2.2. Applications of metal hydrides

These hydride-forming materials have been known for a considerable amount of time and depending on the nature of the hydride (see Section 2.2.1) they can be utilized in many applications. The essence of this section is to provide an overview of the different fields where MHs can be applied. By no means an effort is made to provide a complete record of every application in which they are used:

- **Hydrogen storage**
    1. Electrochemical hydrogen storage in interstitial hydrides (AB_5- and AB_2-type materials) is used in aqueous NiMH secondary batteries.[33,34] Currently, research in the field of NiMH battery technology is also increasingly aimed at automotive applications, like HEVs.[35]
    2. Storage and release of hydrogen from MHs (both complex ionic and interstitial hydrides) via the gas phase can be employed in fuel-cell driven technologies. Here hydrogen gas, which is acting as the 'fuel', is provided by the MHs that serve as an alternative hydrogen storage medium, replacing existing storage solutions like compressed or liquefied hydrogen gas.

- **Chemical selectivity**
    1. MHs as getters. In this role traces of H_2 gas can be selectively gettered in, for example, vacuum-sealed electronic devices. Getters are generally divided into two groups. The first being the non-evaporable getters, which are compact and can be manufactured in a wide range of shapes. Commercial getters of this type often consist of Zr-based alloys (for example Zr-Fe-V). The second type is the evaporable getter such as Ti evaporated films.[36]
    2. Hydrides as purifiers and separators. Here the MH compounds are essentially used to separate H_2 from other gaseous components like NO_2, NH_3 or O_2. This can be achieved by, for example, employing Pd membranes.
    3. Isotope separation. The thermodynamics of hydride-forming compounds is often influenced by whether they absorb/desorb hydrogen, deuterium or even tritium. This will lead to, for example, different plateau pressures or transport phenomena. These fundamental properties can be utilized to separate the isotopes.[37]

- **Optical windows**

    Optically active MH thin films acting as switchable mirrors.[38] The fundamentals of optically active hydrides were first shown for pure rare earth materials like Y and La in 1996.[39,40] Basically, as the rare earth compound absorbs hydrogen, a transition occurs between a reflective metal dihydride to a transparent semiconducting trihydride. This transition is highly reversible and can be easily introduced by just changing the surrounding hydrogen gas pressure. Nowadays, it is well-known that all trivalent rare earth metals as well as some Mg-rare earth alloys exhibit similar optical properties.[41,42]

- **Sensors and detectors**

  Hydride-forming compounds can be utilized as hydrogen sensors.[43] The main idea behind this technology is that the optical properties of, especially, rare earth hydrides can be utilized to sense the presence of H_2 gas. In fiber optic hydrogen sensors the sensing end of the fiber is coated with an optically active MH. When in contact with hydrogen gas, the optical properties of this thin film change. This can subsequently be measured by a detector. To be able to detect, for example, very low concentrations the MH can theoretically be changed to an MH system with a much lower plateau pressure.

2.3. Carbon nanotubes

Fullerenes are large, closed-cage, carbon molecules of which many structures exist. Some examples of possible structures are regular spheres, cones, tubes and even more complicated shapes. The special, highly stable, tube-like structure that can be considered as long, wrapped graphene sheets is usually referred to as a carbon nanotube. These materials were first discovered by Ijima in 1991[44] and were rapidly assigned to have very promising electrical, optical and mechanical characteristics. Ever since, research on different types of CNTs has been conducted in order to resolve their physical and chemical properties.

2.3.1. Carbon nanotube structures

2.3.1.1. Types of carbon nanotubes

Overall, tubular CNT materials can be divided into two classes; single-wall carbon nanotubes (SWNTs) and multi-wall carbon nanotubes (MWNTs). The technique used to produce carbon nanotubes generally determines which type of nanotube is formed. Whether primarily SWNTs, MWNTs, or mixtures of both are formed is dependent on many factors such as, for example, the presence and character of the catalyst and the reactor temperature.

MWNTs can be considered as a collection of concentric SWNTs with different diameters, with a constant separation between the layers nearly equal to that of graphite layer spacing (0.34 nm). A special case of a MWNT is a double wall nanotube (DWNT), which consists of exactly two concentric tubes. The length and diameter of MWNT structures differs a lot from those of SWNTs and therefore their properties are also very different. Fig. 8 shows the schematic structures of a SWNT, a MWNT and a DWNT.[45]

In the example in Fig. 8 the MWNT consists of three concentric tubes, but it should be noted that depending on the production technique used, MWNTs might contain even more than twenty walls. For example, in samples produced with the arc-discharge technique the number of concentric tubes was found to vary from two to several tens. Both the outer and inner diameters of SWNTs and MWNTs might differ significantly. Whereas SWNTs have typical diameters of approximately 0.8 to 1.4 nm, MWNTs can have inner diameters of 1 up to 10 nm and outer diameters in the range of 2 up to 50 nm, depending on the number of concentric layers. The length of SWNTs and MWNTs is quite similar and can be up to 100 μm. In contrast to MWNTs, SWNTs tend to self-organize, by means of Van der Waals forces, into rope-like structures called rope lattices or bundles. These rope lattices, consisting of 100 to 500 SWNTs, are 5 to 20 nm in diameter and 10 to even much more than 100 μm

long.[46] Fig. 9 shows a schematic representation of a cross-section of a hexagonal rope lattice. Fig. 10 shows an actual TEM picture of an arc discharge-produced rope lattice of SWNTs.

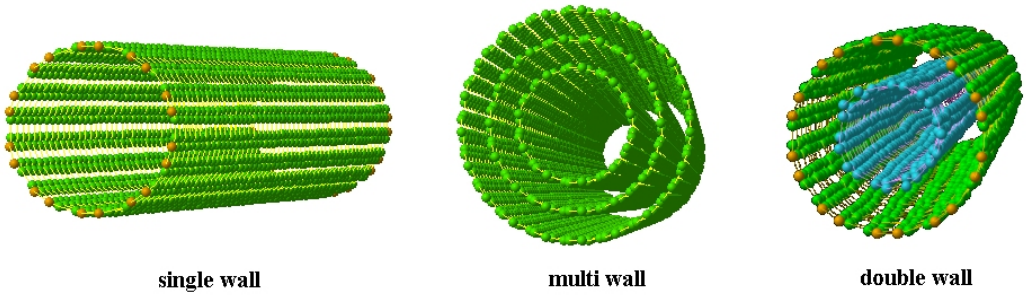

Fig. 8: Schematic structures of pieces of a SWNT, a MWNT and a DWNT (on different scales).

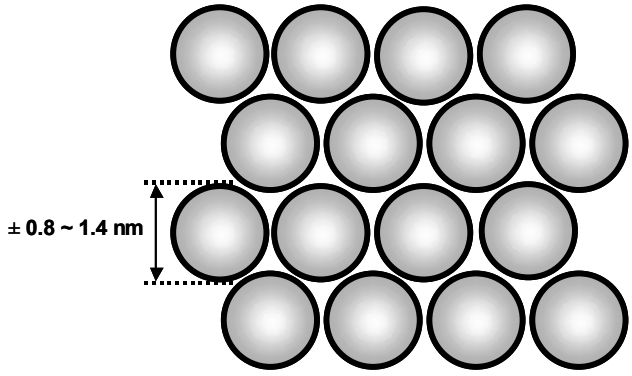

Fig. 9: Schematic representation of a 'rope lattice' of SWNTs.

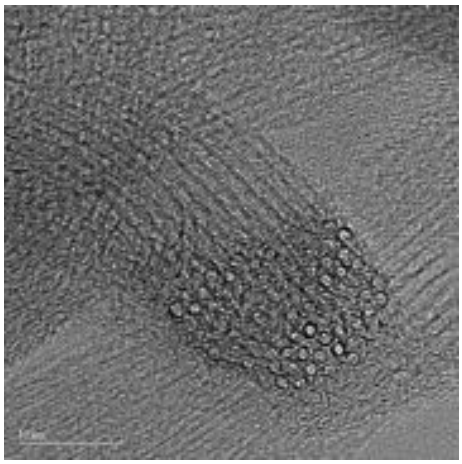

Fig. 10: TEM picture of a rope lattice of arc discharge produced SWNTs.

2.3.1.2. Atomic structures and defects of SWNTs

As was mentioned before, SWNTs can be considered as long, wrapped, graphene sheets. To be more specific, a nanotube consists of two regions with different structures, the sidewall and the end-cap. The structure of the end-cap is derived from a smaller fullerene, like C_{60}, and exists of C-atoms arranged in pentagons and hexagons. The atomic structure of the sidewall can indeed be considered as a long, wrapped, graphene sheet. As this sheet can be wrapped in different directions, the atomic structure of the sidewalls of the nanotubes is not always the same. The simplest way of specifying the structure of an individual tube is in terms of a vector, which we label *C*, joining two equivalent points on the original graphene lattice. Rolling up the sheet such that the two end-points of the vector are superimposed creates the tube cylinder. In Figs. 11 and 12 a schematic structure of a graphene layer is shown, labeled according to the notation of Dresselhaus *et al.*[47,48]. Each pair of integers (*n*, *m*) represents a possible tube structure in this image.

The vector C can be expressed as

$$C = n \cdot a_1 + m \cdot a_2 \tag{7}$$

where a_1 and a_2 are the unit cell base vectors of the graphene sheet, and $n \geq m$ (both integers). There are two possible high symmetry structures for carbon nanotubes, known as 'armchair' ($n = m$) and 'zig-zag' ($m = 0$). These two structures are shown in Fig. 13. In practice, it is believed that most carbon nanotubes do not have these highly symmetric forms but have structures called 'chiral' in which the honeycomb-shaped hexagons are arranged helically around the tube axis.

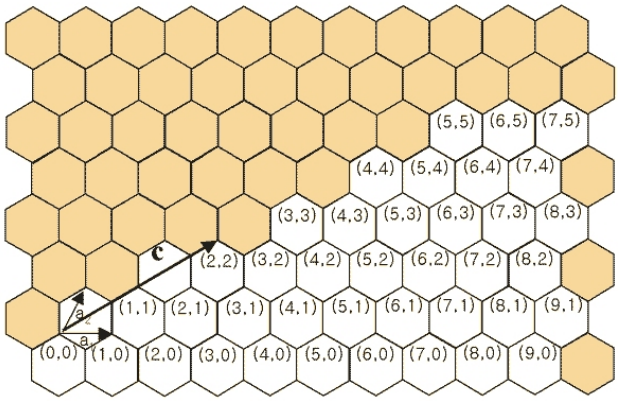

Fig. 11: A graphene sheet labeled according to Dresselhaus *et al.*[47,48].

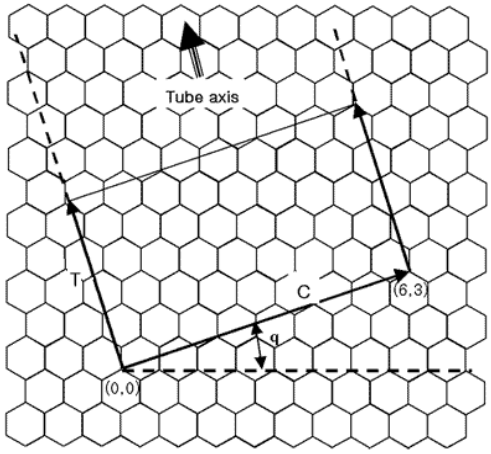

Fig. 12: Example of the construction of a unit cell for a (6, 3) nanotube.

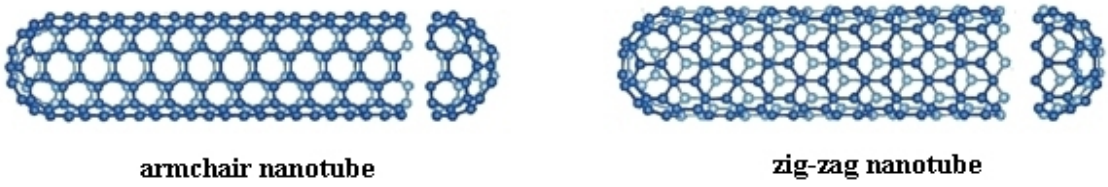

Fig. 13: The high symmetry *armchair* and *zig-zag* structures.

CNTs are regarded as 'one-dimensional crystals' because of their very large length to diameter ratio. It is thus possible to define a translational unit cell along the tube axis. For chiral nanotubes, for example, the low symmetry results in large unit cells. A simple method of constructing these cells is described in Fig. 12. This involves drawing a straight line through the origin O of the irreducible wedge normal to C and extending this line until it passes exactly through an equivalent lattice point. This is illustrated for the case of a (6, 3) nanotube. The length of the unit cell in the tube axis direction is the magnitude of the vector T.

Apart from these ideal structures described above, a CNT might also contain all sorts of defects in its structure. Examples of these defects are; anomalies resulting from the insertion of pentagons and heptagons (Fig. 14), Y-branches in which a tube 'splits' into two tubes, and T-junctions in which the end of one tube seems to be connected to the sidewall of another tube. Defects will result in special structures with their own specific properties that might differ significantly from ideal structures shown before. Especially the electrical properties of the tubes are highly dependent on the exact atomic structure. When defects are introduced the conductivity of the tube might change along its length.

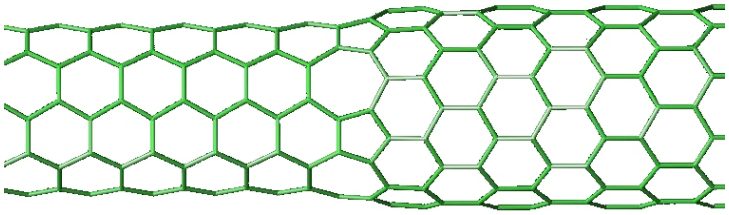

Fig. 14: Change of structure from *armchair* (left) to *zig-zag* (right) by insertion of pentagons and heptagons.

Depending on the structure, CNTs can be either highly conductive (metallic) or behave as a semiconductor. The generally accepted criterion for a SWNT to be metallic is[49]

$$\frac{n-m}{3} = \text{integer} \quad . \tag{8}$$

In practice, however, even a high-grade sample of SWNTs will contain a mixture of different structures (both metallic and semiconducting). It is interesting to note that under the right circumstances it is, to a certain extent, possible to introduce defects in a controlled way. The possibilities of introducing defects in nanotube structures are subject of many studies and will not be further discussed here.

2.3.2. Applications of carbon nanotubes

As CNTs were discovered only about 15 years ago they can still be considered a relatively new class of materials. Therefore, a lot of research on possible applications, in which the beneficial properties of CNTs can be exploited, is currently in progress. As mentioned before, CNTs have been assigned excellent material properties. As a complete list, showing all the possible uses of CNTs and every field of research in which these materials are investigated, would result in an exhaustive summation, only a few examples of possible applications and research areas are listed below[50,51]:

- **Energy storage**
    1. Electrochemical hydrogen storage in CNTs for aqueous rechargeable battery applications.
    2. Hydrogen storage in CNTs via the gas phase as lightweight hydrogen storage alternative to compressed or liquefied H_2 gas. In this role CNT materials could, for example, be used in fuel-cell applications.

3. Electrochemical lithium storage in nanotubes for Li-ion battery applications.[52,53,54]
4. CNTs as electrodes in electrochemical supercapacitors.[55,56]

- **Molecular electronics**
  1. Nanotubes as field emission electron sources for flat panel displays, lamps, gas discharge tubes and X-ray- and microwave-generators.[57]
  2. CNTs being used in nanoscale electronics as transistors.[50]

- **Nanoprobes and sensors**
  1. Nanotubes utilized as STM or AFM tips, resulting in improved resolution.
  2. As miniaturized chemical sensor detecting NO_2, NH_3 or O_2.

- **Nanotubes as electrically conducting components in polymer composites**

- **Molded CNT composites for the shielding of electromagnetic radiation**

- **Incorporation of nanotubes into plastics to increase the Young's modulus**

It should be noted that the research intensity has dropped severely for some of the abovementioned CNT applications after the initial boom in the last decade of the 20th century. This especially holds for the electrochemical and gas phase storage of hydrogen in CNT materials. Other areas, such as molecular electronics and nanoprobes/sensors, have seen an increase in the amount of research, showing continued interest in these types of materials.

2.4. Electrochemical hydrogen storage

2.4.1. Introduction

A large variety of materials are known that are able to absorb, intercalate or chemically bond hydrogen. The most common hydrogen absorbers are the transition metals or transition metal alloys. Metals or alloys generally considered as model hydrogen absorbing systems are, for example, Pd and $LaNi_5$. The last one mentioned leading to the more advanced MischMetal-based hydrogen storage materials currently used in commercial NiMH rechargeable batteries. The current power consumption of portable equipment and a possible hydrogen-based economy in the (near) future demand the development of new hydrogen storage materials with a higher energy density. To this end lighter metals, which can still absorb an appreciable amount of hydrogen, are frequently incorporated in these novel hydrogen storage compounds. Examples are Mg, Ti or V.

To be able to characterize the properties of a hydrogen storage material, a suitable means needs to be applied to load/unload it with hydrogen. This can be achieved via the gas phase, where an amount of material is subjected to a (high) hydrogen pressure in a closed volume. By measuring, for instance, the mass change of the material it is possible to determine the amount of hydrogen absorbed. However, the error made in gas phase measurements can be quite large, especially when using only a small amount of active material. Alternatively, the hydrogen storage compound can be loaded/unloaded with hydrogen by electrochemical means. The main advantage of using electrochemical hydrogen loading, as compared to gas phase loading, is that the hydrogen content in the compound can be accurately tuned. This

can even be done at very low hydrogen concentrations, which may correspond to extremely low partial hydrogen pressures, *i.e.* 10^{-10} to 10^{-30} bar.

2.4.2. Reactions of interest

Simplified, electrochemical hydriding/dehydriding in an alkaline environment is achieved via a three-step mechanism. This is shown schematically in Fig. 15 for a planar MH electrode. The first step is the charge transfer reaction at the electrode/electrolyte interface, which can be represented by

$$H_2O + M + e^- \underset{k_{-1}}{\overset{k_1}{\rightleftarrows}} MH_{ad} + OH^- \quad . \tag{9}$$

In this step, denoted as the Volmer reaction, water is reduced to hydroxyl ions and hydrogen atoms are adsorbed at the surface of the electrode. Subsequently, these adsorbed hydrogen atoms (H_{ad}) can be absorbed by the host material just below the surface[58], forming subsurface hydrogen (H_{ss}), according to

$$MH_{ad} \underset{k_{-2}}{\overset{k_2}{\rightleftarrows}} MH_{ss} \quad . \tag{10}$$

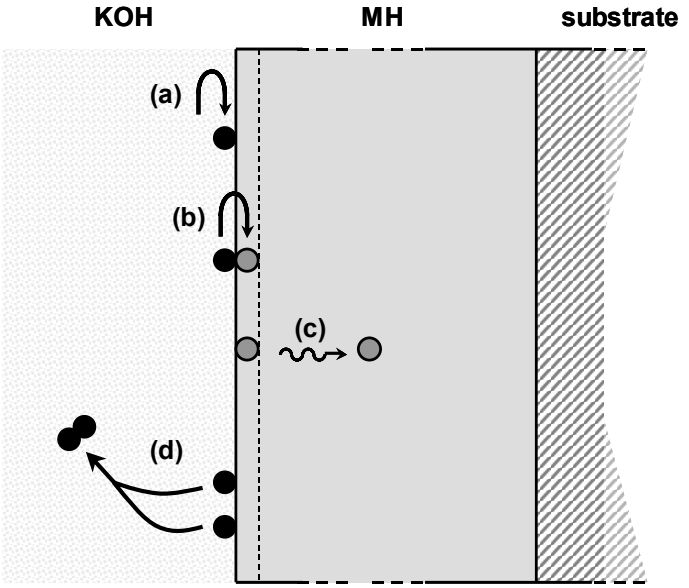

Fig. 15: Schematic representation of a planar MH electrode. Besides the overall geometry of this system, the main (electro)chemical processes related to hydrogen absorption are indicated at their appropriate locations; charge transfer reaction (a), adsorbed hydrogen forming subsurface hydrogen (b), solid-state diffusion of hydrogen in the Pd bulk (c) and formation of gaseous hydrogen via recombination (d).

Finally, H_{ss} penetrates into the bulk of the MH as H_{abs} via solid-state diffusion

$$MH_{ss} \rightleftarrows MH_{abs} \quad . \tag{11}$$

Additionally, H_{ad} at the surface can recombine to gaseous hydrogen in the so-called *Tafel step* according to

$$2\,MH_{ad} \underset{k_{-3}}{\overset{k_3}{\rightleftarrows}} H_2(g) + 2M \quad . \tag{12}$$

It is also possible for an adsorbed hydrogen atom to form a hydrogen molecule by dissociation of a hydrogen atom from a water molecule (again by electron transfer) in the *Heyrovski step* (see Reaction 13). This step is generally omitted as it was reported to be insignificant in the overall kinetics.[59]

$$MH_{ad} + H_2O + e^- \underset{k_{-4}}{\overset{k_4}{\rightleftarrows}} M + H_2(g) + OH^- \tag{13}$$

2.4.3. Kinetics

In order to describe the kinetics coupled to the absorption of hydrogen by a MH electrode, the basic kinetic relations are presented. The process being discussed here is a heterogeneous reaction because reactants have to cross a phase boundary (from liquid to solid). For this reason, rates are expressed as fluxes. The flow of electrons involved in an electrochemical reaction produces a current I, which is directly related to the rate of the charge transfer reaction. The net current, the difference between the anodic (oxidation) and cathodic (reduction) currents, is defined as[60,61]

$$I = I_{ox} - I_{red} = nFk_{ox}c_{red} - nFk_{red}c_{ox} \tag{14}$$

where n is the number of electrons transferred in the reaction; F is the Faraday constant; c_{red} and c_{ox} are the concentrations of reductant and oxidant; and k_i the rate constant.

To participate in a redox reaction at an electrode, a species from solution has to migrate and diffuse to (and through) the solution/electrode interface. Also, when the charge transfer reaction has taken place, the product has to cross the same interface again. This migration, via an intermediate state, is activated and the rate constant can be written as

$$k = B\,e^{\left[\frac{-\Delta G^{\ddagger}_{act}}{RT}\right]} \tag{15}$$

where B is a constant [same dimensions as k]; $\Delta G^{\ddagger}_{act}$ is the activation Gibbs energy; R is the gas constant; and T the absolute temperature. The Gibbs energy of activation does not necessarily have to be the same for both processes. Substituting Eq. 15 into Eq. 14 subsequently yields

$$I = nFB_{ox}c_{red}\, e^{\left[\frac{-\Delta G^{\ddagger}_{act,ox}}{RT}\right]} - nFB_{red}c_{ox}\, e^{\left[\frac{-\Delta G^{\ddagger}_{act,red}}{RT}\right]} \quad . \tag{16}$$

The potential of the electrode influences the Gibbs energy of activation. This is schematically shown in Fig. 16 for a one step, one-electron transfer process. If the electrode potential (E^{eq}) is changed by ΔE to a new value, E, the relative energy of the electron resident on the electrode changes by $-F\Delta E = -F(E - E^{eq})$. Hence, the $O + e$ curve moves up or down by that amount. The lower curve on the left side of Fig. 16 (top) shows this effect for a positive ΔE. It is readily apparent that the barrier of oxidation, $\Delta G^{\ddagger}_{act,ox}$, has become less than $\Delta G^{0,\ddagger}_{act,ox}$ by a fraction of the total energy. Suppose this fraction is called α, where α (the *transfer coefficient*) can range from zero to unity, depending on the shape of the intersection region (see Fig. 16 (bottom)). Including this in the Gibbs energy of activation yields the following expression

$$\Delta G^{\ddagger}_{act,ox} = \Delta G^{0,\ddagger}_{act,ox} - \alpha F(E - E^{eq}) \quad . \tag{17}$$

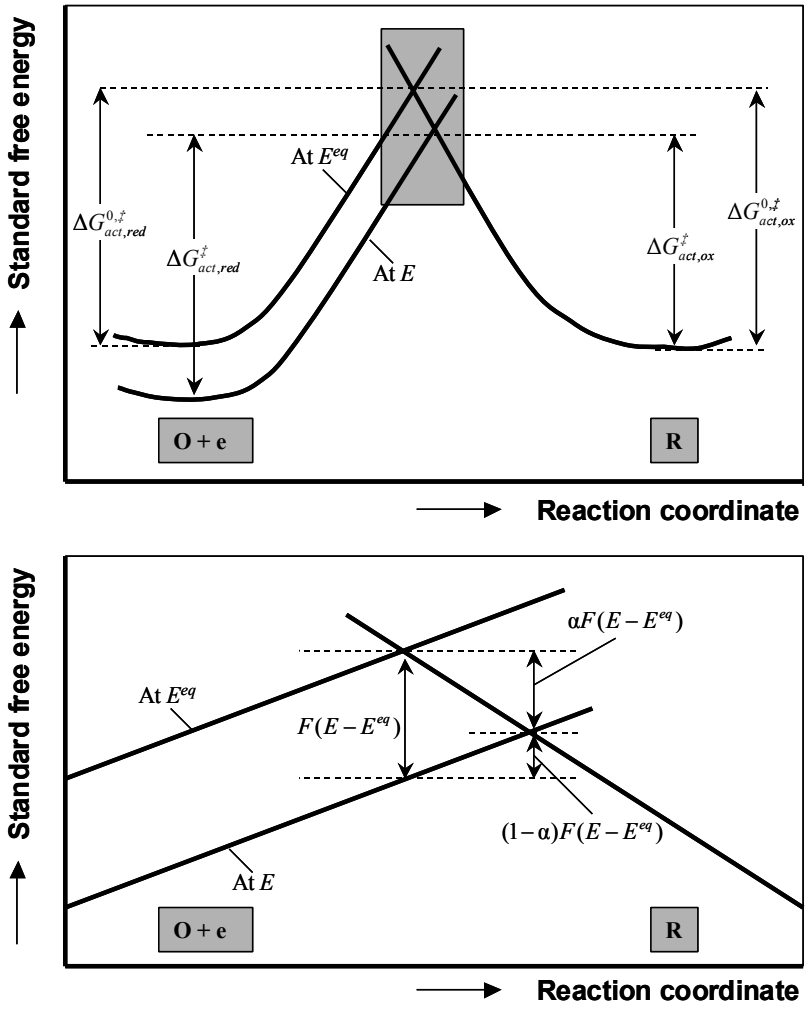

Fig. 16: Effects of a potential change on the standard free energies of activation for oxidation and reduction (top). Magnification of the boxed area in the top schematic (bottom).[61]

Furthermore, the barrier for reduction has become higher than $\Delta G_{act,red}^{0,\ddagger}$ by the amount $(1-\alpha)F(E-E^{eq})$. This, therefore, leads to

$$\Delta G_{act,red}^{\ddagger} = \Delta G_{act,red}^{0,\ddagger} + (1-\alpha)F(E-E^{eq}) \quad . \tag{18}$$

When Eqs. 17 and 18 are substituted in Eq. 16, a complete expression can be obtained for both the reduction and oxidation currents. The resulting expression can, under equilibrium conditions, be rewritten into a slightly different form yielding the *Butler-Volmer equation*

$$I = I_0\left(e^{\left[\frac{\alpha\eta F}{RT}\right]} - e^{\left[\frac{-(1-\alpha)\eta F}{RT}\right]}\right) \tag{19}$$

where η, called the *overpotential*, equals $(E-E^{eq})$; and I_0 is the *exchange current* (for the full expression see Section 3.5.3). This term is used when the reduction and oxidation currents are exactly balanced, thus, when the electrode is at equilibrium.

2.4.4. Thermodynamics

When considering a MH system, at a particular oxidation state, the hydrogen concentration in this system is fixed through its thermodynamics. In general terms, the chemical potential of a hydride-forming compound (μ_{MH}) can be linked to the partial hydrogen pressure via[62]

$$\mu_{MH} = \frac{1}{2}\mu_{H_2} = \frac{1}{2}\mu_{H_2}^0 + \frac{1}{2}RT\ln\left(\frac{P_{H_2}}{P_{ref}}\right) \tag{20}$$

in which μ_{H_2} is the chemical potential of hydrogen gas in equilibrium with hydrogen stored in the MH and $\mu_{H_2}^0$ is the standard chemical potential of hydrogen gas (by convention equal to 0). Furthermore, μ_{MH} is linked to the electrochemical potential via[63]

$$\mu_{MH} = -FE_{MH}^{eq} \tag{21}$$

in which E_{MH}^{eq} is obviously expressed *vs.* the Standard Hydrogen Electrode (SHE) reference electrode (1 bar H_2). Substitution of Eq. 21 in Eq. 20 finally yields the well-known expression[14]

$$E_{MH}^{eq} = -0.931 - \frac{RT}{2F}\ln\left(\frac{P_{H_2}}{P_{ref}}\right) \tag{22}$$

in which P_{ref} is the reference pressure (1 bar) and E_{MH}^{eq} is expressed with respect to the Hg/HgO (6 M KOH) reference electrode (see Section 3.2). It should be noted at this point that the first term on the right-hand side of Eq. 22, which originates from the fact that the

system is measured *vs.* a reference electrode other then the SHE (1 bar H_2), is dependent on the concentration of the electrolyte used. Care should be taken when using concentrated electrolytes (generally > 0.1 M) as in these cases the activity coefficients of the dissolved species can deviate substantially from unity, influencing the pH dependence of the reference redox couple *vs.* which measurements are conducted.[64]

In most MH compounds the absorption of hydrogen is exothermic. This indicates that the lattice expansion and/or phase transition reduces the Gibbs free energy of the system. The heat of formation (ΔH_f) of such a phase transition can be estimated using E_{MH}^{eq} or P_{H_2} via the *Van 't Hoff relation*[62]

$$\Delta H_f = \frac{RT}{2}\left[\ln P_{H_2} - \frac{S_{H_2}^0}{R}\right] \tag{23}$$

where $S_{H_2}^0$ is the standard molar entropy of hydrogen gas (130.8 J/K mol H_2).

3
Experimental

Abstract

A detailed description is given of the measurement set-up used to determine the hydrogen storage properties of a particular material. Additionally, the basics of the measurement techniques used and the difficulties encountered during the electrochemical characterization are presented. The remainder of this chapter deals with parasitic influences that severely distort the measured electrochemical response. Two types of detrimental influences are covered; the influence of oxygen dissolved in the electrolyte and the influence of electrode surface poisoning. It will be shown that oxygen, which is dissolved in the electrolyte, affects the measured results in two ways. Firstly, due to the coexistence of two redox systems a mixed-potential is measured during open-circuit conditions, which is more positive than the true equilibrium potential of the hydride system. Secondly, due to continuous self-oxidation, when performing electrochemical measurements, part of the hydrogen in the electrode is extracted, resulting in a lower capacity during oxidation and a higher capacity during reduction. Surface poisoning, especially when using thin film electrodes, can manifest itself quickly under certain circumstances, thereby severely influencing the kinetic properties. Experiments on identical MgSc thin films, performed in three-electrode set-ups in which the electrolyte is either contaminated or contamination-free, confirm this. Cross-correlation of electrochemical and analytical results points to a clear relationship between the amount of contaminant deposited on the surface and the value of the charge transfer resistance. This surface contamination can be avoided by making sure that all cell components, in contact with the electrolyte, are of the highest purity and do not contain more than trace amounts of impurities.[*]

[*] Part of this chapter is based on: R.A.H. Niessen, and P.H.L. Notten, *The influence of O_2 on the electrochemistry of thin film, hydrogen storage, electrodes*, Electrochim. Acta, 50, 2959 (2005) and R.A.H. Niessen, and P.H.L. Notten, *Reference electrode-induced surface poisoning of thin film electrodes*, J. Electrochem. Soc., 152, A2051 (2005).

3.1. Introduction

In this chapter a detailed description is given of the measurement set-up, the measurement techniques used and difficulties encountered during the electrochemical characterization of the electrode materials under investigation. Firstly, the details of the three-electrode cell used in all experimental work will be given (Section 3.2). Additionally, some words will be devoted to the (dis)advantages of using bulk or thin film geometries in electrochemical materials characterization (Section 3.3). Subsequently, the measurement techniques that were applied are explained. Here a subdivision is made between controlled current and controlled potential experiments (Section 3.4). The remainder of this chapter will deal with parasitic influences that are able to severely distort the electrochemical response of the materials under investigation. Two types of detrimental influences are covered in this chapter; the influence of oxygen dissolved in the electrolyte (Section 3.5) and the influence of electrode surface poisoning (Section 3.6).

3.2. The three-electrode set-up

In order to be able to accurately determine the electrochemical response of a particular material during hydrogen loading/unloading, a thermostated three-electrode set-up in used (see Fig. 17). In this type of set-up, which is schematically shown in Fig. 18, the current is passed between the working electrode (denoted as WE), which comprises of the material under investigation and a counter electrode (CE). The counter electrode can be any convenient one, as long as its behavior does not affect the response of the electrode of interest (working electrode). The potential of the working electrode is monitored *vs.* a reference electrode (RE) that is placed in close proximity to the surface of the working electrode in order to minimize the Ohmic drop of the electrolyte. This reference electrode has, under normal experimental conditions, an invariant potential and is stable in time. The device used to measure the potential difference between the working- and reference electrode has a high input impedance, resulting in the fact that an infinitesimally small current is passed through the reference electrode. Therefore, its potential will remain constant and equal to its open-circuit value. Preferably a combination of a galvanostat and potentiostat is used to measure/apply voltage/current.

As a small amount of oxygen in the electrolyte can already be detrimental to the electrochemical response of the working electrode (see Section 3.5), the electrolyte has to be de-aerated rigorously. To this end standard argon (99.9 %) was first led through an oxygen scrubber based on a methylviologen (MV) solution (see Section 3.5.2) and subsequently led to the electrochemical set-up by means of stainless steel Swagelok™ tubing. The three-electrode cell is equipped with custom-made gas inlets, enabling continuous purging of the electrolyte with oxygen-purified argon. Before the actual measurements, purging of the cell was carried out by vigorously bubbling oxygen-purified argon through the electrolyte in both the working and counter electrode compartments for at least a few hours. During the measurements purging was done in a similar way with the only difference that the purging gas was led over, instead of through, the electrolyte in the working electrode compartment. This is needed as the purging gas bubbles prevent accurate voltage measurements.

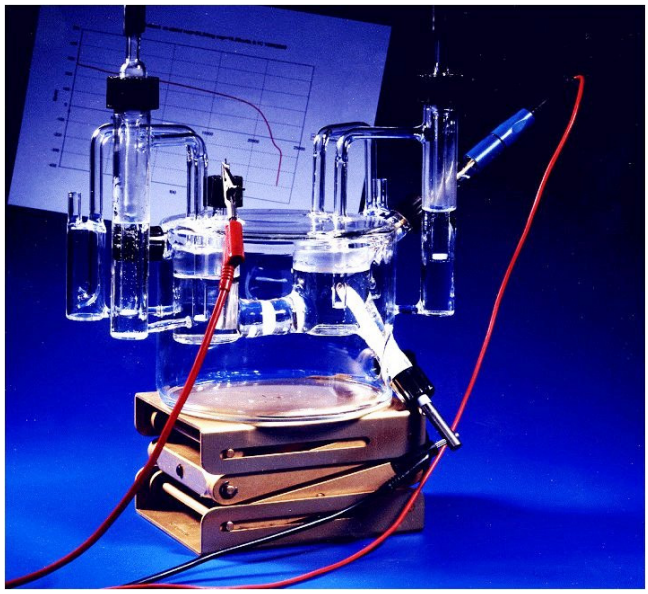

Fig. 17: Photograph of a three-electrode cell, used to measure bulk electrodes.

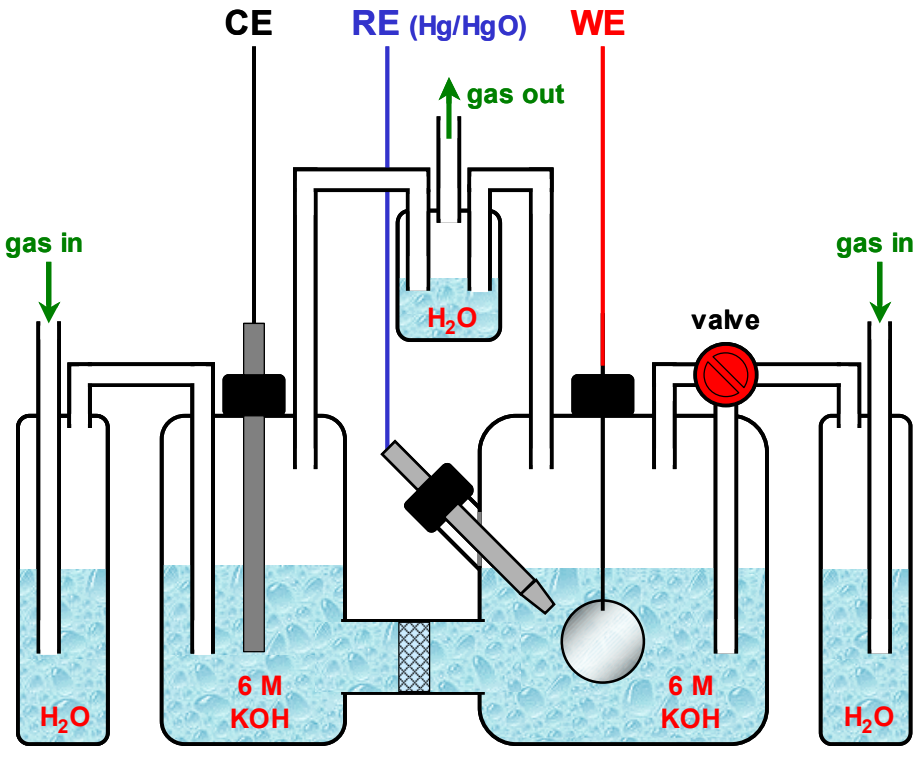

Fig. 18: Schematic representation of a three-electrode set-up. The working, counter and reference electrode are denoted as WE, CE and RE, respectively. The purging gas inlets ('water locks') are shown on either side of the cell. The gas outlet is depicted at the top and also employs a 'water lock' to prevent back-diffusion. A valve on the right-hand side can be used to regulate whether the purging gas flow through or over the electrolyte in the WE compartment.

All electrochemical measurements presented in this thesis were performed using the three-electrode electrochemical cell described in detail above. Unless stated otherwise the set-up was thermostated at 298 K by means of a water jacket surrounding the cell and filled with 6 M KOH electrolyte, in which the material of interest acted as working electrode. The potential of the working electrode was measured with respect to a Hg/HgO reference electrode (Koslow Scientific Company) filled with 6 M KOH solution. The counter electrode, which was a palladium rod (99.999 %, ∅ 5 mm, Drijfhout), was placed in a separate compartment in the cell and care was taken that the total area in contact with the electrolyte was sufficiently large. The compartments, which held both the working and counter electrode, were separated by means of fritted glass. In a separate set-up the counter electrode was pre-charged with hydrogen (PdH_x) according to

$$Pd + \mathrm{x}\, H_2O + \mathrm{x}\, e^- \rightarrow PdH_{\mathrm{x}} + \mathrm{x}\, OH^- \quad . \tag{24}$$

The total amount of charge needed to extract all the hydrogen from this palladium rod far exceeded the charge needed to fully hydrogenate the working electrode. This ensured that during the electrochemical experiments no oxygen was produced at the palladium counter electrode.

When MH thin films were investigated (see Chapters 4 and 5), the active surface area of the working electrode was about 3 cm^2. The thin films were contacted with a silver (Ag) wire, which was attached using a conductive adhesive (E-solder No. 3021 from IMI). A chemically inert isolating lacquer (W40, Apiezon) was applied to the contacts and the edges of the substrate shielding them from the electrolyte.

When examining the energy storage characteristics of the CNT material (see Chapter 6), the working electrode consisted of an inert Ag electrode holder to which a pellet of CNT material, mixed with Ag powder, was attached by means of a shrink sleeve. More information on the exact preparation of the bulk electrodes can be found in Section 6.2.

3.3. Bulk & thin film research

Materials research is generally performed on sample geometries that are best suited to a particular method of characterization. Overall, these sample geometries can be divided into several groups; (i) bulk samples like wires and sheets, (ii) bulk samples in powder form, (iii) active material as a thin film deposited on a substrate, (iv) single particles, and (v) single crystals. In this regard, powder samples are most often used as these can be handled without much difficulty and easily characterized with most equipment. Depending on the apparatus or measurement method it might, for example, be necessary to press the powder into pellets, either pure or mixing it with inactive matrix material. On the other hand, bulk powder samples are often poorly defined (large particle size distribution, rough surfaces, *etc.*) and this might entice a scientist to opt for the more model-like systems like thin films, single particles or single crystals. Of these three, the thin film geometry is the easiest to manufacture and handle. In general, thin films might be regarded as 2D model systems due to their very well-defined surface area and layer thickness.

Both the thin film and the bulk system have their distinct advantages and disadvantages in modern materials research, which also includes electrochemical characterization methods. In this section a brief overview is given hereof, raising awareness of both the difficulties and gains that can arise when using that particular sample geometry.

Thin films

Advantages:

1. Well-defined surface area. The surface of the thin films is, generally, featureless and only shows roughness on the nanometer-scale.
2. Uniform layers can be deposited ranging from several tens of nanometers up to microns. In-plane diffusion lengths can thus be estimated easily.
3. The volume expansion upon hydrogenation is effectively compensated, due to the apparent elasticity of thin films.
4. Optical properties of MHs can be measured without difficulty.
5. Enhanced solid-solubility is observed during deposition of the thin films, making it easier to produce meta-stable compounds.

Disadvantages:

1. The active mass of thin films is generally very low (in the order of μg to mg), making them quite susceptible to parasitic influences.
2. Due to their small surface area, thin films can be poisoned rapidly.
3. X-ray diffraction can be problematic due to preferential orientation of the film, leading to a substantial reduction in the number of diffraction peaks.
4. The morphology can depend heavily on the preparation method. For example, sputtered films might not be exactly the same as e-beam deposited films.
5. Clamping effects can influence the volume expansion upon hydrogenation. This can result, for example, in uni-axial expansion.

Bulk powders

Advantages:

1. Relatively large sample mass, which reduces weighing errors.
2. The total surface area is, as a rule, large (in the order of m^2/g and higher). This large area significantly reduces the effect of surface poisoning.
3. Generally stable in pellet form.
4. X-ray diffraction yields good results on crystalline compounds, due to the fact that there is no preferential, but random, orientation.

Disadvantages:

1. Powders show a large particle size distribution in as-produced form. This leads to, for example, a distribution in diffusion length.
2. The surface of the particles is generally rough and not well-defined.
3. Volume expansion upon hydrogenation is poorly accommodated, leading to hydrogen embrittlement.
4. Meta-stable compounds require a lot of effort to manufacture in bulk form.

3.4. Measurement techniques

3.4.1. Introduction

In this section the electrochemical measuring techniques used in this thesis will be briefly explained. These techniques are based on the fact that the current through, or the potential of the working electrode is controlled (the independent variable or stimulus), while the voltage

or current, respectively is determined as a function of time (the dependent variable or response). The *galvanostatic* approach and *Galvanostatic Intermittent Titration Technique* (GITT) are treated in Section 3.4.2, whereas the controlled potential technique of *Cyclic Voltammetry* (CV) is described in Section 3.4.3.[65] Additionally, *Electrochemical Impedance Spectroscopy* (EIS) will be explained separately as it is quite different from the aforementioned techniques (see Section 3.4.4).[66]

3.4.2. Galvanostatic measurements

3.4.2.1. Galvanostatic charging and discharging

In the situation of galvanostatic experiments a controlled, constant current is applied to the working electrode and the resulting working electrode potential is measured. This technique is also called a *chronopotentiometric* technique, as the voltage is recorded in time. The experimental set-up for these types of experiments is schematically depicted in Fig. 19.

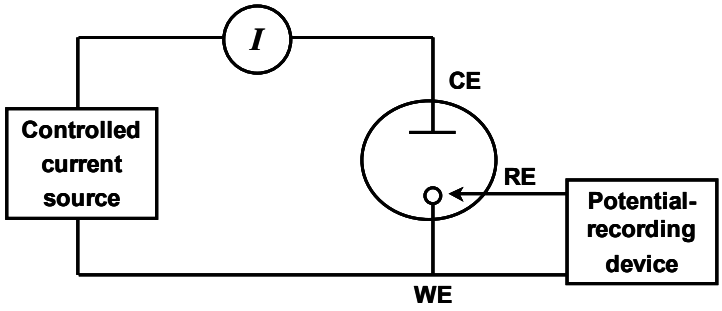

Fig. 19: Simplified block diagram of a chronopotentiometric measurement device. The working-, counter- and reference electrode are denoted as WE, CE and RE, respectively.

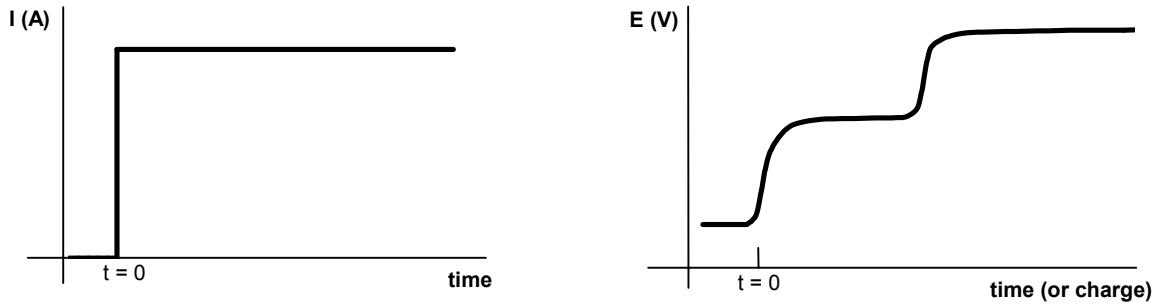

(a) (b)

Fig. 20: An applied constant current at t = 0 (a) and a possible response of the working electrode potential (b).

The constant current applied to the electrode causes reactants at the electrode surface to react. The potential of the working electrode changes to values characteristic of the electrochemical reaction that is occurring. The potential-time curve for a constant current experiment of a material with two well-defined reactions could look like the plot shown in Fig. 20b. It is

noted that in practice for many electrode materials the reactions are usually less well-defined, resulting also in less-obvious plateaus in the potential-time curve.

Galvanostatic experiments provide a means to gain information about the charge and discharge capacities of electrode materials. For example, as the discharge current is constant in time, the multiplication of the applied current and the charging time will yield the exact amount of charge transferred during a particular potential response of the working electrode. This allows for the fact that, for example, the hydrogen concentration in a hydride-forming compound can be precisely tuned, as ideally one electron is transferred per hydrogen atom stored.

3.4.2.2. GITT charging and discharging

A derivative of the standard galvanostatic measurement is GITT. This technique is generally used to obtain equilibrium data (at zero current) of an electrochemical system. However, in order to measure equilibrium properties no external current can or may be applied as this would inevitably result in non-equilibrium conditions. To overcome this problem, galvanostatic pulses and relaxation periods are continuously alternated as is shown in Fig. 21. Firstly, a (short) current pulse is applied to the system during which a small amount of charge is transferred, thereby slightly changing the oxidation state of the material under investigation. Hereafter the electrode is allowed to relax to its new equilibrium under open-circuit conditions. This procedure is repeated until the compound has reached, dependent on the current applied, its fully oxidized or reduced state. Schematically this is shown in Fig. 21 where the applied current (a) and the corresponding potential response of the working electrode (b) are shown with respect to the same time axis.

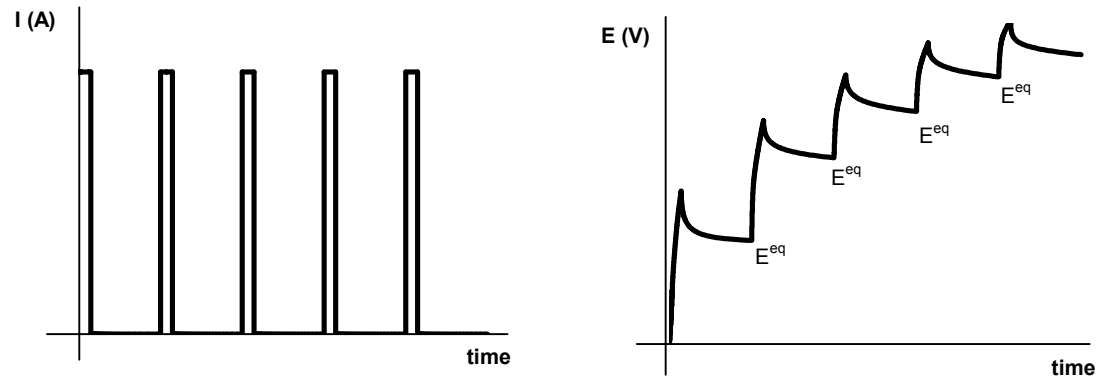

(a) (b)

Fig. 21: Current pulses applied to the working electrode (a) and the resulting potential response (b).

3.4.3. Cyclic voltammetry

A schematic representation of the system used to perform *potentiostatic* (or potential step) measurements is depicted Fig. 22. The same arrangement can be used for other potential-controlled experiments, like potential sweep measurements or CV. In this set-up the potentiostat controls the voltage between the working electrode and the reference electrode.

The potentiostat itself can be seen as an active element whose job it is to force through the working electrode, at any time, whatever current is required to achieve the desired potential between the working and reference electrode. Furthermore, it assures that current is only flowing through both the working- and counter electrode, whereas the current passing through the reference electrode remains infinitesimally small at all times.

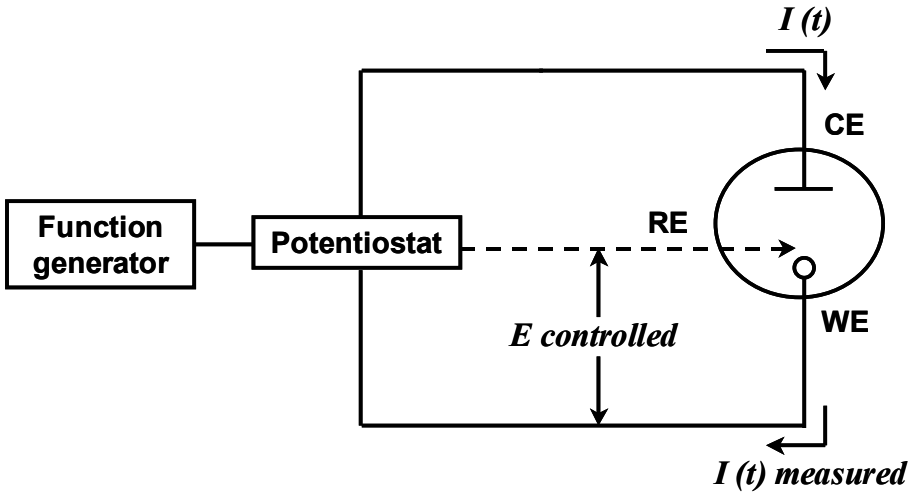

Fig. 22: Experimental arrangement for controlled potential experiments. The working-, counter- and reference electrode are denoted as WE, CE and RE, respectively.

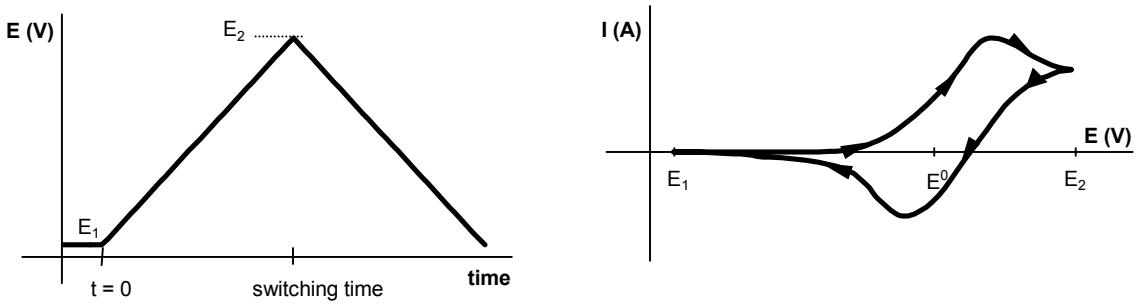

(a) (b)

Fig. 23: The applied potential sweep during the CV experiment (a) and the resulting response in the case of a reversible electrochemical process (b).

When performing CV the potential is changed continuously in time. It involves sweeping, or scanning, the electrode potential between limits E_1 and E_2 at a known sweep rate, ν. Upon reaching the potential E_2 the sweep (or scan) is reversed. On again reaching the initial potential, E_1, the measurement can be stopped or again reversed. In these experiments it is customary to record the current as a function of potential, resulting in an *I-E* plot. Cyclic voltammetry is a very useful technique to obtain an indication of the potentials at which electrochemical processes occur, yielding a 'fingerprint' of the electrode material. At potentials where an electrochemical reaction occurs, a current will flow through the working electrode, resulting in a peak in the *I-E* plot. An example of a typical cyclic voltammogram for a reversible electrochemical process is given in Fig. 23.

For the experiment shown in Fig. 23, the scan is started at E_1, a potential well negative of E^0, which is standard redox potential of a given redox system. When the electrode potential starts to change towards E_2 and reaches the vicinity of E^0, an oxidation reaction is initiated, resulting in a positive current response. As the potential is changed towards more positive values, the surface concentration of the reacting agent drops, hence the flux to the surface and the current, increases. Upon further increasing the potential, the surface concentration drops nearly to zero and the mass transfer to the surface reaches a maximum rate before it declines. The observation is therefore a peaked current-potential curve like that depicted. When the potential scan is reversed at that point (E_2), the potential is suddenly sweeping in a negative direction. In the vicinity of the electrode there is a large concentration of the reducible reactant that had just been oxidized. As the potential approaches and passes E^0, more and more of the reactant will be reduced, resulting in a negative current. The *I-E* curve in this reverse scan has a shape much like that in the forward scan, for essentially the same reasons. It should be noted that the shape of the curve in a cyclic voltammogram may differ significantly from the curve depicted in Fig. 23, depending on the number of reactions that occur, the reversibility of the reaction, the type of reaction, the equilibrium potential of the reaction, the rate of the reaction and the scan rate.

3.4.4. Electrochemical impedance spectroscopy

The principle of EIS is to perturb an electrochemical system, which is in equilibrium at a potential E_{dc}, with an alternating potential signal of small magnitude (E_{ac}) at a certain frequency and to observe the response of the system to this perturbation. The alternating signal should ideally be relatively small, such that linearity, causality and stationarity of the system are preserved. The main advantage of this technique is that by analyzing a large frequency range (MHz – mHz), information can be obtained about the (chemical) processes under investigation.

During an impedance spectroscopy experiment, a potential that consists of a constant value (E_{dc}) and a superimposed alternating value (E_{ac}) is applied to a steady-state system according to

$$E = E_{dc} + E_{ac} = E_{dc} + E_m \sin(\omega t) \tag{25}$$

where E_m is the amplitude of the sinusoidal perturbation, which is usually small (< 10 mV) and ω is the frequency of the perturbation. Typical values for this frequency are between 10^{-4} Hz and 10^6 Hz. If the amplitude of the perturbation is relatively small, the response of the resulting current will be linear, only with a phase shift ϕ (see Eq. 26).

$$i = i_{dc} + i_{ac} = i_{dc} + i_m \sin(\omega t + \varphi) \tag{26}$$

where i_{dc} is the direct current part; i_{ac} is the alternating current part; and i_m is the amplitude of the alternating current.

For a pure resistance R the resulting current can be described as

$$i = \frac{E}{R} = \frac{E_{dc}}{R} + \frac{E_m}{R}\sin(\omega t) \quad . \tag{27}$$

Subsequently, its impedance Z can be defined as

$$Z = \frac{E_{ac}}{i_{ac}} = R \ . \tag{28}$$

For a pure capacitor C the current is given by

$$i_C = C\frac{dE}{dt} = i_{ac} = C\,E_m\,\omega\cos(\omega t) = C\,E_m\,\omega\sin(\omega t + \pi/2) \ . \tag{29}$$

It is clear that the phase shift for a capacitor is π/2 or 90°. To be able to take this phase shift into account when defining an expression for the impedance, a complex impedance is defined, consisting of a real and an imaginary part. Therefore it is more convenient to write

$$E = E_{dc} + E_{ac} = E_{dc} + E_m\,e^{(j\omega t)} \tag{30}$$

where $j = \sqrt{-1}$, and $e^{(j\omega t)} = \cos(\omega t) + j\sin(\omega t)$, according to *Eulers equation*. The alternating current component of the double layer current is now given by

$$i_{ac} = j\,\omega\,C\,E_m\,e^{(j\omega t)} \quad . \tag{31}$$

The j in this equation implies that the *ac* current is in exact opposite phase with the *ac* potential E_{ac}. Subsequently, the impedance of a capacitor can be written according to Eq. 32.

$$Z_C = \frac{E_{ac}}{i_{ac}} = \frac{1}{j\omega C} = -\frac{j}{\omega C} \tag{32}$$

As *Kirchhoff's laws* apply to these complex impedances, a capacitor C and a pure resistance R placed in series (modeling an ideal polarizable electrode and a finite Ohmic resistance of an electrolyte solution) would yield a total impedance according to

$$Z_{tot} = Z_R + Z_C = R - \frac{j}{\omega C} \quad . \tag{33}$$

This equation again shows that the total impedance is generally made up of a complex and a real part.

When a redox reaction occurs at the electrode/electrolyte interface, the total current will be that of the sum of the double layer charging current (i_{dl}) and the Faradaic current (i_{Far}), yielding

$$i_{tot} = i_{dl} + i_{Far} = C_{dl}\frac{dE}{dt} + nFv \tag{34}$$

in which C_{dl} is the double layer capacitance; n is the number of electrons transferred in the reaction; F is the Faraday constant; and ν is the rate of consumption of electrons per cm^2 of the electrode [mol/(s·cm)]. ν is defined as

$$v = \frac{1}{A}\frac{dn}{dt} \tag{35}$$

in which A is the electrode surface area [cm^2].

The sum of two currents is equal to placing two impedances parallel to each other. The total impedance for the double layer impedance and the Faradaic impedance ($Z_{Far} = R_{ct}$, or the charge transfer resistance) is therefore equal to

$$\frac{1}{Z_{tot}} = \frac{1}{Z_C} + \frac{1}{Z_{Far}} = j\omega C_{dl} + \frac{i_{Far,ac}}{E_{ac}} \quad . \tag{36}$$

Rewriting yields

$$Z_{tot} = \left(j\omega C_{dl} + \frac{1}{R_{ct}} \right)^{-1} = \frac{R(1 - j\omega C_{dl} R_{ct})}{1 + \omega^2 C_{dl}^2 R_{ct}^2} \quad . \tag{37}$$

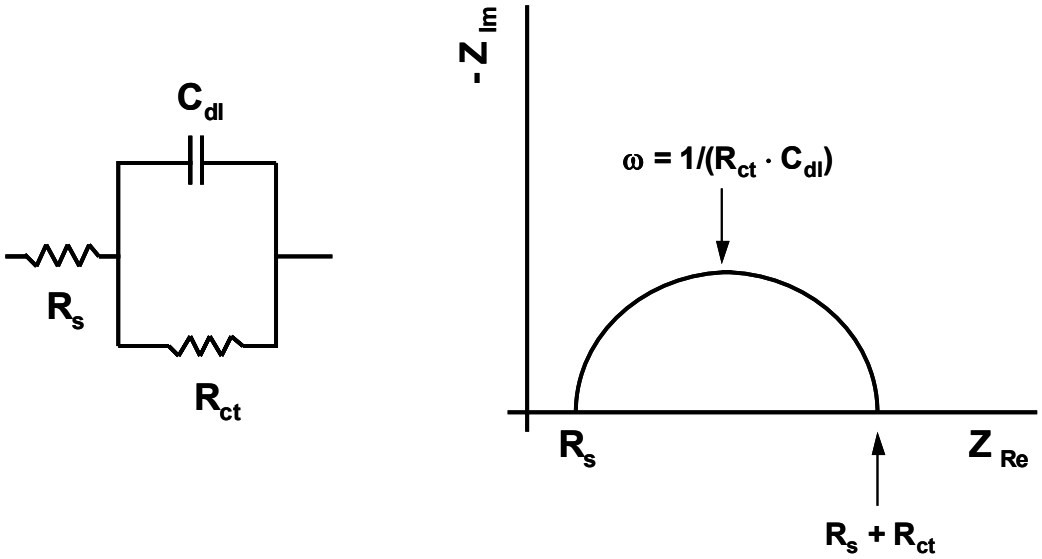

Fig. 24: The equivalent circuit and the Nyquist plot of an electrode in an electrolyte solution at which an electrochemical reaction occurs at the electrode/electrolyte interface.

Usually the impedance of an electrochemical system is measured over a large frequency range and the results are plotted in an *impedance spectrum*. It is most common to plot $-Z_{Im}$ *vs.* Z_{Re} for different values of ω (a Nyquist plot). When the impedance described by Eq. 37 is plotted in a Nyquist plot, it will result in a semicircle. In reality though, there will always be a small Ohmic resistance, R_s, in series with the two parallel impedances, due to the resistance of the electrolyte solution. Because of this, the semicircle originating from the two parallel impedances will shift along the Z_{Re}-axis with a value of R_s. The equivalent electrical circuit and corresponding Nyquist plot are shown in Fig. 24.
Apart from the kinetics of the charge transfer reaction (R_{ct}), mass transport of reactants may also play a role in the total impedance. Semi-infinite diffusion of an active species can be described by a *Warburg* impedance element (W).

$$Z_F = R_{ct} + W \tag{38}$$

Using Fick's laws, this Warburg diffusion element can be described as[67]

$$W = \sigma \frac{1}{\sqrt{\omega}} - j\sigma \frac{1}{\sqrt{\omega}} \tag{39}$$

where σ is a constant given by

$$\sigma = \frac{RT}{n^2 F^2 \sqrt{2}} \left[\frac{1}{c_{ox}^{bulk} \sqrt{D_{ox}}} + \frac{1}{c_{red}^{bulk} \sqrt{D_{red}}} \right] \quad . \tag{40}$$

In this equation the subscripts *red* and *ox* stand for the reduced and oxidized form of the species respectively, c^{bulk} stands for the bulk concentration of the species in the solid and D stands for the diffusion coefficients of the species in the solid. The equations above show that the complex part and the real part of the Warburg impedance are equal. In a Nyquist plot this will result in a straight line with a constant phase angle of π/4 (= 45°), independent of the frequency. Once again it is stressed that this applies only for an ideal situation, in which the theoretical model perfectly describes the electrochemical system.

R_{ct} is characteristic of the exchange current and therefore of the rate constant at equilibrium, whereas σ, and thus W, is directly linked to the diffusion parameters of the system. In the high frequency range of the spectrum the Warburg impedance plays no role, as diffusion cannot keep up with the fast changes in potential. In this situation the system is kinetically controlled. At lower frequencies the diffusion is fast enough and the system can become diffusion-controlled. Fig. 25 shows an example of an equivalent circuit containing a Warburg element and an impedance spectrum of an electrochemical system that is kinetically controlled at high frequencies and diffusion controlled at low frequencies. The particular equivalent circuit shown in Fig. 25 is also known as *Randles equivalent circuit*.

The above theory shows that when EIS is employed it is thus possible to determine various material parameters as long as an accurate electronic equivalent circuit is adopted, able to accurately describe the system under investigation. However, the adopted equivalent circuit remains only an approximation of reality.

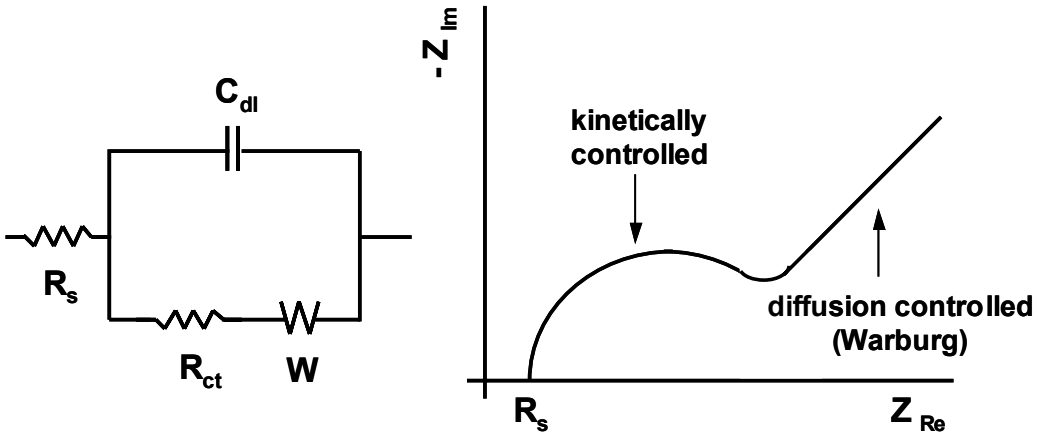

Fig. 25: The Randles equivalent circuit and a typical Nyquist plot showing the Warburg impedance.

3.4.4.1. EIS/GITT

In order to be able to perform EIS measurements at a pre-determined oxidation state (or hydrogen content in the case of an MH), a combination of GITT and EIS can be used. In this type of experiment the oxidation state of the material under investigation is continuously changed using current pulses and subsequent relaxation steps as described in Section 3.4.2.2. Additionally, an EIS measurement is performed at the open-cell potential after the system has reached its new equilibrium (at the end of the relaxation step). By doing this, accurate EIS data is obtained at every oxidation state.

3.5. Oxygen influence on electrochemical response

3.5.1. Introduction

Generally, electrochemical investigations on either bulk or thin film electrodes are conducted in experimental set-ups where an inert purging gas is used to de-aerate the electrolyte. This is done to ensure that the undesirable impact of oxygen on the overall electrochemical response is minimized. In this section a detailed view is presented on the role of oxygen in the electrolyte, influencing the electrochemical properties of thin film electrodes. The electrodes used in the present work are thin films consisting of a MgSc alloy capped with a Pd layer. A three-electrode electrochemical cell is used in combination with either no purging gas or oxygen-free argon purging gas. It will be shown that the oxygen concentration in the electrolyte should be kept to an absolute minimum in order to obtain reliable long-term electrochemical data.[68]

3.5.2. Methylviologen set-up

To ensure that the electrochemical set-up is completely free of oxygen during the measurements, argon gas was used as a purging gas. Prior to the actual measurements, purging of the cell was carried out by vigorously bubbling argon gas through the electrolyte

in both the working and counter electrode compartments for at least a few hours. During the measurements purging was done in a similar way with the only difference that the purging gas was led over, instead of through, the electrolyte in the working electrode compartment. This needs to be done as the purging gas bubbles prevent accurate voltage measurements.

Because standard argon purging gas might still contain traces of oxygen, the argon flow was first led through an oxygen scrubber in order to remove all oxygen. The oxygen-scrubbing device used to de-oxygenate the purging gas, is a system based on the high reactivity of the methylviologen (MV) single radical towards oxygen (further referred to as MV set-up).[69] MV is the common name for 1,1-dimethyl-4,4-bipyridiniumdichloride, of which the molecular structure is shown in Fig. 26.

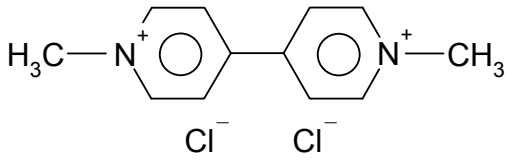

Fig. 26: Structural formula of the 1,1-dimethyl-4,4-bipyridiniumdichloride molecule.

A MV salt is dissolved as colorless MV^{2+} ions in a buffer solution of pH = 6, consisting of 0.1 M KH_2PO_4 and 0.1 M NaOH with which a glass column (h = 900 mm and ∅ 50 mm) is filled. Fig. 27 shows a schematic representation of the MV set-up. A three-electrode set-up is used to potentiostatically (E = - 0.7 V *vs.* SCE) reduce MV^{2+}, at the platinum gauze (99.999 %) working electrode, to the single radical state, according to

$$MV^{2+} + e^- \rightarrow MV^{+\bullet} \qquad E^0 = -0.68 \text{ V } vs. \text{ SCE} \qquad (41)$$

The produced $MV^{+\bullet}$ radicals, which solution has a characteristic deep-blue color, subsequently rapidly react with any oxygen present in the gas flow led through the column, according to

$$2\,MV^{+\bullet} + O_2 + 2\,H^+ \rightarrow 2\,MV^{2+} + H_2O_2 \qquad (42)$$

When $MV^{+\bullet}$ oxidizes to MV^{2+} by reacting with oxygen, none of the material is lost, as the MV^{2+} will be reduced again to $MV^{+\bullet}$ at the working electrode. This regenerative capability is also one of the most distinctive advantages of this set-up as oxygen scrubber. When a too negative potential is applied with respect to the standard redox potential of Reaction 41, not the single radical but the inactive $MV^{\bullet\bullet}$ double radical is formed, which has a brownish color in solution. The deep-blue color of the solution in the column can thus also act as a good indicator, revealing that no oxygen is present in the argon gas exiting the scrubber. It is interesting to note that in order to start-up a freshly prepared column it takes at least a few hours before it has attained its characteristic deep-blue color. Fig. 28a shows a picture of part of the MV column just when a constant potential (E = - 0.7 V *vs.* SCE) has been applied to the working electrode. Clearly visible is the colorless MV^{2+} solution with some bluish streaks of fluid with a high $MV^{+\bullet}$ concentration. Fig. 28b shows depicts the column at the time when enough radicals have been formed to color all fluid deep-blue.

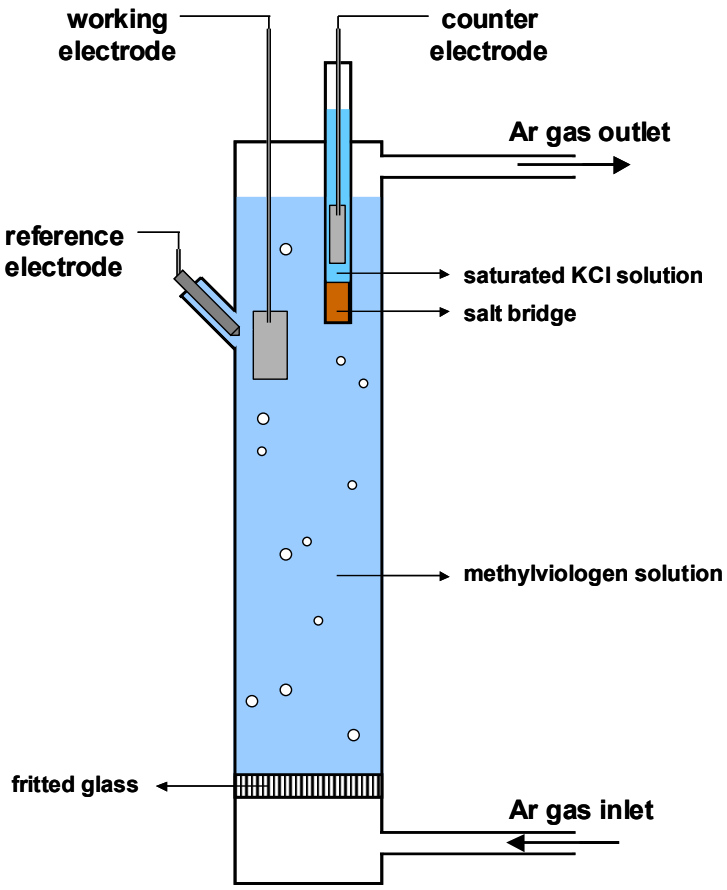

Fig. 27: Schematic representation of the methylviologen set-up as an oxygen scrubber.

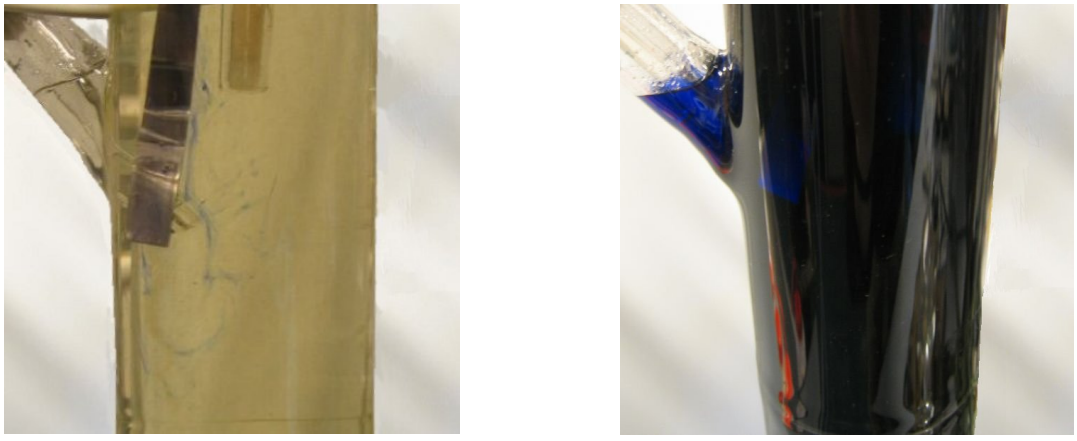

(a) (b)

Fig. 28: Photographs showing part of the methylviologen column. Shortly after a constant potential (E = - 0.7 V *vs.* SCE) has been applied to the working electrode, blue radicals are formed in the colorless fluid (a). After some time enough radicals have been formed to color the entire fluid deep-blue (b).

The oxygen-purified argon gas is transported to the measurement set-ups using stainless steel Swagelok™ tubing. This prevents oxygen from penetrating the walls of the tubing between the column and the electrochemical cells and eventually ending up in the KOH

electrolyte. It is interesting to note that the purging gas, which has passed through the MV set-up, is not only purified of oxygen but also saturated with water, resulting in the fact that it will be unable take up any more water when passing through the electrolyte in the measurement cell. This ensures that the pH of the electrolyte remains unchanged, even when performing long-term experiments.

3.5.3. Theoretical considerations

In order to understand the impact of oxygen on the electrochemical response of, especially, thin film MH electrodes, it is of the utmost importance to know how oxygen influences the overall electrochemistry of the system under investigation. In Fig. 29 the current-voltage (*I-E*) relationships of the redox systems of interest are schematically depicted. The electrochemical charge-transfer process of the MH electrode is indicated by curve (a). The equilibrium potential E_{MH}^{eq} corresponds with the true equilibrium value of the MH electrode at a specific hydrogen concentration. In the case that oxygen is dissolved in the electrolyte a second redox couple, that of O_2/OH^-, is present (curve (b). As can be seen, the oxygen reduction process is assumed to be diffusion-controlled and potential-independent at potentials well below $E_{O_2}^{eq}$ resulting in a constant reduction current. This is reasonable, as all oxygen will instantly react at the electrode surface at very large negative overpotentials. The magnitude of this reduction current is a function of the concentration of oxygen in the electrolyte and will decrease with decreasing oxygen concentration.

When no oxygen is present in the electrolyte, no charge is transferred by the MH electrode under equilibrium conditions and, consequently, the true value E_{MH}^{eq} is measured at any hydrogen concentration. The presence of oxygen drastically changes this as oxygen can be continuously reduced at the MH/electrolyte interface, using electrons supplied by the oxidation of the hydride. This can be represented by the following reaction sequence

$$\begin{array}{l} MH_x + x\,OH^- \rightarrow M + x\,H_2O + x\,e^- \\ \frac{1}{4}x\,O_2 + \frac{1}{2}x\,H_2O + x\,e^- \rightarrow x\,OH^- \\ \hline MH_x + \frac{1}{4}x\,O_2 \rightarrow M + \frac{1}{2}x\,H_2O \end{array} + \quad . \qquad (43)$$

Assuming that the magnitude of the oxygen reduction current is I_1, summation of curves (a) and (b) would result in the overall *I-E* characteristic visualized by curve (c). This implies that under open-circuit conditions a mixed-potential (E_{MH}^{mp}) is established where oxygen is reduced with current I_1 and MH oxidized with an equal but opposite current. Due to the fact that E_{MH}^{mp} is more positive than E_{MH}^{eq} the electrode will continuously self-oxidize hydrogen, causing E_{MH}^{eq} to constantly change because this value is dependent on the hydrogen content in the material. This process will continue until, eventually, all hydrogen stored in the MH has been extracted.

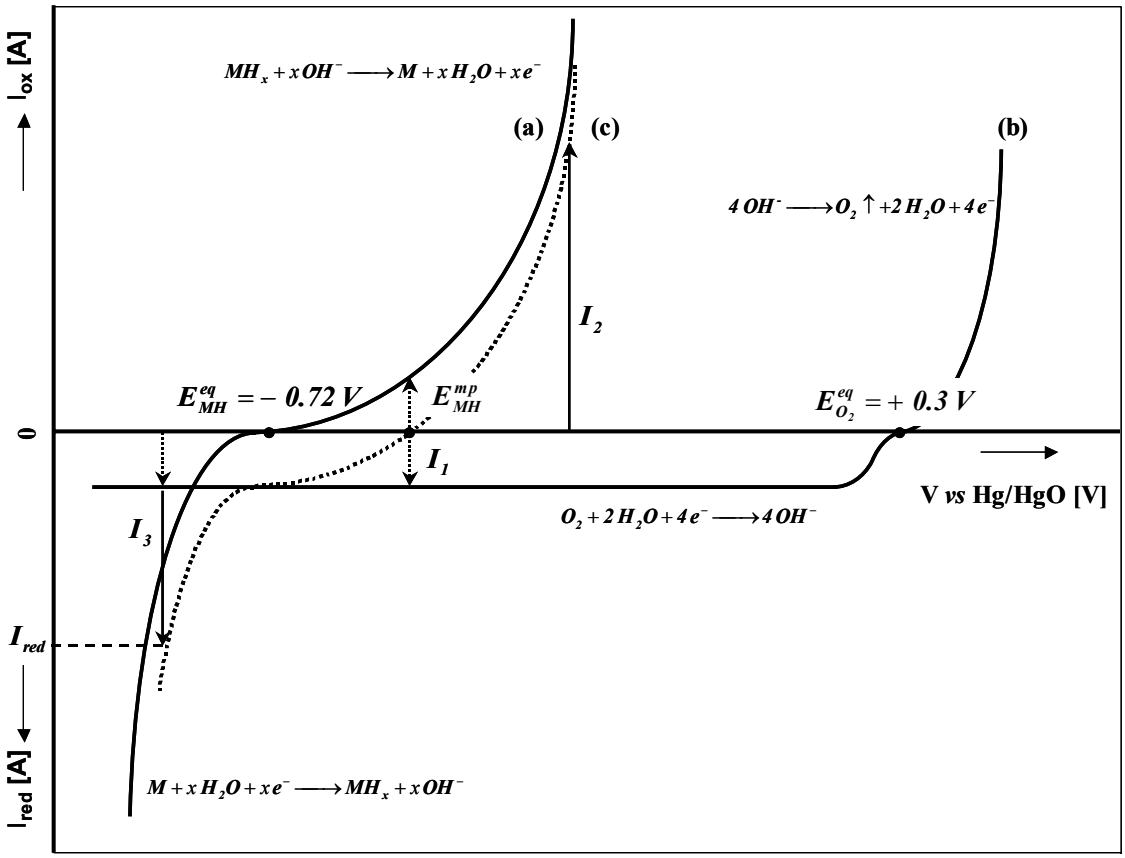

Fig. 29: Electrochemical representation of the *I-E* relationships of the two main redox systems when measuring in an oxygen-containing electrolyte. These are the electrochemical charge-transfer process of the MH electrode (a) and the O_2/OH^- system (b). Curve (c) represents the overall *I-E* characteristic which is the summation of curves (a) and (b). A constant oxygen reduction current (I_1) will give rise, under open-circuit conditions, to a mixed-potential E_{MH}^{mp} more positive than the true equilibrium potential of the hydride system E_{MH}^{eq}.

Summarizing, the presence of oxygen will result, under open-circuit conditions, in an apparent equilibrium potential more positive than the true equilibrium potential. As can be deduced from Fig. 29, a higher oxygen concentration will lead to a higher O_2 reduction current ($> I_1$) and hence to a more positive mixed-potential (E_{MH}^{mp}). This mixed-potential will cause, in turn, continuous self-discharge and lower hydrogen content in the electrode. Consequently, less charge can be withdrawn during the entire discharge process, leading to a lower apparent hydrogen storage capacity. Of course, these deviations are strongly dependent on the time scale of the electrochemical experiment performed. The deviation of the hydrogen storage capacity will therefore be more pronounced when the self-discharge process is given more time to extract hydrogen. At this point it is interesting to note that the influences described above essentially always manifest themselves as long as oxygen is present within the system and are more dominating when the total amount of charge that can be stored in a particular hydride electrode is very small. This holds for both thin film and single-particle electrodes.

3.5.4. Influence on storage capacity

Applying the reasoning above to experimental data of 205 nm thick $Mg_{0.75}Sc_{0.25}$ thin film electrodes (coated with 10 nm of Pd), the analogies can clearly be seen. Figs. 30 and 31 show the galvanostatic discharge curves (curves (a)) and the discharge isotherms (curves (b)) of two identical $Mg_{0.75}Sc_{0.25}$ thin films, one measured in an oxygen-containing (Fig. 30) and one in an oxygen-free electrolyte (Fig. 31).

Focusing on the galvanostatic discharge experiments, which can be done on a relatively short time scale, it can be understood why only little influence can be seen of the oxygen concentration on the potential response. Upon oxidation, the system must obey at any hydrogen concentration in the electrode the overall *I-E* relationship as depicted by curve (c) in Fig. 29. Using a high oxidation current, represented by I_2, will result in the fact that oxidation will occur in the potential region described by the exponential part of curve (c). It is evident that here no large difference in overpotential exists between the processes described by curve (c) and curve (a), resulting only in a negligible difference in the potential response when comparing the galvanostatic oxidation curves measured in an oxygen-containing and an oxygen-free electrolyte. This is in line with the experimental results in Figs. 30 and 31 (curves (a)) where, for example, the main discharge plateau is situated at more or less the same potential (≈ - 0.62 V).

The only profound difference that can be observed between the galvanostatic discharge curves in Figs. 30 and 31 is that a lower discharge capacity (≈ 1400 mAh/g) is measured in the case of the oxygen-containing electrolyte as compared to the oxygen-free electrolyte (≈ 1600 mAh/g). This can of course be ascribed to the self-discharge process shown before (see Reaction 43).

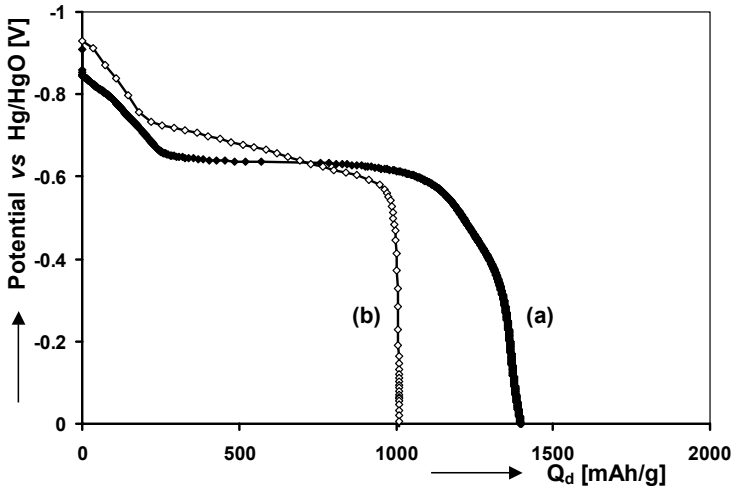

Fig. 30: Electrochemical response of a $Mg_{0.75}Sc_{0.25}$ thin film electrode measured in an oxygen-containing electrolyte. Curve (a) shows galvanostatic discharge at 40 $\mu A/cm^2$ and curve (b) shows the apparent isotherm obtained by GITT, using the same current density.

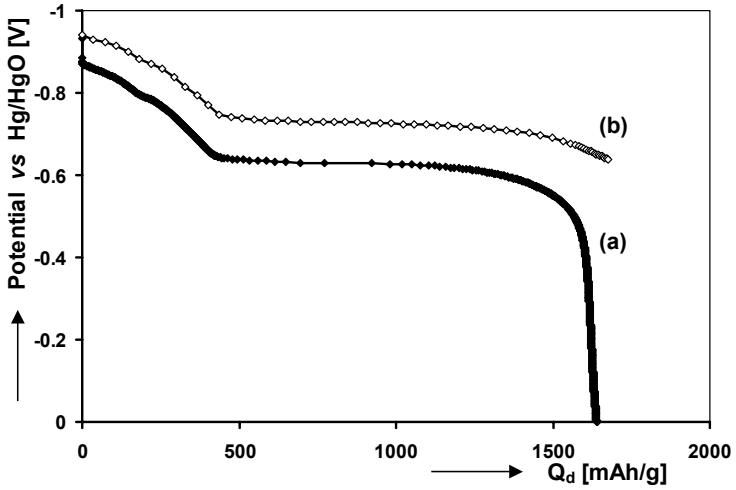

Fig. 31: Electrochemical response of a $Mg_{0.75}Sc_{0.25}$ thin film electrode measured in an oxygen-free electrolyte. Curve (a) depicts the galvanostatic hydrogen extraction curve (current density of 40 $\mu A/cm^2$) and curve (b) shows the equilibrium curve obtained by GITT, using the same current density.

3.5.5. Influence on thermodynamic response

Not surprisingly, long-term experiments like GITT measurements show much larger differences in the measured electrochemical response when comparing the measurements conducted in an oxygen-containing (Fig. 30, curve (b)) and oxygen-free electrolyte (Fig. 31, curve (b)). These differences can be well understood when considering the arguments given in Section 3.5.3.

The discharge isotherm, measured in the oxygen-free electrolyte shows the expected behavior already reported for these MgSc materials by Niessen *et al.*[70]. A flat plateau pointing to a two-phase coexistence region can be observed at around - 0.73 V and the hydrogen storage capacity is close to 1600 mAh/g. However, the isotherm measured in the oxygen-containing electrolyte shows a completely different shape. The most striking difference is that, as opposed to the oxygen-free case, a sloping plateau can be observed ranging from - 0.73 V to - 0.58 V. This would normally be linked to a solid solution-like behavior rather than a phase transition. Additionally, the apparent hydrogen storage capacity is a lot lower, only reaching about 1000 mAh/g. The discharge isotherm shown in Fig. 30, curve (b) is distorted due to two effects. Firstly, the oxygen concentration in the electrolyte results in a certain oxygen reduction current (*i.e.* I_1 in Fig. 29) and subsequently a too positive value for the equilibrium potential for all Depth-of-Discharge (DoD) values. Secondly, the hydrogen content within the electrode continuously decreases, not only due to the GITT titrations, but also due to self-discharge during this time-consuming experiment. This inevitably results in a too low value for the hydrogen storage capacity.

Up until this point only the influence of oxygen on the oxidation response was mentioned, but the electrochemical response is, of course, also affected when the thin films are hydrogenated. If during galvanostatic reduction a current I_{red} is applied (see Fig. 29), part of the applied current is used to intercalate hydrogen into the hydride material (I_3), but a certain amount, proportional to I_1, is also used to directly reduce oxygen at the electrode surface. This again means that storage capacity calculations are not straightforward and that more charge needs to be transferred to the electrode in order to reach the fully charged state. This

phenomenon is evident when examining Fig. 32 where the absorption isotherms are shown obtained by GITT experiments for the reduction of the $Mg_{0.75}Sc_{0.25}$ electrodes. The open-circuit potentials measured when using an oxygen-containing electrolyte (curve (a)) are substantially more positive than those obtained using the oxygen-free set-up (curve (b)), which represent true equilibrium. Focusing on the amount of charge transferred to each electrode, it is clear when oxygen is present, self-discharge during the relaxation period causes part of the hydrogen stored during the preceding titration to be extracted, thus leading again to unreliable values of hydrogen storage capacities. The GITT charging experiment performed using the oxygen-free purging gas does, of course, not suffer from this self-oxidation and therefore yields reliable capacities.

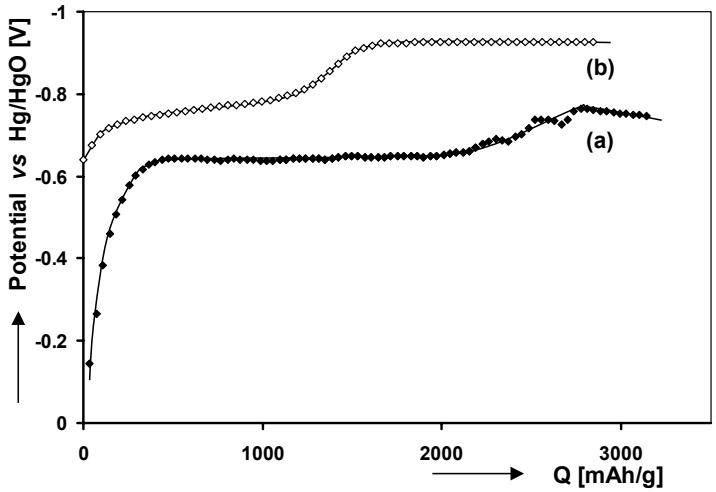

Fig. 32: Equilibrium charge curves, obtained by means of GITT, of $Mg_{0.75}Sc_{0.25}$ thin film electrodes measured in an oxygen-containing (a) and an oxygen-free electrolyte (b). On the x-axis the apparent hydrogen storage capacity is plotted.

3.5.6. Conclusions

The theoretical background (Sections 3.5.3) and experimental data (Sections 3.5.4 and 3.5.5) clearly indicate that influence of oxygen dissolved in the electrolyte on the electrochemical response of thin film electrodes should not be ignored. It was clearly shown that oxygen in the electrolyte affects the measured results in two ways. Firstly, due to the coexistence of two redox systems a mixed-potential is measured during open-circuit conditions, which is more positive than the true equilibrium potential of the hydride system. Secondly, due to continuous self-oxidation, when performing electrochemical measurements, part of the hydrogen in the electrode is extracted resulting in a lower capacity during oxidation and a higher capacity during reduction. Measurements done on a short time scale (galvanostatic measurements) suffer only slightly from the adverse effects of oxygen, yet long-term experiments (GITT measurements) are severely influenced. It is thus imperative that all electrochemical experiments are conducted using oxygen-free purging gas. This can be achieved by a self-regenerative oxygen scrubbing system based on the high reactivity towards oxygen of the methylviologen single radical (see Section 3.5.2).

3.6. Influence of surface contamination

3.6.1. Introduction

The MH materials described in this thesis exhibit very high hydrogen storage capacities and are therefore excellent candidates in a wide range of applications such as battery electrode materials[18] or as hydrogen storage materials for fuel cells. Thin films comprised of these materials can be advantageously used as 2D model systems when characterizing specific material properties. The geometry of the thin film system is especially suited for electrochemical material characterization as, for example, the interfacial area between electrolyte and solid is well defined. This subsequently enables accurate evaluation of, for example, the kinetics of the hydrogen adsorption reaction of the MH electrode under investigation. Although the geometric surface area of a thin film has a well-defined size, it is usually rather small, *i.e.* of the order of several square centimeters. This implies that surface contamination can manifest itself rather quickly under certain circumstances, thereby severely influencing the electrochemical response of the thin film electrode.[71]

3.6.2. Theoretical considerations

In order to accurately investigate the charge transfer kinetics (see Section 2.4.2) of thin film MH electrodes it is crucial that the electrode/electrolyte interface remains unchanged throughout all experiments. In the cases presented in this thesis (see Chapters 4 and 5), this interface consists of palladium (Pd) and KOH solution and the kinetics of the particular thin film electrode are therefore directly linked to the amount of Pd present at this interface. If, for some reason, during electrochemical experiments other materials are deposited onto the Pd the kinetics will certainly be influenced.

For a long time is has been known that (strong) alkaline solutions are effective etching agents, able to leach out contaminants embedded in glass. It is therefore possible that contaminants, originating from cell components made of glass, can end up in the electrolyte. Elements generally found in two different types of glass, measured by means of X-ray Fluorescence (XRF), are listed in Tables 1 and 2.

Table 1: XRF analysis of Pb-glass.

Material		Amount [wt.%]
Main	Trace	
SiO_2		64.0
PbO		20.0
Na_2O		6.9
K_2O		7.3
Al_2O_3		1.9
	Fe_2O_3	0.07
	P_2O_5	0.02
	CaO	0.07
	SrO	0.01
	CeO_2	0.22

Table 2: Composition of Duran® glass measured by means of XRF.

Material		Amount [wt.%]
Main	Trace	
SiO_2		78.0
B_2O_3		15.1
Na_2O		3.6
K_2O		0.6
Al_2O_3		2.5
	Fe_2O_3	0.03
	ZnO	0.007
	PbO	0.01
	MgO	0.015
	P_2O_5	0.003
	TiO_2	0.04
	ZrO_2	0.03
	BaO	0.01

This foreign material can, once present in the electrolyte, be deposited from solution either chemically or electrochemically. This thesis, however, is limited to electrochemical deposition of lead (Pb). The Pourbaix diagram of Pb in aqueous solutions, depicted in Fig. 33, shows that PbO species in contact with strong alkaline solutions are unstable and will mainly form dissolved $HPbO_2^-$ ions according to[72]

$$PbO + OH^- \rightleftharpoons HPbO_2^- \quad . \tag{44}$$

This means that when, for example, Pb-glass is used in a three-electrode set-up filled with an alkaline solution (*i.e.* KOH), Pb will leach out and end up as the dissolved $HPbO_2^-$ species in the electrolyte. As a chemical equilibrium exists between the dissolved and the solid species (see Reaction 44), the electrolyte within the set-up will initially be Pb-contaminated near the source only. Over a long period of time diffusion, migration and convection ensure that the entire electrolyte will be contaminated, resulting in a uniform Pb concentration. It is interesting to note that the solubility of PbO in 6 M KOH, which has a pH of 15.46, is extremely high and theoretically amounts to a concentration of $[HPbO_2^-] \approx 1$ mole/l.[72]

Once an appreciable $HPbO_2^-$ concentration has been built up in the electrolyte, it can be electrochemically deposited or stripped during current flowing conditions. Fig. 33 shows that at a pH = 15.46 and a potential range of 0 V to – 1.2 V *vs.* Hg/HgO (which correspond to standard conditions during hydrogen loading/unloading in this study) $HPbO_2^-$ can theoretically be deposited as metallic Pb at potentials more negative than - 0.74 V, according to

$$2\ HPbO_2^- + 2\ H_2O + 4\ e^- \rightleftharpoons 2\ Pb + 6\ OH^- \qquad E^0 = -0.74 \text{ V } \textit{vs.} \text{ Hg/HgO} \tag{45}$$

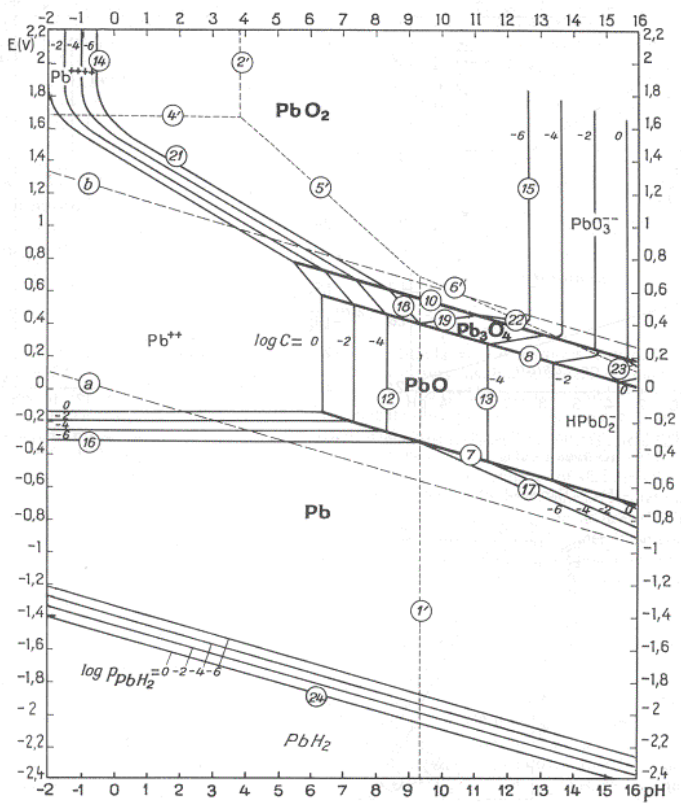

Fig. 33: Pourbaix diagram of lead (Pb) in an aqueous solution in which the equilibrium potential *vs.* NHE [V] is plotted *vs.* pH.[72]

This reaction will occur simultaneously with the electrochemical hydrogen loading of the thin film (Reaction 9). During hydrogen extraction a combination of oxidation processes occurs. Firstly, the metallic Pb covering the Pd topcoat can be oxidized to PbO at working electrode potentials according to

$$Pb + 2\ OH^- \rightleftharpoons PbO + H_2O + 2\ e^- \qquad E^0 = -0.76\ \text{V}\ \textit{vs.}\ \text{Hg/HgO} \qquad (46)$$

Additionally, the reverse of Reaction 45 can occur at potentials more positive than - 0.74 V, converting metallic Pb back into $HPbO_2^-$ species. Finally, when the electrode potential becomes more positive than 0 V, higher oxides like Pb_3O_4 can be formed (see Fig. 33). This shows that the deposits covering the surface can be comprised of a mixture of metallic Pb and Pb-oxides in varying ratios. The exact composition of these Pb deposits depends on the electrochemical potential of the thin film electrode, the concentration of species participating in the electrochemical reactions and the chemical equilibria of the dissolved and solid Pb species.

Deposits covering the thin film electrode will severely influence the kinetics of the charge transfer reaction (Reaction 9). Depending on the material deposited, contaminants can alter the kinetics in two different ways. Firstly, if the deposit is able to form a hydride itself and remains stable in alkaline solutions, the charge transfer reaction (Reaction 9) and the absorption reaction (Reaction 10) will manifest themselves at the Pd as well as the deposit. The rate at which Reaction 9 occurs depends on many different factors that are basically related to the specific compound and will therefore not be the same at both materials. This, in turn, means that a mix of the kinetics at the Pd and at the deposit will bring about the overall

kinetic response of the thin film electrode. It must be noted here that this only holds if the overall kinetics of the hydrogen storage reaction is rate determined by Reaction 9 and not by the hydrogen absorption reaction (Reaction 10). As this study focuses on Pb deposits that are, under normal electrochemical conditions, not able to form hydrides themselves a more detailed view on this possibility is omitted.[72]

The second scenario that can occur is that a material is deposited on top of the Pd, which is not able to form a hydride (in this case Pb). This implies that, although Reaction 9 will occur at both the Pd (palladium) and the Pb (lead), Reaction 10 will only occur at the Pd. The kinetics of Reaction 9 can be described by the previously derived *Butler-Volmer equation*

$$I = I_0\left(e^{\left[\frac{\alpha\eta F}{RT}\right]} - e^{\left[\frac{-(1-\alpha)\eta F}{RT}\right]} \right) \tag{19}$$

where I_0 is the exchange current. It is generally accepted that I_0 is a crucial parameter in describing the kinetics of an electrochemical charge transfer reaction. The relationship for I_0 has been derived by Notten *et al.* and can expressed as[73, 74]

$$I_0 = FA_0 k_a^{(1-\alpha)} k_c^{\alpha} \theta^{x(1-\alpha)} (1-\theta)^{\alpha} a_{OH^-}^{y(1-\alpha)} a_{H_2O}^{\alpha z} \tag{47}$$

with k_i are the rate constants of the electrochemical charge transfer reaction (reaction 1); A_0 is the electrode surface area; θ the surface coverage of H_{ad}; and a_{OH^-} and a_{H_2O} are the activities of the indicated electrolyte species at the electrode interface for which x, y, z are the reaction orders, respectively. The activities of both OH^- and H_2O can be considered as constant as diffusion limitations of these species in the electrolyte are negligible, which is reasonable due to the high concentrations in strong alkaline solutions. From Eq. 47 it is immediately clear that I_0 depends linearly on A_0. As only part of the Pd surface is covered with Pb, the overall I_0 of the system can be represented by the following relationship[74]

$$I_0 = K_{\mathrm{I}} A_{0,\mathrm{I}} k_{\mathrm{I}} \theta_{\mathrm{I}}^{x(1-\alpha)} (1-\theta_{\mathrm{I}})^{\alpha} + K_{\mathrm{II}} A_{0,\mathrm{II}} k_{\mathrm{II}} \theta_{\mathrm{II}}^{x(1-\alpha)} (1-\theta_{\mathrm{II}})^{\alpha} \tag{48}$$

where the subscripts I and II refer to Pd and Pb, respectively; $K = Fa_{OH^-}^{y(1-\alpha)} a_{H_2O}^{\alpha z}$ and $k = k_a^{(1-\alpha)} k_c^{\alpha}$. As the I_0 of the charge transfer reaction (Reaction 9) at Pb is many orders of magnitude lower than that at Pd[75], the second term on the right-hand side in Eq. 48 can effectively be neglected. This means that the overall I_0 is completely dictated by the kinetics of the charge transfer reaction at Pd. Inevitably, when surface-poisoning progresses, $A_{0,I}$ will diminish and therefore I_0 as well.

3.6.3. Influence on kinetics

The impact on the surface kinetics due to surface poisoning is illustrated by comparing two cases. In both cases similar electrochemical investigations are conducted on identical 198 nm thick $Mg_{0.70}Sc_{0.30}$ thin film electrodes, coated with 10 nm of Pd. The measurements were performed using a standard three-electrode set-up filled with 6 M KOH solution, which contained in the first case a Radiometer Type XR430 Hg/HgO reference electrode, and in the second case a Hg/HgO reference electrode from Koslow Scientific Company (further denoted

as RE1 and RE2, respectively). The main difference between RE1 and RE2 lies in the fact that different materials were used in their construction; RE1 is manufactured using a Pb-glass construction of which the composition of the used Pb-glass is listed in Table 1. RE2, however, is manufactured using a polyethylene housing. Because, as argued above, alkaline solutions are able to leach out contaminants embedded in glass, it is therefore expected that the set-up containing RE1 will be mainly contaminated with Pb whereas the set-up with RE2 essentially remains free of contaminants. It should be noted that the Hg, HgO and the filling solution of both REs have been analyzed to be of sufficiently high purity. Furthermore, care was taken that all other components of the set-up, as well as the electrolyte, did not contain more than mere trace amounts of contaminants (not shown here).

Fig. 34 shows the Rutherford Backscattering Spectroscopy (RBS) spectrum of a freshly prepared sample that has not yet been electrochemically hydrided/dehydrided. It is clear that, besides the response of the quartz substrate (A), only the elements are visible that were deposited by means of electron-beam deposition. Peaks B and C can be correlated to Mg and Sc, respectively, while peak D corresponds to Pd of the cap layer. Evidently, the Pd topcoat successfully protects the MgSc thin film from corrosion, as no oxygen response can be observed. Additionally, no other responses are present that point to contamination with other elements at this stage.

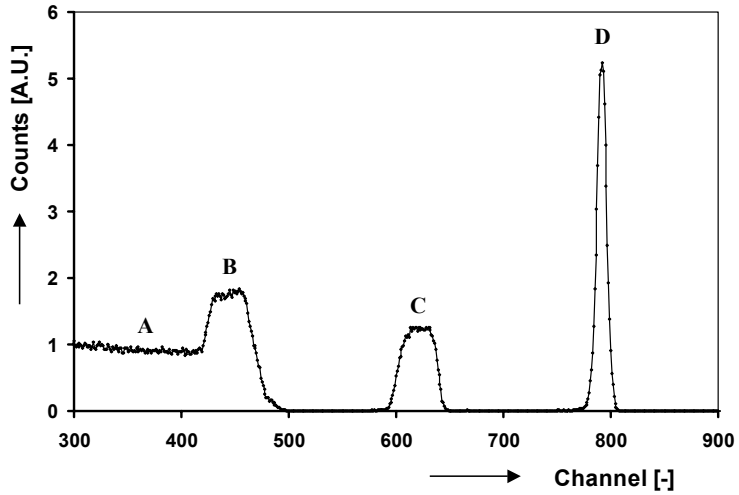

Fig. 34: RBS spectrum of a freshly prepared Pd-coated $Mg_{0.70}Sc_{0.30}$ thin film. The responses of interest are indicated with capitals letters: quartz substrate (A), Mg (B), Sc (C) and Pd (D).

3.6.3.1. Contaminated case (set-up with RE1)

The first set of electrochemical experiments was performed, using the set-up containing RE1. First, the thin film was galvanostatically fully loaded with hydrogen, using a current of - 0.6 mA. Subsequently, it was discharged (extraction of hydrogen) by means of GITT using a current of + 0.12 mA initially and + 0.012 mA during the last five pulses, corresponding to 938 mA/g and 93.8 mA/g, respectively. After each pulse the electrode was allowed to equilibrate for 1 hour. Fig. 35 shows both the obtained equilibrium curve as well as the potential response of the thin film during each current pulse. It is clear that the overpotential is increasing steadily during the GITT measurement. As will be demonstrated later, this

increase is not related to the concentration of hydrogen in the thin film, but to contaminants deposited onto the Pd top layer that influence the electrode kinetics.

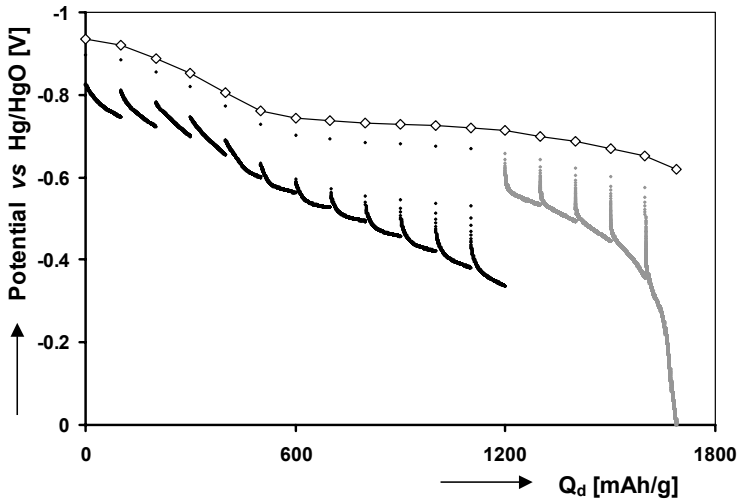

Fig. 35: Electrochemical response of a Pd-coated $Mg_{0.75}Sc_{0.25}$ thin film electrode measured in a Pb-contaminated set-up. Besides the equilibrium curve (◇), the potential responses during every GITT pulse are shown. The current used during the GITT pulses: + 0.12 mA (bold line), + 0.012 mA (gray line).

To investigate the influence of surface poisoning on the electrode kinetics in time, the same thin film electrode was subsequently kept at a constant potential of - 0.925 V for 7 days. At this potential the electrode remained in its fully hydrogenated state while hydrogen gas formation was kept to a minimum as in the used electrolyte this process mainly occurs at potentials more negative than - 0.931 V.[70] At regular intervals EIS measurements were performed of which the Nyquist representations are shown in Fig. 36. Distinct semi-circular impedance responses can be seen which represent the charge transfer kinetics of the thin film system (Reaction 9). It is evident that keeping the thin film electrode at this negative potential (- 0.925 V) for a prolonged period of time causes the diameter of the semi-circle to increase tremendously.

The impedance data was fitted using the electronic circuit shown in the inset of Fig. 36. This circuit is generally used to model the impedance response of a charge transfer reaction (Reaction 9) coupled with semi-infinite diffusion of the hydrogen in the solid.[76] In this model the adsorption step (Reaction 10) is omitted as no apparent impedance response could be linked to this phenomenon.[77] As this section focuses on the kinetic response and not the diffusion behavior of hydrogen, the diffusion response in the EIS data will therefore not be treated. Fig. 37 clearly indicates that the fitted values for the charge transfer resistance (R_{ct}) increase linearly with time (curve (a)). This shows that the charge transfer kinetics of the thin film electrode deteriorate severely during this potentiostatic treatment. These resistance values are also directly linked to exchange current (I_0) via

$$R_{ct} = \frac{\eta}{i} = \frac{RT}{FI_0} \tag{49}$$

which is the low overpotential limit of the well-known *Butler-Volmer equation* (see right-hand axis of Fig. 37.[61]

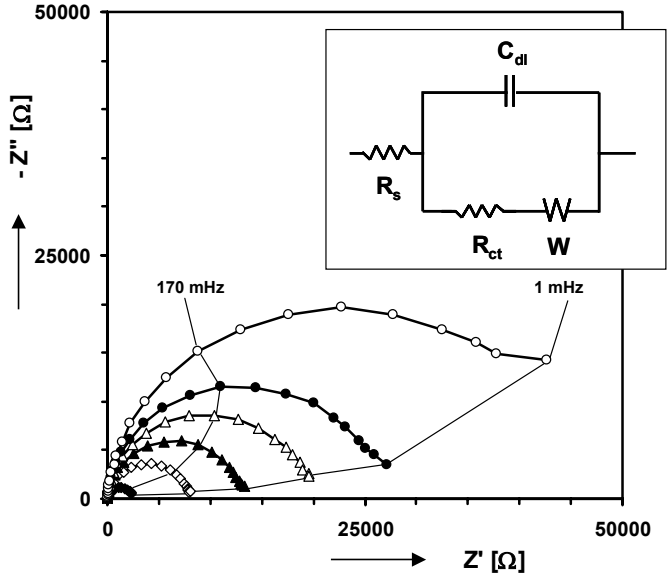

Fig. 36: Nyquist representations of a Pd-coated $Mg_{0.75}Sc_{0.25}$ thin film, measured in a Pb-contaminated set-up, for different periods of continuous polarization at – 0.925 V. Polarization time: 0 days (◆), 1 day (◇), 2 days (▲), 3 days (△), 4 days (●) and 7 days (○). The inset shows the equivalent circuit used to model the impedance data.

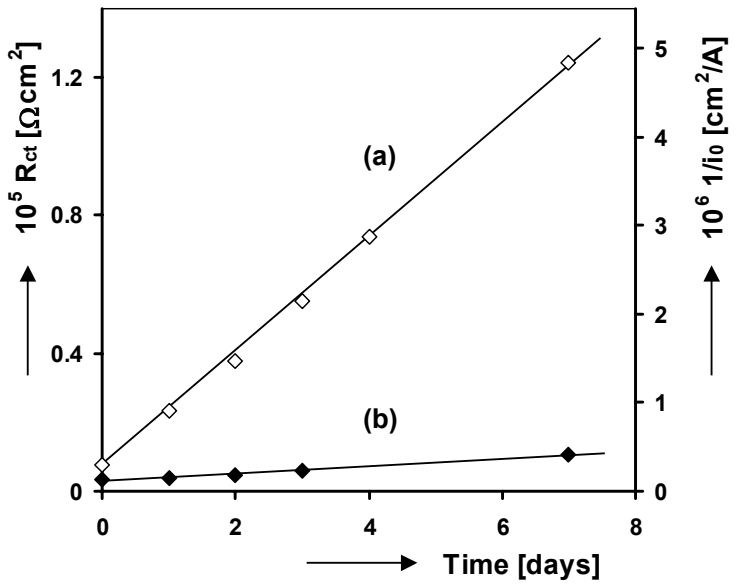

Fig. 37: Dependency of R_{ct} and i_0 *vs.* time for identical Pd-coated $Mg_{0.75}Sc_{0.25}$ thin film electrodes at a constant potential of – 0.925 V for the contaminated case (a) and contamination-free case (b).

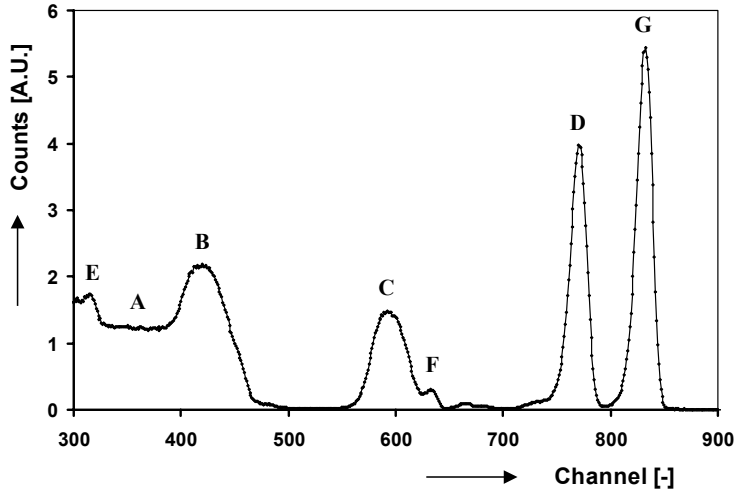

Fig. 38: RBS spectrum of a Pd-coated $Mg_{0.75}Sc_{0.25}$ thin film electrode, measured in a Pb-contaminated set-up, after electrochemical characterization and polarization for 7 days at – 0.925 V. The responses can be attributed to: quartz substrate (A), Mg (B), Sc (C), Pd (D), oxygen (E), Sc at the surface (F) and Pb (G).

To check the total amount of Pb deposited on the Pd topcoat of the thin film, RBS was used (see Fig. 38). The spectrum is very similar to the one shown in Fig. 34, except for the responses designated E through G. Electrochemically measuring the thin film for an extended period of time (at this stage 2 weeks in total) has led to partial oxidation of the thin film electrode giving a clear oxygen response (E). Judging from the position of peak F it appears that the topside of the electrode has become extremely rich in Sc. This implies that the composition of the Mg and Sc in the alloy is no longer constant throughout the entire film. The most remarkable change though, is the existence of a very strong response related to deposited Pb (G). Integration of this peak shows that in total 25 * 10^{15} atoms Pb/cm^2 were deposited, which corresponds to about 30 monolayers of metallic Pb if complete coverage of the Pd topcoat is assumed.

Additionally, Inductively-Coupled Plasma Mass Spectrometry (ICP-MS) was used to determine the Pb concentration of the filling solution (0.1 M KOH) of an unused RE1, as-received by the manufacturer (see Table 3). Clearly, even 0.1 M KOH is able to leach out large quantities of Pb from the glass housing. These Pb contaminants would also end up in the electrolyte when RE1 would be employed directly in a three-electrode set-up. This comes as a big surprise as Hg/HgO reference electrodes are specifically designed to operate in alkaline solutions.[78]

Table 3: Pb concentration in the filling solutions of RE1 and RE2 measured using ICP-MS.

Reference electrode	Pb concentration [µg/l]
RE1	>> 500,000
RE2	31

3.6.3.2. Contamination-free case (set-up with RE2)

Identical electrochemical measurements were performed on a second MgSc thin film using the set-up containing RE2. Fig. 39 shows the corresponding equilibrium curve and the potential response during each current pulse. It should be noted that this GITT experiment was performed using the same parameters as for the contaminated case, only during the last 2 pulses a current of + 0.012 mA was used. Two observations can be made when comparing this case (Fig. 39) to the one shown in Fig. 35. Firstly, the equilibrium data seem to be identical, except for the fact that in the contaminated case the storage capacity was 1700 mAh/g (Fig. 35), while it is only 1500 mAh/g in the contamination-free case (Fig. 39). This discrepancy can be explained by the fact that in the former case not only the oxidation of hydride is measured, but also the oxidation of deposited Pb contributes. This shows that inaccurate storage capacities can be measured if the set-up contains a substantial level of contaminants. Secondly and more importantly, the potential response of the electrode during the current pulses shows a distinctly different behavior. The overpotential remains nearly constant throughout the entire discharge process and only increases when the thin film reaches its hydrogen-depleted state as expected. This clearly proves that the increase in overpotential in the initial case (shown in Fig. 35) is due to surface poisoning by Pb species.

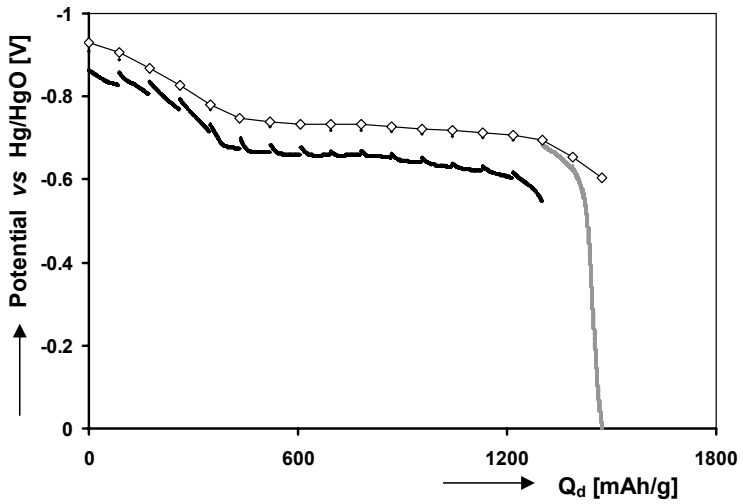

Fig. 39: Electrochemical response of a Pd-coated $Mg_{0.75}Sc_{0.25}$ thin film electrode measured in a contamination-free set-up. The equilibrium curve of the material (◇) and the potential responses during each GITT pulse are shown. The current used during the GITT pulses: + 0.12 mA (bold line), + 0.012 mA (gray line).

The charge transfer kinetics of this electrode were also investigated while keeping the thin film at a constant potential of - 0.925 V (see Fig. 40). This time, as opposed to the impedance responses shown in Fig. 36, not only semi-circular responses linked to kinetics are measured, but also low frequency responses linked to hydrogen diffusion.[79,80] Focusing on the kinetics part, it is apparent that the magnitude of the impedance over time is more than one order of magnitude smaller than the contaminated case. Fig. 37 shows R_{ct} and i_0 plotted *vs.* time for the contamination-free case (curve (b)). Interestingly, though to a much lower extent, a linear increase of R_{ct} can again be observed. From this it must be concluded that even in the contamination-free set-up minor surface poisoning must have occurred. Additionally, when comparing curves (a) and (b) in Fig. 37, the R_{ct} at the start of the potentiostatic experiment (0 days) is not equal for both electrodes. The electrode measured in

the contaminated set-up (see Fig. 35) shows a value of 2500 Ω whereas the R_{ct} of the second electrode, measured in the contamination-free set-up, is only about 1200 Ω (see Fig. 39). This indicates that during the GITT measurement, which preceded the potentiostatic experiment, some surface poisoning had already occurred in the case of the contaminated set-up.

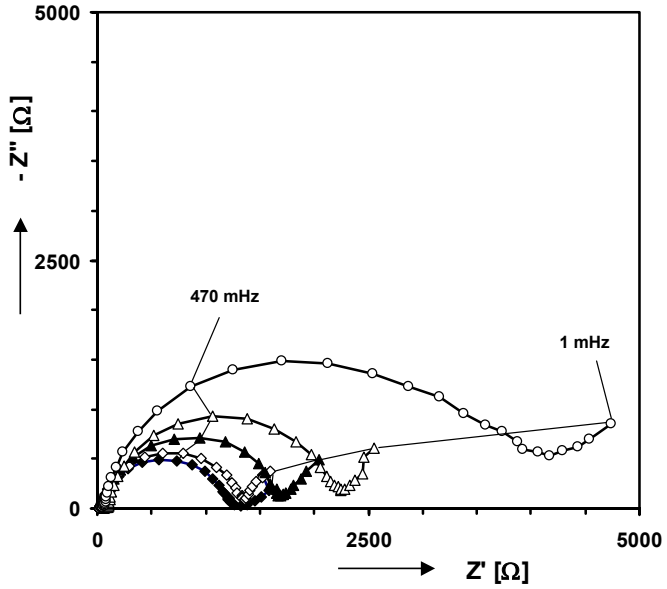

Fig. 40: Impedance responses of a Pd-coated $Mg_{0.75}Sc_{0.25}$ thin film electrode, measured in a set-up containing only trace amounts of contaminants, for different periods of continuous polarization at – 0.925 V. Polarization time: 0 days (◆), 1 day (◇), 2 days (▲), 3 days (△) and 7 days (○).

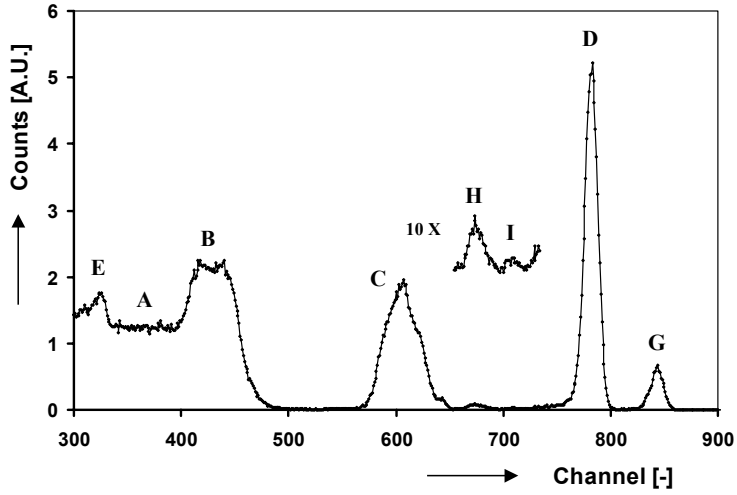

Fig. 41: RBS spectrum of a Pd-coated $Mg_{0.75}Sc_{0.25}$ thin film electrode, measured in a contamination-free set-up, after electrochemical characterization. The responses of interest can be attributed to: quartz substrate (A), Mg (B), Sc (C), Pd (D), oxygen (E), Pb (G), Fe (H) and Zn (I).

To check which materials were deposited on top of the electrode, RBS was again utilized. Fig. 41 shows the corresponding RBS spectrum, which essentially shows the same peaks as explained thus far in this paper. It can be seen that Pb was once more deposited (peak G), although in a much lower quantity ($2.5 * 10^{15}$ atoms Pb/cm^2, corresponding to 3 monolayers).

This shows that even when no apparent Pb-source is present unavoidable trace amounts present in cell components in contact with the electrolyte, can still be deposited. Looking at Figs. 38 and 41 more closely reveals that besides Pb, minute quantities of Fe and Zn were also deposited. These are indicated as peaks H and I, respectively, in the enlarged section in Fig. 41. Most likely, all these contaminants are originating from the Duran® glass from which the electrochemical cell was constructed. Therefore, if surface poisoning is to be avoided altogether, the electrochemical cell should to be constructed from a completely inert material (*e.g.* Teflon).

Table 2 shows the composition of the Duran® glass used. These results confirm the presence of trace amounts of these three elements in the glass. Fe and Zn apparently leach out from the Duran® glass after prolonged contact with strong alkaline electrolyte and are subsequently electrochemically deposited onto the thin film electrode. As the filling solution (6 M KOH) of an unused RE2, as-received by the manufacturer, contained only a trace amount of Pb (see Table 3) no significant poisoning is expected from this reference electrode.

By comparing the contaminated case (set-up employing RE1) to the contamination-free case (set-up employing RE2), it can clearly be demonstrated that dissolution of Pb-contaminants from RE1 leads to a substantial concentration of $HPbO_2^-$ in the electrolyte. This $HPbO_2^-$ can subsequently be deposited electrochemically, leading to very large differences in electrochemical response. The larger overpotential in the contaminated case (Fig. 35) as compared to the contamination-free case (Fig. 39) must be attributed to a higher R_{ct} due to Pb deposits on the surface. Fig. 37 shows that for the contaminated case R_{ct} increases linearly with time when potentiostatically depositing Pb (curve (a)). This is caused by a reciprocal decrease in I_0 brought about by a similar decrease in A_0 (see Eq. 47). This reciprocal decrease of A_0 in time can originate from the following two phenomena: Firstly, when the exposed Pd surface diminishes (due to poisoning), the probability increases that Pb nucleates and starts to form new crystals onto already poisoned areas instead of onto still exposed Pd. Secondly, Pb will preferentially be used to increase the size of existing Pb crystals that have been formed at an earlier stage. To a much lower extent, a linear increase of R_{ct} in time is also demonstrated by the contamination-free case (Fig. 37 curve (b)), which has to be linked to minor surface poisoning due to unavoidable trace amounts of contaminants in the set-up.

3.6.4. Conclusions

The results clearly point to the fact that accurately measuring the electrochemical response of MH thin film electrodes is not straightforward. Due to their small surface area, thin films are sensitive to rapid surface poisoning, which severely influences the kinetic properties. It is clear that extreme care has to be taken in making sure that all cell components are of the highest purity and do not contain more than a trace amount of impurities that can lead to poisoning. Although specifically designed to operate in alkaline solutions, the Radiometer Type XR430 Hg/HgO reference electrode (RE1) appeared to be an unexpected source of significant Pb contamination (see Figs. 35 and 38). Using a Pb-free reference electrode (RE2), an accurate electrochemical response of the thin film electrode could indeed be measured (see Figs. 39 and 41). However, minor surface contamination could not be avoided when the electrode potential was set to - 0.925 V for a very long period of time up to 7 days (see Fig. 41). At this point it is very important to note that during normal electrochemical characterization the potential of the thin film electrode might be in the potential range where Pb deposition occurs only for a few hours. Therefore, the cases presented in this section are extreme examples and the actual decrease in kinetics (or i_0), especially in the set-up that only contained trace amounts of impurities, is much less than shown in Fig. 37 (curve (b)).

Cross-correlation of the results presented in Figs. 37, 38 and 41 indicates that there seems to be a clear correlation between the amount of Pb deposited on the surface and the value of R_{ct}. When comparing the contaminated case to the contamination-free case, a ten times higher Pb concentration on the electrode surface (measured by means of RBS) resulted in an increase of R_{ct} by one order of magnitude (obtained from the impedance data).

4

Hydrogen storage in thin film $Mg_ySc_{(1-y)}$ alloys

Abstract

The electrochemical hydrogen storage properties of Pd-coated $Mg_ySc_{(1-y)}$ alloys, in which *y* varied from 0.50 to 0.90, are investigated. The maximum reversible hydrogen storage capacity is obtained with the $Mg_{0.80}Sc_{0.20}$ composition and equals 1795 mAh/g, corresponding to 2.05 H/M or 6.7 wt.% H. Both $Mg_ySc_{(1-y)}$ thin films and MgSc bulk materials show similar trends in hydrogen storage capacity and in the shape of the discharge curves with varying Sc content. However, the rate capability of the thin films is superior. Isotherms of $Mg_ySc_{(1-y)}$ thin films show that the plateau pressure is not a strong function of the Sc content and is almost equal to the equilibrium pressure of pure MgH_2. Elementary thermodynamics and the equilibrium data of pure Pd and Pd-coated $Mg_ySc_{(1-y)}$ thin film electrodes can be used to determine the exact hydrogen concentration in Pd topcoat. This reveals that the composition of the Pd topcoat is close to $PdH_{0.001}$ during the major part of the hydrogen extraction process. Impedance measurements on Pd-coated $Mg_ySc_{(1-y)}$ thin films ($y = 0.65 - 0.85$) and pure Pd films show that the surface kinetics are completely dominated by the Pd topcoat. The overall kinetic impedance, when the $Mg_ySc_{(1-y)}$ thin film electrodes are in their hydrogen-depleted state, is dominated by the transfer of hydrogen across the Pd/$Mg_ySc_{(1-y)}$ interface. Structural data obtained from MgSc bulk systems clearly demonstrate that the fully charged $Mg_ySc_{(1-y)}$ hydrides attain a single-phase fcc-structured hydride and no phase segregation takes place. Upon dehydrogenation, this fcc structure is retained and the electrochemically observed 2-phase coexistence region can be attributed to a phase transformation from a hydrogen-rich (fluorite) to a hydrogen-depleted (sphalerite) fcc structure.[*]

[*] Part of this chapter is based on: R.A.H. Niessen, and P.H.L. Notten, *Hydrogen storage in thin film Magnesium-Scandium alloys*, in press J. Alloys Compd., (2005); R.A.H. Niessen, P. Vermeulen, and P.H.L. Notten, *The electrochemistry of Pd-coated $Mg_ySc_{(1-y)}$ thin film electrodes; a thermodynamic and kinetic study*, in press Electrochim. Acta (2005); and W.P. Kalisvaart, R.A.H. Niessen, and P.H.L. Notten, *Mg-Sc alloys for electrochemical hydrogen storage; a comparative study between thin films and bulk materials*, in press J. Alloys Compds. (2005).

4.1. Introduction

Present-day MH compounds that are commercially used can generally store up to 1.2 wt.% of hydrogen. A lot of research is performed to try to increase this storage capacity in order to meet the DoE Target of 2010 (which is 6 wt.%). Interstitial hydrides comprising of alloys rich in Mg, are able to achieve capacities close to this number or even to exceed it. This chapter is devoted to the hydrogen storage characteristics of the highly promising MgSc alloys. In order to obtain a better understanding of the chemistry occurring during the (de)hydrogenation, MgSc thin films were investigated (see Section 3.3). This chapter will touch several major aspects related to the hydrogenation of these compounds. The focus lies on the galvanostatic behavior, the thermodynamic behavior, material characteristics obtained from impedance measurements and structural information via X-ray Diffraction (XRD) investigations. Each of these topics is presented and discussed in a separate section.

At present only a limited amount of research has been done on the hydrogenation properties of MgSc alloys. One of the first reviews on this system was given by Selvam *et al.* in 1986.[81] This work briefly discussed the properties of the MgSc and MgY alloys. Some years prior to this, the hydrogen absorption of a $Mg_{90}Sc_{10}$ bulk alloy was studied by Ogawa *et al.*[82]. This showed that desorption of hydrogen from a hydrided $Mg_{90}Sc_{10}$ alloy was slow, even at 400 °C. A more recent study by Morizumi *et al.* focusing on the mechanical properties of internally hydrided MgSc alloys supports these results.[83] To date, only one publication exists regarding the electrochemical hydrogenation of MgSc bulk alloys with a Sc content higher than 10 at.%. Herein, Notten *et al.* showed that compositions having a Mg content between 50 and 80 at.% revealed excellent (de)hydrogenation characteristics.[18] This was attributed to the formation of an fcc-structured MgSc hydride with beneficial properties.

Aside from the abovementioned research on bulk MgSc compounds, only a very limited amount of research performed on MgSc thin films has been published. Combined research on both bulk and thin films, performed at *Philips Research Laboratories Eindhoven*, was reported by Ouwerkerk in 2003.[84] This showed that both geometries showed comparable results when employing gas phase and/or electrochemical hydrogen (un)loading. Based on this work Giebels *et al.* performed optical measurements on MgSc thin films hydrogenated via the gas phase.[85,86]

4.2. Experimental

Thin films comprising of $Mg_ySc_{(1-y)}$, with a nominal thickness of 200 nm, were coevaporated on quartz substrates (∅ 20 mm) by means of electron-beam deposition using a Balzers BAK 550. During deposition a base pressure $8 * 10^{-8} – 4 * 10^{-7}$ mbar was maintained. The Mg content in the films was varied in the range $y = 0.50 – 0.90$. In addition, pure Mg films with a thickness equal to that of the $Mg_ySc_{(1-y)}$ films were manufactured. During deposition of the alloys the deposition rates of Mg and Sc were between 0.15 and 0.63 nm/s. In order to protect the films from corrosion and to catalyze the hydrogenation, cap layers consisting of 10 nm thick Pd were deposited on top of the thin films. In order to assess the impact of the Pd topcoat on the overall chemistry, pure Pd thin films (10 nm thick) were manufactured using the same deposition technique. A 10 Å Gd adhesion layer was evaporated onto the quartz substrates prior to the deposition of these Pd layers. This was done in order to ensure a good adhesion of the Pd film on the quartz substrate. Uniformity of composition throughout all deposited films was checked by means of RBS, which showed

that the deposition rates were controlled well. The calculation of the hydrogen content in the thin film is based purely on these RBS measurements (accuracy around 1 %). As a maximum discrepancy in the hydrogen storage capacity of the MgSc material can occur of at most 3 %, no correction is made for the hydrogen contained in the Pd cap layer.

The exact composition and mass of the thin films was measured by means of RBS (High Voltage Engineering RBS device, Model AN – 2500). The measured data was fitted using RUMP software. To investigate the crystallography of the films, XRD measurements were performed using a Panalytical MRD-PRO diffractometer. Cu-Kα radiation was used which was detected with an X'Celerator RTMS detector. These measurements were done on a rotating sample.

Electrochemical measurements were performed in a three-electrode set-up of which the specifications were given in Section 3.2. Galvanostatic measurements were performed using a Maccor M2300 battery tester (Maccor, Tulsa, USA). Electrochemical Impedance Spectroscopy (EIS) and was done on an Autolab PGSTAT30 (Ecochemie B.V., Utrecht, the Netherlands). EIS measurements were conducted at equilibrium voltage conditions using an ac amplitude of 5 mV rms and scanning the frequency from 50 kHz to 1 mHz. A non-linear least squares fitting program (EQUIVCRT) was used to analyze the EIS data.

To determine the structural properties of the hydrided materials, the hydrogenated form of the MgSc thin films were subjected to XRD analysis. During hydrogenation the samples were measured *in-situ* by placing them in a hermetically sealed sample holder with a Be-window, which was equipped with a gas inlet. Hydriding was performed in the gas-phase using a H_2 pressure of 0.9 bar. Full dehydrogenation of the sample was achieved by means of electrochemistry at room temperature and XRD analysis was subsequently performed *ex-situ*.

4.3. Results & discussion

4.3.1. Structural characterization of the as-prepared thin films

Prior to investigating the electrochemical hydrogen storage characteristics of the $Mg_ySc_{(1-y)}$ thin films, basic structural information was obtained via XRD and RBS. Fig. 42 shows the X-ray diffractogram of a $Mg_{0.65}Sc_{0.35}$ thin film coated with Pd. A hexagonal α-Mg structure is found for this composition, which is significantly different from what would be expected from the equilibrium phase diagram of Mg and Sc shown in Fig. 43.[87] From this diagram it is evident that a CsCl type solid solution of Sc in Mg is generally found between 50 and 65 at.% Mg. The single-phase α-Mg is only detected beyond 80 at.% Mg. Judging from Fig. 42, it therefore seems possible to achieve large solid-solubility extensions when using the e-beam deposition method. Most likely, the low mobility of the atoms that are directly deposited from the gas phase (at room temperature) can account for this.

The diffractogram furthermore shows that the sample is strongly oriented in the (002) direction, indicating that the crystals are oriented with their c-axis perpendicular to the substrate. All other compositions show the same crystallography and preferential orientation. The inset in Fig. 42 shows the (002) reflections of all compositions tested. A minor, but noticeable, shift in the peak position towards larger angles, *i.e.* smaller d-spacings, is apparent with decreasing Sc content. This shift of the (002) peak is brought about by partial substitution of Mg by Sc, which has a larger molar volume than Mg, causing the lattice to expand. Closer examination of Fig. 42 shows that the fcc-structured Pd topcoat is weakly oriented in the (111) direction.

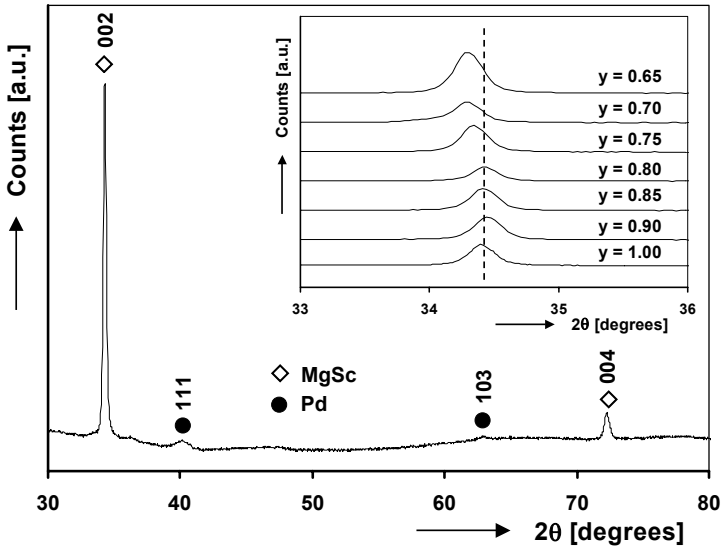

Fig. 42: X-ray diffractogram of a 200 nm thick $Mg_{0.65}Sc_{0.35}$ thin film capped with 10 nm of Pd. The (002) peak of the hexagona l α-Mg structure is shown in the inset for all measured $Mg_ySc_{(1-y)}$ compositions. The dashed line indicates the literature value of pure Mg (34.4 ° 2θ).

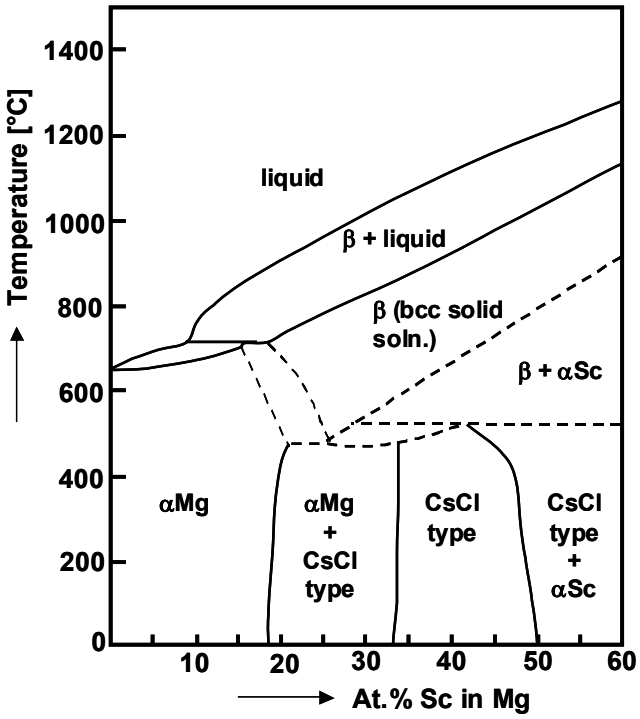

Fig. 43: Phase diagram of the MgSc system according to Beaudry *et al.*[87].

RBS measurements were performed on each batch that was manufactured in order to determine the composition, homogeneity of composition throughout the entire thin film, mass of the active material and the thickness of the individual layers. The RBS data showed that the ratio of Mg and Sc remained constant during the deposition of the thin films. The nominal composition, layer thickness and mass of all $Mg_ySc_{(1-y)}$ films described in this chapter are listed in Table 4. In all cases the $Mg_ySc_{(1-y)}$ thin films were covered with a Pd topcoat which had a thickness of 10 ± 0.5 nm.

Table 4: Layer thickness and mass of $Mg_ySc_{(1-y)}$ films with varying composition, pure Mg thin films and pure Pd thin films. *

Nominal composition [-]	Layer thickness [nm]	Mass [μg]
$Mg_{0.50}Sc_{0.50}$	200	154
$Mg_{0.65}Sc_{0.35}$	196	130
$Mg_{0.70}Sc_{0.30}$	198	127
$Mg_{0.75}Sc_{0.25}$	205	128
$Mg_{0.80}Sc_{0.20}$	200	121
$Mg_{0.85}Sc_{0.15}$	221	130
$Mg_{0.90}Sc_{0.10}$	203	115
Mg	288	151
Pd	10	35

4.3.2. The $Mg_ySc_{(1-y)}$ thin film system

Before the electrochemical responses of the Pd-coated $Mg_ySc_{(1-y)}$ thin films will be investigated it is wise to provide a basic idea of how these thin film systems can be regarded, both from a geometrical and chemical point of view. Fig. 44 depicts a 2D representation of a $Mg_ySc_{(1-y)}$ thin film, covered with a Pd topcoat. Each of the phases involved in the electrochemical hydrogen loading and the thickness of each layer have been schematically indicated. Additionally, the (electro)chemical processes of interest are shown at their appropriate locations; (a) the charge transfer reaction at the KOH/Pd interface; (b) adsorbed hydrogen forming subsurface absorbed hydrogen; (c) solid-state diffusion of H_{abs} in the Pd bulk; (d) the transfer of hydrogen across the $Pd/Mg_ySc_{(1-y)}$ interface and finally; (e) solid-state diffusion of H_{abs} in the $Mg_ySc_{(1-y)}$ bulk. Of the five separate processes listed here, the first three have already been discussed in Section 2.4.2 (Reactions 9 to 11). For the sake of completeness they will be reproduced here in a slightly different form.

The primary step is the charge transfer reaction at the solution/solid interface (process (a)). Here water is reduced and hydrogen adsorbed in atomic form (H_{ad}) at the Pd surface according to

$$H_2O + Pd + e^- \underset{k_{-1}}{\overset{k_1}{\rightleftarrows}} PdH_{ad} + OH^- \quad . \tag{9}$$

In the second processes (b), H_{ad} can be absorbed by the host material just below the surface, forming subsurface hydrogen (H_{ss}), according to

$$PdH_{ad} \underset{k_{-2}}{\overset{k_2}{\rightleftarrows}} PdH_{ss} \quad . \tag{10}$$

* All $Mg_ySc_{(1-y)}$ and pure Mg thin films are covered with a 10 nm Pd topcoat.

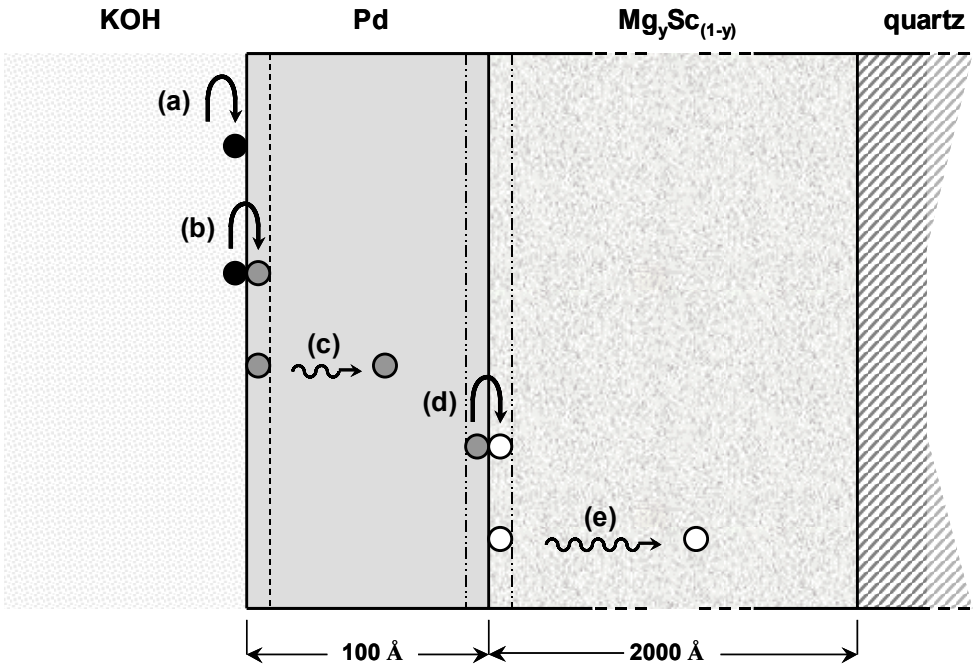

Fig. 44: Schematic representation of a Pd-coated $Mg_ySc_{(1-y)}$ thin film electrode showing the overall geometry of this 2-layer system. The main (electro)chemical processes related to (de)hydrogenation are depicted at the appropriate locations; charge transfer reaction (a); adsorbed hydrogen forming subsurface absorbed hydrogen (b); solid-state diffusion of hydrogen in the Pd bulk (c); transfer of hydrogen across the Pd/ $Mg_ySc_{(1-y)}$ interface (d); and solid-state diffusion of hydrogen in $Mg_ySc_{(1-y)}$ bulk (e).

Finally, H_{ss} penetrates into the bulk of the Pd topcoat as H_{abs} (process (c)). This occurs through solid-state diffusion via

$$PdH_{ss} \rightleftarrows PdH_{abs} \quad . \tag{11}$$

Hereafter, the hydrogen needs to cross the Pd/$Mg_ySc_{(1-y)}$ boundary (process (d)). This is a process equal to that of process (b) and can be represented by

$$PdH_{abs} \underset{k_{-5}}{\overset{k_5}{\rightleftarrows}} Mg_ySc_{(1-y)}H_{abs} \quad . \tag{50}$$

In the final process hydrogen penetrates into the bulk of the $Mg_ySc_{(1-y)}$ layer via solid state diffusion (e). This process is, of course, physically identical to process (c).

4.3.3. Contribution Pd topcoat to the measured response

As shown in Fig. 44, a Pd-coated $Mg_ySc_{(1-y)}$ film can essentially be regarded a model-like 2-layer system. When performing electrochemistry, the response of this entire 2-layer system is measured. This makes the interpretation of the measured response not always as

straightforward as it might seem due to the fact that both the Pd topcoat and the main $Mg_ySc_{(1-y)}$ layer are chemically active when considering hydrogen absorption. Therefore they will both influence certain parameters of the total system (*e.g.* kinetics, hydrogen transport, *etc.*) in different ways during, for example, current-flowing or equilibrium conditions.

As it is rather difficult to determine the contribution of the separate layers to the overall electrochemical response of the 2-layer system, the electrode complexity has to be reduced. The easiest way to do this is to reduce the number of layers, while keeping all other parameters constant, *e.g.* thickness, surface area and crystallography. Fig. 45 depicts a schematic representation of a Pd thin film electrode. Similar to Fig. 44, the phases, layer thickness and reactions of interest are indicated. By means of XRD it was confirmed that these pure Pd films showed identical reflections to the Pd topcoat covering the $Mg_ySc_{(1-y)}$ thin films, corresponding to fcc-structured Pd, oriented in the (111) direction.

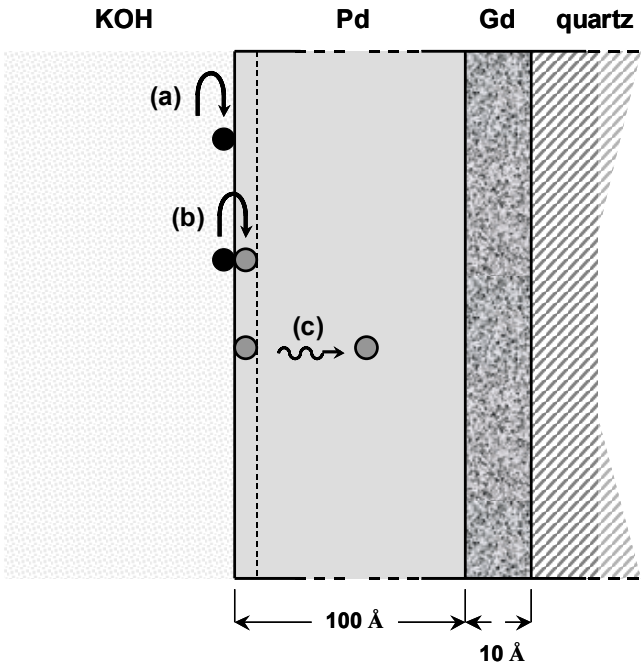

Fig. 45: Schematic representation of a Pd thin film electrode with a Gd adhesion layer. Besides the overall geometry of this 1-layer system, the main (electro)chemical processes related to hydrogen absorption are indicated at their appropriate locations; charge transfer reaction (a), adsorbed hydrogen forming subsurface absorbed hydrogen (b) and solid-state diffusion of hydrogen in the Pd bulk (c).

As opposed to the $Mg_ySc_{(1-y)}$ thin films, this electrode can be considered as a 1-layer system. This can be explained by the fact that it was experimentally determined (not shown here) that the Gd adhesion layer, which is only 10 Å thick (≈ 3 monolayers), does not contribute to the measured electrochemical response. This is corroborated by work done by Baldauf *et al.*, which showed that Pd deposits less than 3 monolayers thick are unable to absorb hydrogen.[88] Additionally, Horkans stated that even using 20 nm thick Nb adhesion layers did not show an observable electrochemical effect.[89] As Gd chemically behaves very similar to Nb, a possible influence of the adhesion layer will be neglected and it is assumed that no hydrogen can cross the Pd/Gd interface.

It is evident that when the Pd topcoat completely covers the $Mg_ySc_{(1-y)}$ layer, the charge transfer kinetics (Reaction 9) and hydrogen absorption reaction (Reaction 10) will be the same for both systems, as schematically shown in Figs. 44 and 45. However, if transport of hydrogen in the bulk is considered, the 2-layer system (Fig. 44) may lead to a substantially different response than that of the 1-layer system (Fig. 45) due to the existence of an additional interface and bulk phase.

When a particular current is applied to the MH thin film electrode, the measured potential response basically depends on two main factors. First of all, the response depends on the equilibrium potential (E_{MH}^{eq}), which is directly linked to the thermodynamics of the system.[62] The thermodynamics, or more precisely, the chemical potential (μ) is directly linked to the amount of hydrogen incorporated in the particular MH. GITT measurements were performed on separate Pd thin films (like those shown in Fig. 45) and the obtained thermodynamic data was correlated to that of the Pd-coated $Mg_ySc_{(1-y)}$ thin films. These thermodynamical considerations involving the Pd topcoat are presented in Section 4.3.5.2.

The second factor, which gives rise to the measured electrochemical response, is the overpotential (η). η itself is a combination of various potential drops related to different phenomena in the (de)hydrogenation process. Summarizing, the electrode potential can be expressed by

$$E = E_{MH}^{eq} + \eta = E_{MH}^{eq} + \eta_{kin} + \eta_{dif} + IR_s \tag{51}$$

where η_{kin} is the kinetic overpotential, brought about by the reaction resistances of Reactions 9, 10 and 50 (see Section 4.3.2); η_{dif} the overpotential, originating from solid-state diffusion of hydrogen in the bulk phases; and IR_S is the Ohmic drop. Unfortunately, when galvanostatic measurements are used, η cannot be easily resolved into its separate components as they are each dependent on the applied current in a different way. To this end, combined GITT/EIS measurements were performed, as they are able to resolve responses related to kinetic or hydrogen transport effects while measuring in equilibrium conditions. Like for the determination of the thermodynamics, measurements on separate Pd films were used to fully understand the kinetics of the 2-layer system. These measurements are presented and discussion in Section 4.3.6.

4.3.4. Galvanostatic behavior of $Mg_ySc_{(1-y)}$ materials

4.3.4.1. Pd-coated $Mg_ySc_{(1-y)}$ thin films

When MgSc bulk alloys were first described as hydrogen storage materials by Notten *et al*., the first hydrogenation of these compounds was represented as follows[18]

$$Mg_xSc_{(1-x)} + (3-x)\,H_2O + (3-x)\,e^- \xrightarrow{k_6} Mg_xSc_{(1-x)}H_{(3-x)} + (3-x)\,OH^- \ . \tag{52}$$

Because the divalent Mg forms a dihydride (MgH_2) and Sc can be both di-and trivalent, the theoretical storage capacity of the initial hydrogenation was assumed to correspond to 2 H/Mg and 3 H/Sc. As ScH_2 has a very negative heat of formation (close to - 100 kJ/mole H[90]) only 1 H/Sc and 2 H/Mg are assumed to be reversible according to

$$Mg_xSc_{(1-x)}H_{(3-x)} + (x+1)OH^- \underset{k_{-7}}{\overset{k_7}{\rightleftarrows}} Mg_xSc_{(1-x)}H_{(2-2x)} + (x+1)H_2O + (x+1)e^- \quad . \quad (53)$$

To accurately investigate the storage capacity of the MgSc alloys, the thin films were fully hydrogenated (charging) and dehydrogenated (discharging) galvanostatically. The samples were charged using a current of - 0.6 mA (200 μA/cm^2 or ~ 5000 mA/g), discharged with + 0.12 mA (40 μA/cm^2 or ~ 1000 mA/g) and deep-discharged with + 0.012 mA (4 μA/cm^2 or ~ 100 mA/g). Because the same absolute current density (in μA/cm^2) was used for every composition, it is impossible to give a precise value for the used current density in mA/g. This results from the fact that MgSc layers with equal thickness but different composition (*i.e.* Sc content) vary in mass slightly.

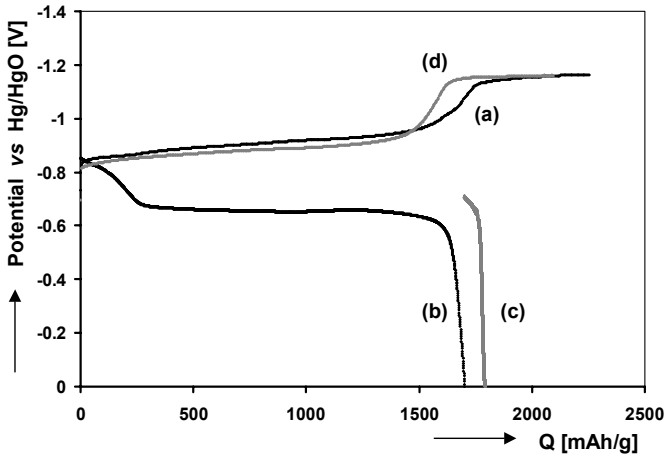

Fig. 46: Galvanostatic response of a Pd-coated $Mg_{0.80}Sc_{0.20}$ thin film, showing the first hydrogenation at - 0.6 mA (a), first discharge at + 0.12 mA (b), subsequent deep-discharge at + 0.012 mA (c) and the second hydrogenation at - 0.6 mA (d).

Fig. 46 shows the galvanostatic behavior of a $Mg_{0.80}Sc_{0.20}$ thin film. The sample was first fully hydrogenated (curve (a)) and hereafter allowed to reach equilibrium under open-circuit conditions for 1 hour. Then the layer was discharged until the cut-off potential was reached (curve (b)), after which the electrode was allowed to equilibrate for 1 hour. Subsequently, deep–discharging was performed (curve (c)). Finally the electrode was again charged to the fully loaded state (curves (d)). This procedure was used to determine the galvanostatic behavior of all $Mg_ySc_{(1-y)}$ thin films ($y = 0.50 – 0.90$), as well as the pure Mg films.

By systematically varying the Sc content, the impact on the observed electrochemical responses of the $Mg_ySc_{(1-y)}$ thin layers can be assessed. Fig. 47 shows the measured discharge curves, at a high discharge current of + 0.12 mA, for different $Mg_ySc_{(1-y)}$ thin film electrodes with varying Sc content. The first part of the discharge curve clearly shows solid solution behavior for high Mg content, but becomes more plateau-like for increasing Sc content. The amount of charge extracted from the material in this region clearly increases with an increase in Sc content. Beyond this solid solution, a wide plateau region is observed at around - 0.65 V for compositions where $y \leq 0.80$. This plateau points to a two-phase coexistence region. Surprisingly, for compositions where $y > 0.80$, no two-phase coexistence can be discerned and the potential rapidly increases to the cut-off potential upon continued discharging. This shows that when increasing the Mg content beyond 80 at.%, remarkable changes occur, resulting in very poor discharge characteristics. Interestingly enough, the shapes of the discharge curves of the MgSc thin film materials, shown in Fig. 47, are nearly identical to

those of MgSc bulk materials with the same composition.[91] This shows that thin films electrochemically behave very similar to their bulk counterparts.

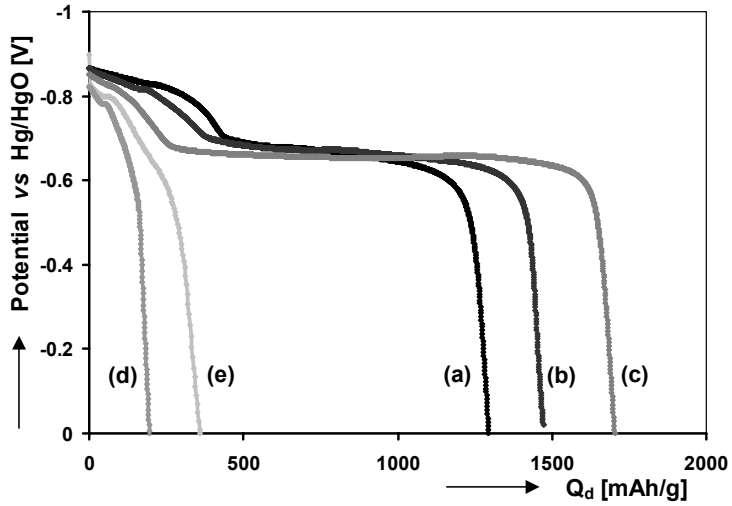

Fig. 47: Selected galvanostatic discharge curves of Pd-coated $Mg_ySc_{(1-y)}$ thin films; $Mg_{0.65}Sc_{0.35}$ (a), $Mg_{0.70}Sc_{0.30}$ (b), $Mg_{0.80}Sc_{0.20}$ (c), $Mg_{0.85}Sc_{0.15}$ (d) and $Mg_{0.90}Sc_{0.10}$ (e). A high discharge current of + 0.12 mA (~ 1000 mA/g) was used.

This phenomenon can also be seen when plotting the extracted amount of charge *vs.* the Mg content of the $Mg_ySc_{(1-y)}$ thin film electrodes (see Fig. 48). In this figure, the discharge capacities obtained at a high and low discharge rate (using currents of + 0.12 mA (curve (a)) and + 0.012 mA (curve (b)), respectively, are shown. Additionally, the theoretical discharge capacities (according to Reaction 53) are plotted for each composition. Initially, an increase in Mg content results in an increasing discharge capacity. This is rather straightforward as the material becomes lighter when more Mg is incorporated. This is also in line with the reasoning that two hydrogen atoms can be reversibly adsorbed/desorbed per Mg atom, whereas Sc is assumed to have only one. Overall, this trend is maintained up to an optimum around the $Mg_{0.80}Sc_{0.20}$. The reversible hydrogen storage capacity of this composition is 1795 mAh/g, corresponding to 2.05 hydrogen atoms per metal or 6.7 wt.%. This is close to six times higher than commercial AB_5-type materials.[92,93] Notably, in this region ($y \leq 0.80$) not much difference exists between the high and low-rate discharge capacities. This indicates that these materials exhibit excellent rate capability and almost all hydrogen can be extracted using a high current.

Lower discharge capacities are observed for compositions with a Mg content with $y > 0.80$. $Mg_ySc_{(1-y)}$ thin film electrodes with $y = 0.85$ and $y = 0.90$ show low discharge capacities when using a high current (see also Fig. 47). However, at a low discharge current the total capacity is still very substantial and roughly 40 % lower than for $y = 0.80$. This observation leads to the conclusion that mostly the rate capability is affected, rather than the hydrogen storage capability of these materials. The origin of this poor dehydrogenation performance is believed to be due to a change in crystal structure of the hydride, which will be dealt with later (4.3.7). Like for the shape of the discharge curves, the curves (a) and (b) in Fig. 48 show shapes identical to that of their bulk counterparts.[18,91]

From Fig. 48 it also becomes apparent that the measured capacities are very close to the theoretically predicted ones. So despite the oversimplification of the hydrogenation behavior made earlier, the agreement between the predicted and measured capacities is quite good for these materials. Note that for the compositions where $y = 0.65$ and $y = 0.80$, the measured

capacities are even somewhat higher than the theoretical ones, but these discrepancies fall within the stated margin of error (see Section 4.2).

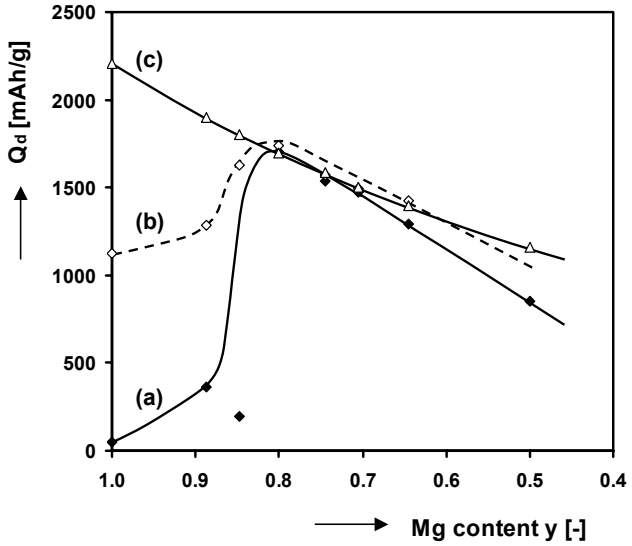

Fig. 48: Discharge capacity of $Mg_ySc_{(1-y)}$ thin films as a function of composition. Discharging at + 0.12 mA (a), deep-discharging at + 0.012 mA (b) and the theoretical capacity (c).

So far, only the discharge behavior of the MgSc thin films has been discussed. In order to assess whether or not hydrogen is irreversible incorporated in the material (as suggested before), the electrochemical response during hydrogenation has to be examined. It is has been suggested that during the first hydrogenation, hydrogen is irreversibly bonded to the Sc. As ScH_2 has a very negative heat of formation of around - 100 kJ/mol H, it is plausible that once this hydrogen has been absorbed by the compound, it is not released anymore.[90] By charging (hydrogenating) a MgSc thin film to different hydrogen concentrations and subsequently extracting the reversible part, it can be established when hydrogen is irreversibly incorporated during the charging process. Fig. 49 shows the electrochemical response of a $Mg_{0.65}Sc_{0.35}$ thin film when performing such an experiment. The electrode was charged using a current of - 0.6 mA to a Depth-of-Charge (DoC) of 230, 460, 690 and 1320 mAh/g in the 1st, 2nd, 3rd and 4th charging step, respectively. After each charging step the sample was allowed to equilibriate for one hour after which the electrode was discharged using a current of + 0.12 mA. Hereafter, the sample was again allowed to reach equilibrium during one hour. It should be noted that this subsequent charging and discharging was performed on the same sample.

It is evident that when the electrode is charged to a DoC of 230 mAh/g during the first step (see Fig. 49a), no hydrogen can be extracted (see Fig. 49b). This shows that during the initial stage of the charging process all hydrogen is irreversible incorporated in the $Mg_{0.65}Sc_{0.35}$ compound. In step 2 and 3, an increasingly larger part of the hydrogen stored can be reversible extracted. Finally, during the last step (step 4) almost all of the hydrogen that was inserted can be extracted from the material. The bar graph in Fig. 50 schematically shows to what extent hydrogen remains trapped in the $Mg_{0.65}Sc_{0.35}$ compound during all four steps. A summation of the irreversible portions of the first three steps yields a total value of 627 mAh/g. It can be calculated that this amount of charge is exactly that what is needed to hydrogenate all Sc in the thin film to ScH_2 (taking into account the exact amount of Sc in this layer, measured by means of RBS).

Although less charge was extracted during step 4 as opposed to inserted (~ 50 mAh/g), it is thought not to be irreversibly incorporated in the MgSc compound, but lost at the expense of hydrogen gas formation. It is known that this parasitic process occurs at the end of the hydrogenation process (see the inset in Fig. 49a).

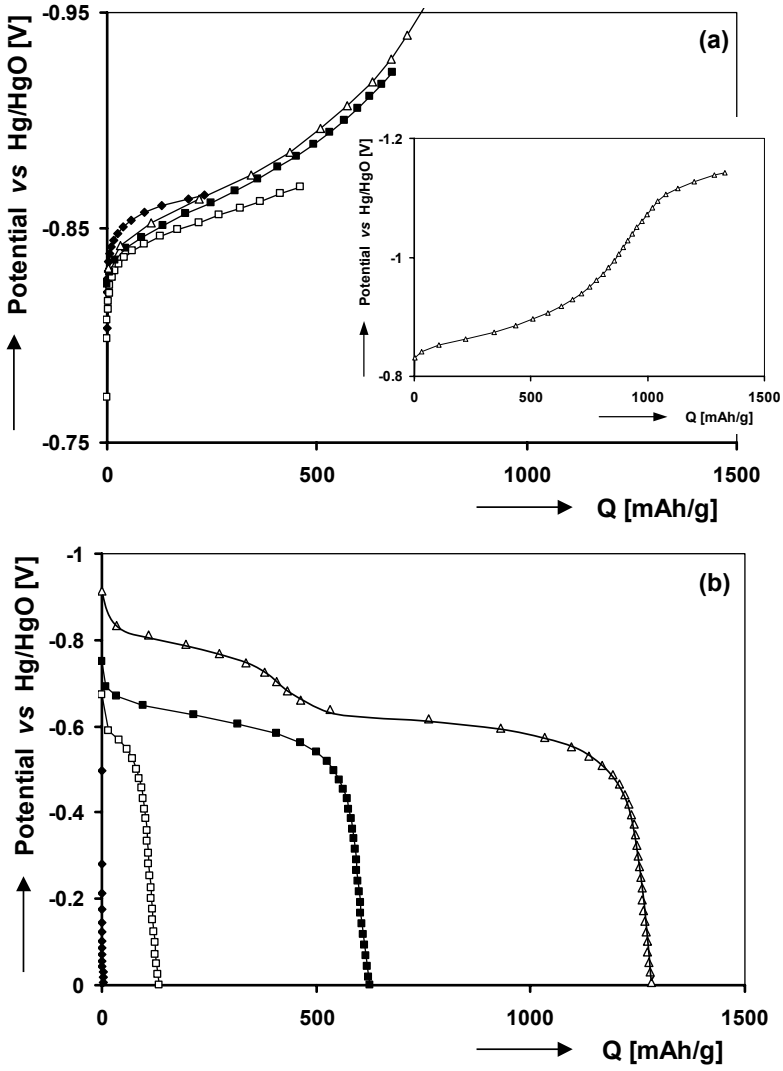

Fig. 49: Partial charge (a) and discharge curves (b) of a Pd-coated $Mg_{0.65}Sc_{0.35}$ thin film. The electrode was charged using a current of - 0.6 mA to a DoC of 230, 460, 690 and 1320 mAh/g in the 1st, 2nd, 3rd and 4th charging step, respectively. During discharge, which followed each charging step, a current of + 0.12 mA was used. The inset in (a) shows the complete voltage response of the 4th charging step. The symbols used in the figure represent: step 1 (◆), step 2 (□), step 3 (■) and step 4 (△).

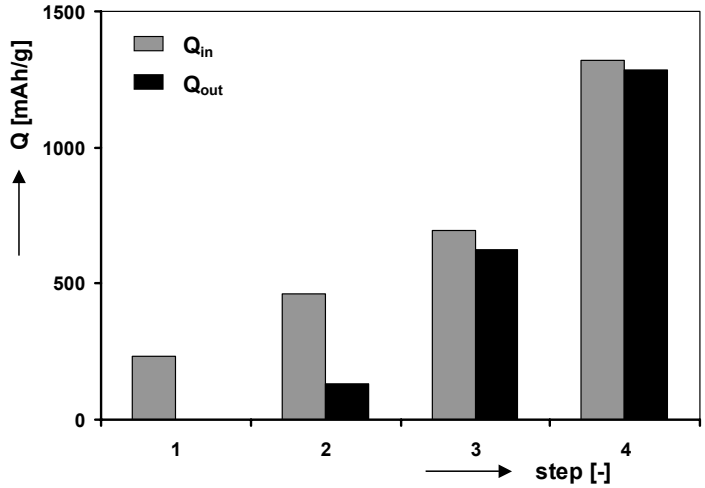

Fig. 50: Bar graph showing the reversible and irreversible part of the stored charge when consecutively charging a $Mg_{0.65}Sc_{0.35}$ thin film to 230 mAh/g (step 1), 460 mAh/g (step 2), 690 mAh/g (step 3) and 1320 mAh/g (step 4). The gray and black bars show the amount of charge inserted and extracted, respectively, during each step.

4.3.4.2. Pd-coated Mg thin films

To obtain a good understanding to what extent alloying (*e.g.* by Sc) has on the electrochemical characteristics of Mg-based alloys, the electrochemical hydrogenation characteristics of pure Mg need to be studied as well. The hydrogenation of Mg is, although well-studied, quite hard to perform at lenient conditions. Often high temperatures and substantial hydrogen gas pressures are required to fully convert Mg into MgH_2 via the gas phase.[81,94,95,96] Additionally, too fast hydrogenation can lead to the formation of MgH_2 blocking layers, preventing hydrogenation of the remaining Mg material.[97] Giebels showed that hydrogenation of Pd-coated Mg thin films, via the gas phase at 1 mbar H_2 and 100 °C, is possible for film thicknesses up to 150 nm.[98] The electrochemical hydrogenation of Mg is, partly due to the abovementioned reasons, researched even less well.

Fig. 51 shows the galvanostatic response of a Pd-coated Mg thin film. In order to be able to hydrogenate the Pd-coated Mg thin films electrochemically at room temperature, a very low charging current of – 0.012 mA was utilized (curve (a)). As a direct consequence, prolonged charging times were required. To avoid influence of surface contaminants (see Section 3.6)[71], which are known to severely affect the measured electrochemical response, the Mg thin film was charged until hydrogen gas formation was observed. Hereafter, similar experimental conditions as for the Mg_ySc_{1-y} thin films were used to extract the hydrogen from the Mg thin film electrode. Discharging (curve (b)) and deep-discharging (curve (c)) was performed using currents of + 0.12 mA and + 0.012 mA, respectively. Although the theoretical storage capacity of Mg is 2200 mAh/g, corresponding to full conversion of all Mg to MgH_2, the experimentally measured discharge capacity is only 1125 mAh/g (see Figs. 51 and 48).

The most notable feature of the voltage response shown in Fig. 51 is the very low discharge capacity when applying a high discharge current (curve (b)). This is full agreement with the poor hydrogen transport behavior of the rutile-structured Mg hydride. A very similar behavior was already observed in Fig. 47 for the Mg-rich $Mg_ySc_{(1-y)}$ compounds with y = 0.85 - 0.90, showing a rapid increase in potential upon hydrogen extraction. This very

similar electrochemical behavior appears to be related to the hydride structure as in both cases (*i.e.* the pure Mg films and the Mg-rich $Mg_ySc_{(1-y)}$ thin films) samples were investigated with roughly the same layer thickness, surface area and surface kinetics.* A viable hypothesis might be that the formed $Mg_ySc_{(1-y)}$ hydrides (with y = 0.85 - 0.90) and MgH_2 are identical in structure and that the poor hydrogen transport through the rutile structure plays a dominant role in the inferior dehydrogenation behavior.

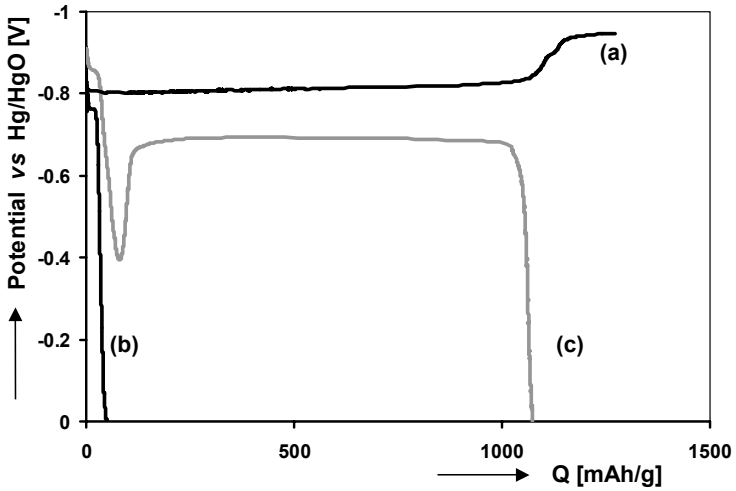

Fig. 51: Galvanostatic response of a Pd-coated Mg thin film, showing the first hydrogenation at - 0.012 mA (a), first discharge at + 0.12 mA (b), subsequent deep-discharge at + 0.012 mA (c).

Analogous to the Mg-rich $Mg_ySc_{(1-y)}$ compounds with y = 0.85 - 0.90 (see Fig. 48), using a low discharge current enables the extraction of all absorbed hydrogen. The potential response shown in Fig. 51 curve (c) now also shows a two-phase coexistence region, similar to that of the $Mg_ySc_{(1-y)}$ materials. However, deep-discharging of the pure Mg thin films reveals a very interesting response during the initial stages. Although the origin of it is not fully understood at this point, it causes the potential to increase to about - 0.4 V initially (up to 100 mAh/g) and, upon continued discharging, again to decrease and stabilize at roughly - 0.72 V (between 100 and 200 mAh/g). Hereafter a normal discharge curve is measured which finally increases rapidly in potential when the electrode reaches its hydrogen-depleted state (200 to 1100 mAh/g). The observed voltage response indicates that the overpotential somehow increases at the outset of hydrogen extraction, subsequently diminishes and eventually behaves like expected. A quite similar evolution of the overpotential under galvanostatic conditions is generally seen when investigating nucleation and growth mechanisms.[99] Therefore, this characteristic response measured on the pure Mg film might be linked to a similar process. Interestingly, this reactivation behavior is not seen when electrochemically dehydrogenating $Mg_ySc_{(1-y)}$ thin films.

* In Section 4.3.6.2 it will be shown that the surface kinetics of the investigated thin films is completely dominated by the Pd topcoat. RBS and XRD investigations indicate that the pure Mg thin films were covered with Pd topcoats identical to those covering the $Mg_ySc_{(1-y)}$ thin films.

4.3.5. Thermodynamics of $Mg_ySc_{(1-y)}$ compounds

4.3.5.1. $Mg_ySc_{(1-y)}$ thin films

The thermodynamic properties of the MgSc alloys were evaluated by means of GITT. First, the thin films were galvanostatically fully loaded with hydrogen, using a current of - 0.6 mA. Subsequently, they were discharged by means of GITT using a current of + 0.12 mA initially and + 0.012 mA during the last five pulses. After each pulse the electrode was allowed to equilibrate for 1 hour. It should be noted that GITT discharging was carried out by dividing the total capacity reached with low discharge current (see Fig. 48), into 20 equally large steps. Fig. 52 shows the obtained equilibrium curve (open symbols) as well as the potential response of the $Mg_{0.80}Sc_{0.20}$ compound during each current pulse. The insets show the potential response and subsequent relaxation of a typical GITT pulse at the start (left-hand side) and at the end of the main discharge plateau (right-hand side). It is clear that η remains nearly constant throughout the entire discharge process, only to increase significantly at the very end of the discharge process. This latter behavior is expected as the thin film reaches its hydrogen-depleted state. After the electrodes where fully discharged, the described procedure was reversed and the electrodes were charged to the fully hydrogenated state using GITT. The same parameters were applied except for the fact that currents were used of - 0.12 mA and - 0.012 mA, respectively.

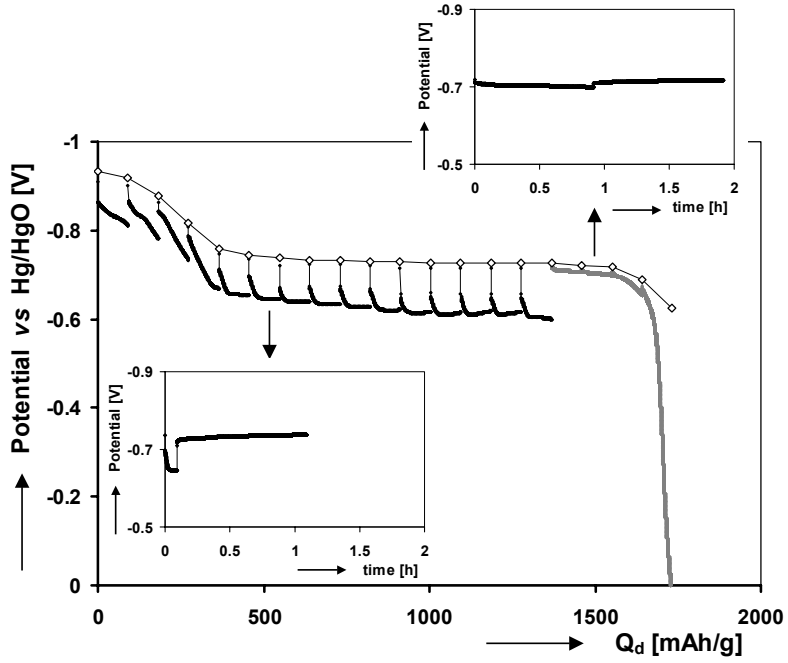

Fig. 52: Electrochemical response of a $Mg_{0.80}Sc_{0.20}$ thin film electrode during a GITT measurement. Besides the equilibrium curve of the material (◇), the potential response during each GITT pulse is shown. Current used during the GITT pulses: + 0.12 mA (bold line), + 0.012 mA (gray line). The insets show the potential response and subsequent relaxation of a particular GITT pulse at the start (left-hand side) and at the end of the main discharge plateau (right-hand side).

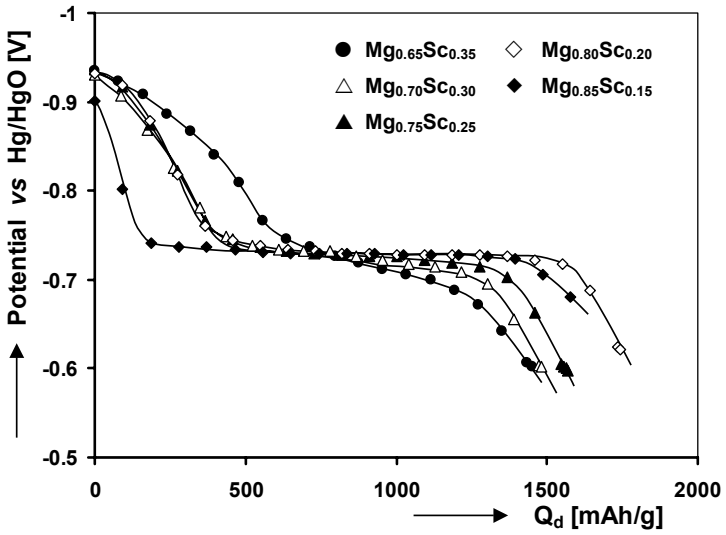

Fig. 53: Equilibrium discharge curves of Pd-coated $Mg_ySc_{(1-y)}$ thin films with a Mg content *y* ranging from 0.65 to 0.85.

In Fig. 53 equilibrium voltage curves are shown for different $Mg_ySc_{(1-y)}$ compositions. Changing the Sc content appears to have only a very limited effect on the potential of the main plateau. This was already apparent from the galvanostatic discharge curves presented in Fig. 47. However, the 2-phase coexistence plateau does get more sloping when Sc content of the alloy increased, leading to a sloping plateau for $y = 0.65$ and a very flat plateau when $y = 0.85$.

A remarkable difference between galvanostatic (Fig. 47) and the equilibrium discharge curves (Fig. 53) is that the amount of charge extracted in the first solid solution part monotonously decreases with decreasing Sc content in the case of the galvanostatic responses, yet shows a less clear dependency in the GITT curves. Here the isotherms lie virtually on top of each other for the compositions where $y = 0.70$, 0.75 and 0.80. The overall trend, when considering all the measured compositions, is the same; the amount of charge extracted before the onset of the plateau region decreases with decreasing Sc-content.
The measured equilibrium voltages (E_{eq}) can be converted into an equivalent hydrogen pressure (P_{H_2}), using Eq. 22 in Section 2.4.4. A plateau voltage of - 0.72 V to - 0.74 V, as exhibited by the MgSc materials presented here, corresponds to an equivalent hydrogen pressure of $7 * 10^{-5}$ to $3.5 * 10^{-4}$ mbar. This leads to the conclusion that these materials are very hard to dehydrogenate in a gas-phase environment and are therefore unlikely to be used in an application that demands a high H_2 gas pressure at room temperature. Note that a potential difference of about 30 mV corresponds to a change in equivalent hydrogen pressure by 1 order of magnitude. As, for example, fuel cell applications require H_2 gas pressures of about 1000 mbar, the discharge plateau of these materials should, ideally, be shifted to a substantially more negative equilibrium potential.

The low plateau pressures of the MgSc materials are directly related to the high stability of their hydrides. By using the *Van 't Hoff relation* (see Eq. 23 in Section 2.4.4) the electrochemical equilibrium data presented in Fig. 53 can be linked to the thermodynamics of these compounds. The average enthalpy of formation (ΔH_f) corresponding to the previously calculated plateau pressure range roughly amounts to - 37 kJ/mole H. It is rather remarkable that ΔH_f seems to be identical to that reported for the transition from Mg to MgH_2.[90]

4.3.5.2. Hydrogen concentration in the Pd topcoat

In order to accurately assess the equilibrium behavior of the Pd topcoat, it was measured separately as a 1-layer system (see Section 4.3.3). Fig. 54 depicts a typical equilibrium curve of a 10 nm thick Pd thin film electrode, obtained by means of GITT. The electrodes were charged to their fully hydrogenated state using a current of - 0.6 mA and subsequently allowed to relax to their equilibrium potential. Hereafter, the Pd thin films were discharged by means of GITT, using a current + 0.012 mA. The electrode was allowed to equilibrate during 1 hour after each pulse. Stable equilibrium potentials were obtained in all cases.

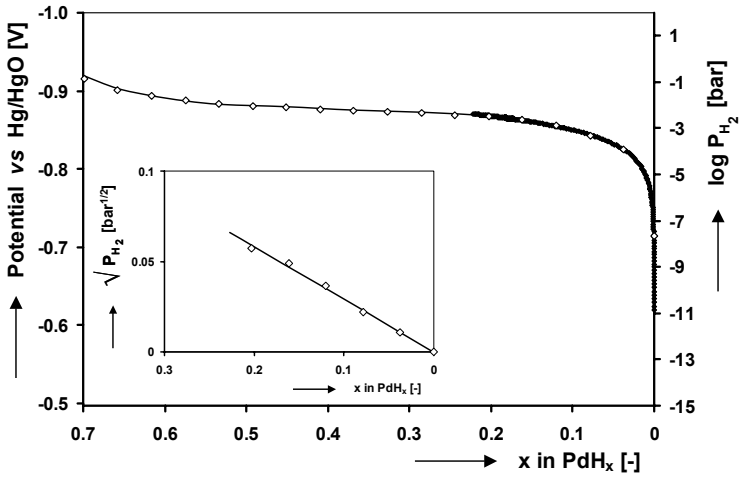

Fig. 54: Equilibrium curve, experimentally obtained by means of GITT, of a 10 nm Pd thin film electrode during dehydrogenation. A current of + 0.012 mA was used during each GITT pulse, followed by 1 hour of relaxation. The bold curve at $x < 0.25$ shows a fit in accordance to *Sieverts' Law*. The inset shows, for the same experimental points, the same ideal solid solution behavior by plotting $\sqrt{P_{H_2}}$ *vs.* PdH_x.

At an equilibrium potential of - 0.905 V, the film has an approximate composition of $PdH_{0.7}$. When the hydrogen concentration is lowered, a quasi-plateau can be seen down to a stoichiometry of about $PdH_{0.2}$. Unlike bulk Pd, which shows a well-defined plateau corresponding to the coexistence of the β- and α-phases[100], these very thin Pd films demonstrate a much narrower two-phase coexistence region.

It was shown by Nicolas *et al.* that the critical temperature (T_c) is well below room temperature for very thin Pd films (60 Å < d < 600 Å).[101] This drop in T_c was attributed to film-substrate interactions, such as clamping. Indeed, as the experiments on the pure Pd films presented in this study were conducted well above this T_c, instantaneous transition from β- to α-phase is expected to occur. Ideal solid solution behavior can be verified by applying *Sieverts' law*,

$$C_H^{eq} = K_S \sqrt{P_{H_2}} \tag{54}$$

where C_H^{eq} is the equilibrium concentration of hydrogen in the Pd (in H/M); K_s is Sieverts' constant and P_{H_2} the partial hydrogen pressure (in bar). P_{H_2} was obtained from E_{MH}^{eq} via the Eq. 22 in Section 2.4.4. (see right-hand axis in Fig. 54). The inset in Fig. 54, in which $\sqrt{P_{H_2}}$

is plotted *vs.* x in PdH_x, shows a linear dependence up to about $PdH_{0.25}$, indeed indicating ideal solid solution behavior according to Eq. 54. The value of K_s is 3.44 $bar^{-½}$ in this case.

In the 2-layer system (see Section 4.3.4.1), at a particular equilibrium potential, the hydrogen concentration in the Pd topcoat and the $Mg_ySc_{(1-y)}$ layer are fixed through the thermodynamics of both hydride systems (PdH_x and $Mg_ySc_{(1-y)}H_x$). As explained in Chapter 2, the chemical potential of a hydride-forming compound (μ_{MH}) can be linked to the partial hydrogen pressure and the equilibrium potential via Eqs. 20 and 21. As the electrochemical potentials of both the Pd and $Mg_ySc_{(1-y)}$ layers are equal under equilibrium conditions, the chemical potentials of the Pd (μ_{PdH}) as well as the $Mg_ySc_{(1-y)}$ (μ_{MgScH}) hydrides have to be the same, regardless of the absolute amount of hydrogen stored in the electrode. Assuming both layers consist of a single-phase hydride, this can be expressed as

$$\mu_{PdH} = \mu_{MgScH} = \mu^0_{PdH} + RT\ln\left(\frac{a_{PdH}}{a_{ref}}\right) = \mu^0_{MgScH} + RT\ln\left(\frac{a_{MgScH}}{a_{ref}}\right) \quad (55)$$

in which μ^0_{PdH} and μ^0_{MgScH} are the standard chemical potentials of the Pd and $Mg_ySc_{(1-y)}$ hydrides, respectively; a_{PdH} and a_{MgScH} are the activities of hydrogen in their respective hydrides; and a_{ref} is an arbitrary reference activity (unity). Eq. 55 shows that a_{PdH} and a_{MgScH} have to be different, as μ^0_{PdH} and μ^0_{MgScH} are undoubtedly of different magnitude due to the different nature of the hydrides.

The activity of hydrogen in hydride *i* (a_i) can be described by

$$a_i = \gamma_i c_i \quad (56)$$

where γ_i is the activity coefficient and c_i the hydrogen concentration in hydride *i*. Eq. 55 shows that, when activities equal concentrations (γ_i = 1), the hydrogen concentration in the Pd and $Mg_ySc_{(1-y)}$ layer can be very different when a Pd-coated $Mg_ySc_{(1-y)}$ thin film electrode has a certain equilibrium potential. However, as the concentration of hydrogen in a MH compound is very high when expressed in mole/l, γ_i cannot readily be assumed unity. Because the values for γ_i are dependent on the hydrogen concentrations in both layers, they are not constant throughout the (de)hydrogenation process. To make matters even more complicated, as is clear from the equilibrium curves shown in Figs. 54 and 53, the Pd as well as the $Mg_ySc_{(1-y)}$ materials undergo a phase transition. This implies that Eq. 55 has to be modified to accommodate either one (α or β) or two phases (α and β), depending on the equilibrium potential of the 2-layer electrode. This shows that Eq. 55 cannot be simply used to calculate the hydrogen concentrations in the Pd topcoat and the $Mg_ySc_{(1-y)}$ layer on a theoretical basis.

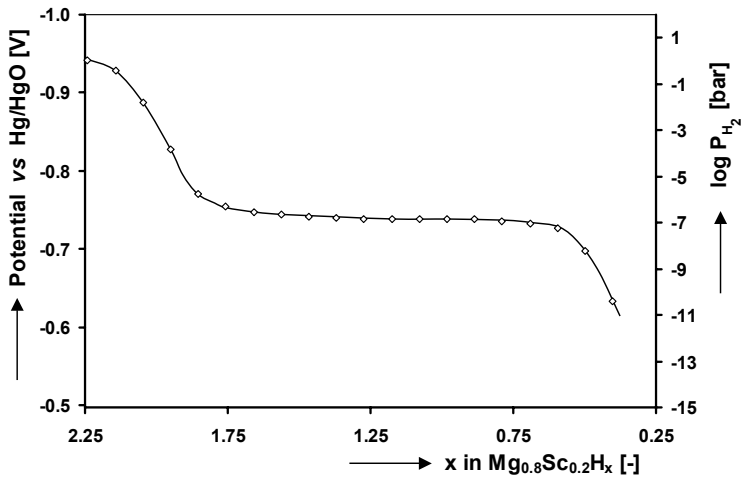

Fig. 55: Equilibrium curve of a 200 nm $Mg_{0.80}Sc_{0.20}$ thin film, coated with 10 nm of Pd, during dehydrogenation. The equilibrium data was obtained by means of GITT using a current of + 0.12 mA during each pulse and an equilibration time of 1 hour. The same discharge isotherm in shown in Fig. 53, where it is plotted *vs.* extracted amount of charge.

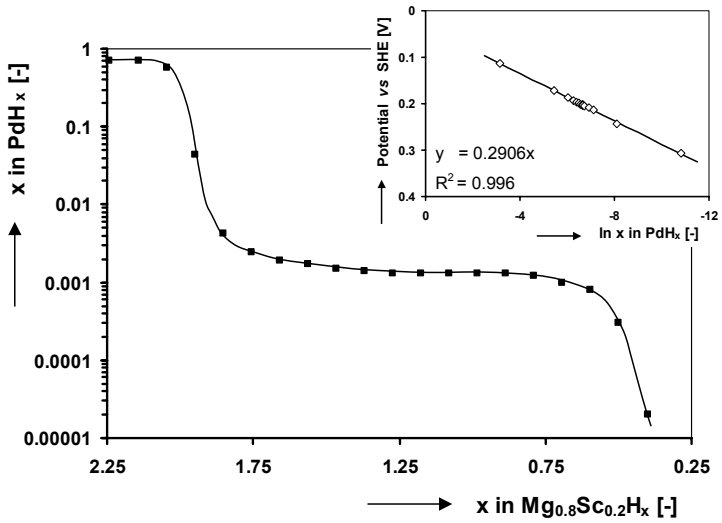

Fig. 56: Experimentally determined hydrogen concentrations, of both the $Mg_ySc_{(1-y)}$ layer and the Pd topcoat, of a Pd-coated $Mg_ySc_{(1-y)}$ thin film electrode (y = 0.80) during equilibrium conditions. The inset shows the linear relation between ln x in PdH_x and E_{Pd}^{eq} (*vs.* SHE).

Fortunately, the exact hydrogen concentrations can be determined experimentally. By pairing the hydrogen content in, for example, a $Mg_{0.80}Sc_{0.20}$ electrode (see Fig. 55) and the pure Pd layer (see Fig. 54), at equal equilibrium potentials, the estimated hydrogen concentration in the Pd topcoat can be plotted *vs.* $Mg_{0.8}Sc_{0.2}H_x$ (see Fig. 56). It is evident from this plot that when the $Mg_{0.80}Sc_{0.20}$ thin film electrode is in its fully hydrogenated state ($Mg_{0.8}Sc_{0.2}H_{2.25}$), the composition of the topcoat is close to $PdH_{0.7}$ (β-phase). When hydrogen is extracted from the $Mg_{0.80}Sc_{0.20}$ material, the hydrogen concentration in the topcoat rapidly decreases to a very low value (α-phase). Using the Sieverts' dependence shown in the inset of Fig. 54, an almost constant value can be calculated corresponding to $PdH_{0.0013}$. Finally, if the $Mg_{0.80}Sc_{0.20}$ thin film reaches its hydrogen-depleted state, the calculated composition of

the topcoat attains a value close to $x = 10^{-5}$. This shows that the Pd topcoat remains in an extremely dilute α-phase for the greater part of the dehydrogenation process of these $Mg_ySc_{(1-y)}$ thin films.

Combining Eq. 21 and the left-hand part of Eq. 55, shows that the hydrogen activity in the Pd topcoat is a function of E_{MH}^{eq}. The ideal solid solution behavior of this topcoat in the α-phase (see the inset in Fig. 54), justifies the assumption that in the low concentration region $\gamma = 1$. This implies that the activity of hydrogen can be replaced by the hydrogen concentration. The inset in Fig. 56, in which ln x in PdH_x is plotted *vs.* E_{MH}^{eq} (*vs.* SHE), shows a linear dependence. From the intercept, a value for μ_{PdH}^{0} can be calculated of - 3284 J/mol. This value is in good agreement with the value reported by Pourbaix.[102]

4.3.6. Impedance spectroscopy on $Mg_ySc_{(1-y)}$ thin films

In order to resolve responses related to kinetic and hydrogen transport effects, under equilibrium conditions, combined GITT/EIS experiments were performed. Like for the thermodynamics, measurements on separate Pd films (1-layer system) were used to fully understand the impedance responses of the Pd-coated $Mg_ySc_{(1-y)}$ thin films (2-layer system).[103]

4.3.6.1. EIS of a 1- and 2-layer system

As the electrochemical response of the Pd topcoat can be measured separately, it is possible to check to what extent this layer plays a role when considering the kinetics of both the surface reactions (processes (a) and (b) in Fig. 44) and the transfer of hydrogen across the $Pd/Mg_ySc_{(1-y)}$ interface (process (d) in Fig. 44). Evidently, the surface reactions are identical for both the 2-layer $Mg_ySc_{(1-y)}$ thin films and the 1-layer Pd film (see Section 4.3.3).

Impedance spectroscopy was used to identify the specific parameters linked to these separate reactions. Fig. 57 shows the impedance data, obtained at equilibrium, of a $Mg_{0.80}Sc_{0.20}$ thin film electrode at different hydrogen concentrations. For hydrogen concentrations higher than $Mg_{0.8}Sc_{0.2}H_{1.6}$, a single semi-circular response can be seen at high frequencies, followed by a capacitive behavior at low frequencies. When the hydrogen concentration drops below this value, a second semi-circle emerges. This second semi-circle increases tremendously in magnitude when the $Mg_{0.80}Sc_{0.20}$ thin film reaches its hydrogen depleted state ($\approx Mg_{0.8}Sc_{0.2}H_{0.4}$).

To be able to identify which (electro)chemical reaction is responsible for the particular semi-circles apparent in Fig. 57, the EIS data can be compared to those of the Pd thin film electrode shown in Fig. 58. Similar to the $Mg_{0.80}Sc_{0.20}$ electrode, a single semi-circular response can be observed, followed by a capacitive behavior at the lowest frequencies. Interestingly, the EIS data of the Pd electrode do not show a second semi-circle, irrespective of the hydrogen concentration.

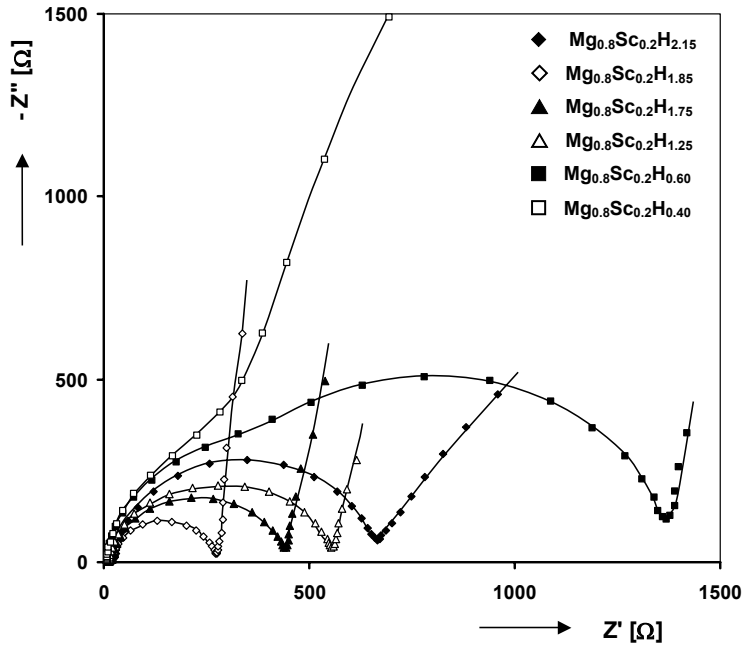

Fig. 57: Nyquist representations of a Pd-coated $Mg_{80}Sc_{20}$ thin film electrode at various hydrogen concentrations; $Mg_{0.8}Sc_{0.2}H_{2.15}$ (◆), $Mg_{0.8}Sc_{0.2}H_{1.95}$ (◇), $Mg_{0.8}Sc_{0.2}H_{1.75}$ (▲), $Mg_{0.8}Sc_{0.2}H_{1.15}$ (△), $Mg_{0.8}Sc_{0.2}H_{0.50}$ (■) and $Mg_{0.8}Sc_{0.2}H_{0.40}$ (□).

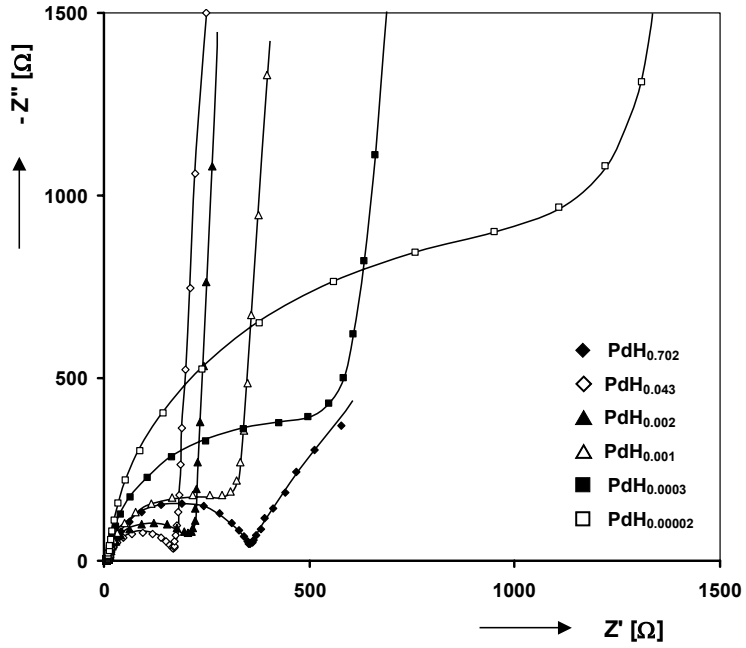

Fig. 58: Impedance spectra of a Pd thin film electrode at various hydrogen concentrations. The hydrogen concentrations where estimated using the dependence shown in Fig. 56; $PdH_{0.702}$ (◆), $PdH_{0.043}$ (◇), $PdH_{0.002}$ (▲), $PdH_{0.001}$ (△), $PdH_{0.0003}$ (■) and $PdH_{0.00002}$ (□).

In order to extract parameters from the measured EIS data, an equivalent circuit (EQC) has been adopted, able to accurately model the system under investigation. The EQC, describing a two-step hydrogen absorption mechanism in which the charge transfer is coupled with absorption, is thoroughly described by MacDonald[104], Montella[105] and Gabrielli *et al.*[77]. Although using a slightly different nomenclature, this model is adequate to model the 1-layer Pd thin films (see Fig. 59). In this EQC, R_s is the series resistance that includes the electrolyte resistance and contact resistances (in this study, this value never exceeds a few Ohms); R_{ct} the charge transfer resistance linked to Reaction 9; C_{dl} the double-layer capacitance; R_{abs} the resistance linked to Reaction 10; and C_{ad} a capacitance depending on the amount of hydrogen present at the surface. The diffusion behavior of hydrogen in the Pd bulk (see Fig. 45, process (c)) has been approximated by a Warburg-element (W_{Pd}), corresponding to the mass-transfer impedance for finite-length diffusion and a reflecting interface. The mathematical form of this element has been extensively treated by Lasia.[106]

This model can be readily simplified when comparing the EIS response of the pure Pd layer (see Fig. 58) to that of the $Mg_{0.80}Sc_{0.20}$ thin film (see Fig. 57). In this thesis, it was previously assumed that the surface reactions (see Figs. 44 and 45, processes (a) and (b)) are identical for both electrodes. As only one semi-circle is apparent in the EIS response of the Pd electrode, either the charge transfer resistance (R_{ct}) or the absorption reaction resistance (R_{abs}) is negligible. In this discussion it is assumed that the absorption rate constant is very high ($R_{abs} \rightarrow 0$) and that the semi-circle is attributed to the charge transfer reaction. This assumption seems to be valid, as the capacitance associated with this same semi-circle remains constant irrespective of the hydrogen concentration in the electrode. This, and the absolute value of this capacitance, point to fact that this element can be ascribed to C_{dl} rather than C_{ad}. Furthermore, EIS investigations of hydrogen sorption into Pd thin films and foils by Gabrielli *et al.*[80] and Yang *et al.*[107] generally showed that $R_{abs} << R_{ct}$. The EQC that remains after elimination of the absorption response is shown in Fig. 60 and is equal to the EQC described by Johnsen *et al.*[108]. It should be noted that the parallel arrangement of C_{ad} and W_{Pd} generally reduces to just the W_{Pd} element for these thin films.

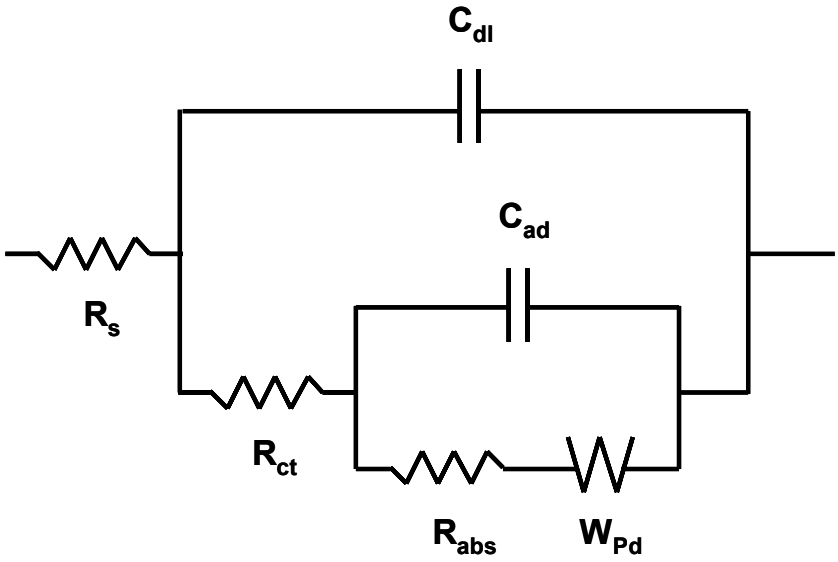

Fig. 59: Complete equivalent circuit able to model a 1-layer Pd thin film electrode, in which the charge transfer reaction is coupled to absorption and subsequent solid-state diffusion of hydrogen in the Pd bulk. It should be noted that finite diffusion with reflective boundary conditions is used here.

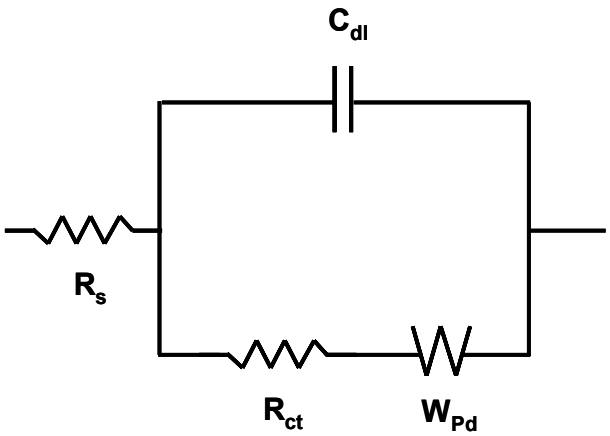

Fig. 60: Simplified version of the circuit shown in Fig. 59, obtained when assuming infinitely fast absorption ($R_{abs} \rightarrow 0$).

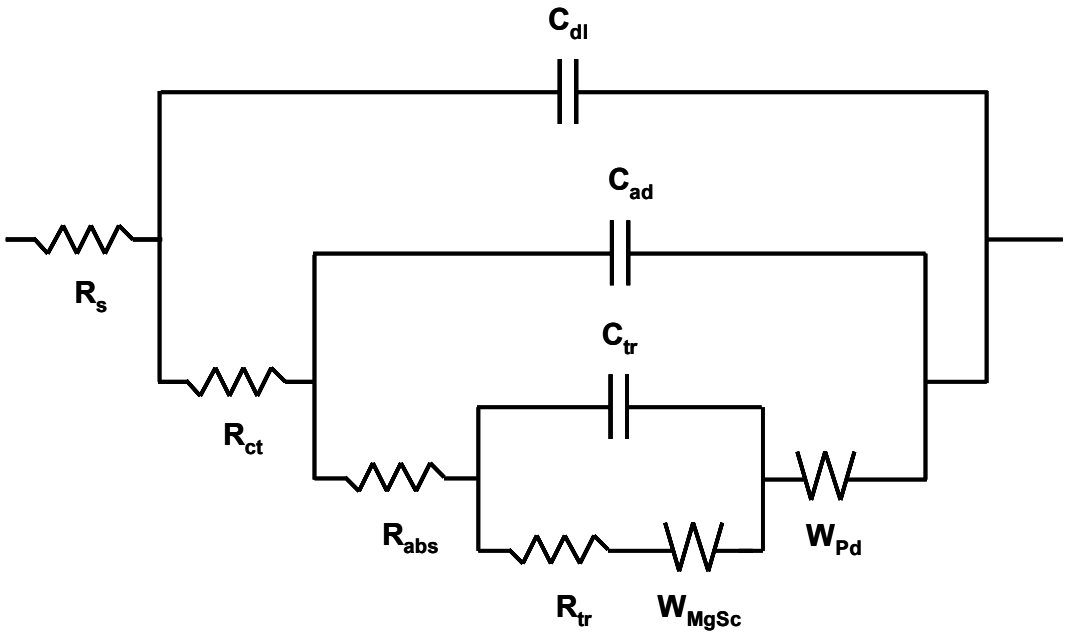

Fig. 61: Complete equivalent circuit able to model a 2-layer $Mg_ySc_{(1-y)}$ thin film electrode. In this circuit the charge transfer is coupled to absorption, subsequent solid-state diffusion of hydrogen in the Pd bulk, followed by transfer of hydrogen across the Pd/$Mg_ySc_{(1-y)}$ interface and solid-state diffusion of hydrogen in the $Mg_ySc_{(1-y)}$ bulk.

As the Pd-coated $Mg_{0.80}Sc_{0.20}$ thin film electrode is a 2-layer system, the chemical description of this system is somewhat more complex, as already demonstrated previously by other authors.[109,110] Apart from the chemical processes described by the EQC in Fig. 59, it must also include the transfer of hydrogen across the Pd/$Mg_ySc_{(1-y)}$ interface (Fig. 44, process (d)) and solid-state diffusion of hydrogen in the $Mg_ySc_{(1-y)}$ layer (Fig. 44, process (e)). In Fig. 61 the complete EQC is shown which also includes these phenomena. Here R_{tr} is the resistance linked to Reaction 50 and C_{tr} the capacitance, describing hydrogen trapped at the Pd/$Mg_ySc_{(1-y)}$ interface. The diffusion behavior of hydrogen in the $Mg_ySc_{(1-y)}$ bulk is described by a Warburg-element (W_{MgSc}), corresponding to the mass-transfer impedance for finite-length diffusion and a reflecting interface.[106] As the Pd topcoat does not have a

reflective boundary like in the 1-layer case (the hydrogen can penetrate the Pd layer and subsequently diffuse into the MgSc layer), W_{Pd} describes diffusion with transmissive boundary conditions.

Because this study focuses only on kinetic effects, rather than on the hydrogen transport effects in the bulk, the EQC for the $Mg_ySc_{(1-y)}$ electrode can be simplified to that shown in Fig. 62. This simplification implies that the EQC elements, corresponding to diffusion of hydrogen in the bulk of the materials, can be neglected as long as care is taken that only EIS data are modeled that are not influenced by diffusion effects. This essentially means that, in the cases presented in this study, EIS data down to $f \approx 5$ mHz can be accurately modeled as diffusion does not contribute. As the absolute values of C_{ad} and C_{tr} are assumed to be of the same order of magnitude, C_{ad} cannot be simply neglected, unlike for the pure Pd electrode (see Figs. 59 and 60).

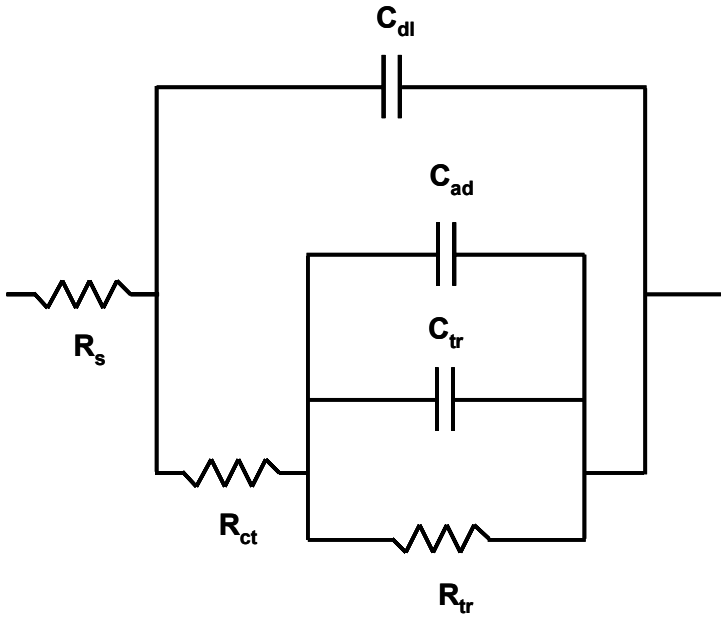

Fig. 62: Simplified version of the circuit shown in Fig. 61, obtained when assuming infinitely fast absorption ($R_{abs} \rightarrow 0$) and omitting elements coupled to solid-state diffusion of hydrogen in both the Pd- and $Mg_ySc_{(1-y)}$ bulk.

4.3.6.2. Surface kinetics

The first kinetic parameter that will be treated in detail is R_{ct}. Different $Mg_ySc_{(1-y)}$ electrodes, of which the Mg content was varied in the range $y = 0.65 – 0.80$, were investigated by means of EIS. The raw impedance data (not shown here) were similar to those shown in Fig. 57. Values of R_{ct}, obtained by using the EQC shown in Fig. 62, were converted to exchange current densities (i_0), using Eq. 49 listed in Section 3.6.3.1.

In Fig. 63 i_0 is plotted *vs.* the hydrogen concentration in the $Mg_ySc_{(1-y)}$ thin film. Similar shapes can be observed irrespective of the Mg content y. Taking the $Mg_{0.80}Sc_{0.20}$ composition as example, a maximum in i_0 can be observed around $Mg_{0.8}Sc_{0.2}H_{2.0}$ and a plateau-like behavior between $Mg_{0.8}Sc_{0.2}H_{1.7}$ and $Mg_{0.8}Sc_{0.2}H_{0.7}$. Without careful interpretation, this experimental evidence might lead to the false conclusion that the charge transfer kinetics are somehow related to the composition of the $Mg_ySc_{(1-y)}$ material. This is actually not expected as it was assumed that the Pd topcoat dictates the surface reaction kinetics.

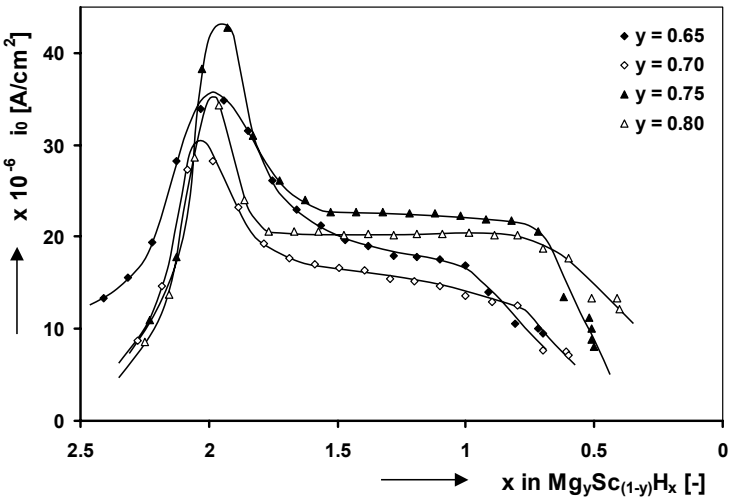

Fig. 63: Relationship between the exchange current density and the hydrogen concentration of Pd-coated $Mg_ySc_{(1-y)}$ thin film electrodes with varying Mg content y; $y = 0.65$ (◆), $y = 0.70$ (◇), $y = 0.75$ (▲) and $y = 0.80$ (△).

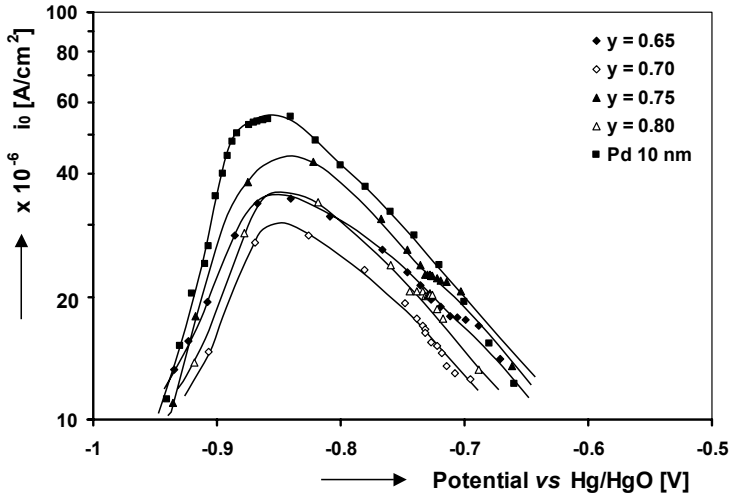

Fig. 64: Exchange current density as a function of the equilibrium potential for various Pd-coated $Mg_ySc_{(1-y)}$ thin film electrodes and a 10 nm thick Pd thin film electrode (■). The Mg content of the $Mg_ySc_{(1-y)}$ thin film electrodes was varied between $y = 0.65 – 0.80$; $y = 0.65$ (◆), $y = 0.70$ (◇), $y = 0.75$ (▲) and $y = 0.80$ (△).

To check the validity of this assumption the i_0 of the $Mg_ySc_{(1-y)}$ materials, as well as the i_0 of the 10 nm thick Pd electrode, are plotted logarithmically *vs.* the equilibrium potential (see Fig. 64). The i_0 values of the pure Pd electrode were obtained from the EIS data shown in Fig. 58 using the EQC depicted Fig. 60. From Fig. 64 it is clear that, when plotted logarithmically *vs.* potential, the shape of the i_0-curve is similar for all $Mg_ySc_{(1-y)}$ electrodes and also for the pure Pd electrode. It is evident that the slopes of the curves in the potential regions of - 0.70 V to - 0.82 V and - 0.90 V to - 0.94 V are equal and that the maximum is situated at the same potential (- 0.86 V). This clearly shows that the Pd completely dictates the surface kinetics. The small deviations in the absolute value of i_0 for the individual electrodes can be attributed to slight variations in geometric surface area and surface

roughness. The same characteristic shape of the i_0 *vs.* potential curves has been presented previously by Notten *et al.*[73,93]. In this work, a shape identical to the curves shown in Fig. 64 was theoretically derived, as well as experimentally proven for various hydride-forming compounds.

4.3.6.3. Hydrogen transport in a 2-layer system

As stated in Section 4.3.6.1, the Pd-coated $Mg_{80}Sc_{20}$ thin film electrodes showed two semi-circular responses when plotting the measured impedance data in a Nyquist plot (see Fig. 57). Unlike the 10 nm Pd thin film electrode, which only showed a single semi-circle (see Fig. 58), a second semi-circular response at hydrogen concentrations lower than $Mg_{0.8}Sc_{0.2}H_{1.6}$ can be discerned at intermediate frequencies. As only the 2-layer $Mg_ySc_{(1-y)}$ electrodes showed this behavior and the 1-layer Pd electrodes did not, it is reasonable to assume that this additional impedance response is linked to a kinetic effect induced by the addition of this second layer. Excluding solid-state diffusion of hydrogen in the $Mg_ySc_{(1-y)}$ layer, the only chemical process from which the second semi-circle can originate, is the transfer of hydrogen across the $Pd/Mg_ySc_{(1-y)}$ interface (see Fig. 44, process (d)).

Values for R_{tr}, which is the resistance attributed to the transfer of hydrogen across the $Pd/Mg_ySc_{(1-y)}$ interface, were obtained by modeling the EIS data using the EQC shown in Fig. 62. If $\ln R_{tr}$ is plotted *vs.* the equilibrium potential of the thin film electrodes, similar shapes can be observed for different $Mg_ySc_{(1-y)}$ compositions (see Fig. 65). The curves can basically be divided into two regions, denoted as region I and II. Region I, situated at more negative equilibrium potentials, exhibits quasi-linear dependencies. These values correspond to the EIS measurements performed at equilibrium potentials where the $Mg_ySc_{(1-y)}$ thin film electrode exhibits its two-phase coexistence region (see Fig. 47).

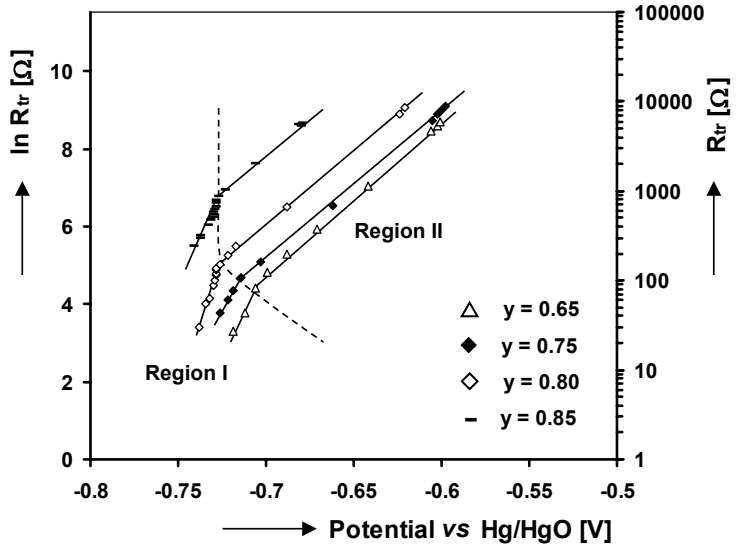

Fig. 65: Relationship between the hydrogen transfer resistance across the $Pd/Mg_ySc_{(1-y)}$ interface and the equilibrium potential for various Pd-coated $Mg_ySc_{(1-y)}$ thin film electrodes. The Mg content of the $Mg_ySc_{(1-y)}$ thin film electrodes was varied between $y = 0.65 – 0.85$; $y = 0.65$ (△), $y = 0.75$ (◆), $y = 0.80$ (◇) and $y = 0.85$ (–). The data in region I was obtained in the two phase-coexistence region, whereas the data in region II was measured when the $Mg_ySc_{(1-y)}$ electrode was in its hydrogen-depleted state. The left-hand y-axis shows $\ln R_{tr}$ plotted on a linear scale, the right-hand y-axis shows the absolute value of R_{tr} plotted logarithmically.

In region II, the lnR_{tr} *vs.* potential relationship shows perfectly linear dependencies. Here the data corresponds to EIS measurements performed at equilibrium potentials where the thin film electrodes are in their hydrogen-depleted state (solid solution behavior). It is evident that the absolute value of R_{tr} is heavily influenced by y in $Mg_ySc_{(1-y)}$, becoming larger when the amount of Mg is increased. Interestingly, at a Mg content higher that the optimum ($Mg_{0.80}Sc_{0.20}$) composition[18,91,70], the absolute value of R_{tr} is about one order of magnitude higher in the hydrogen-depleted solid solution, as well as on the plateau. This shows that R_{tr} is quite dominant throughout the (de)hydrogenation process, thus contributing to a significant overpotential during current-flowing conditions and thereby seriously influencing the rate capability of the 2-layer thin film electrode.

Region II of Fig. 65 also reveals that the slopes of the curves are equal, indicating that the potential dependence of lnR_{tr} is equal, irrespective of composition. The most important observation that can be made is that these slopes equal $\frac{F}{RT}$. Montella proposed that, if the MH is in the hydrogen-depleted state, the resistance of Reaction 10 varies proportionally with potential according to[105]

$$\ln R_{abs} \propto \frac{FE_{MH}^{eq}}{RT} . \tag{57}$$

Interestingly, an identical relation for lnR_{tr} can be seen in Fig. 65, showing that the chemistry of the transfer of hydrogen from the surface (H_{ad}) to the subsurface (H_{ss}), closely resembles that of hydrogen transfer across the Pd/$Mg_ySc_{(1-y)}$ interface (see Fig. 44, processes (b) and (d), respectively).

Although the linear dependence of lnR_{tr} in the hydrogen-depleted state can be explained as above, the exact reason why R_{tr} behaves in a similar way as R_{abs} is not yet understood. Furthermore, additional research is also required in order to fully understand the higher slope of lnR_{tr} *vs.* potential, when the thin film electrode is in its two-phase region.

4.3.7. The $Mg_ySc_{(1-y)}$ hydride structure

In order to comprehend the crystallographic changes that occurs during the (de)hydrogenation of the $Mg_ySc_{(1-y)}$ materials, the hydrogenated forms of the compounds were subjected to XRD analysis. As explained in Section 4.2, the thin film samples were measured *in-situ* during hydrogenation under 0.9 bar H_2 pressure. The results hereof are shown in Fig. 66. This figure shows that accurate structural measurements are very difficult to perform on thin film samples as the signal-to-background-ratio is rather small, the peaks are very broad and only one peak is clearly visible at 2θ-values between 25 and 45 ° 2θ due to strong preferential orientation. Assuming that this single visible reflection arises from the (111) planes of an fcc structure, the lattice parameter a is about 4.93 Å for y = 0.65 For increasing Mg-content the lattice parameter increases further as the diffraction peak has shifted to slightly lower angles. For y = 0.80 a lattice parameter of 4.97 Å can be calculated. The strongest reflection of MgH_2, which would be at 28 ^{o} 2θ, is clearly absent, indicating that there is no MgH_2 formed upon hydrogenation.

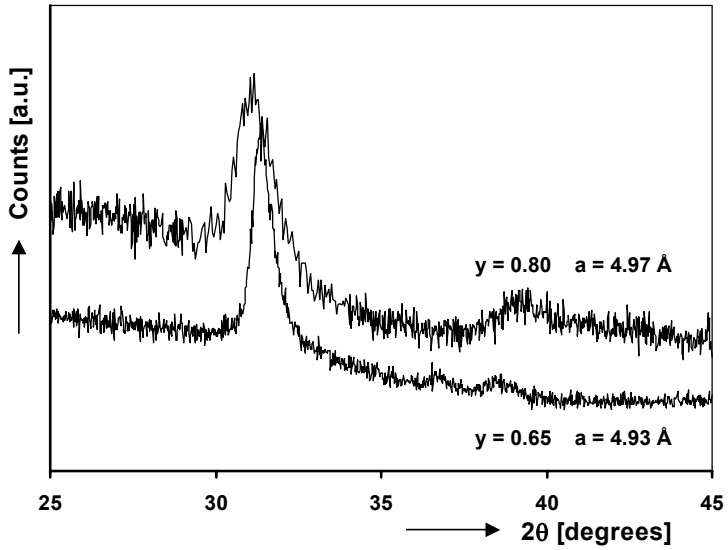

Fig. 66: X-ray diffractograms of fully hydrogenated $Mg_ySc_{(1-y)}$ thin films with $y = 0.65$ and 0.80.

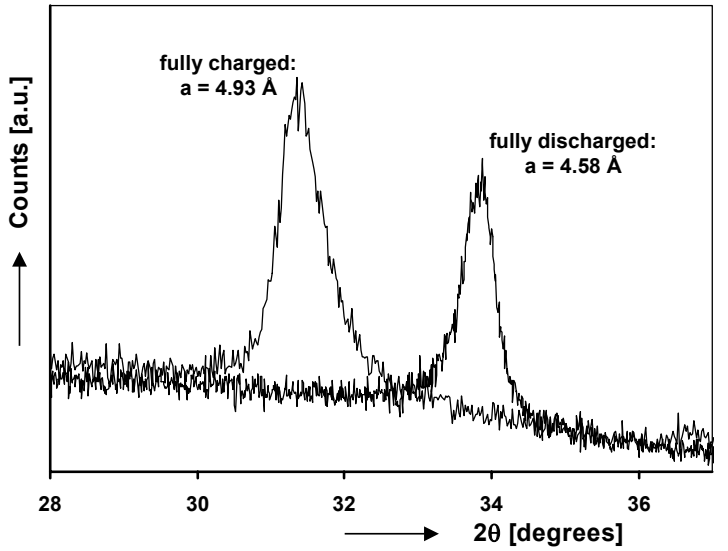

Fig. 67: X-ray diffractograms of a fully hydrogenated and completely dehydrogenated $Mg_{0.65}Sc_{0.35}$ thin film sample.

Fig. 67 shows the (111) reflections of a fully charged and completely discharged $Mg_{0.65}Sc_{0.35}$ thin film sample. As quantitative dehydrogenation is very difficult for thin film samples because of the extremely small amounts of hydrogen contained in the sample, only the extreme cases (full and empty) could be measured. Fully charged the lattice constant equals 4.93 Å. After completely desorbing all reversibly stored hydrogen this value decreased to 4.58 Å. This implies that the lattice has contracted substantially, leading to about 25 % total volume change.

Preferential orientation and the difficulty in accurately tuning the amount of hydrogen of the thin films in a gas-phase environment, makes structural investigations very challenging. In order to accurately investigate the crystallography of the MgSc compounds *ex-situ* XRD measurements were performed on a somewhat user-friendly system, namely MgSc bulk materials.[91] As was shown in Fig. 47, the discharge process of the $Mg_ySc_{(1-y)}$ compounds (with $y \leq 0.80$) is dominated by a 2-phase coexistence region. To investigate the phase

transition that is occurring a $Mg_{0.65}Sc_{0.35}$ bulk sample, fully charged via the gas-phase, was partially unloaded by heating it in a thermogravimetric analyzer. 1.8 wt.% H was discharged from the material, roughly corresponding to an extracted amount of charge of 500 mAh/g (see Fig. 48). This is relatively close to the beginning of the plateau region. The measured XRD data of the fully hydrogenated (top) and partially discharged $Mg_{0.65}Sc_{0.35}$ hydride (bottom) are shown in Fig. 68.

The diffractogram shows that in the fully hydrogenated state a pattern is observed that is in full agreement with an fcc arrangement of the metal atoms. Again, there is no indication that MgH_2 is present. The lattice constant of the resulting material, 4.84 Å, is slightly larger than the literature value for pure ScH_2, which is a = 4.78 Å[111] and elemental analysis showed the hydrogen content of this material to be approximately 2.2 H/M. The diffractogram of the partially dehydrogenated material (Fig. 68 bottom) clearly shows two separate phases present in the sample, both of them fcc structures. For the sake of clarity the reflections for which the splitting is most clear, namely the (111), (311) and (222) reflections, have been labeled by the same symbol in both diffractograms. The lattice constants that were found for the two structures are 4.80 Å for the hydrogen-rich structure and 4.68 Å for the hydrogen-depleted structure. 4.80 Å is still slightly larger than pure ScH_2, while 4.68 Å for the hydrogen-depleted phase is clearly smaller. The discrete lattice expansion, *i.e.* the relative volume change associated with this phase transformation, can be calculated from the lattice constants in Fig. 68. The volume change equals $(V_\beta - V_\alpha)/V_\alpha = (4.80^3 - 4.68^3)/4.68^3 \approx 8$ %, quite a lot smaller than the 21 % for AB_5-type materials like $LaNi_5$. [112]

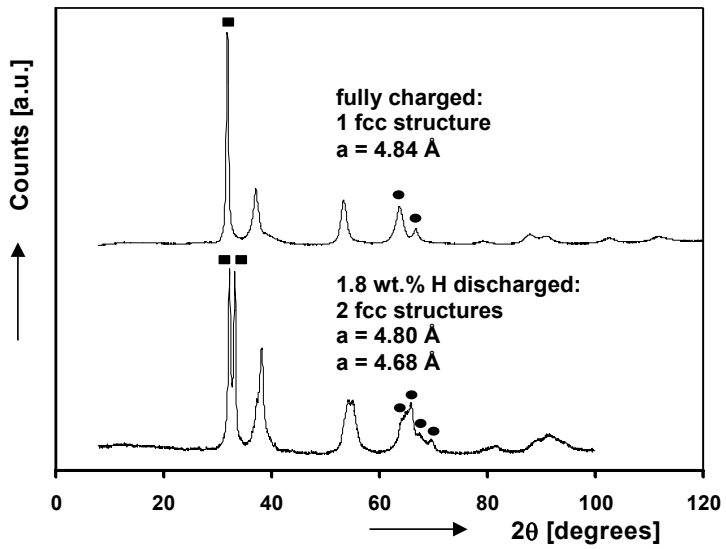

Fig. 68: X-Ray diffractograms of a fully hydrogenated (top) and partially dehydrogenated (bottom) bulk $Mg_{0.65}Sc_{0.35}$ material. Indicated are the reflections with the clearest peak splitting; (111) reflection (■), (311) and (222) reflections (●).

According to the second *Westlake criterion*[113,114,115], the distance between neighboring hydrogen atoms should be at least 2.1 Å. Like all rare earth dihydrides, ScH_2 has a so-called fluorite structure where the metal atoms are in an fcc arrangement and the hydrogen atoms fill the tetrahedral sites. This structure is shown in Fig. 69 (top). Here the location of an empty octahedral site is also indicated. The Tetrahedral-Octahedral (T-O) distance in pure ScH_2 with a = 4.78 Å is equal to ¼ * √3 * a = 2.07 Å. This distance is, in principle, too small to allow simultaneous occupation of T- and O-sites and cubic ScH_2 indeed does not transform to the trihydride phase at atmospheric pressures. YH_2 and LaH_2, for example, which have

T-O distances of 2.252 Å and 2.455 Å, respectively, do readily convert to their respective trihydrides.

Basically there are two ways to try and synthesize ScH_3. Firstly, increasing the chemical potential of hydrogen gas by increasing the pressure as was done by Bashkin *et al.*[116,117]. A second possibility is expanding the ScH_2 lattice by synthesizing a solid solution with another hydride. Pure MgH_2 has a rutile structure, which is shown in Fig. 69 (bottom). Both structures shown in Fig. 69 depict a single unit cell, containing 4 formula units in the case of ScH_2 (top) and 2 formula units for MgH_2 (bottom). The molar volume of MgH_2 (30.38 $Å^3$/f.u.)[118] is more than 10 % larger than that of ScH_2 (27.30 $Å^3$/f.u.), so dissolving MgH_2 in ScH_2 will increase the molar volume and the T-O distance, allowing the O-sites to be occupied according to the second *Westlake criterion*.

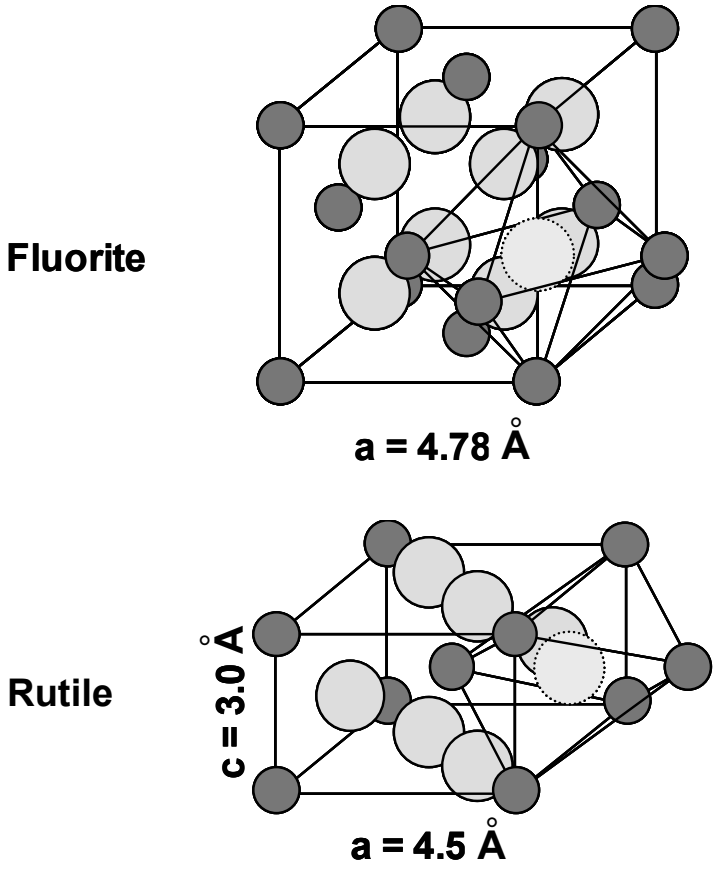

Fig. 69: Schematic representation of a unit cell of a fluorite structure (top) and a rutile structure (bottom). The small dark spheres represent the metal atoms and the larger light spheres interstitial H-atoms. An empty octahedral interstitial site is indicated for both structures (light sphere with dashed line).

As was concluded from Fig. 48, the measured capacities, especially for the thin films, matched the theoretical predictions based on the uptake of 3 H/Sc and 2 H/Mg very well. Furthermore, XRD measurements have shown that a cubic single-phase hydride is formed when the MgSc compounds are fully hydrogenated. As was already apparent from Figs. 66 and 68, the measured lattice constants of this fcc-structured hydride is significantly larger than that of pure ScH_2 for both the bulk and thin film MgSc hydrides. Moreover, the hydride structure in the thin film seems to expand even more strongly than the bulk materials. It should be kept in mind, however, that the bulk materials were measured *ex-situ*, possibly losing some hydrogen between the actual hydrogenation and the actual XRD measurement.

The hydrogen-rich phase in the 2-phase region of the bulk material (Fig. 68) is, with a lattice constant of 4.80 Å, still larger than ScH_2, so even though the T-O distance in the fully charged compound is still smaller than 2.1 Å (2.092 Å), it is clear that a solid solution of Sc hydride and MgH_2 has been formed and that above H/M = 2 the octahedral sites are partly filled.

The structural model discussed above also explains why the first solid solution part of the discharge curves is heavily influenced by the amount of Sc in the MgSc alloy. If the material absorbs 3 H/Sc and 2 H/Mg, the total H/M ratio in the fully hydrogenated state increases with increasing Sc content. Therefore, more octahedral sites have to be occupied in the fully hydrogenated material and the amount of hydrogen extracted before the onset of the two-phase coexistence region increases (see Fig. 47).

For the bulk materials, see Fig. 68, the hydrogen-poor phase has a lattice constant that is significantly smaller than that of pure ScH_2, but since the H/M ratio is now much smaller than 2, this is to be expected. The fact that the fcc structure of the metal sub-lattice is retained upon discharging leads to the assumption that the two-phase coexistence region corresponds to a phase transition from a fluorite structure, where all the tetrahedral sites are occupied by hydrogen, to a sphalerite structure, where only half of the tetrahedral sites are filled. Fig. 70 depicts the entire dehydrogenation process for the $Mg_xSc_{(1-x)}H_{(3-x)}$ compounds, when going from a high to a low H/M ratio. However, by assuming H/M = 3-x in the fully charged state, the point where H/M = 2 does not exactly coincide with the onset of the plateau region. Particularly for the compositions rich in Sc this deviation can be quite substantial. Work is currently in progress to determine, by neutron diffraction, the exact site occupancies of the hydrogen interstitials in the fully charged and partially discharged materials.

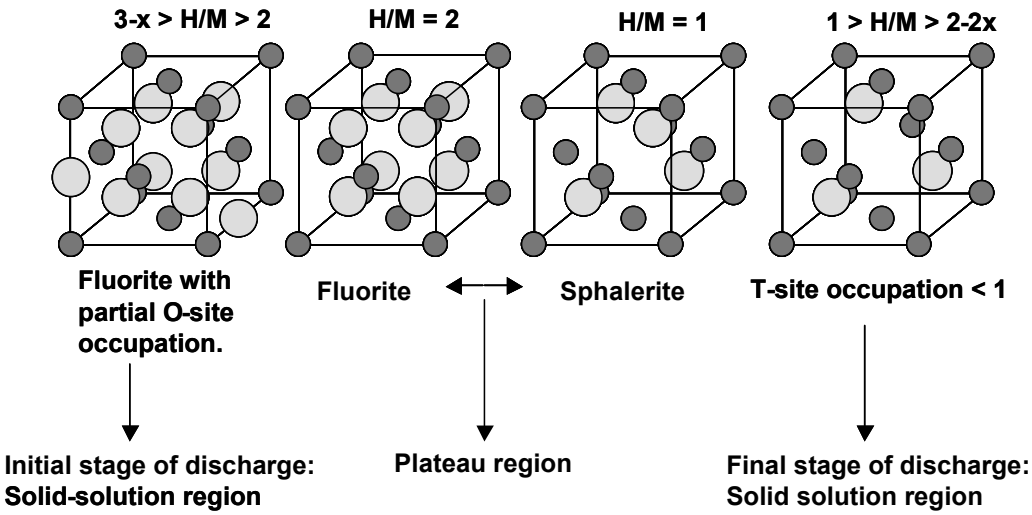

Fig. 70: Evolution of the structure of the $Mg_xSc_{(1-x)}H_{(3-x)}$ materials upon dehydrogenation.

It is interesting to look at how the hydrogenation behavior of the MgSc alloys presented in this study compares to previous investigations on Mg-rare earth systems. Isidorsson *et al.* investigated how the optical properties of MgLa thin layers changed upon loading with hydrogen.[119] A so-called 'black state' was observed, which was attributed to the coexistence of nanocrystalline Mg and MgH_2. It was interpreted that these films disproportionated upon hydrogenation and although structural determinations are always difficult to carry out on thin film samples because of very small grain size and preferential orientation, XRD on fully hydrogenated $La_{0.60}Mg_{0.40}$ confirmed the coexistence of LaH_3 and MgH_2. Giebels *et al*. also

performed measurements on MgSc thin layers.[86] Based on the observation of a black state, the same as in MgLa, and the fact that the enthalpy change calculated from GITT curves measured by Notten *et al.*[18] almost exactly coincided with the formation enthalpy of MgH_2, Giebels *et al*. concluded that these materials also segregated into MgH_2 and ScH_3.[120] However, direct evidence for the presence of MgH_2 in the fully charged material, as in the MgLa case[119], was not found. As the MgSc bulk materials investigated during this study do not seem to have any tendency to segregate and the electrochemical responses of thin films and bulk materials are nearly identical, there is no reason to assume that MgSc thin films disproportionate.

Studies on other bulk Mg-rare earth alloys seem to confirm the findings presented in this section as well. Mg_2La and Mg_2Ce were shown by Gingl *et al.* to form tetragonal single-phase hydrides at room temperature and 100 bar of hydrogen pressure.[121] Comparable process conditions are used for gas-phase hydrogenation of the MgSc materials presented in this study. For MgY it was shown by Goto *et al.* that cubic $MgY_2H_{7.8}$ can be formed at 1073 K and 3 GPa hydrogen pressure.[122] The resulting compound was found to retain its fcc structure upon dehydrogenation to $MgY_2H_{4.9}$ at 600 - 800 K and atmospheric pressures, analogous to the MgSc materials presented here.

It may seem rather amazing that compounds that are not isostructural, ScH_3 is hexagonal, ScH_2 is cubic and MgH_2 is rutile, have such an extensive solid solubility region, up to at least 80 at.% Mg. However, both ScH_3 and MgH_2 have cubic high-pressure modifications that are stable above 1 GPa[116] and 3.8 GPa[123], respectively, making it a lot less surprising that a cubic modification is formed upon synthesis of the mixed ternary hydride.

As was already stated, and could also be seen in Fig. 48, there is a limit to the solid solubility of ScH_2 and MgH_2. The sudden drop in the discharge capacity for $y > 0.8$ indicates that there is a change in the crystal structure of the hydride beyond this composition. Pure MgH_2 has a rutile-structure, which is known to exhibit very poor hydrogen sorption kinetics.[62] A study by Vigeholm *et al*. showed that hydrogenation of pure Mg metal ceases when a metal/hydride interface is no longer present at the surface.[124] This implies that hydrogen diffusion through the rutile-structured MgH_2 is almost infinitely slow and can act as a blocking layer. Because of the short diffusion distances of only 200 nm in the thin films, compared to 40 μm for the bulk materials, it is still possible to extract a considerable amount of hydrogen at low current density, even for pure Mg films. For the bulk materials, however, the discharge capacity almost drops to zero.

Although it has long been known that MgH_2 effectively blocks hydrogen diffusion, a reason for this is almost never given. However, it can be easily understood by considering the distances between the H-atoms and the empty interstitial sites in the lattice. In Fig. 69 an O-site has also been indicated for the rutile structure. The distance between the indicated O-site and the neighboring H-atom is only 1.27 Å, which is much less than the 2.1 Å prescribed by the *Westlake criterion*. This shows that during hydrogenation, diffusion through rutile-structured MgH_2 can only take place via vacancies on the hydrogen sub-lattice, which is a very slow process. Even though the T-O distance in the observed MgSc cubic structures is marginally smaller than 2.1 Å, it has been shown that simultaneous occupation of T- and O-sites is possible. This means that the, mostly empty, octahedral sites provide a very rapid diffusion path for the hydrogen atoms enabling much faster diffusion as compared to the rutile structure.

4.4. Concluding remarks

The electrochemical hydrogen storage properties of $Mg_ySc_{(1-y)}$ alloys were studied in thin film form. Using electrode materials in which *y* was varied from 0.50 to 0.90, it was shown that the discharge capacity of thin film electrodes is 5 – 20 % higher than that of previously reported MgSc bulk powders. The maximum reversible hydrogen storage capacity is obtained with the $Mg_{0.80}Sc_{0.20}$ composition and is 1795 mAh/g, corresponding to 2.05 H/M or 6.7 wt.% H, making these materials a promising candidate for usage as battery electrode material or hydrogen carrier. Interestingly, the electrochemical properties of Pd-coated $Mg_ySc_{(1-y)}$ thin films and MgSc bulk materials are very similar. Both types of materials show similar trends in both the storage capacity and in the shape of the discharge curves with varying Sc content. However, the rate capability of the thin films is much better than that of the bulk materials due to shorter diffusion lengths and complete coverage by the Pd catalyst layer. Using GITT, the thermodynamics of the $Mg_ySc_{(1-y)}$ alloys was evaluated. This showed that the plateau pressure is not a strong function of the Sc content and almost equal to the equilibrium pressure of pure MgH_2.

Additionally, the thermodynamic and kinetic characteristics of the Pd-coated $Mg_ySc_{(1-y)}$ thin film electrodes were investigated. These thin film electrodes can be described as a 2-layer structure, in which the Pd- and $Mg_ySc_{(1-y)}$ layer both contribute to the overall electrochemical response. Thin films consisting of solely Pd, with identical thickness and orientation as the Pd topcoat of the $Mg_ySc_{(1-y)}$ thin film electrodes, were examined in order to identify the response of the Pd topcoat in the 2-layer system. Using elementary thermodynamics and the equilibrium data of Pd- and $Mg_ySc_{(1-y)}$ thin film electrodes, the exact hydrogen concentration in each layer was determined. It was determined that during the major part of the hydrogen extraction process of the $Mg_ySc_{(1-y)}$ thin film, the composition of the Pd topcoat is close to $PdH_{0.001}$. Using EIS, the kinetics of the surface reactions were investigated. Based on the results of $Mg_ySc_{(1-y)}$ thin films ($y = 0.65 – 0.85$) and pure Pd films, it was concluded that the surface kinetics are completely dominated by the Pd topcoat. Furthermore it was shown that the charge transfer reaction, and not the absorption reaction is the rate-determining step. An additional impedance response, dominating the overall kinetic impedance of the $Mg_ySc_{(1-y)}$ thin film electrode when in its hydrogen-depleted state, was attributed to the transfer of hydrogen across the Pd/$Mg_ySc_{(1-y)}$ interface. Moreover, the absolute impedance associated with this process increases with decreasing Sc content.

Electrochemical investigations indicated that the thin films showed a drop in both rate capability and, to a lesser extent, storage capacity at the same composition as the bulk system. So despite the lack of unambiguous structural data, it is reasonable to assume that the crystal structure of the thin films is the same as that of the bulk materials. Diffraction data obtained from the MgSc bulk systems clearly demonstrated that the fully charged $Mg_ySc_{(1-y)}$ hydrides attain a single-phase fcc-structured hydride and no phase segregation takes place. Upon dehydrogenation, this fcc structure is retained and the electrochemically observed 2-phase coexistence region can be attributed to a phase transformation from a fluorite to a sphalerite structure.

Overall, the $Mg_ySc_{(1-y)}$ thin films can be regarded as suitable model systems for their bulk alloy counterparts. Both the electrochemical responses and the trends in storage capacity and kinetics with composition and hydrogen content are quite similar, showing that thin films can provide a better insight in the electrochemical processes taking place in bulk systems.

5

Hydrogen storage in thin film MgX alloys (X = Ti, V, Cr)

Abstract

XRD measurements show that highly crystalline $Mg_yX_{(1-y)}$ (X = Ti, V, Cr) thin films can be manufactured by means of electron-beam deposition. Single-phase compounds were obtained in all cases, clearly showing a solid solution of Ti, V or Cr in the Mg host structure. The hydrogen storage properties of Pd-coated $Mg_yX_{(1-y)}$ thin films, with *y* ranging from 0.50 to 0.95 (X = Ti) and *y* = 0.80 (X = V, Cr), are electrochemically investigated. The reversible hydrogen storage capacity of the $Mg_{0.80}X_{0.20}$ (X = Ti, V, Cr) compounds is determined to be 1750 mAh/g for $Mg_{0.80}Ti_{0.20}$, 1700 mAh/g for $Mg_{0.80}V_{0.20}$ and 1270 mAh/g for $Mg_{0.80}Cr_{0.20}$, corresponding to, 6.5, 6.4 and 4.9 wt.% H, respectively. Electrochemical measurements convincingly show that low-cost Ti is an excellent substitute for the expensive Sc in $Mg_ySc_{(1-y)}$ materials, without introducing detrimental effects. The rate capability of the $Mg_{0.80}X_{0.20}$ compounds is profoundly influenced by element X in MgX. It will be shown that the rate capability of the Ti-containing material is similar to that of the Sc-containing material and far superior to that of the V- and Cr-containing compounds. Isotherms of the $Mg_{0.80}X_{0.20}$ systems reveal that the equilibrium potential of the main charge/discharge plateau only slightly depends on X in MgX. Impedance data indicate that the surface kinetics of the $Mg_{0.80}X_{0.20}$ (X = Ti, V, Cr) thin films are dictated by the Pd topcoat. Aside from the surface kinetics, two additional processes dominate the impedance data; the transfer of hydrogen across the Pd/$Mg_yX_{(1-y)}$ interface and solid-state diffusion of hydrogen in the bulk. The absolute resistance of these processes is significantly higher for the V- and Cr-containing thin films, as compared to the Ti- and Sc-containing materials. This results in an inferior rate capability for the V- and Cr-containing thin films.[*]

[*] Part of this chapter is based on: R.A.H. Niessen, and P.H.L. Notten, *Electrochemical hydrogen storage characteristics of thin film MgX (X = Sc, Ti, V, Cr) compounds*, Electrochem. Solid St. Lett., 8, A534 (2005) and P. Vermeulen, R.A.H. Niessen, and P.H.L. Notten, *Hydrogen storage in metastable $Mg_yTi_{(1-y)}$ thin films*, in press Electrochem. Comm. (2005).

5.1. Introduction

As shown in Chapter 4, MgSc compounds exhibit very high hydrogen storage capacities, which are close to six times that of the commercially used MischMetal-based materials. Although these MgSc materials can reversibly store a large amount of hydrogen, the main drawback is the very high cost of the incorporated Sc. It is therefore desirable that the Sc in the alloy is (partly) replaced by a less expensive material, without introducing detrimental effects. It was argued that (see also Section 4.3.7), depending on the Sc content, the MgSc hydride is either rutile-structured or fcc-structured of which the latter structure shows superior hydrogen transport properties.[18,91] The favorable fcc structure of the MgSc hydride most likely originates from the fact that the fcc structure of ScH_2 is retained, even when Sc is partially substituted by Mg (see Section 4.3.7).

Therefore, a logical substitute for Sc would be a material that also forms an fcc-structured hydride by itself. Additionally, the material should (ideally) be similar in weight as compared to Sc. Promising candidates, based on these criteria, are Ti, V and Cr. Unfortunately, these materials do not form intermetallics with Mg under standard alloying conditions.[87] During the last few years, several researchers have investigated both the preparation and the hydrogen sorption characteristics of the MgTi, MgV and MgCr hydride systems. Kyoi *et al.* used 8 GPa and 873 K to synthesize metastable Mg_7TiH_x.[125] The same 'anvil-cell' technique was used to create Mg_6VH_x by Kyoi *et al.* in 2004.[126] Finally, Mg_3CrH_x was discovered by the same group in 2003 and additionally investigated by Rönnebro *et al.*[127,128]. Although the complexity of the 'anvil-cell' technique is very high and the conditions applied very extreme, it does show that crystalline MgX hydrides (X = Ti, V, Cr) can exist in bulk form.

Until now, only a few researchers have tried to synthesize and characterize the same compounds via a thin film approach. Richardson *et al.* used magnetron sputtering to prepare MgTi thin films and subsequently examined the properties of this system during hydrogenation. However, as these films were amorphous in their as-deposited state, no indication could be given whether or not a single-phase compound was formed.[129] Additionally, no information was given on the stoichiometry of the hydride.

In this chapter it will be shown that $Mg_yX_{(1-y)}$ (X = Ti, V, Cr) thin films, manufactured by means of electron-beam deposition, are highly crystalline and single-phase. This shows that it is possible to synthesize these metastable compounds without using extremes in pressure and temperature. The hydrogen storage properties of these promising $Mg_yX_{(1-y)}$ compounds are investigated electrochemically in an alkaline environment. Section 5.3.2 only deals with the galvanostatic behavior of $Mg_yTi_{(1-y)}$ materials (with varying y), whereas in the remainder of this chapter focuses on the comparison of key material parameters of the $Mg_{0.80}Ti_{0.20}$, $Mg_{0.80}V_{0.20}$ and $Mg_{0.80}Cr_{0.20}$ compounds. The investigated characteristics include the galvanostatic behavior (Section 5.3.3), the thermodynamics (Section 5.3.4) and the electrochemical impedance (Section 5.3.5).

5.2. Experimental

$Mg_yX_{(1-y)}$ (X= Ti, V, Cr) thin films were manufactured using electron-beam deposition (base pressure between 10^{-7} and $2 * 10^{-7}$ mbar). The Mg content in the $Mg_yTi_{(1-y)}$ films was varied in the range $y = 0.50 - 0.95$, whereas only a selected composition was deposited for the $Mg_yV_{(1-y)}$ and $Mg_yCr_{(1-y)}$ materials ($y = 0.80$). During deposition of the alloys the deposition rates of Mg and element X were between 0.8 and 6.0 nm/s and the substrates kept at room

temperature. The thin films, having a nominal thickness of 200 nm, were deposited on quartz substrates (∅ 20 mm). A Pd topcoat, 10 nm thick, was deposited on top of the $Mg_yX_{(1-y)}$ thin films. RBS was used to check the film composition. Based on these measurements it was concluded that the $Mg_yX_{(1-y)}$ composition was uniform throughout the film. Calculations regarding the hydrogen storage capacity are solely based on the RBS measurements. As a maximum deviation in the hydrogen storage capacity of the MgX compounds can occur of no more than 3 %, no correction is made for the Pd cap layer.

XRD was employed to identify the crystallographic phases of the freshly prepared samples (Panalytical MRD-PRO diffractometer). Cu-Kα radiation was used which was detected with an X'Celerator RTMS detector. These measurements were done on a rotating sample. The mass and composition of the thin films was determined by means of RBS (High Voltage Engineering RBS device, Model AN – 2500). The RBS data was fitted using the RUMP software package. The crystallography of the films was investigated using XRD equipped with a Panalytical MRD-PRO diffractometer.

A three-electrode set-up, of which the details are described in Section 3.2, was used to electrochemically characterize the thin films. Special care was taken to prevent surface poisoning of the thin film electrodes induced by some commercial reference electrodes, as it was shown to seriously affect the electrochemical response (see Section 3.6).

Galvanostatic measurements were performed using a Maccor M2300 battery tester (Maccor, Tulsa, USA). EIS, GITT and measurements were done on an Autolab PGSTAT30 (Ecochemie B.V., Utrecht, the Netherlands). EIS measurements were conducted at equilibrium voltage conditions using an ac amplitude of 5 mV rms and scanning the frequency from 50 kHz to 1 mHz. A non-linear least squares fitting program (EQUIVCRT) was used to analyze the EIS data. Unless stated otherwise, the cut-off voltage applied during all galvanostatic hydrogen extraction (discharge) experiments was set to 0 V *vs.* Hg/HgO and all potential values are given *vs.* Hg/HgO (6 M KOH).

5.3. Results & discussion

5.3.1. Structural characterization of the as-prepared thin films

All $Mg_yX_{(1-y)}$ thin films that were manufactured were analyzed by means of XRD and RBS in order to determine their crystallography, layer thickness and mass. Fig. 71 depicts the X-ray diffractogram of a $Mg_{0.80}Ti_{0.20}$ thin film coated with Pd. Analogous to the MgSc materials (see Section 4.3.1) a strong preferential orientation reduces the number of reflections significantly. The dominant reflection is that of a (002) oriented hexagonal α-Mg structure. This peak is shifted with respect to pure Mg (34.4 ° 2θ) due to the fact that the Ti atoms are incorporated into the Mg structure.[130] The inset in Fig. 71 shows the (002) reflections of all $Mg_yTi_{(1-y)}$ thin films investigated, in which the Mg content ranges from $y = 0.75 – 0.95$. Also included in this inset is the XRD response of the pure Mg thin film, clearly showing its (002) reflection at the literature value (34.4 ° 2θ). A clear shift in the peak position towards smaller angles, *i.e.* larger d-spacing, is apparent with decreasing Ti content. According to *Vegard's Law* this shift of the (002) peak is brought about by partial substitution of Mg by Ti, which has a smaller molar volume than Mg, causing the lattice to contract.[131] It should be noted that the $Mg_{0.70}Ti_{0.30}$ and $Mg_{0.50}Ti_{0.50}$ compositions are omitted as their XRD spectra showed that these thin films were almost completely X-ray amorphous, only showing very weak reflections of the (002) peak.

Aside from the reflections that can be attributed to the $Mg_yTi_{(1-y)}$ thin films, responses were measured that can be linked to the Pd topcoat. It seems that the orientation of the Pd is virtually independent on the degree of orientation of the underlying $Mg_yTi_{(1-y)}$ layer and a strong reflection of (111) oriented fcc-structured Pd was observed in all cases.

The fact that over such a large composition range Ti is fully incorporated in the Mg structure is in itself quite surprising, as under normal circumstances Mg and Ti do not show any solid-solubility.[87] Like for the MgSc thin films, the e-beam deposition method has introduced a significant enhancement of the solid-solubility and for this case it even appears to be possible to manufacture meta-stable $Mg_yTi_{(1-y)}$ compounds.

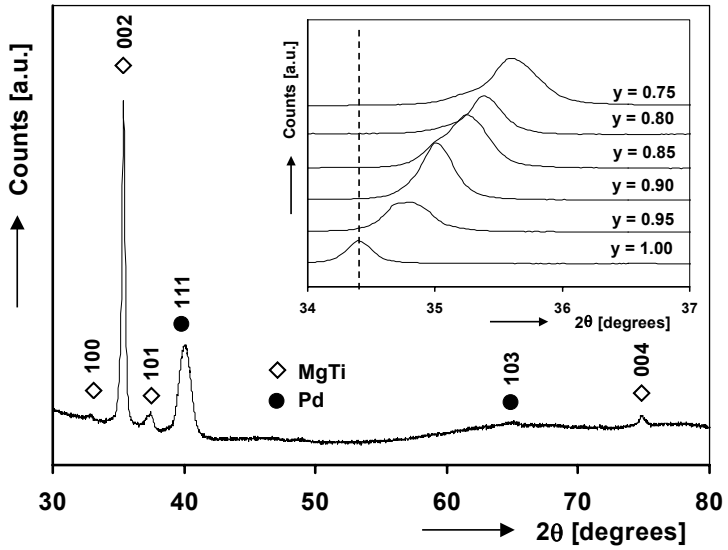

Fig. 71: X-ray diffractogram of a 200 nm thick $Mg_{0.80}Ti_{0.20}$ thin film capped with 10 nm of Pd. The reflections of both the MgTi thin film and the Pd topcoat are indicated. The (002) peak of the hexagonal α-Mg structure is shown in the inset for all measured $Mg_yTi_{(1-y)}$ compositions. The dashed line in the inset indicates the literature value of pure Mg (34.4 ° 2θ).

Fig. 72 shows the XRD spectra of $Mg_{0.80}X_{0.20}$ (X = Ti, V, Cr) thin films freshly prepared by means of high-vacuum deposition ($Mg_{0.80}Ti_{0.20}$ (a); $Mg_{0.80}V_{0.20}$ (b); $Mg_{0.80}Cr_{0.20}$ (c)). Unsurprisingly, all three thin films show a strong preferential orientation. The strongest reflection is attributed to the (002) orientation of hcp-structured MgX. For all three compounds, this peak is shifted with respect to pure Mg (34.4 ° 2θ) due to the fact that Ti, V or Cr host atoms are incorporated into the Mg structure.[130]

As no reflections were observed that could be linked to the hcp structure of pure Ti, or the bcc structure of either pure V or Cr, it is concluded that a single-phase solid solution of Ti, V or Cr in Mg was formed. In addition to the responses of the $Mg_{0.80}X_{0.20}$ layers, reflections were measured that could be linked to the Pd topcoat. Interestingly, the orientation of the Pd topcoat is strongly dependent on the $Mg_{0.80}X_{0.20}$ alloy on which it is deposited. For the $Mg_{0.80}Ti_{0.20}$ thin film a strong reflection is present of (111) oriented fcc-structured Pd (as was also shown in Fig. 71). The Pd topcoat of the $Mg_{0.80}V_{0.20}$ and $Mg_{0.80}Cr_{0.20}$ thin films has a different preferred orientation, namely the (200) direction (see Fig. 72, curves (b) and (c)). Exactly why a different orientation is observed in these cases is unclear at this moment. It should be noted that RBS measurements (not shown here) indicated that all Pd was indeed present as a separate layer on top of the $Mg_{0.80}X_{0.20}$ layers and was not dissolved into the underlying MgX layer.

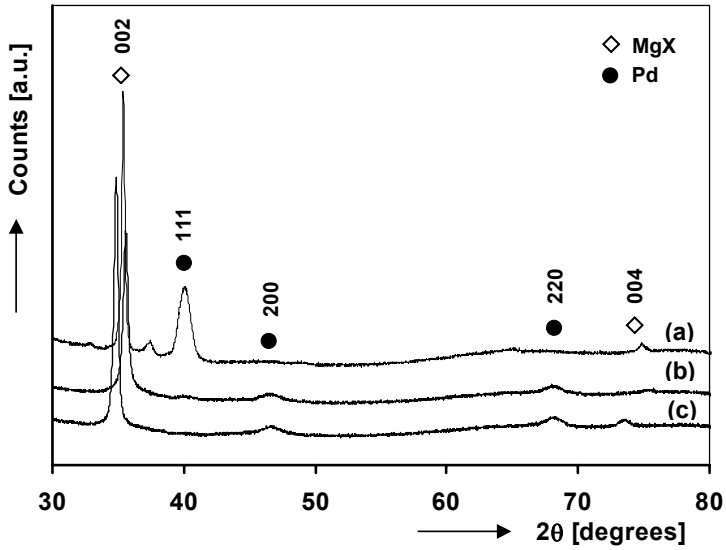

Fig. 72: XRD spectra of 200 nm thick, $Mg_{0.80}Ti_{0.20}$ (a), $Mg_{0.80}V_{0.20}$ (b) and $Mg_{0.80}Cr_{0.20}$ (c) thin films, capped with 10 nm of Pd. Also indicated are the main reflections and orientation.

Table 5: Layer thickness and mass of $Mg_yX_{(1-y)}$ films (X = Ti, V, Cr) with varying composition. Also listed are the specifications of the pure Mg thin films. *

Nominal composition [-]	Layer thickness [nm]	Mass [µg]
$Mg_{0.50}Ti_{0.50}$	170	154
$Mg_{0.70}Ti_{0.30}$	170	126
$Mg_{0.75}Ti_{0.25}$	178	121
$Mg_{0.80}Ti_{0.20}$	183	123
$Mg_{0.85}Ti_{0.15}$	210	126
$Mg_{0.90}Ti_{0.10}$	176	104
$Mg_{0.95}Ti_{0.05}$	168	93
$Mg_{0.80}V_{0.20}$	171	120
$Mg_{0.80}Cr_{0.20}$	175	127
Mg	288	151

RBS measurements were performed on each batch that was manufactured in order to determine the composition, homogeneity of composition throughout the entire thin film, mass of the active material and the thickness of the individual layers. The RBS data showed that the ratio of Mg and element X (X = Ti, V, Cr) remained constant during the deposition of the thin films, as already noted in Section 4.2. The nominal composition, layer thickness and mass of all $Mg_yX_{(1-y)}$ films described in this chapter are listed in Table 5. Additionally, information is listed on pure Mg thin films (see Section 4.2 for the preparation of these samples).

* All $Mg_yX_{(1-y)}$ and pure Mg thin films are covered with a 10 nm Pd topcoat.

5.3.2. Galvanostatic behavior of $Mg_yTi_{(1-y)}$ materials

To accurately investigate the galvanostatic behavior of the MgTi materials[132], the thin films were fully hydrogenated (charging) and dehydrogenated (discharging) in a similar manner to that used for the MgSc compounds (see Section 4.3.4). First the samples were fully charged using a current of - 0.6 mA (200 $\mu A/cm^2$ or ~ 5000 mA/g). After 1 hour of equilibration they were discharged with + 0.12 mA (40 $\mu A/cm^2$ or ~ 1000 mA/g) and subsequently deep-discharged using + 0.012 mA (4 $\mu A/cm^2$ or ~ 100 mA/g). Ultimately, they were again charged to their fully hydrogenated states using - 0.6 mA in order to determine whether any hydrogen was irreversibly incorporated in the compounds.

The dehydrogenation behavior of the $Mg_yTi_{(1-y)}$ compounds, with varying Ti content, is shown in Fig. 73. From this figure it is immediately evident that the galvanostatic behavior of these $Mg_yTi_{(1-y)}$ alloys is very similar to that of the MgSc materials discussed before (see Section 4.3.4). By systematically altering the Ti content, the impact on the observed electrochemical responses of the $Mg_yTi_{(1-y)}$ thin layers can be assessed. The first part of the discharge curve shows a very narrow solid solution region for all compositions. The width of this region appears not to be influenced by the amount of Ti in the $Mg_yTi_{(1-y)}$ materials. This observation is very different from that made for the MgSc compounds where the width of this first solid solution region clearly depended on the amount of Sc. In Section 4.3.4 it was shown that this part of the discharge process could be attributed to the single hydrogen atom that could be reversibly extracted from the Sc. Interestingly, this solid solution region does show a plateau-like discontinuity for the MgTi materials at around - 0.80 V to - 0.85 V. However, if the amount of charge involved is taken into consideration, it is clear that this feature corresponds to the full dehydrogenation of the Pd topcoat (see also 4.3.5.2). A closer look at Fig. 47 reveals that this feature is, although somewhat less obvious, present in all galvanostatic discharge curves of the MgSc materials.

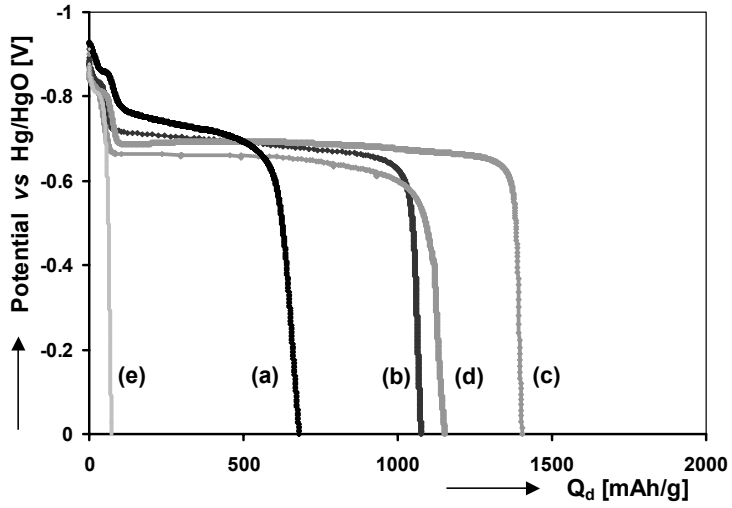

Fig. 73: Selected galvanostatic discharge curves of Pd-coated $Mg_yTi_{(1-y)}$ thin films; $Mg_{0.50}Ti_{0.50}$ (a), $Mg_{0.70}Ti_{0.30}$ (b), $Mg_{0.80}Ti_{0.20}$ (c), $Mg_{0.85}Ti_{0.15}$ (d), and $Mg_{0.90}Ti_{0.10}$ (e). A high discharge current of + 0.12 mA (~ 1000 mA/g) was used.

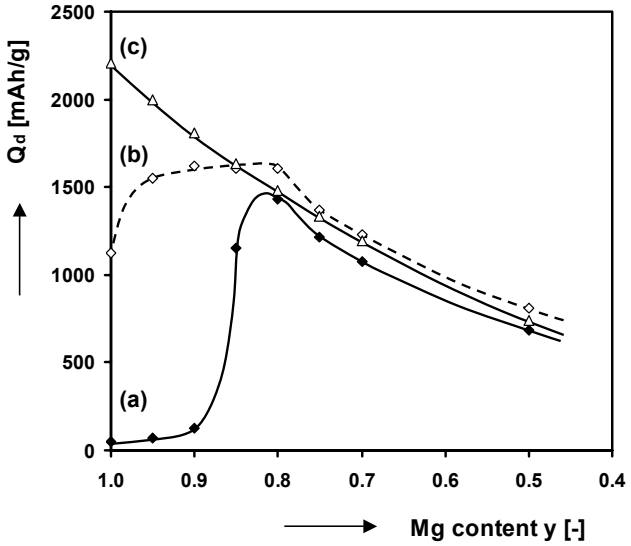

Fig. 74: Obtained discharge capacity of $Mg_yTi_{(1-y)}$ thin films as a function of composition using a discharge current of + 0.12 mA (a) and + 0.012 mA (b). The theoretical capacity, based on just two reversible hydrogen atoms per Mg atom, is also included (c).

Beyond this solid solution a wide plateau region, pointing to a two-phase coexistence region, is observed within a potential region of - 0.67 V to - 0.73 V for $Mg_yTi_{(1-y)}$ compounds where $y \leq 0.85$. Both the potential at which that plateau is situated and the sloping of this plateau seem to be dependent on the amount of Ti. For example, very Ti rich materials like $Mg_{0.50}Ti_{0.50}$ exhibit significant sloping and a two-phase coexistence plateau that is situated at a substantially more negative potential. Mg rich compositions, however, show very flat plateaus at about - 0.67 V. Analogous to the MgSc materials, no two-phase coexistence exists when the Mg content exceeds a certain critical composition and the potential rapidly increases to the cut-off potential upon continued discharging. The critical composition at which this occurs in the MgTi case is $y > 0.85$, slightly different to that of the MgSc case ($y > 0.80$).

Fig. 74 depicts the compositional dependence of the extracted amount of charge of the measured $Mg_yTi_{(1-y)}$ thin film electrodes. Here, the discharge capacities obtained at a high and low discharge rate, using currents of + 0.12 (curve (a)) and + 0.012 mA (curve (b)), respectively, are plotted. Like for the MgSc compounds (see Fig. 48), an increase in Mg content results in an increasing discharge capacity. Overall, this trend is maintained up to an optimum around the $Mg_{0.80}Ti_{0.20}$. In this case, the reversible hydrogen storage capacity of this composition is over 1600 mAh/g, corresponding to 1.84 hydrogen atoms per metal or 6 wt.%. This shows that Ti can successfully substitute Sc in the Mg-based alloy, while retaining excellent rate capability and only showing a slight drop in discharge capacity. Although the high-rate discharge capacity is somewhat lower as compared to that of $Mg_{0.80}Sc_{0.20}$, it is still close to five times that of commercial AB_5-type materials.[92,93] In the region where $y \leq 0.80$ not much difference exists between the high and low-rate discharge capacities, indicating excellent rate capability.

Similar to the MgSc alloys much lower discharge capacities are measured for compositions that are rich in Mg ($y > 0.80$). For $Mg_yTi_{(1-y)}$ compounds with $y = 0.85$ still a significant amount of charge can be extracted during the high-rate discharge, yet only a fraction of the stored hydrogen can be extracted when $y = 0.90 - 0.95$ (see also Fig. 73). Nonetheless, at a low discharge current the total capacity is still very significant and only

decreasing slightly when the composition is changed from $y = 0.80$ to pure Mg. This leads to the same conclusion as was already drawn for the Mg-rich MgSc materials (see Section 4.3.4), implying that the rate capability is the parameter that is affected here. A similar decrease in rate capability of the MgSc compounds was attributed to the formation of a rutile-structured hydride (see Section 4.3.7 and Fig. 48). It is therefore very plausible that the decrease in rate capability observed for the $Mg_yTi_{(1-y)}$ materials originates from a similar unfavorable hydride structure.

Aside from the curves depicting the high- and low-rate discharge capacities (curves (a) and (b), respectively), the theoretical discharge capacity is shown (curve (c)) in Fig. 74. This theoretical approximation is based on the fact that two hydrogen atoms can be reversibly extracted from the $Mg_yTi_{(1-y)}$ materials per Mg atom, whereas Ti is assumed not to be able to release any hydrogen. This seems a reasonable estimate, as it is known that the enthalpy of formation of TiH_2 is very low (- 70 kJ/mol H[90]), indicating that is it unlikely that this hydrogen can be reversibly extracted. It is clear from Fig. 74 that for compositions with $y < 0.80$ the experimentally determined and theoretically predicted discharge capacities are nearly identical when considering the low discharge current.

In order to investigate the compositional dependence on the charging behavior in more detail, the electrochemical responses of $Mg_yTi_{(1-y)}$ compounds with varying Ti content (y = 0.50, 0.70, 0.80, 0.90, 0.95) are depicted in Fig. 75. It should be noted that these potential responses were measured during the first hydrogenation of the freshly prepared thin films. At a glance, the presented charging curves can be divided into three regions. During the initial stages of the charging process a plateau is revealed that is clearly dependent on the amount of Ti in the $Mg_yTi_{(1-y)}$ material.

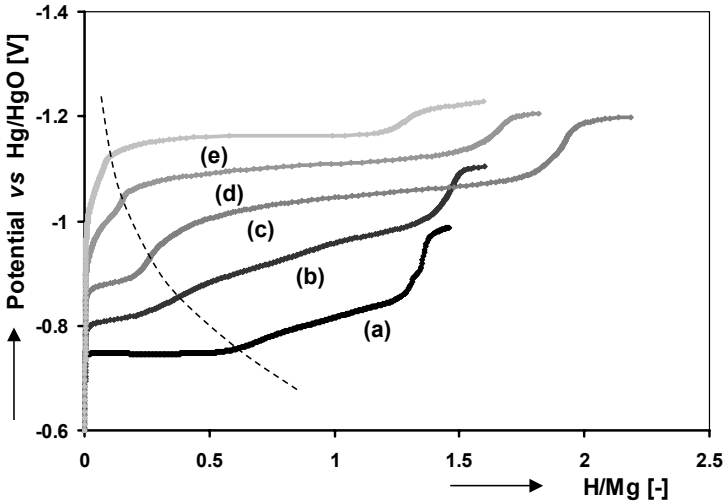

Fig. 75: Galvanostatic behavior, during the first hydrogenation step, of $Mg_yTi_{(1-y)}$ thin films with different Ti content; y = 0.50 (a), y = 0.70 (b), y = 0.80 (c), y = 0.90 (d) and y = 0.95 (e). A current of – 0.6 mA was applied. The dashed line is a guide to the eye, indicating the transition from the first to the second plateau.

This plateau, which increases in width with increasing Ti content, roughly corresponds to the hydrogenation of Ti to TiH. This is quite unexpected as full conversion to TiH_2 is expected. However, it was shown by Kaess *et al.* that the activation enthalpy for hydrogen diffusion in TiH_x increases significantly when approaching stoichiometry (*i.e.* $x = 2$).[133] Other studies on the TiH_x system support this observation and show that Ti hydride layers show low permeability for hydrogen when hydrogenating Ti at room temperature, indicating that the formation up to TiH_2 does not necessarily occur.[134] Additionally, research by Bhosle *et al.*

has shown that, given the right conditions, a TiH phase can be formed, which is more stable than the stoichmetric dihydride.[135] TiH was previously discussed by Schur *et al.* who showed, quite remarkably, that this phase consisted of a meta-stable fct-structured compound.[136]

After reaching this point, a second plateau can be discerned which could be attributed to the conversion of Mg to roughly MgH_2. However, careful calculation based on the width of the second plateau shows that full conversion to MgH_2 might not happen at every composition, especially at very high and low Ti content. The fact that both Ti and Mg do not fully convert to their respective stoichiometric dihydrides, might suggest that no segregation occurs upon hydrogenation and that a single-phase hydride is formed. An additional effect, clearly evident from Fig. 75, is that the Ti content clearly affects the degree of sloping of the second plateau. Ti-rich alloys (*i.e.* y = 0.50 and 0.70) are characterized by a rather sloping second plateau, whereas Mg-rich materials (*i.e.* y = 0.95) exhibit a very flat plateau region.

Finally, the potential decreases further until a stable value is reached at which hydrogen gas formation occurs (see Section 2.4.2, Reaction 12). Surprisingly, this potential value is quite susceptible to the overall composition (*i.e.* Ti content) of the $Mg_yTi_{(1-y)}$ compound. Although the Pd/KOH interface is expected to have similar electrocatalytic properties for all $Mg_yTi_{(1-y)}$ layers, the difference in potential at which hydrogen gas is evolved suggests otherwise. Apparently the surface kinetics at the Pd topcoat are significantly influenced by *y* in the underlying $Mg_yTi_{(1-y)}$ layer. A possible reason for this could be that the degree of expansion of the $Mg_yTi_{(1-y)}$ lattice upon hydrogenation changes with Ti content, introducing more or less stress. For example, those compounds rich in Mg expand significantly more than those rich in Ti.

From the discussion given above it is evident that it is not straightforward to estimate, based on the obtained electrochemical responses shown in Figs. 75 and 73, whether Ti and Mg fully convert to their stoichiometric dihydrides and if only Mg is able to reversible release its hydrogen. Therefore, the simplified view of the hydrogenation of the $Mg_yTi_{(1-y)}$ compounds, see Fig. 74 curve (c), may not be correct. This might hint towards the absence of phase segregation during hydrogenation and the formation of single-phase $Mg_yTi_{(1-y)}$ hydrides, as this would mean that it is impossible to estimate the hydrogenation behavior of the separate elements (*i.e.* Ti and Mg).

5.3.3. Galvanostatic behavior of $Mg_{0.80}X_{0.20}$ (X = Ti, V, Cr) thin films

In the previous section the electrochemical hydrogen storage characteristics of $Mg_yTi_{(1-y)}$ compounds were exclusively treated. As the optimum composition of the Ti-containing material was situated at *y* = 0.80, V- and Cr-containing thin films were prepared with the same composition and their electrochemical hydrogen storage characteristics compared. In order to see whether the second metal has a profound influence on these characteristics, the electrochemical response of $Mg_{0.80}Ti_{0.20}$, $Mg_{0.80}V_{0.20}$ and $Mg_{0.80}Cr_{0.20}$ thin films are compared.[137] Additionally, parallels are drawn between these compounds and the $Mg_{0.80}Sc_{0.20}$ material presented earlier (see Chapter 4).

The electrochemical response of the $Mg_{0.80}X_{0.20}$ thin films (X = Ti, V, Cr) was compared during galvanostatic hydrogenation (charging) and dehydrogenation (discharging). Figs. 76 to 78 show the charge, discharge and deep-discharge curves of each of the three compounds. Currents were used of – 0.6 mA (~ 5000 mA/g), + 0.12 mA (~ 1000 mA/g) and + 0.012 mA (~ 100 mA/g), respectively. It should be noted that in these experiments the layers were first fully hydrogenated (curves (a)) and hereafter allowed to reach equilibrium under open-circuit conditions for 1 hour. Then the layers were discharged until the cut-off potential was reached (curves (b)), after which the electrode was allowed to equilibrate for 1 hour. Subsequently,

deep-discharging was performed (curves (c)). Finally the electrodes were again charged to the fully loaded state (curves (d)).

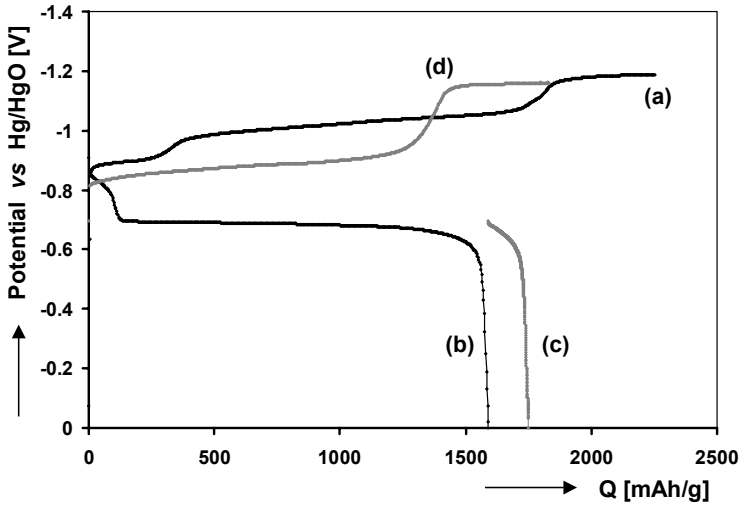

Fig. 76: Electrochemical response of a $Mg_{0.80}Ti_{0.20}$ thin film, showing the first hydrogenation at - 0.6 mA (a), first discharge at + 0.12 mA (b), subsequent deep-discharge at + 0.012 mA (c) and the second hydrogenation at - 0.6 mA (d).

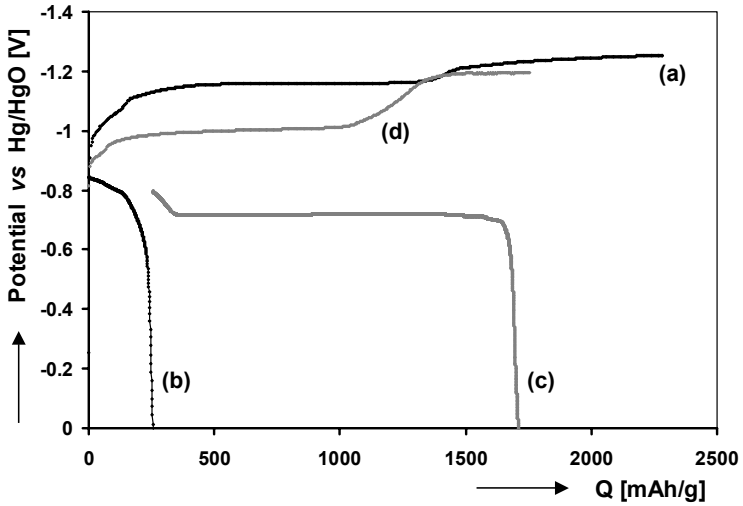

Fig. 77: Galvanostatic response of a $Mg_{0.80}V_{0.20}$ thin film, showing the first hydrogenation at - 0.6 mA (a), first discharge at + 0.12 mA (b), subsequent deep-discharge at + 0.012 mA (c) and the second hydrogenation at - 0.6 mA (d).

Focusing on the response of the $Mg_{0.80}Ti_{0.20}$ compound, corresponding to the first time the electrode is hydrogenated, it is clear that the curve reveals three plateaus (see Fig. 76, curve (a)). As was shown in Section 5.3.2, the first plateau roughly corresponds to the hydrogenation of Ti to TiH, the second plateau to the hydrogenation of Mg to MgH_2 and the third plateau to that of hydrogen gas formation. When comparing this response to that of the $Mg_{0.80}Sc_{0.20}$ compound shown in Fig. 46, curve (a), a similar behavior during this initial hydrogenation can be seen. However, the transition from the first (Sc to ScH_2) to the second plateau (Mg to MgH_2) is much less pronounced. This is not as expected as the stability of ScH_2 is much higher than that of TiH_2 (- 100 kJ/mol H and - 70 kJ/mol H, respectively[90]), theoretically resulting in a larger separation between the first and second plateau. First-time

charging of the $Mg_{0.80}V_{0.20}$ and $Mg_{0.80}Cr_{0.20}$ compounds shows a more complex response, especially during the early stage of charging (see Figs. 77 and 78, curves (a)). Most notably, the main plateau, linked to hydrogen absorption, is more flat and manifests itself at more negative potentials (- 1.00 V to - 1.15 V) as compared to the $Mg_{0.80}Sc_{0.20}$ and $Mg_{0.80}Ti_{0.20}$ compounds (- 0.80 V to - 1.10 V). Like before, the final plateau can be attributed to hydrogen gas formation.

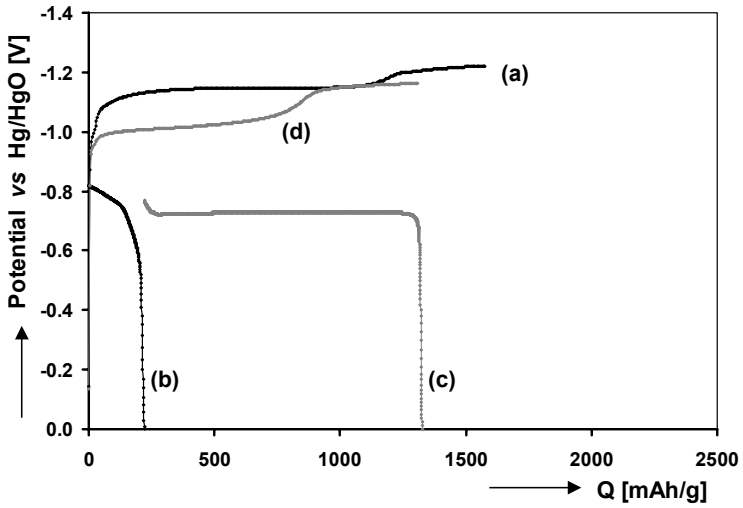

Fig. 78: Typical galvanostatic behavior of a $Mg_{0.80}Cr_{0.20}$ thin film, showing the first hydrogenation at – 0.6 mA (a), first discharge at + 0.12 mA (b), subsequent deep-discharge at + 0.012 mA (c) and the second hydrogenation at – 0.6 mA (d).

The discharge curves of all $Mg_{0.80}X_{0.20}$ compounds, see curves (b) in Figs. 76 to 78, reveal a sloping response when the film is in the hydrogen-rich state. This response can be linked to a solid solution behavior, which clearly depends on the element X. Furthermore, a very flat plateau at about - 0.67 V can be seen for the $Mg_{0.80}Ti_{0.20}$ compound, indicative of a two-phase coexistence region (see Fig. 76, curve (b)). This discharge response is very similar to that of the $Mg_{0.80}Sc_{0.20}$ material shown in Fig. 46, curve (a). The $Mg_{0.80}V_{0.20}$ and $Mg_{0.80}Cr_{0.20}$ compounds, however, cannot be discharged this effectively using the same current and no plateau is observed (see Figs. 77 and 78, curves (b)). Subsequent deep-discharging results in the fact that all compounds can be completely discharged. In the case of the $Mg_{0.80}Sc_{0.20}$ and $Mg_{0.80}Ti_{0.20}$ compounds the largest part of the hydrogen was already extracted at high current, effectively only showing a second solid solution behavior in the hydrogen-depleted state (Figs. 46 and 76, curves (c)). The lower current used during deep-discharging enabled the release of the remaining hydrogen from the $Mg_{0.80}V_{0.20}$ and $Mg_{0.80}Cr_{0.20}$ compounds (Figs. 77 and 78, curves (c)). The potential response now also shows a two-phase coexistence region for these materials, similar to that of the $Mg_{0.80}Sc_{0.20}$ and $Mg_{0.80}Ti_{0.20}$ compounds. Comparing the extracted charge at both high and low currents, it is clear that the rate capability of the $Mg_{0.80}V_{0.20}$ and $Mg_{0.80}Cr_{0.20}$ materials is significantly lower than that of the $Mg_{0.80}Sc_{0.20}$ and $Mg_{0.80}Ti_{0.20}$ compounds. To illustrate this fact; about 1300 mAh/g of charge can be extracted from the $Mg_{0.80}Sc_{0.20}$ and $Mg_{0.80}Ti_{0.20}$ thin films within 1.3 hours, whereas it takes over 11 hours to extract the same amount from the $Mg_{0.80}V_{0.20}$ or $Mg_{0.80}Cr_{0.20}$ films.

The hydrogen storage capacity of the $Mg_{0.80}X_{0.20}$ compounds (X = Ti, V, Cr) was determined by adding the measured discharge capacity of the first discharge and the first deep-discharge (see Figs. 76 to 78, curves (b) and (c)). The results, including that of

$Mg_{0.80}Sc_{0.20}$ material (see Section 4.3.4.1), are listed in Table 6 and are given as gravimetrical storage capacities in both [mAh/g] and [wt.% H]. As a reminder, the measured hydrogen storage capacities of the listed Mg-based compounds are close to six times that of commercially used AB_5-type materials.[15,93]

Table 6: Gravimetrical storage capacities of MgX compounds (X = Ti, V, Cr). The hydrogen storage capacity of $Mg_{0.80}Sc_{0.20}$ is included as well.

Nominal composition [-]	Gravimetrical storage capacity [mAh/g]	[wt.% H]
$Mg_{0.80}Sc_{0.20}$	1790	6.67
$Mg_{0.80}Ti_{0.20}$	1750	6.53
$Mg_{0.80}V_{0.20}$	1700	6.38
$Mg_{0.80}Cr_{0.20}$	1325	4.90

If the charging curves are compared, measured when hydrogenating the thin films for the first and second time, other interesting facts come to light (see Figs. 76 to 78, curves (a) and (d)). It is evident that the amount of charge (or hydrogen) that can be stored in the materials when charged for the second time, is less than during their first hydrogenation. This shows that part of the hydrogen stored during the first charging step is irreversibly incorporated and cannot be released under the experimental conditions applied. The curves corresponding to the second time the $Mg_{0.80}Sc_{0.20}$ and $Mg_{0.80}Ti_{0.20}$ compounds are charged, only show a single large plateau. This indicates that hydrogen must have been irreversibly bound (see Figs. 46 and 76, curves (a) and (d)). The curves corresponding to the second time that the $Mg_{0.80}V_{0.20}$ and $Mg_{0.80}Cr_{0.20}$ films are charged reveal a similar trend and less hydrogen could be absorbed (Figs. 77 and 78, curves (a) and (d)). The most notable difference between the first and the second time the compounds are hydrogenated is, however, the significant reduction of the overpotential (η). η can be represented by

$$\eta = IR_s + \eta_{kin} + \eta_{dif} \tag{58}$$

where IR_s is the Ohmic drop; η_{kin} is the kinetic overpotential and η_{dif} the diffusion overpotential.

Preliminary EIS measurements (not shown here) indicate that the Ohmic drop can be ignored, as it is negligible when applying currents equal to those used in this contribution. More importantly, it can be concluded from the EIS data that the reduction in η can be attributed to a decrease in η_{kin}, which is brought about by improved surface kinetics. As these kinetics are directly linked to the nature of the interface at which the charge transfer takes place (Reaction 9 in Section 2.4.2), it has to be concluded that hydriding/dehydriding the thin film electrodes induces irreversible changes at the Pd/KOH interface. This was also given as a possible explanation of this phenomenon in Section 5.3.2.

5.3.4. Thermodynamics of $Mg_{0.80}X_{0.20}$ (X = Ti, V, Cr) compounds

The isotherms of the $Mg_{0.80}X_{0.20}$ compounds (X = Ti, V, Cr) were determined electrochemically by means of GITT measurements. The thin films were first galvanostatically charged to their fully hydrogenated state, using a current of - 0.6 mA. Subsequently, the electrodes were allowed to equilibrate for 1 hour. Hereafter, $Mg_{0.80}Ti_{0.20}$ electrodes were discharged by means of GITT using a current of + 0.12 mA during the first fifteen and + 0.012 mA during the last few pulses. Due to their inferior rate capabilities (see Section 5.3.3), the $Mg_{0.80}V_{0.20}$ and $Mg_{0.80}Cr_{0.20}$ thin films were discharged using only a current of + 0.012 mA. After each current pulse all the electrodes were allowed to equilibrate for 1 hour.

The equilibrium discharge curves of all the $Mg_{0.80}X_{0.20}$ compounds, as well as that of the $Mg_{0.80}Sc_{0.20}$ material, are depicted in Fig. 79. As expected from the galvanostatic responses shown before (see Fig. 46 and Figs. 76 to 78), the isotherms show a similar behavior for all $Mg_{0.80}X_{0.20}$ compounds. Clearly, the initial solid solution behavior, up to a discharge capacity of about 400 mAh/g, seems to be dependent on whether Sc, Ti, V, or Cr is present in the Mg-based alloy. This solid solution has the most negative equilibrium potential for the $Mg_{0.80}Sc_{0.20}$ and $Mg_{0.80}V_{0.20}$ compounds, which can be understood when the correlation between equilibrium potential (E_{MH}^{eq}) and the heat of formation (ΔH_f) is used. Combining Eqs. 22 and 23 (see Section 2.4.4) shows that a more negative value of E_{MH}^{eq} corresponds to a less negative value of ΔH_f. This is indeed in line with the expected values of ΔH_f, based on experimental data shown in Chapter 4, indicating that systematically increasing the amount of Sc in MgSc extends the initial solid solution region.

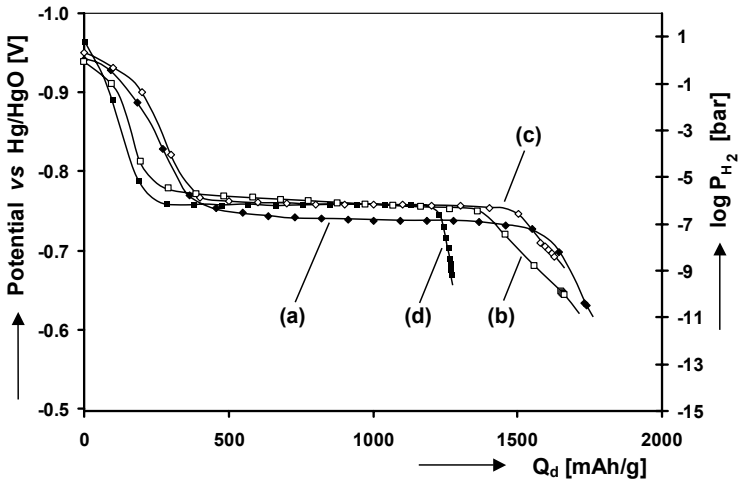

Fig. 79: Equilibrium discharge curves of $Mg_{0.80}Sc_{0.20}$ (a), $Mg_{0.80}Ti_{0.20}$ (b), $Mg_{0.80}V_{0.20}$ (c) and $Mg_{0.80}Cr_{0.20}$ (d) compounds obtained by means of GITT. Additionally, the equivalent hydrogen pressure is plotted on the right-hand axis.

For VH_x the situation is somewhat more complex. Reilly *et al.* showed that VH_2 (γ-phase) is unstable at room temperature, but that low-pressure hydrides exist with compositions up to VH (α- and β-phases).[138] These have ΔH_f values of around - 20 kJ/mol H and lower, which correspond to the experimentally observed equilibrium pressures of the initial solid solution of the $Mg_{0.80}V_{0.20}$ compound (see Fig. 79, curve (c)).

The main plateau in the isotherms is situated at - 0.75 V for all MgX compounds, except for $Mg_{0.80}Sc_{0.20}$, which has a somewhat more positive potential at around - 0.74 V to - 0.72 V.

The calculated ΔH_f corresponding to these plateaus are - 37 kJ/mol H and - 40 kJ/mol H for $Mg_{0.80}X_{0.20}$ (X = Ti, V, Cr) and $Mg_{0.80}Sc_{0.20}$, respectively (using Eqs. 22 and 23). It is rather remarkable that, with the exception of $Mg_{0.80}Sc_{0.20}$, ΔH_f seems to be unaffected by X in MgX. Moreover, ΔH_f seems to be identical to that reported for the transition from Mg to MgH_2.

Fig. 80 shows the equilibrium curves of the $Mg_{0.80}X_{0.20}$ compounds during charging. Like before, the isotherm of the $Mg_{0.80}Sc_{0.20}$ material is also included. Similar to its discharge isotherm (see Fig. 79, curve (a)), the charging isotherm of $Mg_{0.80}Sc_{0.20}$ has the most positive equilibrium potential (Fig. 80, curve (a)). The gradually sloping plateau is situated at potential values of - 0.76 V to - 0.79 V, corresponding to - 36 kJ/mol H to - 33 kJ/mol H, respectively. This difference in measured equilibrium potential during discharging and charging points to hysteresis, which is frequently observed for both thin film and bulk hydrogen storage materials. The origin of this hysteresis might be attributed to various states, induced by (uniaxial) expansion of the lattice, during charging and discharging.[139] Unlike the practically superimposing equilibrium plateaus during discharging (see Fig. 79, curves (b) to (d)), the plateau value during charging of the $Mg_{0.80}X_{0.20}$ (X = Ti, V, Cr) compounds appear to be slightly dissimilar (Fig. 80, curves (b) to (d)). The $Mg_{0.80}V_{0.20}$ thin film exhibits the most negative plateau at around - 0.805 V, corresponding to - 31 kJ/mol H. Comparing Figs. 79 and 80, it is interesting to note that all compounds show a similar hysteresis effect between charging and discharging. In all cases the difference in plateau value is approximately 50 mV or, according to Eq. 22, a factor 50 in plateau pressure.

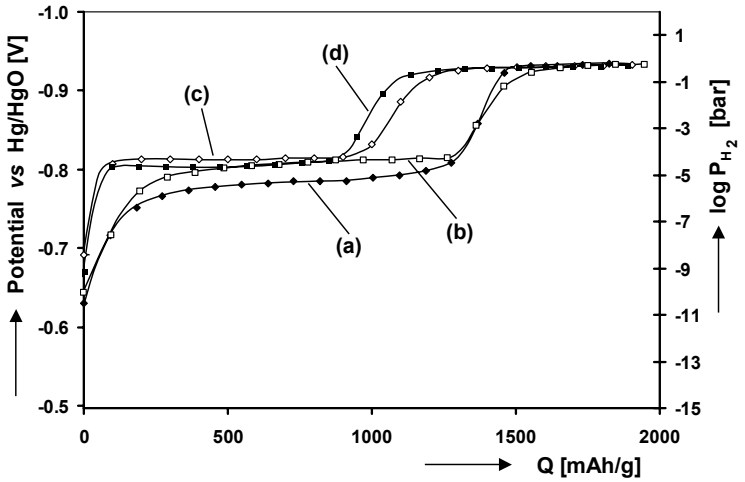

Fig. 80: Equilibrium charging curves of $Mg_{0.80}Sc_{0.20}$ (a), $Mg_{0.80}Ti_{0.20}$ (b), $Mg_{0.80}V_{0.20}$ (c) and $Mg_{0.80}Cr_{0.20}$ (d) materials measured using GITT.

5.3.5. Impedance spectroscopy on $Mg_{0.80}X_{0.20}$ (X = Ti, V, Cr) materials

EIS measurements carried out on Pd-coated $Mg_{0.80}X_{0.20}$ compounds were compared to those of Pd-coated $Mg_{0.80}Sc_{0.20}$ samples (see 4.3.6) with the intention to identify (dis)similarities in both kinetics and diffusion responses. The idea behind this is two-fold: Firstly, investigating why $Mg_{0.80}Ti_{0.20}$ electrochemically behave nearly identical to $Mg_{0.80}Sc_{0.20}$, as was shown in Section 5.3.2. Secondly, trying to find an explanation why the $Mg_{0.80}V_{0.20}$ and $Mg_{0.80}Cr_{0.20}$ compounds show an inferior electrochemical response. In all cases the thin films are treated as 2-layer systems, exhibiting the same basic reaction steps (see Section 4.3.2). The measured EIS data are modeled using the simplified equivalent circuit for a 2-layer system (see Fig. 62

in Section 4.3.6.1). The EIS responses corresponding to hydrogen diffusion through the $Mg_{0.80}X_{0.20}$ compounds are only treated qualitatively.

The electrochemical impedance of the $Mg_{0.80}X_{0.20}$ systems (X = Ti, V, Cr) was measured in a similar manner to that of the $Mg_{0.80}Sc_{0.20}$ material, using a combination of GITT and EIS (see Section 3.4.4.1). Here, the electrodes are first fully charged using a current of - 0.6 mA and subsequently allowed to relax to equilibrium. Hereafter, the electrodes are discharged using GITT, utilizing a current of + 0.012 mA (~ 4 μA/cm^2) during each GITT pulse.

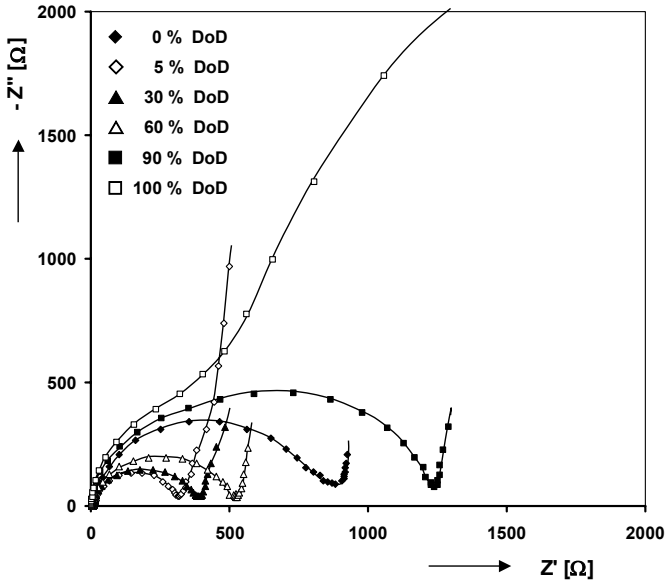

Fig. 81: Nyquist representations of a $Mg_{0.80}Ti_{0.20}$ thin film electrode at various Depths-of-Discharge; 0 % (◆), 5 % (◇), 30 % (▲), 60 % (△), 90 % (■) and 100 % (□).

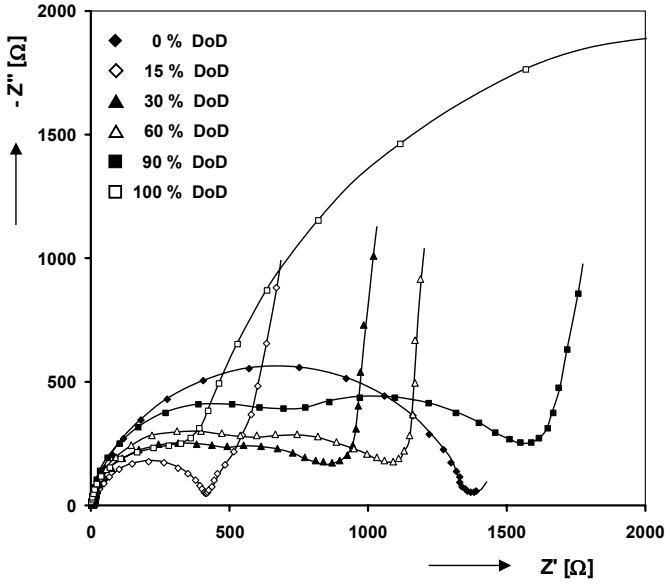

Fig. 82: Impedance spectra of a $Mg_{0.80}V_{0.20}$ thin film electrode at various Depths-of-Discharge; 0 % (◆), 15 % (◇), 30 % (▲), 60 % (△), 90 % (■) and 100 % (□).

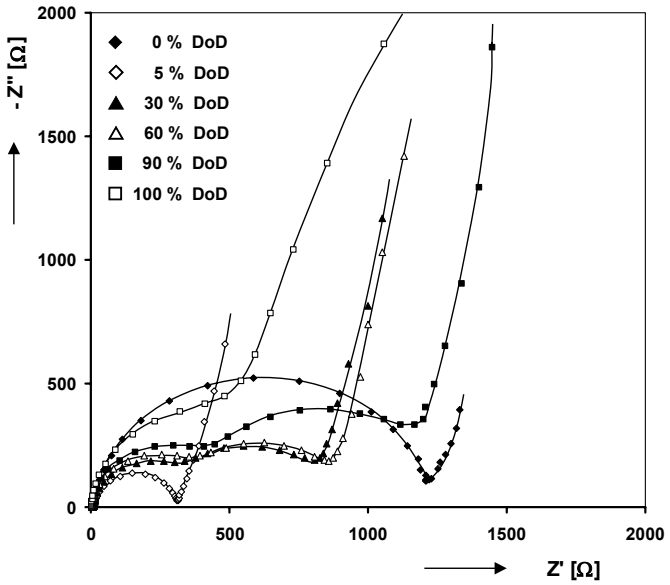

Fig. 83: Experimentally determined EIS data of a $Mg_{0.80}Cr_{0.20}$ thin film electrode at various Depths-of-Discharge; 0 % (◆), 5 % (◇), 30 % (▲), 60 % (△), 90 % (■) and 100 % (□).

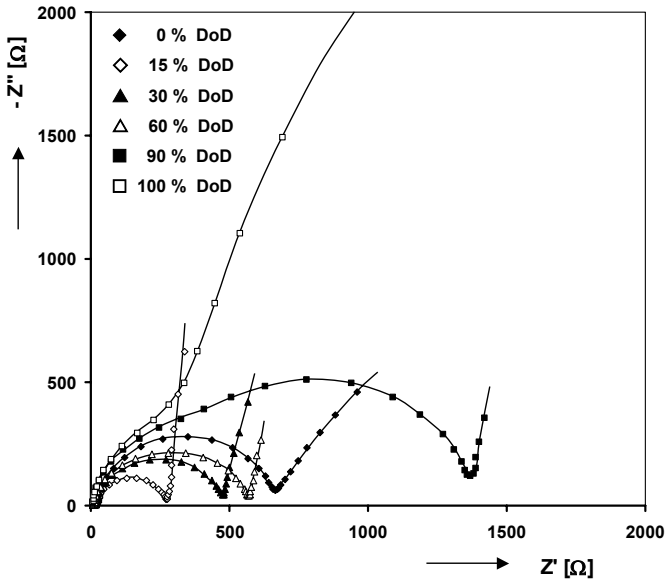

Fig. 84: Nyquist representations of a $Mg_{0.80}Sc_{0.20}$ thin film electrode at various Depths-of-Discharge; 0 % (◆), 15 % (◇), 30 % (▲), 60 % (△), 90 % (■) and 100 % (□).

The obtained EIS response of the $Mg_{0.80}X_{0.20}$ materials is shown in Fig. 81 (X = Ti), Fig. 82 (X = V) and Fig. 83 (X = Cr). As the exact hydrogen concentration is very difficult to estimate, as was explained in detail in Section 5.3.3, the EIS data is plotted as a function of Depth-of-Discharge (DoD). Here 0 % DoD corresponds to the fully hydrogenated state and 100 % DoD to the completely discharged state (based on the GITT discharge curves shown in Fig. 79). Caution should be taken not to confuse this fully discharged state with a material without any hydrogen, as some hydrogen might have been irreversible incorporated. Fig. 84 shows the impedance response of the $Mg_{0.80}Sc_{0.20}$ compound as a function of DoD. The EIS

data measured on this compound was, although in a slightly different manner, previously used in Section 4.3.6. It should be noted that the EIS responses are plotted at the same DoD values for all materials. However, due to their much wider initial solid solution regions (see Sections 5.3.3 and 4.3.4.1), the EIS data at 15 % DoD rather than 5 % DoD are shown for the $Mg_{0.80}V_{0.20}$ and $Mg_{0.80}Sc_{0.20}$ compounds.

When comparing the EIS responses of the $Mg_{0.80}X_{0.20}$ systems (X = Ti, V, Cr) to that of the $Mg_{0.80}Sc_{0.20}$ thin film, it is obvious that the overall features are very similar. At low DoD, *i.e.* the hydrogen-rich state, a single semi-circular response can be seen at high frequencies, which was attributed to the charge transfer kinetics at the Pd/KOH interface (see Section 4.3.6.1). This is followed by a capacitive behavior at low frequencies, linked to mixed semi-infinite and finite diffusion of hydrogen in the Pd and Mg-alloy bulk.

If hydrogen is extracted from the electrodes, *i.e.* at higher DoD, a second semi-circle emerges at intermediate frequencies. It was shown in Section 4.3.6.3 for the $Mg_{0.80}Sc_{0.20}$ thin film system that this response could clearly be linked to the transfer of hydrogen across the $Pd/Mg_{0.80}Sc_{0.20}$ interface. The magnitude of the second semi-circle at 30 - 90 % DoD is very dependent on the type of material, remaining infinitesimally small in the case of $Mg_{0.80}Ti_{0.20}$ and $Mg_{0.80}Sc_{0.20}$ (see Figs. 81 and 84), yet being quite significant in the case of $Mg_{0.80}V_{0.20}$ and $Mg_{0.80}Cr_{0.20}$ (see Figs. 82 and 83). Like for the hydrogen-rich state, the lowest frequencies show a capacitive behavior due to diffusion processes.

Upon continued dehydrogenation ($\geq$ 90 % DoD), the EIS spectra essentially show the same features, however, the second semi-circle increases tremendously in magnitude for all cases.

5.3.5.1. Surface kinetics

Based on the galvanostatic responses shown in Section 5.3.3 it was stated that the rate capability of the $Mg_{0.80}X_{0.20}$ (X = Ti, V, Cr) materials, during dehydrogenation, is dictated by the material properties of the MgX alloy. It was shown that the Ti-containing compound had a rate capability equal to that of the $Mg_{0.80}Sc_{0.20}$ material (see Figs. 76 and 46), while those of the $Mg_{0.80}V_{0.20}$ and $Mg_{0.80}Cr_{0.20}$ alloys were significantly lower (see Figs. 77 and 78). In order to establish whether or not the surface kinetics at the Pd/KOH interface can explain this different in rate capability, EIS was performed on all measured $Mg_{0.80}X_{0.20}$ thin films. The experimentally obtained EIS data of these thin films, as well as that of the $Mg_{0.80}Sc_{0.20}$ film are shown in Figs. 81 and 84. This data was analyzed by means of a least-squares fitting program using the EQC shown in Fig. 62. The obtained values for R_{ct}, were converted to exchange current densities (i_0), using Eq. 49 in Section 3.6.3.1.

The i_0 of the $Mg_{0.80}X_{0.20}$ materials (X = Ti, V, Cr), as well as those of the previously presented $Mg_{0.80}Sc_{0.20}$ thin film and the 10 nm thick Pd electrode (see Section 4.3.6.2), are logarithmically plotted *vs.* the equilibrium potential in Fig. 85. It is clear that, when plotted *vs.* potential, the shape of the i_0-curve is again similar for all electrodes, pointing to the fact that the surface kinetics of all electrodes can be considered identical. This, in turn, substantiates the suspicion that the preferential orientation of the Pd topcoat does not significantly influence its catalytic properties, as it was shown in the XRD spectra of the $Mg_{0.80}X_{0.20}$ materials that the preferential orientation of the topcoat was indeed dependent on the underlying MgX layer (see Section 5.3.1).

Conclusively, investigation of the charge transfer kinetics by means of EIS corroborates the hypothesis that the reduced rate capability of the $Mg_{0.80}V_{0.20}$ and $Mg_{0.80}Cr_{0.20}$ alloys is not due to surface kinetics, again indicating that the solution to this problem has to be sought in phenomena related to the transport of hydrogen.

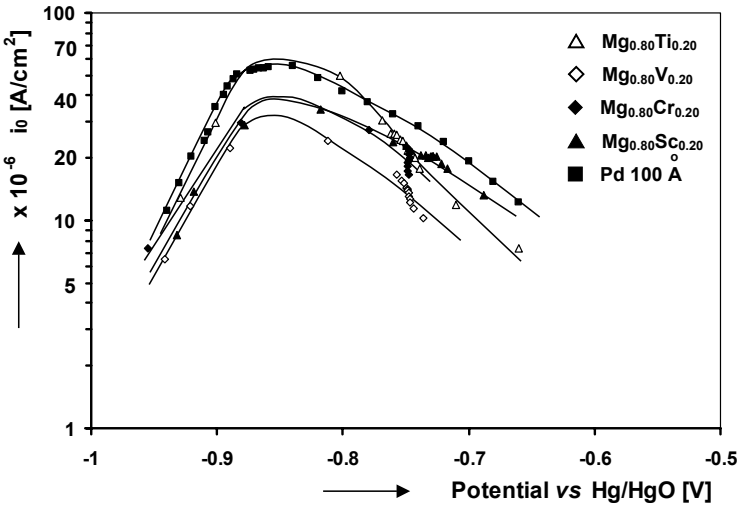

Fig. 85: Exchange current density as a function of the equilibrium potential for various Pd-coated $Mg_{0.80}X_{0.20}$ thin film electrodes; X = Ti (△), X = V (◇) and X = Cr (◆). Additionally, the i_0 *vs.* the equilibrium potential is also shown for a Pd-coated $Mg_{0.80}Sc_{0.20}$ thin film (▲) and a 10 nm thick Pd thin film electrode (■).

5.3.5.2. Hydrogen transport in $Mg_{0.80}X_{0.20}$ (X = Ti, V, Cr) thin films

As explained above, the impedance behavior of the Pd-coated $Mg_{0.80}X_{0.20}$ thin films are, overall, very similar to that of the $Mg_{0.80}Sc_{0.20}$ film and the same characteristic features are measured. These consist of 2 semi-circular responses at high and intermediate frequency and a capacitive behavior at low frequency. In this section only the semi-circle at intermediate frequency and the capacitive behavior at low frequency will be discussed.

The impedance response at intermediate frequency can, like for the Pd-coated $Mg_{0.80}Sc_{0.20}$ film (see Section 4.3.6.3), be attributed to the transfer of hydrogen across the Pd/$Mg_{0.80}X_{0.20}$ interface. Values for R_{tr}, the resistance attributed to the transfer of hydrogen across this interface, were obtained by modeling the EIS data shown in Figs. 81 to 84. In Fig. 86 $\ln R_{tr}$ is plotted *vs.* the equilibrium potential of the $Mg_{0.80}X_{0.20}$ thin film electrodes. It is immediately clear that this results in similar shapes for all MgX films, closely matching that of the $Mg_{0.80}Sc_{0.20}$ thin film. As discussed in Section 4.3.6.3, the curves can be divided into two regions, which are again denoted as region I and II.

Region I, situated at more negative equilibrium potentials, shows linear dependencies for all thin films presented. These values where derived from EIS measurements performed at equilibrium potentials where the $Mg_{0.80}X_{0.20}$ thin film electrodes exhibited their two-phase coexistence regions (see Fig. 79). The most interesting observation that can be made is that in this region R_{tr} is significantly higher for the V- and Cr-containing thin films as compared to the Ti- and Sc-containing materials. More importantly, values for R_{tr} are readily obtained all along the main discharge plateau and in the final hydrogen-depleted solid solution in the case of the V- and Cr-containing thin films (see Fig. 79). The second semi-circle, from which R_{tr} is derived, can easily be seen when subjecting the impedance spectra of these thin films to a closer look (see Figs. 82 and 83, ~ 15 % DoD to 100 % DoD). However, for the Ti- and Sc-containing thin films, R_{tr} is more difficult to detect in the early stages of the discharge, increasing gradually in magnitude when lowering the low hydrogen content. This results in the fact that, not until the hydrogen-depleted state has been reached (90 % DoD to

100 % DoD), the second semi-circle can hardly be seen in the impedance response of these samples (see Figs 81 and 84).

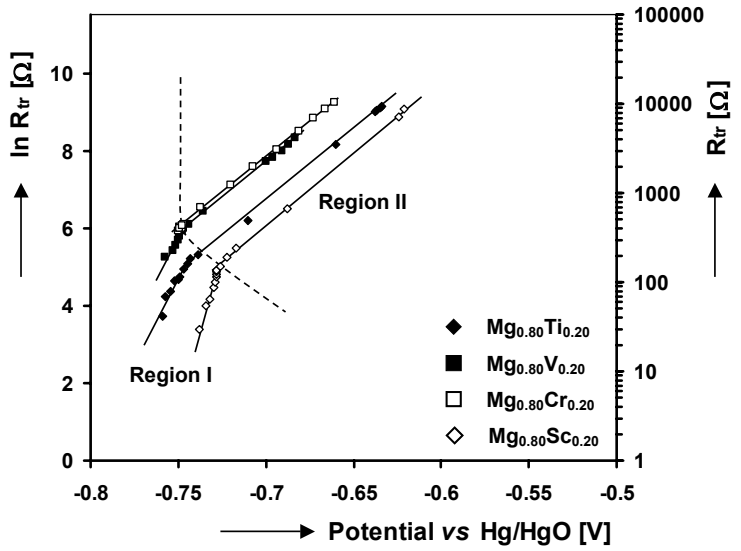

Fig. 86: Relationship between the hydrogen transfer resistance across the Pd/$Mg_yX_{(1-y)}$ interface and the equilibrium potential for various Pd-coated $Mg_yX_{(1-y)}$ thin film electrodes; $Mg_{0.80}Ti_{0.20}$ (◆), $Mg_{0.80}V_{0.20}$ (■) and $Mg_{0.80}Cr_{0.20}$ (□). As a reference the $Mg_{0.80}Sc_{0.20}$ thin film is included as well (◇). The data in region I was obtained in the two phase-coexistence region, whereas the data in region II was measured when the electrodes were in their hydrogen-depleted state. The left-hand y-axis shows lnR_{tr} plotted on a linear scale, whereas the right-hand y-axis shows the absolute value of R_{tr} plotted logarithmically.

The data in region II corresponds to EIS measurements performed at equilibrium potentials where the thin film electrodes are in their hydrogen-depleted state. Here, the lnR_{tr} *vs.* potential reveals perfectly linear dependencies with slopes equal to $\frac{F}{RT}$. In Section 4.3.6.3 it was already argued that this might hint towards to fact that the transfer of hydrogen across the Pd/Mg-alloy interface is chemically closely related to the transfer of hydrogen from the surface (H_{ad}) to the subsurface (H_{ss}). Clearly, the dopant (*i.e.* Sc, Ti, V, Cr) in the Mg-alloy seems to have no influence on this. However, the doping material does seem to have a huge impact on the absolute value of R_{tr}. From Fig. 86 it is evident that R_{tr} increases almost one order of magnitude when using V or Cr instead of Sc as a doping material.

Overall, the absolute value of R_{tr} in region I and II is affected quite heavily by the doping material used. When comparing the Ti- and Sc-containing materials to the V- and Cr-doped thin films, this results in a difference in R_{tr} of up to two orders of magnitude and one order of magnitude in regions I and II, respectively. This significantly larger impedance for the V- and Cr-doped materials will result, as a consequence, in an inferior rate capability during galvanostatic dehydrogenation.

The transport of hydrogen in these Pd-coated thin films electrodes is expressed by two different impedance responses; firstly, by the semi-circle at intermediate frequencies which corresponds to the transfer of hydrogen across the Pd/Mg-alloy interface and secondly, the capacitive behavior at low frequencies which describes the solid-state diffusion of hydrogen in the bulk. As the latter is difficult to describe in the case of these 2-layer systems (see Section 4.3.6.1), an attempt is made to qualitatively treat this response. When focusing on the low frequency responses of the impedance data shown in Figs. 81 to 84, it is clear that

the absolute value of the impedance at the lowest frequency measured (1 mHz) is quite different for the four materials. The $Mg_{0.80}Sc_{0.20}$ compound (see Fig. 84) exhibits only very marginal capacitive tails at DoD values of 30 % to 90 %, which correspond to EIS measurements done along the main discharge plateau (see Fig. 79). The Ti-containing thin film, shown in Fig. 81, essentially shows the same low frequency behavior. The $Mg_{0.80}V_{0.20}$ and $Mg_{0.80}Cr_{0.20}$ thin film electrodes, on the other hand, clearly reveal substantially more dominant capacitive tails at the same DoD values. This higher impedance indicates that the solid-state diffusion in the V- and Cr-containing compounds is considerably more difficult as compared to the Ti- and Sc-containing materials. This will again result in the fact that the dehydrogenation under current-flowing conditions will be easiest for the $Mg_{0.80}Ti_{0.20}$ and $Mg_{0.80}Sc_{0.20}$ compounds, as already concluded in Section 5.3.3.

5.4. Concluding remarks

Pd-coated $Mg_yTi_{(1-y)}$ thin films, with y ranging from 0.50 to 0.95, have been prepared by means of e-beam deposition. Based on XRD measurements it was concluded that single-phase compounds were obtained, clearly showing a solid solution of Ti in the Mg host structure. The hydrogen storage properties of these meta-stable materials were investigated electrochemically. Additionally, pure Mg thin films were investigated in order to serve as a reference. The reversible storage capacity of these MgTi materials generally increases with increasing Mg content, reaching an optimum at $y \approx 0.80$. However, the amount of Ti doping has a profound impact on the rate capability, leading to $Mg_yTi_{(1-y)}$ materials with excellent rate capability up to the composition where $y \approx 0.80$. However, if $y > 0.80$ the high-rate storage capacity rapidly decreases. The evolution of both the high and low-rate storage capacity with composition, is very similar to that of the $Mg_ySc_{(1-y)}$ thin films presented in Chapter 4. Analogous to the $Mg_ySc_{(1-y)}$ materials, this drop in rate capability might originate from a change in hydride structure from fcc to rutile. It is interesting to note that even a small addition of Ti induces a positive effect on the storage properties. Overall, electrochemical measurements convincingly showed that low-cost Ti is an excellent substitute for the expensive Sc in $Mg_ySc_{(1-y)}$ materials, without introducing detrimental effects.

As the optimum composition of both the Ti- and Sc-containing materials was situated at $y = 0.80$, V- and Cr-containing thin films were prepared with the same composition and their electrochemical hydrogen storage characteristics compared. Electron-beam deposition was used to prepare these materials and based on XRD measurements it was concluded that single-phase $Mg_{0.80}V_{0.20}$ and $Mg_{0.80}Cr_{0.20}$ compounds were obtained. The reversible hydrogen storage capacity of the $Mg_{0.80}X_{0.20}$ (X = Ti, V, Cr) compounds was determined to be up to six times higher than commercial AB_5-type materials, reaching 1750 mAh/g for $Mg_{0.80}Ti_{0.20}$, 1700 mAh/g for $Mg_{0.80}V_{0.20}$ and 1270 mAh/g for $Mg_{0.80}Cr_{0.20}$, corresponding to, 6.5, 6.4 and 4.9 wt.% H, respectively. These discharge capacities are of the same order as the $Mg_{0.80}Sc_{0.20}$ material. The rate capability of the $Mg_{0.80}X_{0.20}$ compounds is profoundly influenced by the element X incorporated in MgX. Galvanostatic measurements indicated that the rate capability of the Ti-containing material is similar to that of the Sc-containing material and far superior to that of the V- and Cr-containing compounds. It was shown that same amount of hydrogen could be released close to ten times faster from the Ti- and Sc-containing compounds, as compared to the V- and Cr-containing compounds. Isotherms of the MgX systems were obtained using GITT and showed that the equilibrium potential of the main charge/discharge plateau only slightly depended on X in MgX. Interestingly, comparison

with the $Mg_{0.80}Sc_{0.20}$ compound showed that they were situated at more negative equilibrium potentials.

Using EIS, the kinetics of the surface reactions were investigated. It was concluded that the surface kinetics of the $Mg_{0.80}X_{0.20}$ (X = Ti, V, Cr) thin films are very comparable to that of $Mg_{0.80}Sc_{0.20}$ and pure Pd thin films. This again indicates that the surface kinetics are dictated by the Pd topcoat. A second impedance response, dominant at intermediate frequencies, was attributed to the transfer of hydrogen across the $Pd/Mg_yX_{(1-y)}$ interface. The resistance of this process measured on the Ti- and Sc-containing materials was compared to that of the V- and Cr- containing thin films. This showed that the absolute value of R_{tr} was up to two orders of magnitude higher for the latter pair. This significantly larger impedance for the V- and Cr- containing materials results, as a consequence, in an inferior rate capability during galvanostatic dehydrogenation. The capacitive behavior observed at low frequencies in the EIS response of the $Mg_{0.80}X_{0.20}$ (X = Ti, V, Cr) thin films, which describes the solid-state diffusion of hydrogen in the bulk, is qualitatively treated. The absolute value of the impedance related to this response is only marginal in the case of $Mg_{0.80}Ti_{0.20}$ and $Mg_{0.80}Sc_{0.20}$, whereas it is substantially more dominant for $Mg_{0.80}V_{0.20}$ and $Mg_{0.80}Cr_{0.20}$. This indicates that the solid-state diffusion in the V- and Cr-containing compounds is considerably more difficult as compared to the Ti- and Sc-containing materials, again resulting in the fact that dehydrogenation under current-flowing conditions will occur more rapidly for the $Mg_{0.80}Ti_{0.20}$ and $Mg_{0.80}Sc_{0.20}$ compounds.

6

Energy storage in carbon nanotubes

Abstract

The hydrogen storage potentials of many different CNT materials are investigated electrochemically, indicating that the response during charging and discharging is rather featureless and does not show any phase transitions or clear redox responses. The maximum discharge capacity of all the materials measured is ~ 150 mAh/g for an a.p. SWNT material. Measurements indicate that the electrochemical activity of the matrix material, used to manufacture composite electrodes, should not be ignored. Especially materials that are electrochemically active, in the potential range generally used when studying the energy storage properties of CNT materials, can lead to dominating redox responses (*e.g.* Ni) that can be falsely attributed to the hydrogen storage properties of the CNT material. Highly pure CNTs yield a substantially lower response, as compared to their as-produced counterpart, indicating that the CNTs itself can only account for a small part of the total response. Generally, the measured response of CNT materials is related to a number of processes, including the irreversible oxidation of carbonaceous material, the reversible oxidation/reduction of residual metal catalyst or carbonaceous impurities and a significant electrostatic charging component. Steady-state impedance measurements, cross-correlated with cyclic voltammetry, unambiguously prove that the electrostatic storage of energy can be directly linked to the charging/discharging of the electrical double layer. Characterization of highly pure CNT materials shows that close to 90 - 95 % of the total charge was stored in this way. Only 20 - 30 % of the total amount of charge could be explained in this way for the as-produced materials. The remainder being caused by the other processes mentioned above. Based on these results it can be concluded that no hydrogen can be stored in CNT material and that the exact amount of charge that can be reversibly stored in CNT material heavily depends on its morphology and the level of purity.[*]

[*] Part of this chapter is based on: R.A.H. Niessen, and P.H.L. Notten, *The electrochemistry of carbon nanotubes, part I: aqueous electrolyte*, in preparation (2005).

6.1. Introduction

The large empty spaces inside SWNTs and MWNTs, coupled with their large geometric surface areas, provides sufficient potency on a chemical level to study the energy storage characteristics of CNT materials. It was hypothesized that the hollow cores of nanotubes would be excellent sites for the storage of small molecules, like hydrogen. Furthermore, if the main aim is to develop a novel storage material with high capacity, low-mass and high-stability CNTs seem to be an excellent class of materials to achieve this as they are chemically stable and have a low mass density.

A vast amount of research has been performed on the energy and hydrogen storage characteristics of CNT materials. Focusing on the storage of hydrogen in CNTs, this research can generally be divided into two parts, based on the hydrogen storage method used. The first method stores hydrogen via the gas phase: Here, the CNT material is exposed to a H_2 atmosphere, mostly at elevated pressures and temperatures, and the ad- or absorbed amount is determined using a Sieverts-type of device. H_2 molecules are thought to be adsorbed at the exterior surfaces of CNTs or absorbed into the interstitial spaces between CNTs.[140] The second possibility, and the one described in this chapter, is storing hydrogen electrochemically: Here the CNT material is employed as the working electrode in an electrochemical three-electrode set-up and hydrogen is expected to be electrochemically ad- or desorbed as explained in Section 2.4.2 for a standard MH material.

Many researchers have studied the electrochemical hydrogen storage characteristics of CNTs over the past years, and even though the results showed large variations and were not always reliable, they were still promising. Nützenadel *et al.*[141,142] found reversible hydrogen storage capacities of up to 170 mAh/g for unpurified arc discharge produced samples, containing only a few percent of SWNTs. For purified SWNT samples Rajalakshmi *et al.*[19] found that the discharge capacity had increased to 800 mAh/g, with only relatively small variations in capacity with varying discharge currents. Based on a theoretical model, Lee *et al.*[143] calculated that (10,10)-SWNTs could have storage capacities of up to 4500 mAh/g, which is much higher than values of up to 300 mAh/g found for conventional MH electrode materials, like $LaNi_5$. It should be emphasized though that this value was just a theoretical value. More recently, work done by Gao *et al.*[144], Züttel *et al.*[145] and Zhang *et al.*[146] was published which showed that the hydrogen storage capacities of both MWNTs and SWNTs materials are generally around 200 mAh/g. However, all these CNT materials were synthesized using transition metals and well-known hydride-forming materials as catalysts. It is conceivable that in these cases the hydrogen uptake was falsely attributed to the CNT material.

Although different groups carried out the electrochemistry-based hydrogen storage research on CNTs, a suitable mechanism, able to explain the measured response, was never given. Even unambiguously showing that it was hydrogen that was ‘stored’, or that the stored energy could be related to other processes, was never really confirmed. Furthermore, the hydrogen storage capacities deduced from the electrochemical data showed a huge spread and did not seem to be clearly dependent on the purity of the material or the type of CNT investigated.

When electrochemically characterizing CNT material in an alkaline environment and a cathodic current is applied, water is reduced at the CNT/electrolyte interface. During this process hydrogen atoms may adsorb at the surface of the CNTs, similar to the case for a conventional MH described by Reaction 9 in Section 2.4.2. As the exact charge transfer mechanism remains unclear at the moment, it is generally approximated by[147]

$$H_2O + CNT + e^- \rightleftharpoons CNT \cdots H + OH^- \quad . \tag{59}$$

It is also possible that the adsorbed hydrogen at the CNT surface instantly recombines to molecular hydrogen (according to Reaction 12 in Section 2.4.2), forming gas bubbles at the surface of the electrode. In Reaction 59, reduction occurs during the charging process and oxidation during the discharge process of the CNT electrode. As both the reduction and oxidation reaction are accompanied by charge transfer, the amount of hydrogen that possibly adsorbs and desorbs can be determined by measuring the electric charge, which is equal to the product of current and time in a galvanostatic set-up.[148]

The main aim of this chapter is to shed some light on the processes that can account for the electrochemical responses measured at CNT electrodes. To this end a great variety of CNT materials was investigated, ranging from as-produced (a.p.) samples to commercially purified materials. This will also give more insight in the contribution of impurities on the electrochemical responses. Based on selected characteristic responses, obtained by means of a variety of electrochemical methods, a clear picture will be generated that is able to link the energy storage characteristics of CNT to very basic chemical processes.

6.2. Experimental

CNT materials were obtained from various manufacturers including *Iljin Nanotech*[149] *(Korea)*, *MER Corp. (USA)*, *University of Montpellier (France)*, *IMRE (Singapore)*, *Shell Global Solutions (the Netherlands)*, *Philips Research Aachen (Germany)*, *Carbolex (USA)*, and *Dresden University of Technology (Germany)*. These materials included a.p., purified and aligned samples of SWNTs, MWNTs and CNFs, produced with a variety of techniques including Chemical Vapor Deposition (CVD), Arc Discharge (AD) and Laser Ablation (LA). Additionally, some of these samples were chemically purified in-house before electrochemically investigated.[150] Only a small selection of these materials will be presented in this chapter. As a large amount of different chemical treatments were utilized, each consisting of many individual steps, they will not be discussed in this thesis.

The CNT materials that were electrochemically analyzed are available as a powder. An amount of the CNT material close to 10 mg was accurately weighed. Approximately 75 mg of silver powder was added to this sample, which was also weighed exactly. After mixing, the powders were pressed into a pellet using a special stainless steel mould. A pressure of 3 bar was applied for 2 minutes. The pellets obtained in this manner were cylinder-shaped, having a diameter of 8 mm and a thickness of approximately 0.2 mm. Subsequently, the pellet was weighed to correct for possible loss of material in the mould. Hereafter, the pellet was placed on the tip of a silver electrode holder after which a shrink sleeve, which was placed around the electrode, was heated with warm air. This caused the sleeve to shrink around the pellet and the silver rod, attaching the two to each other firmly. The remaining part of the sleeve was cut off in order to make the pellet accessible for the electrolyte. The shrink sleeve used is comprised of a synthetic material that is electrochemically inert under the conditions applied.

A range of different analysis techniques was employed to characterize the CNT samples before they were investigated electrochemically. Transmission Electron Microcopy (TEM) was utilized to investigate the materials on an Ångstrom scale. A Philips CM12 microscope, equipped with a LaB_6 filament, was used at an acceleration voltage of 120 kV. High Resolution Scanning Electron Microcopy (HR-SEM) was used to analyze the morphology of the CNT materials (Philips XL40FEG microscope). The typical electron beam acceleration

voltage was 7 kV. Whenever this value was different, it is stated explicitly. To obtain clearer pictures it was in some cases necessary to coat the samples with a 5 nm thick layer of platinum-palladium. Additionally, Energy Dispersive X-ray Spectroscopy (EDS) was employed to detect the different elements present in the samples. The EDS system used was an EDAX-DX4 with SUTW (super ultra thin window) detecting unit. This system was attached to a Philips SEM XL40 LaB_6. To obtain reliable values in element mapping, measurements lasted for approximately 16 hours. For some of the powder samples the Brunauer-Emmet-Teller (BET) method was used to determine the surface area. These measurements were performed with the NOVA Data Analysis Package (v1.10). The adsorbate used was nitrogen and the bath temperature was 77.40 K. The initial pressure (P_0) was 772 mm Hg. XRD was employed to identify the crystallography of the samples (Panalytical MRD-PRO diffractometer). Cu-Kα radiation was used, which was detected with an X'Celerator RTMS detector.

Electrochemical measurements were performed using a three-electrode set-up of which the specifications were given in Section 3.2. Galvanostatic measurements were performed using a Maccor M2300 battery tester (Maccor, Tulsa, USA). EIS and CV were done on an Autolab PGSTAT30 (Ecochemie B.V., Utrecht, the Netherlands). EIS measurements were conducted at equilibrium voltage conditions using a stimulus of 5 mV rms and scanning the frequency from 50 kHz to 1 mHz. EQUIVCRT was used to analyze the EIS data.

6.3. Results & discussion

6.3.1. Structural characterization of the CNT materials

A general overview of the morphologies of the materials that were electrochemically investigated is given in this section. SEM and TEM photographs are shown for both SWNTs and MWNTs, providing a good indication of the structure of the materials.

6.3.1.1. General morphology of SWNT material

All SWNT material used for the electrochemical experiments consisted of black, fluffy powder. The manufacturer's information stated that the materials were produced using a variety of, mostly, transition metals as catalysts. The most commonly used mixtures for AD-synthesized SWNTs were Fe/Ni/Co, Y/Ni/Co, or Ni/Y mixtures. The thus-prepared SWNTs have an average length of about 20 μm and an average diameter of 1.4 nm. Apart from SWNTs, the a.p. material still contains a large fraction of metal catalyst (± 20 wt.%) and also a large amount of carbonaceous impurities like amorphous carbon, graphite sheets and fullerenes (C_{60} and larger). The metal particles and amorphous carbon particles are mainly present in the material as small spheres and clusters with diameters in the range of approximately 50 – 150 nm. These spheres, and clusters of spheres, cover a large part of the nanotube surface. A HR-SEM picture of such material, at a magnification of 80,000 times, is shown in Fig. 87. Bundles consisting of nanotubes and the by-products mentioned can clearly be discerned.

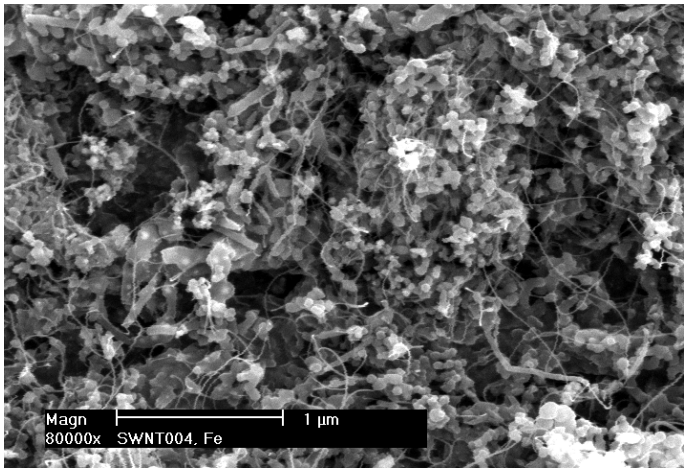

Fig. 87: SEM photograph of an a.p. SWNT material produced by means of the AD method (*Iljin Nanotech*). As well as some SWNT bundles, numerous cluster-like deposits can be seen.

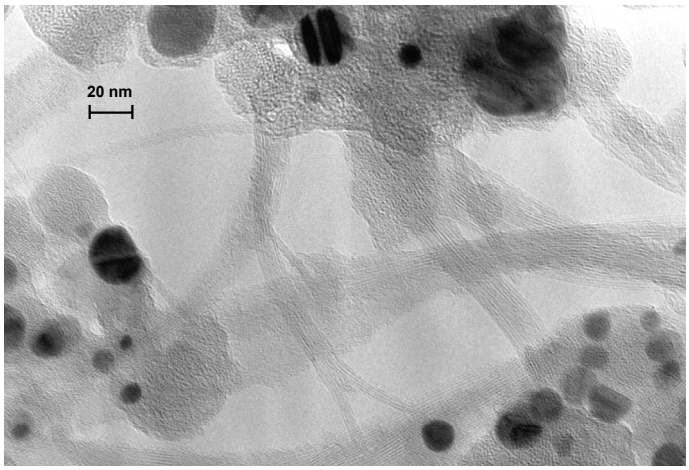

Fig. 88: TEM picture of the a.p. SWNT material, which was already shown in Fig. 87. The dark spots point to the metal impurities, which are covered with carbon shells (represented as the grayish clusters). Additionally, bundles or 'ropes' of SWNTs can be seen, comprised of many individual SWNTs.

TEM showed that a large fraction of the metal catalyst, present in the a.p. material, is covered with a layer of carbon (see Fig. 88). The dark spots in the photograph are metal clusters. These are mostly surrounded by carbon material, which is represented by the gray material in the picture. Furthermore, the bundles SWNTs are clearly visible, which consist of up to 100 individual tubes.

Commercially purified SWNTs, produced by the AD method, are shown in Fig. 89 (magnification of 40.000 times). Although it is known that an acid treatment and partial oxidation were some of the steps in the purification process, the exact process is unknown. This material only contained approximately 2 wt.% of residual metal catalyst and substantially less carbonaceous impurities.

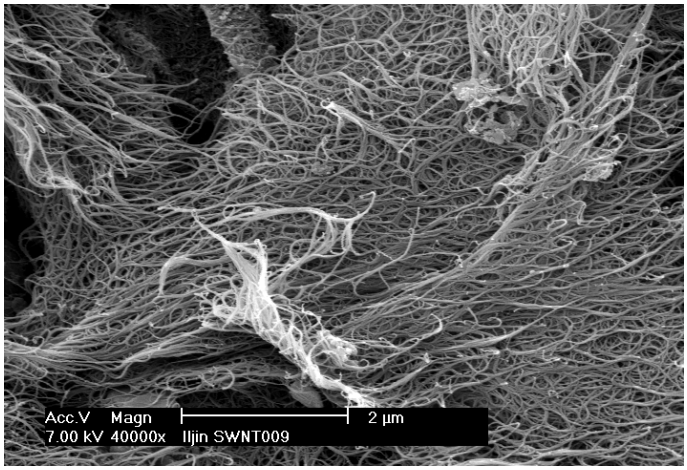

Fig. 89: SEM photograph of a commercially purified SWNT material (*Iljin Nanotech*). The a.p. version of this material was previously shown in Fig. 87.

6.3.1.2. General morphology of MWNT material

A large variety of MWNT samples, all manufactured with CVD, were electrochemically investigated. Aside from a.p. and purified MWNTs, aligned MWNTs and MWNTs doped with either Pd or Pt, were also studied. Similar to their SWNT counterparts, metal catalysts were used in their manufacturing process, consisting of a Mg/Mo/Co mixture, pure Ni, or pure Fe. The length of these MWNTs could be up to 200 µm and the average diameter up to 50 nm. Unlike the AD-produced CNT materials, the materials produced using CVD are generally a lot cleaner, only containing a small amount of residual metal catalyst (± 5 wt.%) and substantially less carbonaceous impurities. Simple acid treatments can readily remove a substantial part of the catalyst, indicating that these metal impurities are easily accessible and thus not heavily encapsulated by carbon shells. Fig. 90 shows an acid-treated MWNT sample which only contains 1.5 wt.% of metal catalyst. It should be noted that a SEM picture of an a.p. MWNT sample is quite similar to that shown in Fig. 90.

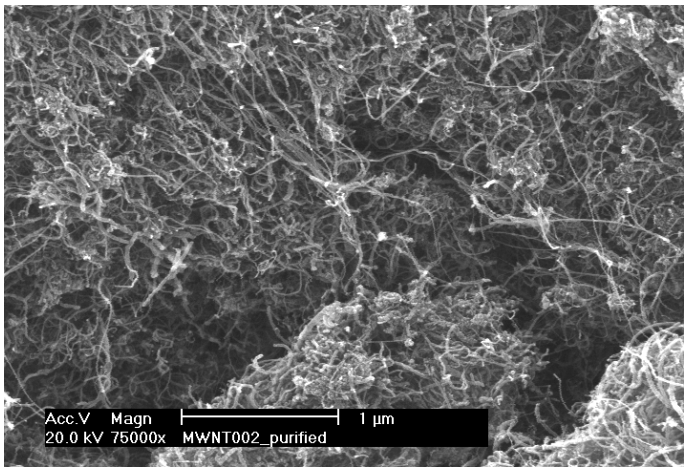

Fig. 90: SEM picture (magnification of 75.000 times) of a purified MWNT material, produced by CVD (*IMRE*). The bulk of the material consists of entangled MWNTs. The residual impurities, like catalyst particles and carbonaceous impurities, are hard to distinguish.

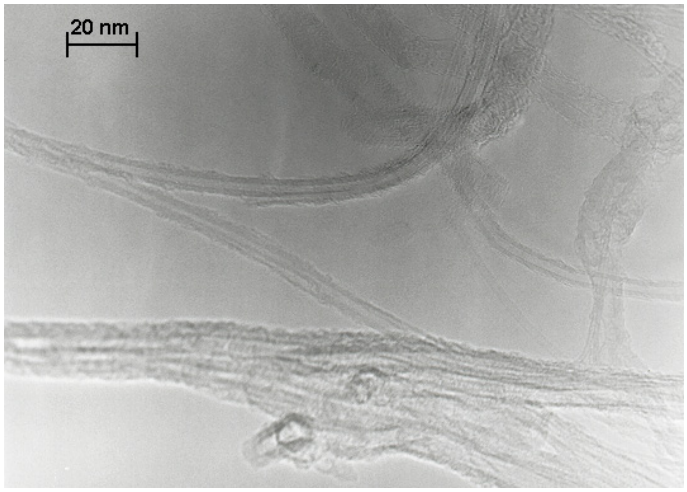

Fig. 91: TEM photograph of a purified MWNT sample (*IMRE*). The MWNTs in this sample consist of a hollow core about 4 nm in diameter and up to 10 walls. The tubes depicted are mostly quite clean (top), but sometimes heavily coated with carbonaceous impurities (bottom).

TEM investigations on purified MWNTs showed that the remaining catalyst is very hard to detect and probably only present as isolated clusters (see Fig. 91). The MWNTs in these samples are sometimes quite clean (top), but more often heavily coated with carbonaceous impurities (bottom). It is interesting to note that the degree of coating by carbonaceous impurities can only be investigated effectively by means of TEM and not SEM.

In addition to the non-aligned MWNT materials, aligned MWNTs were also investigated. Essentially, the reasoning given above regarding the purity of the material also holds for this class of MWNTs. Fig. 92 shows some examples of aligned MWNTs produced with CVD under different experimental conditions.

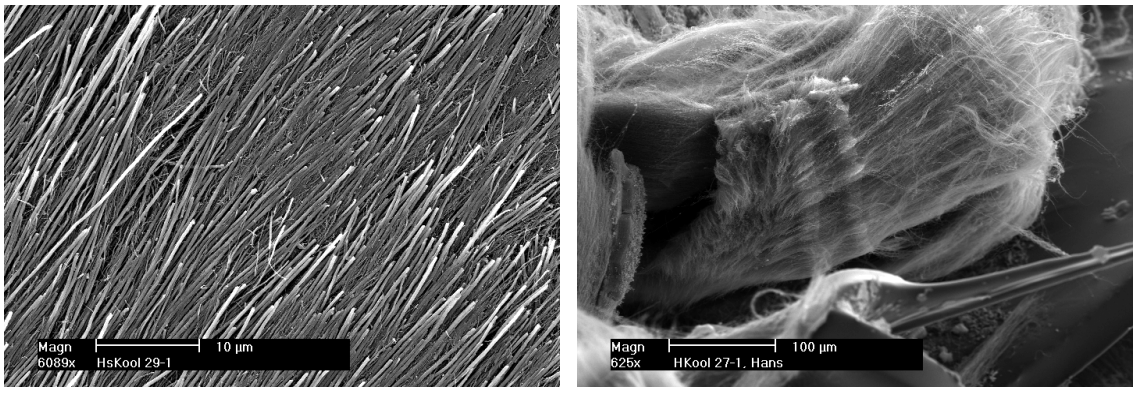

Fig. 92: Some examples of aligned MWNT materials prepared with CVD at different experimental conditions.

6.3.2. Galvanostatic behavior of the CNT materials

An electrode containing 75 mg of silver powder and 10 mg of a.p. AD-produced SWNTs (*Iljin Nanotech*) was charged with a current density of - 200 mA/g. Hereafter, the current was switched off for 1 hour in order to let the potential relax to its equilibrium value.

Subsequently, the electrode was discharged using a current density of + 200 mA/g until the potential reached the cut-off potential. At this point the current was switched off again. Fig. 93 shows the value of the electrode potential *vs.* the transferred amount of charge for this experiment. Here, the potential responses during charging and discharging are depicted by curves (a) and (b), respectively.

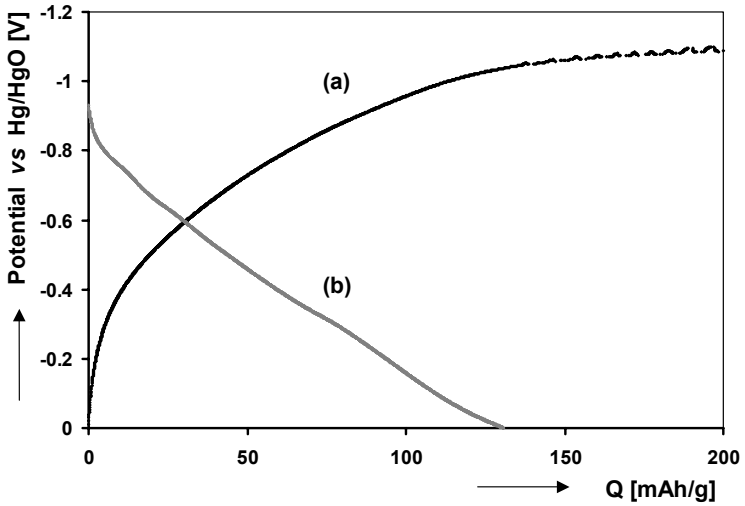

Fig. 93: Electrochemical response of an a.p. SWNT material, manufactured by means of AD (*Iljin Nanotech*). The charging (a) and discharge (b) behavior, using a current density of 200 mA/g, are shown.

It is evident that when the electrode is charged, the potential slowly, and continuously, decreases to more negative values. Eventually, at a charge capacity of about 150 mAh/g, the potential stabilizes at a value close to - 1.1 V. At this point hydrogen gas bubbles were visually observed, indicating the onset Reaction 12 (see Section 2.4.2). From the overall charging response it can be deduced that about 150 mAh/g of charge could be stored in the material, the rest being irreversibly lost due to hydrogen gas evolution. The subsequent discharge shows a rather featureless potential response up until the cut-off potential and close to 130 mAh/g of charge could be reversible extracted.

As it is rather difficult to determine where hydrogen evolution exactly starts during charging, it is not straightforward to calculate a precise value for the charge capacity. Additionally, during hydrogen evolution it is still possible that a small part of the current is used to add more charge to the SWNT material itself. Because of these complicating factors, only the discharge capacities can yield valid information about the amount of energy stored in a particular CNT material.

At this point it should be noted that a featureless potential response, as depicted in Fig. 93 for a SWNT electrode, was observed during galvanostatic charging and discharging for all measured CNT materials (SWNTs, MWNTs, CNFs). The only distinction that could be made between these materials was that the amount of charge inserted/extracted from the material could differ slightly, depending on the actual morphology of the sample measured. Overall, the highest discharge capacities were measured for a.p. SWNTs, amounting to ~ 150 mAh/g. Strikingly, discharge capacities of commercially purified SWNTs were, generally, less than 10 mAh/g.

No plateau-like responses were ever observed during the charging or discharging of the CNT material. However, a plateau-like behavior was reported in work carried out by Rajalakshmi *et al.*[19], Gao *et al.*[144] and Qin *et al.*[151]. Careful study of this work reveals that

redox responses originating from the matrix material were falsely attributed to hydrogen storage in the CNT material. In the work reported by Rajalakshmi *et al.* the oxidation and reduction of the copper compacting powder was measured. The studies performed by Gao *et al.* and Qin *et al.* are aimed at hydrogen storage in MWNTs, using either nickel as compacting powder in the electrode preparation, or Ni-coated MWNTs. In both these contributions the measured redox response was attributed to hydrogen storage in the MWNTs, leading to storage capacities of 450 and 500 mAh/g, respectively. However, the reported blank measurements on pure Ni essentially showed oxidation and reduction responses at exactly the same potentials as the Ni-coated MWNTs, only less intense. Based on this observation, it is more than likely that the measured redox responses are linked to the oxidation/reduction of Ni and not to the storage of hydrogen.

In order to prove that pure Ni can account for these effects, galvanostatic measurements were performed on a pure Ni electrode consisting of 200 mg of Ni (Aldrich, ∅ 0.8 μm), a composite electrode consisting of 10 mg of AD-produced a.p. SWNT material (*MER Corp.*) mixed with 200 mg of Ni, and a composite electrode containing 10 mg of the same a.p. SWNT material mixed with 200 mg of Ag. Fig. 94 shows the potential responses of these electrodes during galvanostatic discharging using a current of + 0.2 mA. The response of the pure Ni electrode (curve (a)) reveals a sloping plateau around – 0.7 V, which is nearly identical to the response found by Qin *et al.* for a MWNT/Ni composite electrode. As expected, the SWNT/Ni composite electrode reveals a very similar curve (curve (b)). This indicates that this response is dominated by the electrochemical oxidation of the Ni matrix and only to a minor extent by that of the SWNT material. Pourbaix has shown that Ni is electrochemically active in 6 M KOH solutions at potentials between – 0.8 V and 0 V.[152] Based on the data provided, the plateaus observed in curves (a) and (b) can most likely be attributed to the oxidation of Ni to $Ni(OH)_2$.

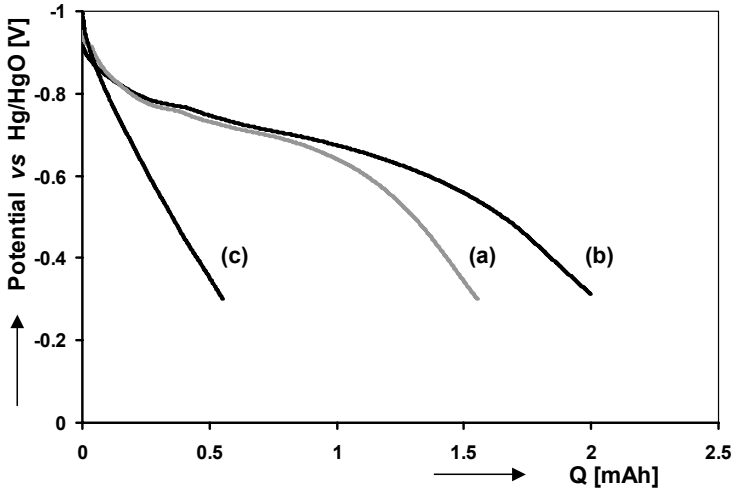

Fig. 94: Galvanostatic discharge curves of a pure Ni electrode (a), a SWNT/Ni composite electrode (b) and a SWNT/Ag composite electrode (c). The applied discharge current was + 0.2 mA and the cut-off potential was set to – 0.3 V. The a.p. SWNT material was obtained from *MER Corp.* and produced with AD.

The small difference between curves (a) and (b) results from the response of the a.p. SWNT material. By using an inert matrix material in the composite electrode (*i.e.* Ag), the electrochemical response of the SWNT material can easily be measured (see Fig. 94, curve (c)). This again results in a featureless discharge curve, characteristic for these types of

materials (see also Fig. 93). Furthermore, adding the amount of charge extracted from the pure Ni electrode (curve (a)) and the SWNT/Ag composite electrode (curve (c)), yields approximately the value given by curve (b).

The featureless galvanostatic response of the CNT materials makes it very hard to interpret which process or mechanism lies at its origin. In order to obtain a clearer picture of the energy storage mechanism, specific electrochemical measurements can be utilized. Basically, energy can be electrochemically stored via two main processes: (i) Via a redox reaction, coupled with charge transfer. In this process the electrode material is either oxidized or reduced at the solid/electrolyte interface, resulting in the consumption or release of electrons. Essentially, electrical energy is converted into chemical energy, and *vise versa*. (ii) Via electrostatic charging/discharging of a capacitive element. In this process, usually associated with materials that have a very large surface area, charge is stored electrostatically across the solid/electrolyte interface. Here, no charge transfer takes place. This process is actually identical to the storage of charge across the plates of an electronic capacitor.

Using the appropriate electrochemical techniques it is possible to estimate to what extent charge is stored via a redox reaction, electrostatically, or a combination of both. In order to establish whether or not a charge transfer mechanism plays a role in the electrochemical energy storage of SWNTs, it is investigated whether a Tafel-like behavior (indicative of charge transfer) can be measured.[153] Fig. 95 depicts the potential responses of an a.p. SWNT material (AD-produced, *Carbolex*) when charging at different current densities. A characteristic featureless shape is observed during charging, as was already shown in Fig. 93 for a different SWNT sample. If the logarithm of the applied current is plotted *vs.* the measured potential at specific DoC values, a Tafel plot can be constructed. This plot is shown in Fig. 96 for DoC values of 10 to 40 mAh/g.

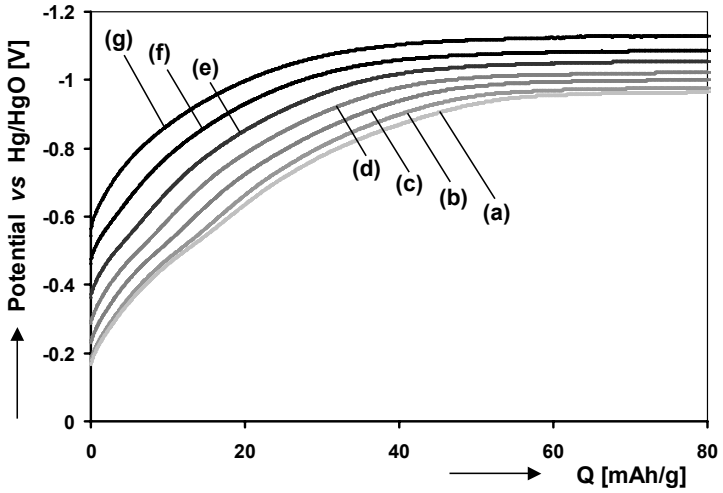

Fig. 95: Galvanostatic charging curves of an a.p. SWNT material produced means of AD (*Carbolex*). The current densities used were; 2 mA/g (a), 4 mA/g (b), 10 mA/g (c), 20 mA/g (d), 50 mA/g (e), 100 mA/g (f) and 200 mA/g (g).

As can be seen in Fig. 96, the SWNT material clearly exhibits Tafel behavior for the higher current densities used. This indicates that, in this case, a charge transfer reaction is definitely occurring and also significantly contributing to the overall energy storage of this material. It is interesting to note that α slowly changes from about 0.25 at low DoC (*i.e.* 10 mAh/g), to approximately 0.5 at high DoC (*i.e.* 40 mAh/g). This points to that fact that the kinetics of the charge transfer reaction is changing from asymmetric to fully

symmetric (see Section 2.4.3). However, the exact reason explaining such a behavior cannot be given at this moment. This will require additional research.

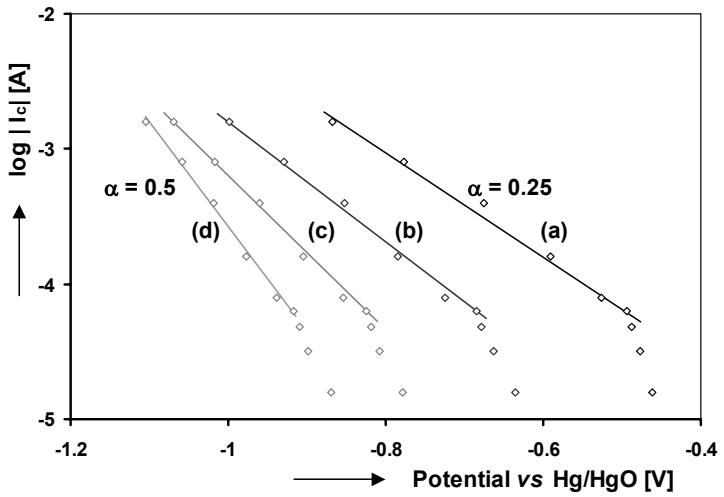

Fig. 96: Tafel behavior, at different DoC values, of the a.p. SWNT material shown in Fig. 95. Tafel plots are shown for 10 mAh/g (a), 20 mAh/g (b), 30 mAh/g (c) and 40 mAh/g (d). Additionally, the calculated values for α are shown for the extreme cases.

6.3.3. Thermodynamics

The isotherms of the CNT materials were determined electrochemically by means of GITT measurements. The electrode was charged by applying 50 current pulses of 1.5 minutes, using a current density of - 200 mA/g. 50 pulses seemed to be sufficient to completely charge the electrode and reach the stage at which hydrogen gas bubbles were produced. After each current pulse the current was switched off for 1 hour, so the potential could relax to its equilibrium state. After GITT charging, the electrode was discharged using GITT employing the same parameters, with the only difference that a current density of + 200 mA/g was used.

Fig. 97 shows the obtained equilibrium data for both charging (curve (a)) and discharging (curve (b)). Additionally, the galvanostatic charge and discharge curves of this sample are shown, also using a current density of 200 mA/g (curves (c) and (d), respectively). It can be seen that these are nearly identical to those shown in Fig. 93. It should be noted that during the galvanostatic discharge shown, no cut-off potential was set. Comparing both the equilibrium and the galvanostatic data, it is clear that the shapes of the curves are exactly the same. During charging the equilibrium potential gradually decreases until a constant potential is reached after the storage capacity reaches a value close to 150 mAh/g. The potential observed from this point onwards is – 0.96 V and all charge supplied to the electrode is used to produce hydrogen gas. Strangely enough, the equilibrium potential is substantially more negative than – 0.931 V and, according to Eq. 22, equal to a partial hydrogen pressure of 9.5 bar. As the maximum partial hydrogen pressure of a hydride system in equilibrium measured in an open system (such as the three-electrode set-up used) can never exceed 1 bar, this behavior is difficult to understand.

During GITT discharging (see curve (b)) a featureless curve can be seen up to a potential of – 0.2 V, equal to that of the galvanostatic discharge up to 0 V (see curve (d)). However, upon continued discharging a sloping plateau is revealed in both the GITT curve (between

– 0.2 V and 0 V) and the galvanostatic curve (between + 0.1 V and + 0.4 V). A very similar response was also seen by Jurewicz *et al.* for activated carbon and attributed to a possible over-oxidative modification of the carbon.[154] This shows that this process, of which the equilibrium potential extends from – 0.2 V to at least 0 V, is not related to hydrogen extraction. This hypothesis was also confirmed by experimental data, which showed that this process could also be measured when investigating a CNT sample that was not yet electrochemically charged (not shown here). Additionally, these measurements showed that this process was of irreversible nature.

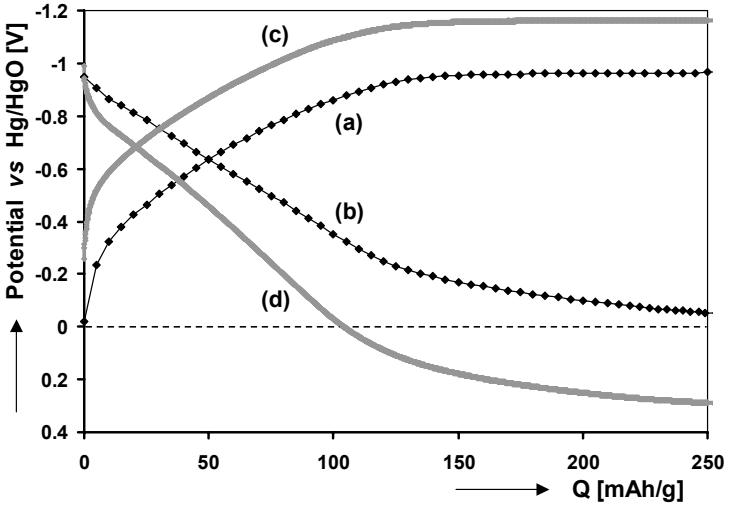

Fig. 97: Equilibrium charge (a) and discharge (b) curves of an AD-produced SWNT material. Additionally, the galvanostatic charge (c) and discharge (d) responses are shown for the same sample. In all cases a current density of - 200 mA/g was used for charging and + 200 mA/g for discharging.

Disregarding hydrogen gas formation and the process related to oxidation of the CNT material itself, leaves only the responses up to about 120 mAh/g unexplained (both during charging and discharging). Although both galvanostatic measurements and GITT experiments both show similar responses in this region, neither technique can provide a clear indication what type of process is taking place. In this next section, CV is used in an attempt to obtain a clearer picture hereof.

6.3.4. Cyclic voltammetry

6.3.4.1. Cyclic voltammetry on a.p. SWNT materials

To gain more detailed information on the, yet unknown, electrochemical responses measured using galvanostatic methods, CV is used. An a.p. SWNT electrode was charged and discharged by means CV, using a scan rate of 5 mV/s and cycling between 0 V and – 1.2 V. The resulting *I-E* plot is depicted in Fig. 98, showing the 5th cycle. It should be noted that for the bulk of the CNT materials investigated, a stable cyclic voltammogram was usually obtained after the 2nd cycle. Furthermore, measurements on just the silver powder, indicated that the response hereof was negligible compared to the response of an electrode containing CNT material (not shown here).

The voltammogram shows that, when changing the potential of the electrode in negative direction (charging), a gradually increasing negative current is measured. Although the highest reduction current is measured around - 1.2 V, hydrogen evolution was experimentally observed, indicating that a substantial part of the measured current can be attributed to this process. Like in the galvanostatic experiments presented in Section 6.3.2, almost no discontinuities or features can be observed during the charging process. When the scan is reversed at - 1.2 V, a gradually increasing oxidation current is observed, which reaches a plateau current in the potential region between – 0.6 V and 0 V. Very close to 0 V the current seems to increase once more, probably due to the electrochemical process related to the oxidation of the carbon material (see Sections 6.3.2 and 6.3.3).

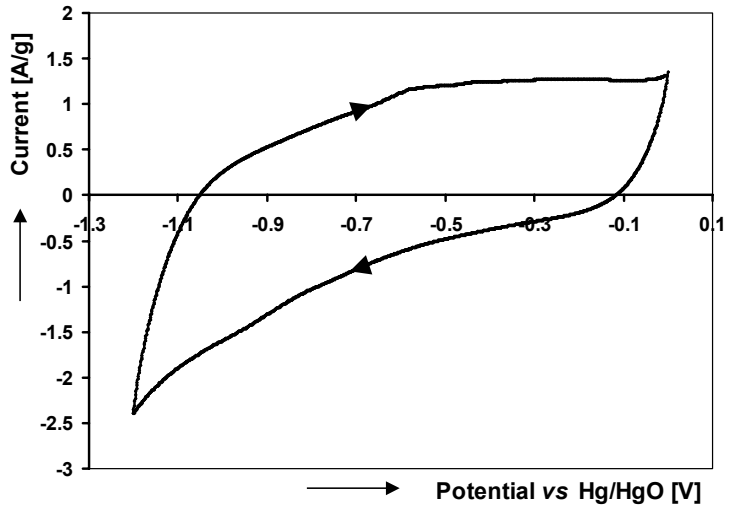

Fig. 98: Cyclic voltammogram of an a.p. SWNT material produced by means of AD (ν = 5 mV/s).

6.3.4.2. Cyclic voltammetry on different SWNT fractions

In order to obtain a clear picture what part of the CNT material gives rise to which current response, CV was performed on different samples consisting of; key components also present in the a.p. material (*i.e.* metal catalyst), CNT material obtained after partial purification of a.p. material (*i.e.* temperature-treated) or commercially purified CNTs. Overall, the samples presented in this section give a very good indication of which fraction is actually (electro)chemically active and which one does not contribute to the measured electrochemical response.

For the sake of clarity only one type of CNT material is presented. As the AD-produced SWNT material obtained from *Iljin Nanotech* showed the most promising electrochemical response, this material was chosen. Although many different fractions were investigated, selected CV responses are shown here. It should be noted that the electrochemical behavior of many of the materials, obtained from a variety of manufacturers (see Section 6.2), showed a very similar trend in the electrochemical response and are therefore omitted.

The four key materials of which the CV responses are compared include:

(a) *Unpurified a.p. SWNTs*
AD-produced SWNTs containing about 50 - 60 vol.% of CNTs. The main impurities present in this material are residual metal catalyst (22 wt.%) and carbonaceous impurities. XRD showed some graphite and TEM analysis indicated large quantities of amorphous carbon and carbon shells. Additionally, the material contains close to 4 wt.% of smaller fullerenes (C_{60}, C_{70}).

(b) *Heat treated SWNTs*
Material obtained by heating the a.p. SWNT material at 350 °C for 1.5 h. This was done in an O_2/Ar atmosphere (50/50 vol.%). The result of this heat treatment is the combustion of a significant part of the amorphous carbon impurities. Especially the carbon shells, encapsulating a large portion of the metal catalyst in the a.p. material, are removed during this purification step. The result being that almost all metal impurities are electrochemically accessible. Close to 30 wt.% of the material consists of metal impurities.

(c) *Pure metal fraction*
Mixture of metals identical to that present in the a.p. SWNT material. The sample consisted of a mixture of Fe, Ni and Co powders (2:3:3 on weight basis). However, the particle size of the powders used (300 nm) was larger than the cluster size of the metal impurities in the SWNT material (50 - 100 nm, see Fig. 88). This mixture was heated at 350 °C for 1.5 h in an O_2/Ar atmosphere (50/50 vol.%). This was done in order to mimic the heat treatment of the purification procedure.

(d) *Commercially purified SWNTs*
Material obtained after extensive purification of a.p. SWNT material. The precise purification procedure is not known, but involves several acid treatment and partial oxidation steps. At this point the material contains only 2 wt.% of residual catalyst. The main carbonaceous impurity is graphite (XRD analysis). The final product is reported to contain close to 80 - 90 vol.% of SWNTs.

For all these samples at least five consecutive CV scans were made using a scan rate of 5 mV/s and scanning between 0 V and – 1.2 V. For each sample, a stable cyclic voltammogram was obtained after the 2nd scan. These scans are depicted in Fig. 99, in which the current values are normalized to 10 mg of active electrode material enabling direct comparison.

Curve (a) in Fig. 99 shows the cyclic voltammetric response of the a.p. SWNT material which was already shown in Fig. 98. This response can be largely explained by focusing on the response induced by the metal catalyst fraction. To this end the a.p. material has been heat treated, resulting in the fact that almost all metal is directly electrochemically accessible. The corresponding voltammogram is depicted as curve (b) in Fig. 99, revealing not a predominantly featureless response as for the a.p. material (curve (a)), but showing distinct redox responses. These are measured during reduction between – 1.0 and – 1.2 V and during oxidation between – 0.7 V and – 0.4 V. As most metal impurities are electrochemically accessible in this material, it is likely that the measured redox responses originate from the reduction/oxidation of Fe, Ni and Co species.

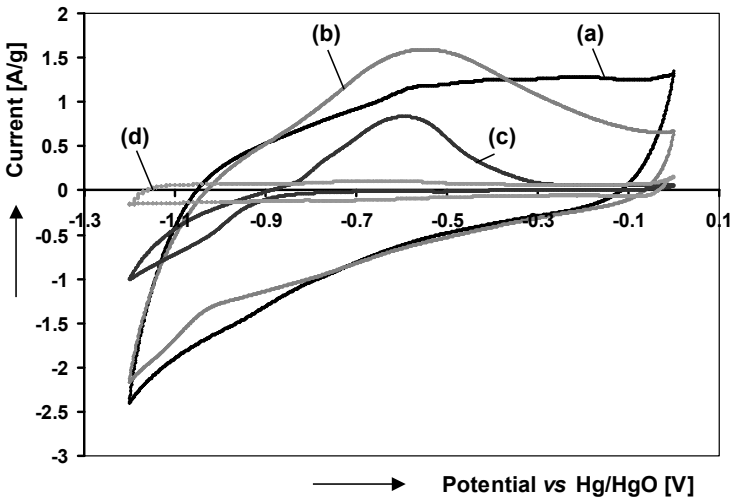

Fig. 99: Cyclic voltammograms of different fractions of SWNT material, showing a.p. SWNTs (a), heat treated SWNTs (b), metal catalyst fraction (c) and commercially purified SWNTs (d). A scan rate of 5 mV/s was used and all voltammograms were normalized to enable direct comparison.

This hypothesis is verified by curve (c), showing the response of the metal fraction only. Although the exact oxidation state and cluster size of the metal impurities in the a.p. material can never be duplicated, the mixture shows a distinct reduction and oxidation response at exactly the same potentials as the heat treated material. This unambiguously proves that the metal fraction accounts for a substantial part of the measured electrochemical response shown in curves (a) and (b).

Removing practically all the metal catalyst and the bulk part of the carbonaceous impurities, effectively only leaving the SWNTs, results in a very poor electrochemical response (curve (d)). This curve shows a featureless cyclic voltammogram, very similar to the 'block' response of an ideal capacitor.[155] Compared to the a.p. SWNT material (curve (a)), the measured current is over one order of magnitude lower, indicating very poor energy storage characteristics for purified SWNTs.

In conclusion it can be said that the electrochemical response of a.p. SWNT material can mainly be attributed to residual metal catalyst and some redox behavior of carbonaceous impurities. This would be in line with the evidence found in Section 6.3.2, indicating that charge is, to some extent, stored in the material via a charge transfer reaction. The response of commercially purified SWNTs, however, appears to be completely capacitor-like, indicating electrostatic storage of energy only.

6.3.5. Electrochemical impedance spectroscopy

6.3.5.1. Introduction

EIS measurements were conducted on a wide variety of CNT samples with the intention to identify the processes giving rise to the electrochemical response measured during galvanostatic or CV experiments. As opposed to the EIS measurements presented so far (Chapters 4 and 5), the impedance measurements are not preformed in combination with GITT (see Section 3.4.4.1), but separately at predetermined potentials. Hereafter, they are compared to CV measurements, which were conducted on the same samples.

The impedance measurements shown in this section were performed on a few selected materials including; a.p. SWNTs and commercially purified SWNTs from *Iljin Nanotech* and HNO_3 purified MWNTs from *IMRE*. All EIS measurements were done under steady-state conditions at potentials between 0 V and – 1.2 V, at 50 mV intervals. The experiment was started at an electrode potential of 0 V. In order to obtain steady-state, the electrode potential was fixed for 1 h at this potential. Hereafter, the EIS measurement was performed. Subsequently, the electrode potential was changed step-wise to a more negative value and again fixed for 1 h, before the next EIS experiment was conducted. This procedure was repeated until a potential of – 1.2 V was reached. At this point the electrode was discharged with the same small potential steps and again the impedance was measured at each of these potentials.

The main advantage of using EIS is the fact that the impedance response can be analyzed using an EQC, yielding data on both resistive and capacitive influences (as explained in Section 3.4.4). In this way, it is possible to gain more information about the electrostatic storage of charge across the electrode/electrolyte interface (*i.e.* the double layer capacitance). When the double layer capacitance is determined via impedance measurements for a whole range of potentials, the corresponding double layer charging or discharging current can be calculated for a cyclic voltammogram in that same potential range. The double layer current (I_{dl}) at a certain potential is equal to the product of the double layer capacitance (C_{dl}) at that potential and the scan rate (ν) at which the CV is performed.

$$I_{dl}(E) = C_{dl}(E) \cdot \nu \tag{60}$$

When the double layer current is calculated for the whole potential range, it can be compared to the cyclic voltammogram. In this manner the double layer charging and discharging current can be distinguished from the Faradaic current, which is, of course, directly coupled to the amount of charge stored via a charge transfer reaction. It should be noted that for this approach the results of the steady-state impedance experiment are combined with the results of the dynamic CV experiment. However, if the assumption remains valid that C_{dl} is the same in dynamic and static conditions (at the same potential) this method can prove highly useful.

6.3.5.2. Results of impedance measurements

A.p. SWNTs

For an electrode consisting of a.p. SWNTs (*Iljin Nanotech*) the impedance was measured in steps of 50 mV between 0 V and – 1.2 V, during both charging and discharging of the electrode. For the EIS measurements performed during charging, the corresponding Nyquist representations are shown in Fig. 100. In this figure selected measurements are shown for the sake of clarity. All impedance plots shown consist of a single, large semi-circular response in the intermediate and low frequency range. The diameter of this circle diminishes in size at very negative potentials (- 1.1 V to - 1.2 V). In the high frequency range some effects can be observed which can be related to porosity effects.[156] As this high-frequency part is not of particular interest when considering the electrochemical energy storage characteristics, it will not be treated in this thesis. By modeling the experimental data with the simplified EQC shown in the inset in Fig. 100, values for R_{ct} and C_{dl} could be determined at each potential. Subsequently, the double layer charging current (I_{dl}) was estimated for CV conditions at ν = 5 mV/s, using Eq. 60.

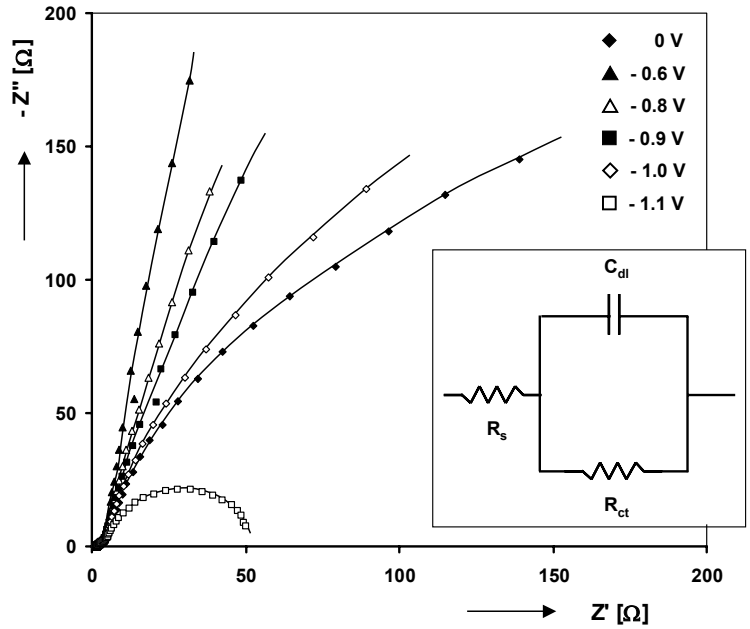

Fig. 100: Impedance spectra of an a.p. SWNT material (*Iljin Nanotech*), obtained at 0 V (◆), - 0.6 V (▲), - 0.8 V (△), - 0.9 V (■), - 1.0 V (◇) and – 1.1 V (□). The inset shows the equivalent circuit used to model the impedance data.

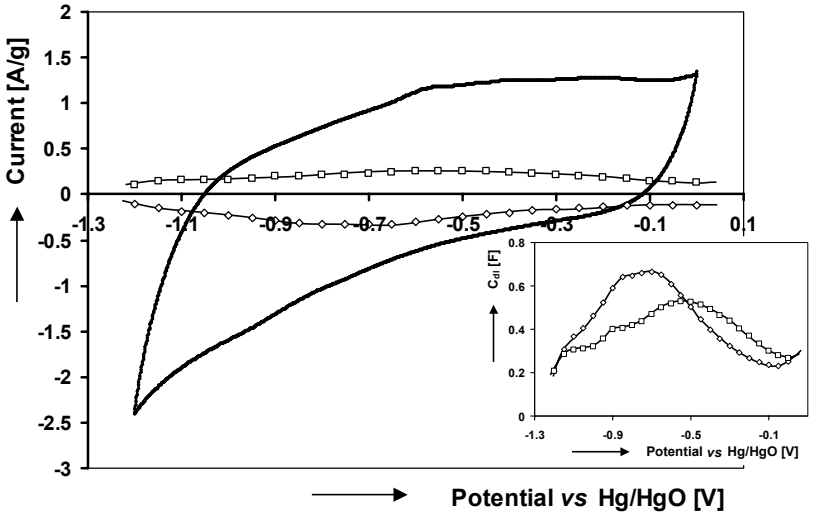

Fig. 101: Cyclic voltammogram of an a.p. SWNT material (*Iljin Nanotech*) obtained at a scan rate of 5 mV/s (bold continuous line). The calculated double layer charging current, during charging (◇) and discharging (□) of the SWNT material is also plotted. The inset shows the absolute value of C_{dl}, obtained by means of EIS, both for charging (◇) and discharging (□).

Fig. 101 shows the CV plot of material obtained at a scan rate of 5 mV/s (bold continuous line). This response was already described in Section 6.3.4.1. Additionally, the calculated I_{dl} during charging and discharging are depicted in this figure (open symbols). It is evident that, when comparing these currents, charging and discharging of the double layer cannot be neglected. Near a potential of – 0.8 V, the double layer current accounts for over one third of the total current response in the CV plot. Apparently, a quite significant part of the energy is stored electrostatically, whereas the remainder is the result of Faradaic processes

(electrochemical charge transfer). This shows that this electrostatic process contributes significantly to the overall energy storage properties of these a.p. SWNTs. This is not unlikely as the a.p. SWNT material was analyzed to have a BET surface area of around 100 m^2/g. This large surface area, if assumed to be completely accessible by the electrolyte, can certainly account for the high I_{dl}. Straightforward calculation readily confirms this hypothesis: Using 35 μF/cm^2 as an average value for the specific double layer capacitance ($C_{dl,spec}$) of SWNT material in an aqueous electrolyte[157], the previously mentioned BET surface area and an active mass of 10 mg per electrode, yields C_{dl} = 0.35 F/electrode. This value is close to the C_{dl} values obtained via EIS, which are shown in the inset in Fig. 101. It should be noted that the $C_{dl,spec}$ value used is based on a substantial number of different CNT materials investigated by Emmenegger *et al.*, showing that $C_{dl,spec}$ ranges from 10 to 60 μF/cm^2 depending on the morphology of the material. Additionally, it was experimentally determined that the contribution of the silver matrix material (see Section 6.2) to the measured C_{dl} is negligible (not shown here).

Commercially purified SWNTs

Above it was shown that the electrochemical response of an a.p. SWNT material could be attributed, for a substantial part, to the electrostatic charging of the double layer. As this material is comprised of not only SWNTs (50 vol.%), but also metal catalyst and carbonaceous impurities, it is hard to estimate which fraction accounts for the electrostatic part and which for the Faradaic part. To this end, commercially purified SWNTs (*Iljin Nanotech*), consisting of close to 90 vol.% of CNTs, were investigated by impedance experiments.

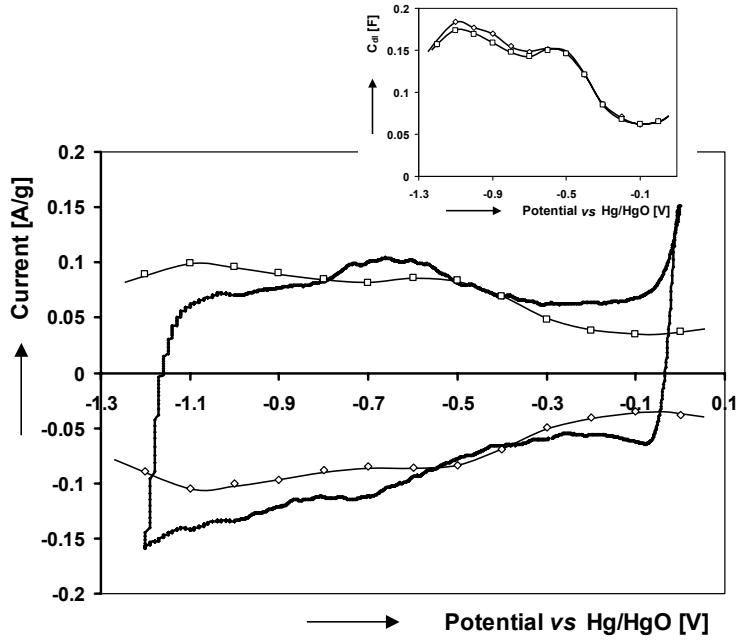

Fig. 102: Cyclic voltammogram of a commercially purified SWNT material (*Iljin Nanotech*) obtained at a scan rate of 5 mV/s (bold continuous line). The calculated double layer charging current, during charging (◇) and discharging (□) is also plotted. The inset shows the absolute value of C_{dl}, obtained by means of impedance measurements, both for charging (◇) and discharging (□).

Like before the EIS results were used to calculate the charging and discharging current of the electrical double layer. These results are shown in Fig. 102, together with a cyclic

voltammogram (ν = 5 mV/s). Apart from some minor differences, the calculated double layer current is indeed almost identical to the CV plot at all potentials. The differences can be explained by; oxidation of the carbon near 0 V (also see Section 6.3.3), hydrogen gas evolution in the potential region between – 1.0 and – 1.2 V and redox responses linked to oxidation/reduction of metal remaining catalyst around – 0.7 V (see Section 6.3.4.2).

This observation must lead to the conclusion that even the low current measured in the cyclic voltammogram is not caused by an actual electrochemical reaction (Faradaic), but merely by the charging and discharging of the electrical double layer. This unambiguously shows that SWNTs, of which the purified material mainly consists, are only able to store energy electrostatically and not electrochemically. Like for the a.p. SWNT material the validity of the calculated electrostatic storage can be checked. Using $C_{dl,spec}$ = 10 μF/cm^2, based on work done on purified SWNTs by Frackowiak *et al.*[55], the measured BET surface area of this material (175 m^2/g) and an active mass of 10 mg per electrode, C_{dl} can be calculated. The determined value (0.17 F/electrode) is equal to those experimentally determined in the potential region of – 0.4 V to – 1.2 V (inset in Fig. 102).

Purified MWNTs

Although it was stated in Section 6.3.2 that the overall electrochemical response of all investigated CNT materials was very similar, only that of the SWNT materials has been explained in detail up until now (see Sections 6.3.2 to 6.3.4). It was shown that the response could be attributed to the electrostatic charging of the double layer and the Faradaic response linked to the oxidation/reduction of the (metal) impurities. That this reasoning also holds for MWNTs will be shown next.

CV and EIS measurements were performed on a HNO_3 purified MWNT material (*IMRE*). This material consists of solely CNTs, contains a very low amount of residual catalyst (< 1 wt.%) and only a minor amount of carbonaceous impurities (see Figs. 90 and 91). Fig. 103 shows the cyclic voltammogram of this material, using a scan rate of 5 mV/s and cycling between 0 V and – 1.15 V. The voltammogram is highly symmetrical when comparing the reduction and oxidation currents (negative and positive currents, respectively). This symmetrical shape shows that all charge stored in the material can be released with a very high Coulombic efficiency (~ 95 %). This was also confirmed using galvanostatic experiments (not depicted here). As shown before, the reduction response near – 1.1 V can be linked to hydrogen gas formation. The overall shape of the CV curve is very similar to that what would be expected for purely capacitive behavior.

Focusing on the calculated double layer current, which is depicted in Fig. 103 both for charging (◇) and discharging (□), it is evident that the electrochemical response of this MWNT material is completely dominated by electrostatic (dis)charging of the double layer. There is no experimental evidence of a significant, reversible Faradaic contribution. Like for the a.p. SWNT and commercially purified SWNT materials, the BET surface area (350 m^2/g) can be used to calculate the expected value for C_{dl}, resulting in a value matching that experimentally determined (inset in Fig. 103).

The double layer capacitance of this material, in the potential range of 0 V to – 1 V, is 30 - 50 F/g. This very large capacitance, and the fact that all energy can be released with a very high Coulombic efficiency, shows that MWNTs might be advantageously used in the field of electrochemical double layer capacitors. However, the energy storage and release related to these materials is, although significant, still substantially lower than reported for polypyrrole-coated MWNTs (up to 300 F/g)[55,56] and traditional RuO_2 pseudo-capacitors (well over 100 F/g)[158] in acidic media.

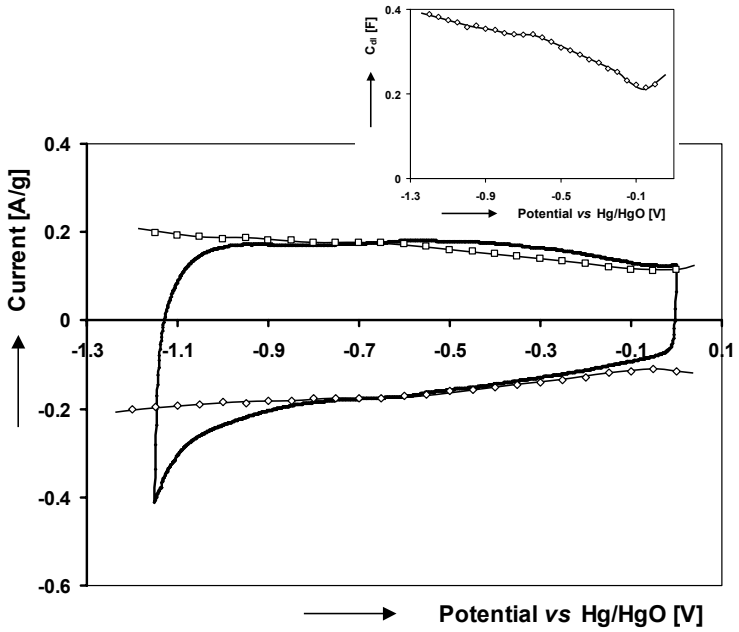

Fig. 103: CV plot of a HNO_3 purified MWNT material (*IMRE*) measured using ν = 5 mV/s (bold continuous line). The calculated double layer charging currents, during charging (◇) and discharging (□) are also shown. The inset shows the measured C_{dl}, as a function of potential (◇). Only C_{dl} during charging is shown, as the values obtained during the discharge where practically identical.

6.3.6. Temperature dependence

The electrochemical measurements performed up to this point were all conducted at room temperature. It was shown, after thorough electrochemical investigation of many different CNT materials, that the measured response is due to electrostatic charging of the double layer and redox responses originating from impurities. No evidence whatsoever was found pointing to actual storage of hydrogen by these materials. In order to investigate whether this process, or possibly other reactions, can occur at higher temperatures, measurements were performed at elevated temperatures.

The galvanostatic response of an electrode, consisting of 10 mg of a.p. SWNT material (*MER Corp.*) and 75 mg of Ag, was measured in the temperature range of 25 °C to 80 °C (see Fig. 104). The curves show that the electrochemical response, up to about – 0.3 V, is only weakly influenced by the temperature. This, again, is an indication that a substantial part of this response is electrostatic in nature, as these types of processes are generally hardly influenced by moderate temperature changes. The only change that can be observed when increasing the temperature is a shift of the plateau-like response between – 0.2 V and 0 V. This indicates that this response is heavily dependent on the temperature, characteristic of charge transfer. In Section 6.3.2 this plateau was attributed to the irreversible oxidation of carbonaceous material, indeed a process of Faradaic nature. Even at elevated temperatures no evidence can be found that unambiguously shows that these materials are able to store any hydrogen.

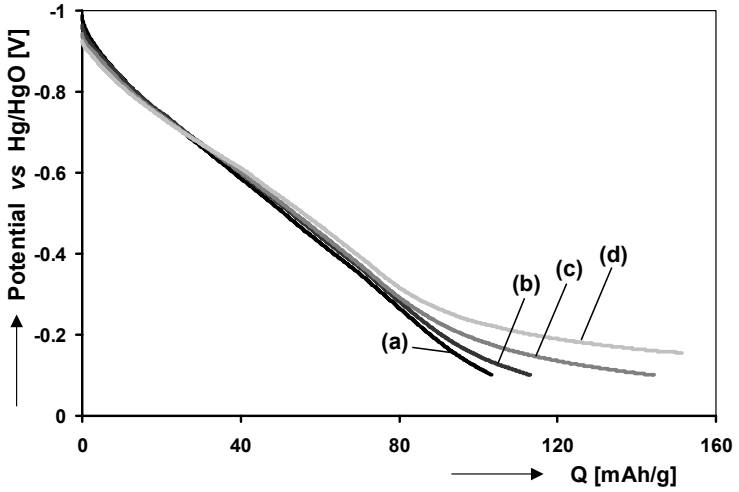

Fig. 104: Galvanostatic discharge curves of an a.p. SWNT material (*MER Corp.*), using a current of + 0.2 mA. The measurements were performed at; 25 °C (a), 40 °C (b), 60 °C (c), 80 °C (d).

6.4. Concluding remarks

The electrochemical energy storage properties of many different CNT materials were investigated. These materials included as-produced, purified and aligned samples of SWNTs, MWNTs and CNFs, produced by CVD, AD and LA techniques. Additionally, some of these samples were chemically treated in-house before electrochemically investigated. From all the measured electrochemical responses only a small selection was presented in this chapter.

Galvanostatic measurements showed that the general electrochemical response of these materials, during charging and discharging, is rather featureless and does not show any phase transition or clear redox responses. The maximum discharge capacity of all the materials measured was ~ 150 mAh/g for a.p. SWNT materials, which is generally what is reported in most of the literature dealing with this subject. Higher capacities, around 500 – 800 mAh/g, were found by several researchers and attributed to the storage of hydrogen in these materials.[19,144,151] However, these results were poorly substantiated, meaning they should be questioned. Surprisingly, the commercially purified SWNT materials that were investigated showed very low discharge capacities (generally less than 10 mAh/g).

Measurements indicated that the electrochemical activity of the matrix material, used to manufacture composite electrodes, should not be ignored. Especially Ni, which is electrochemically active in the potential range generally used when studying the energy storage properties of CNT materials, can lead to dominating redox responses. It was shown that this response was falsely attributed, by a number of other researchers in the past, to the ability of the CNT material to store hydrogen.[19,144,151] Therefore, only electrochemically inactive matrix materials were used in the current study (Ag). Interestingly, Tafel plots did indicate that part of the measured response of a SWNT electrode could be linked to a charge transfer reaction, as a clear linear dependency was measured. These dependencies showed that at low DoC the reaction was high asymmetrical ($\alpha = 0.25$), whereas at high DoC it was symmetrical ($\alpha = 0.5$).

To evaluate the equilibrium behavior of the CNT materials, GITT was performed. The resulting isotherms revealed curves identical in shape to those obtained from galvanostatic experiments. The only observation that could be made was that a sloping plateau emerged at

around – 0.2 V during the GITT discharge. Based on literature and extensive experimentation, this plateau is attributed to the irreversible oxidation of the carbon material.

In addition to the galvanostatic experiments CV was performed. As commercially purified SWNTs showed a substantially lower response, as compared to their a.p. counterpart, it is believed that the SWNTs itself are only able to account for a small part of the measured response. Analysis on a number of characteristic SWNT samples showed that the measured response of a.p. SWNTs materials is related to a number of processes. Among these are; hydrogen gas formation at the most negative potentials (around –1.1 V), irreversible oxidation of carbonaceous material around 0 V, reversible oxidation/reduction of residual metal catalyst or carbonaceous impurities between – 0.1 V and – 0.9 V, and a significant electrostatic charging component.

Impedance measurements, obtained at steady-state, were cross-correlated with CV data. This unambiguously proved that the electrostatic storage of energy could be linked directly to the charging and discharging of the electrical double layer. Characterization of highly pure CNT materials, like commercially purified SWNTs and purified MWNTs, showed that close to 90 - 95 % of the total charge was stored in this way. However, only 20 - 30 % of the total amount of charge could be explained in this way for the a.p. SWNT materials. The remainder being caused by the processes mentioned above.

To establish whether other reactions occur at elevated temperatures, measurements were performed from 25 °C up to 80 °C. Galvanostatic discharge curves of an a.p. SWNT material only showed a very weak dependence with temperature up to – 0.3 V, pointing to a mainly electrostatic behavior. Elevating the temperature does induce a serious shift in the plateau situated between – 0.3 V and 0 V. Based on various electrochemical experiments, this response is attributed to the irreversible oxidation of carbonaceous material. Again, no evidence could be found showing that storage of hydrogen occurs in these materials.

Overall, it can be concluded that no hydrogen can be stored in CNT material and that the measured responses are due to electrostatic charging of the double layer and the oxidation/reduction of (metal) impurities. The exact amount of charge that can be reversibly stored in CNT material heavily depends on its morphology and the level of purity. It was shown in Section 6.3.5.2 that the storage of energy in purified MWNTs can be completely attributed to electrostatic double layer charging. The double layer capacitance of this material, in an alkaline environment, is 30 - 50 F/g and all energy related to the double layer charging process can be released with a very high Coulombic efficiency. These characteristics show that MWNTs are promising candidates in the field of electrochemical double layer capacitors. However, the energy storage/release related to these materials is, although significant, substantially lower than reported for polypyrrole-coated MWNTs (up to 300 F/g) and traditional RuO_2 pseudo-capacitors (well over 100 F/g) in acidic media.

Summary

Energy storage has nowadays become an important issue due to the fact that mobile equipment is being scaled down, while energy consumption is generally not reduced. One of the most promising, potentially clean, energy sources of the future is hydrogen. Currently, hydrogen can be stored using one of the following technologies; under high pressures in metal containers, as a liquid at low temperatures, using physisorption on high surface area materials or in the form of a metal hydride (MH). If one of these hydrogen storage technologies is to be viable in the future it should at least meet the requirements of the DoE target for the year 2010. This means that, on a system level, at least 6 wt.% of hydrogen must be stored.

Presently, high energy densities can be achieved by using the appropriate MH. The excellent hydrogen storage properties of interstitial MHs has resulted in the fact that these materials are currently used as electrodes in commercially available NiMH batteries. However, as their storage capacity is limited to about 1.2 wt.%, their applicability in future applications should be improved. The development of new, lightweight hydrogen storage materials that are based on Mg, can provide a possible answer as the gravimetrical storage capacity of pure Mg is 7.66 wt.%.

It is known that apart from MHs, high surface area materials like activated carbons and other highly porous materials, can physisorb up to 2 wt.% of hydrogen at cryogenic temperatures. Analogous to activated carbons, CNTs are also characterized by very large surface areas. After work was published that showed that CNTs could store up to 10 wt.% of hydrogen, a worldwide research effort towards the hydrogen storage properties of various types of CNTs was triggered. However, this seemed no more than a Philosopher's Stone as these findings could not be reproduced. Since then, numerous researchers have reported on the storage capacities of CNTs yielding, on average, values around 0.3 wt.% of hydrogen.

Electrochemistry is used as the main tool to investigate the hydrogen storage properties of these two very different classes of materials in detail. However, obtaining a reliable electrochemical response is not straightforward and requires, aside from a special three-electrode set-up, intricate knowledge of parasitic processes. The theoretical considerations and the experimental implications, hereof, are explained in Chapters 2 and 3.

It is shown that oxygen dissolved in the electrolyte affects the electrochemically measured results in two ways: Firstly, due to the coexistence of two redox systems, M/MH and O_2/OH^- in this case, a mixed-potential is measured during open-circuit conditions, which is more positive than the true equilibrium potential of the hydride system. Secondly, due to continuous self-oxidation, during the electrochemical measurements, part of the hydrogen in the electrode is extracted resulting in a virtual lower storage capacity during oxidation and a higher one during reduction. Overall, measurements done on a short time scale suffer only slightly from the adverse effects of oxygen, yet long-term experiments are severely influenced. These parasitic effects of oxygen were negated by the incorporation of an oxygen scrubbing system in the measurement set-up. This device ensures that the argon gas, used to continuously purge the three-electrode set-up, is free of oxygen. This self-regenerative scrubbing device is based on the high reactivity of methylviologen single radicals towards oxygen.

All Mg-based alloys, described in this thesis, were characterized in thin film form as this geometry can be advantageously used as a 2D model system when determining specific material properties. This enables accurate evaluation of, for example, the kinetics of the hydrogen adsorption reaction of these MH electrodes. The main drawback, however, is the

small geometric surface area of the thin films. It is demonstrated that surface contamination can manifest itself quickly under certain circumstances, thereby severely influencing the kinetic properties. This is substantiated by identical experiments on MgSc thin films, performed in three-electrode set-ups in which the electrolyte was either contaminated or contamination-free. Cross-correlation of electrochemical and analytical results indicates that a clear correlation exists between the amount of Pb deposited on the surface and the value of the charge transfer resistance. This surface contamination can be avoided by making sure that all cell components in contact with the electrolyte, are of the highest purity and do not contain more than trace amounts of impurities.

Chapter 4 describes the electrochemical investigation of MgSc hydride-forming compounds. Research on these Pd-coated MgSc thin films was focused on their galvanostatic behavior, thermodynamic behavior, material characteristics obtained from impedance measurements and structural information obtained through XRD investigations.

At present only a limited amount of research has been done on the hydrogenation properties of MgSc alloys. To date, a single publication exists regarding the electrochemical hydrogenation of MgSc bulk alloys with a Sc content higher than 10 at.%. Herein, it was shown that MgSc materials with a Mg content between 50 and 80 at.% revealed excellent (de)hydrogenation characteristics. This was attributed to the formation of an fcc-structured MgSc hydride with beneficial properties. This favorable fcc structure was hypothesized to originate from the fact that the fcc structure of ScH_2 is retained, even when Sc is partially substituted by Mg.

The electrochemical hydrogen storage properties of $Mg_ySc_{(1-y)}$ alloys are investigated using electrode materials in which y was varied from 0.50 to 0.90. Experiments showed that the discharge capacity of these thin film electrodes was 5 – 20 % higher than that of MgSc bulk powders. The maximum reversible hydrogen storage capacity is obtained with the $Mg_{0.80}Sc_{0.20}$ composition and is 1795 mAh/g, corresponding to 2.05 H/M or 6.7 wt.% H, making these materials a promising candidate for usage as battery electrode material or hydrogen carrier. Both Pd-coated $Mg_ySc_{(1-y)}$ thin films and MgSc bulk materials show similar trends in hydrogen storage capacity and in the shape of the discharge curves with varying Sc content. However, the rate capability of the thin films is superior to that of the bulk materials due to shorter diffusion lengths and complete coverage of the Mg-alloy by the Pd catalyst. The thermodynamics of the $Mg_ySc_{(1-y)}$ thin films is evaluated with GITT. This showed that the plateau pressure is not a strong function of the Sc content and is almost equal to the equilibrium pressure of pure MgH_2.

The measured thin film electrodes can be described as a 2-layer structure, in which the Pd- and $Mg_ySc_{(1-y)}$ layer both contribute to the overall electrochemical response. Pure Pd thin films, identical in thickness and orientation as the Pd topcoat of the $Mg_ySc_{(1-y)}$ thin film electrodes, were examined in order to identify the response of the Pd topcoat in the 2-layer system. Elementary thermodynamics and the equilibrium data of pure Pd and Pd-coated $Mg_ySc_{(1-y)}$ thin film electrodes were used to determine the exact hydrogen concentration in each layer. This revealed that the composition of the Pd topcoat, covering the $Mg_ySc_{(1-y)}$ thin film, is close to $PdH_{0.001}$ during the major part of the hydrogen extraction process. Impedance measurements performed on $Mg_ySc_{(1-y)}$ thin films (y = 0.65 – 0.85) and pure Pd films show that the surface kinetics are completely dominated by the Pd topcoat. Further evidence demonstrates that the charge transfer reaction, and not the absorption reaction is the rate-determining step. Additionally, the overall kinetic impedance, when the $Mg_ySc_{(1-y)}$ thin film electrodes are in their hydrogen-depleted state, is dominated by the transfer of hydrogen across the Pd/$Mg_ySc_{(1-y)}$ interface. Moreover, the absolute impedance associated with this process increases with decreasing Sc content.

Electrochemical investigations indicate that the thin films show a drop in both rate capability and storage capacity at the same composition as the bulk system. Therefore, despite the lack of unambiguous structural data, it is reasonable to assume that the crystal structure of the thin films is the same as that of the bulk materials. Diffraction data obtained from MgSc bulk systems clearly demonstrate that the fully charged $Mg_ySc_{(1-y)}$ hydrides attain a single-phase fcc-structured hydride and no phase segregation takes place. Upon dehydrogenation, this fcc structure is retained and the electrochemically observed 2-phase coexistence region can be attributed to a phase transformation from a hydrogen-rich (fluorite) to a hydrogen-depleted (sphalerite) fcc structure.

It was shown that MgSc compounds exhibit very high hydrogen storage capacities, able to reach six times that of the commercially used MischMetal-based materials. However, the main commercial drawback is the very high cost of the incorporated Sc. It is therefore desirable that Sc is (partly) replaced by a less expensive material, without introducing detrimental effects. It was shown that the superior hydrogen transport properties in the MgSc hydride could be attributed to its fcc structure. Consequently, a logical substitute for Sc would be an element that also forms an fcc-structured hydride when alloyed with Mg. Additionally, the material should be similar in weight as compared to Sc. Possible candidates, based on these criteria, are Ti, V and Cr. Unfortunately, no intermetallics are formed under standard conditions when alloying Ti, V or Cr with Mg. By using extreme pressures and temperatures, several researchers have managed to prepare MgTi, MgV and MgCr hydride systems via the so-called 'anvil-cell' technique. Although the complexity of this technique is very high, it does show that crystalline MgX hydrides (X = Ti, V, Cr) can exist in bulk form. Until now, only few researchers have tried to synthesize and characterize the same compounds via a thin film approach.

In Chapter 5 the preparation and characterization of MgX thin films is described. XRD measurements show that highly crystalline $Mg_yX_{(1-y)}$ (X = Ti, V, Cr) thin films can be manufactured by means of electron-beam deposition. Single-phase compounds were obtained in all cases, clearly showing a solid solution of Ti, V or Cr in the Mg host structure. It is therefore possible to synthesize these metastable compounds without using extremes in pressure and temperature.

The hydrogen storage properties of Pd-coated $Mg_yX_{(1-y)}$ thin films (X = Ti), with y ranging from 0.50 to 0.95, are electrochemically investigated. Additionally, Pd-coated Mg thin films are used as reference material. It is shown that the reversible storage capacity of these MgTi materials increases with increasing Mg content, reaching an optimum at $y \approx 0.80$. Galvanostatic measurements indicate that the amount of Ti doping has a profound impact on the rate capability, leading to $Mg_yTi_{(1-y)}$ materials with excellent rate capability up to the $Mg_{0.80}Ti_{0.20}$ composition. However, if $y > 0.80$ the high-rate storage capacity decreases rapidly. The evolution of both the high and low-rate storage capacity with composition is very similar to that of the $Mg_ySc_{(1-y)}$ thin films. Like for the $Mg_ySc_{(1-y)}$ materials, this drop in rate capability might originate from a change in hydride structure. In conclusion, electrochemical measurements convincingly show that low-cost Ti is an excellent substitute for the expensive Sc in $Mg_ySc_{(1-y)}$ materials, without introducing detrimental effects.

As the optimum composition of both the Ti- and Sc-containing materials was situated at $y = 0.80$, V- and Cr-containing thin films are prepared with the same composition and their electrochemical hydrogen storage characteristics compared. The reversible hydrogen storage capacity of the $Mg_{0.80}X_{0.20}$ (X = Ti, V, Cr) compounds is determined to be 1750 mAh/g for $Mg_{0.80}Ti_{0.20}$, 1700 mAh/g for $Mg_{0.80}V_{0.20}$ and 1270 mAh/g for $Mg_{0.80}Cr_{0.20}$, corresponding to, 6.5, 6.4 and 4.9 wt.% H, respectively. Interestingly, the rate capability of the $Mg_{0.80}X_{0.20}$ compounds is profoundly influenced by element X in MgX. Electrochemical measurements

indicate that the rate capability of the Ti-containing material is similar to that of the Sc-containing material (*i.e.* $Mg_{0.80}Sc_{0.20}$) and far superior to that of the V- and Cr-containing compounds. This results in the fact that the same amount of hydrogen can be released almost ten times faster from the Ti- and Sc-containing compounds, as compared to the V- and Cr-containing compounds. Isotherms of the MgX systems revealed that the equilibrium potential of the main charge/discharge plateau only slightly depends on X in MgX. Comparison with the $Mg_{0.80}Sc_{0.20}$ compound reveals that they are situated at more negative equilibrium potentials.

Impedance data show that the surface kinetics of the $Mg_{0.80}X_{0.20}$ (X = Ti, V, Cr) thin films are very comparable to that of $Mg_{0.80}Sc_{0.20}$ and pure Pd thin films, indicating that they are dictated by the Pd topcoat. Aside from the surface kinetics, two additional processes dominate the impedance data; the transfer of hydrogen across the $Pd/Mg_yX_{(1-y)}$ interface (at intermediate frequencies) and solid-state diffusion of hydrogen in the bulk (at the lowest frequencies). The absolute resistance of these processes is significantly higher for the V- and Cr-doped thin films, as compared to the Ti- and Sc-containing materials. This results, as a consequence, in an inferior rate capability for the V- and Cr-containing thin films.

The hydrogen storage potentials of many different CNT materials are also electrochemically investigated. This research is described in Chapter 6. These materials included as-produced (a.p.), purified and aligned samples of SWNTs, MWNTs and CNFs, produced by many different techniques. Some of these samples were chemically treated in-house in order to obtain specific fractions. The electrochemical response of these materials is, during charging and discharging, rather featureless and does not show any phase transitions or clear redox responses. The maximum discharge capacity of all the materials measured is about 150 mAh/g for an a.p. SWNT material. Measurements indicate that the electrochemical activity of the matrix material, used to manufacture composite electrodes, should not be ignored. Especially materials that are electrochemically active in the potential range generally used when studying the energy storage properties of CNT materials, can lead to dominating redox responses (*e.g.* Ni). It is shown that this response was falsely attributed, by a number of researchers in the past, to the hydrogen storage properties of the CNT material.

Experiments reveal that commercially purified CNTs yield a substantially lower response as compared to their a.p. counterpart. This indicates that the CNTs itself can only account for a small part of the total response. Analysis of a number of characteristic CNT samples shows that the measured response of a.p. materials is related to a number of processes. These include the irreversible oxidation of carbonaceous material, the reversible oxidation/reduction of residual metal catalyst or carbonaceous impurities and a significant electrostatic charging component. Steady-state impedance measurements, cross-correlated with CV information, unambiguously prove that the electrostatic storage of energy can be directly linked to the charging/discharging of the electrical double layer. Characterization of highly pure CNT materials (*i.e.* commercially purified SWNTs and MWNTs) shows that close to 90 - 95 % of the total charge is stored in this way. However, only 20 - 30 % of the total amount of charge can be explained in this way for the a.p. materials. The remainder being caused by the other processes mentioned above.

Based on the research described in this thesis, it can be concluded that no hydrogen can be stored in CNT material and that the measured responses are due to electrostatic charging of the double layer and the reversible oxidation/reduction of (metal) impurities. This conclusion is at right angles to the work reported by other researchers in the recent past, who attributed responses related to these processes to hydrogen storage in CNT material, thereby obtaining storage capacities up to 800 mAh/g (3 wt.% of hydrogen). Additionally, the present

study indicates that the exact amount of charge that can be reversibly stored in CNT material heavily depends on its morphology and the level of purity.

As the CNT materials do show very high double layer capacitance values (of the order of 10 - 100 F/g) and all energy related to the double layer charging process can be released with a very high Coulombic efficiency, they are promising candidates in the field of electrochemical double layer capacitors. However, the energy storage/release related to this phenomenon is, although significant, substantially lower than already existing capacitor systems such as RuO_2.

In conclusion, the research described in this thesis shows that Mg-based alloys like MgSc and MgTi show excellent (de)hydrogenation kinetics and very high reversible hydrogen storage capacities (up to 6.7 wt.%), making these materials very promising candidates when considering applications like battery electrode material or hydrogen carrier. CNTs, however, are not able to store any hydrogen. Charge stored in these materials is stored mainly electrostatically across the double layer and partially due to reversible oxidation/reduction of (metal) impurities. The good electrostatic energy storing properties of these materials might be utilized in electrochemical double layer capacitor applications.

Samenvatting

Tegenwoordig is energieopslag een zeer belangrijke kwestie omdat draagbare apparatuur verkleind wordt, terwijl het energieverbruik in het algemeen niet verminderd wordt. Eén van de meest veelbelovende, schone, energiebronnen van de toekomst is waterstof. Momenteel kan waterstof opgeslagen worden d.m.v. één van de volgende technologieën; onder hoge druk in metalen cylinders, als een vloeistof bij zeer lage temperaturen, gefysisorbeerd op materialen met een zeer groot oppervlak, of in de vorm van een metaalhydride (MH). Als men één van deze waterstofopslagtechnologieën in de toekomst met succes wil toepassen moet deze tenminste voldoen aan de eisen van het DoE doel voor het jaar 2010. Dit betekent dat op systeemniveau tenminste 6 gew.% waterstof opgeslagen moet kunnen worden.

Momenteel kunnen met het geschikte MH zeer hoge energiedichtheden worden bereikt. De uitstekende waterstofopslageigenschappen van interstitiële MHs hebben geresulteerd in het feit dat deze materialen momenteel gebruikt worden als elektrodemateriaal in commercieel verkrijgbare NiMH batterijen. Aangezien hun opslagcapaciteit is beperkt tot ongeveer 1,2 gew.%, is de toepasbaarheid van deze materialen in toekomstige applikaties onzeker. De ontwikkeling van nieuwe, lichtgewicht waterstofopslagmaterialen die op magnesium (Mg) gebaseerd zijn, kunnen een mogelijk alternatief zijn daar de gravimetrische opslagcapaciteit van puur Mg maar liefst 7,66 gew.% is.

Naast MHs zijn hoge oppervlakte materialen zoals geactiveerde kool en andere zeer poreuze materialen, in staat om tot 2 gew.% waterstof op te slaan bij cryogene temperaturen. Net als geactiveerde kool hebben koolstof nanobuizen (‘carbon nanotubes’ of CNTs) ook een heel groot oppervlak. Nadat werk was gepubliceerd waarin werd getoond dat CNTs tot 10 gew.% waterstof zouden kunnen opslaan, werd wereldwijd onderzoek gestart met als doel de waterstofopslageigenschappen van verschillende soorten CNTs te achterhalen. Helaas bleek het niet mogelijk om deze bevindingen te reproduceren. Sindsdien heeft een groot aantal onderzoekers de waterstofopslagcapaciteit van CNTs onderzocht, resulterend in een veel lagere waarde van rond de 0,3 gew.%.

Elektrochemie is gebruikt als onderzoeksmethodiek om de waterstofopslageigenschappen van deze twee heel verschillende klasses van materialen gedetailleerd te onderzoeken. Echter het verkrijgen van een betrouwbare elektrochemische respons is niet ongecompliceerd en vereist, naast een speciale drie-elektrode opstelling, voldoende kennis op het gebied van parasitaire processen. De theoretische overwegingen en de experimentele implikaties op dit gebied worden respectievelijk beschreven in Hoofdstuk 2 en 3.

Aangetoond wordt hoe zuurstof, dat opgelost is in het elektrolyt, de elektrochemisch gemeten resultaten op twee manieren beïnvloed: Ten eerste de coëxistentie van twee redox systemen, M/MH en O_2/OH^- in dit geval, leidt tot een mengpotentiaal (gemeten tijdens open-circuit omstandigheden), die positiever is dan de ware evenwichtspotentiaal van het hydridesysteem. Ten tweede als gevolg van aanhoudende zelf-oxidatie wordt een deel van het waterstof dat in de elektrode is opgeslagen verwijderd. Dit resulteert in een feitelijk lagere opslagcapaciteit tijdens het reductieproces (ontladen) en een hogere tijdens het oxidatieproces (beladen). De metingen die worden uitgevoerd op een korte tijdsschaal worden door de ongunstige invloeden van zuurstof maar marginaal beïnvloed, doch langetermijnexperimenten worden sterk beïnvloed. Door gebruik te maken van een zuurstofreinigingssyteem in de meetopstelling worden de parasitaire invloeden van zuurstof tenietgedaan. Dit reinigingssyteem zorgt ervoor dat het argongas, dat onafgebroken de gehele drie-elektrode opstelling spoelt, vrij is van zuurstof. Dit zelf-regeneratief reinigingssyteem is gebaseerd op de hoge reactiviteit van het methylviologeenradicaal voor zuurstof.

Alle Mg-gebaseerde legeringen, die in dit proefschrift beschreven worden, zijn bemeten in de vorm van een dunnefilm. De geometrie van deze dunnefilms kan gezien worden als een 2D model systeem. Dit vergemakkelijkt het vaststellen van specifieke materiaaleigenschappen zoals bijvoorbeeld de kinetische eigenschappen van de waterstof adsorptiereactie van deze MH-elektrodes. Het grootste nadeel is nochtans het kleine geometrische oppervlak van deze dunnefilms. Hierdoor kan onder de juiste omstandigheden oppervlaktevervuiling onstaan waardoor de kinetische eigenschappen worden beïnvloed. Dit wordt bevestigd door identieke experimenten aan MgSc dunnefilms, uitgevoerd in drie-elektrode opstellingen waarin het elektrolyt wel of niet vervuild is. Door de elektrochemische en analytische resultaten te correleren wordt een duidelijk verband aangetoond tussen de hoeveelheid lood (Pb) gedeponeerd op het oppervlak en de waarde van de ladingsoverdrachtweerstand. Deze oppervlaktevervuiling kan vermeden worden als alle celcomponenten die in contact komen met het elektroliet van de hoogste zuiverheid zijn en ten hoogste sporen van onzuiverheden bevatten.

Hoofdstuk 4 beschrijft het elektrochemische onderzoek van MgSc hydride-vormende materialen. Onderzoek op deze met Pd bedekte MgSc dunnefilms concentreert zich vooral op het galvanostatisch gedrag, het thermodynamische gedrag, de materiaaleigenschappen verkregen d.m.v. impedantiemetingen en structurele informatie verkregen d.m.v. Röntgendiffractieonderzoek.

Op dit moment is nog maar een zeer beperkte hoeveelheid onderzoek gedaan naar de hydrogenatie-eigenschappen van MgSc legeringen. Slechts één enkele publicatie is tot op heden verschenen die de elektrochemische hydrogenatie van MgSc bulklegeringen met een Sc gehalte hoger dan 10 at.% beschrijft. Deze publicatie liet zien dat MgSc materialen met een Mg gehalte tussen 50 en 80 at.% uitstekende hydrogenatie-eigenschappen vertoonde. Dit werd toegeschreven aan de vorming van een fcc-gestructureerd MgSc hydride. De aanname die hierbij gemaakt werd, was dat dit fcc-gestructureerd hydride gevormd kon worden doordat de fcc structuur van ScH_2 behouden bleef, zelfs wanneer Sc gedeeltelijk vervangen werd door Mg.

De elektrochemische waterstofopslageigenschappen van $Mg_ySc_{(1-y)}$ legeringen zijn onderzocht voor composities waarin *y* gevarieerd werd van 0,50 tot 0,90. Experimenten toonden aan dat de ontlaadcapaciteit van deze dunnefilmelektrodes 5 - 20 % hoger was dan die van MgSc bulkpoeders. De maximale reversibele waterstofopslagcapaciteit werd gemeten voor de $Mg_{0.80}Sc_{0.20}$ compositie en komt overeen met 1795 mAh/g, 2,05 H/M oftewel 6,7 gew.% waterstof. Deze getallen laten zien dat dit materiaal een veelbelovende kandidaat is voor gebruik als batterij-elektrodemateriaal of waterstofopslagmedium. De Pd bedekte $Mg_ySc_{(1-y)}$ dunnefilms en MgSc bulkmaterialen tonen dezelfde trend in waterstofopslagcapaciteit en in de vorm van de ontlaadcurves wanneer de hoeveelheid Sc gevariëerd wordt. Nochtans, het vermogen om met een hoge stroom de dunnefilms te ontladen is vele malen groter dan dat van de bulkmaterialen tengevolge van kortere diffusielengte en de volledige bedekking van de Mg legering door de Pd katalysator. De isothermen van de $Mg_ySc_{(1-y)}$ dunnefilms tonen dat de plateaudruk maar marginaal wordt beïnvloed door het Sc gehalte en bijna gelijk is aan de evenwichtsdruk van puur MgH_2.

De gemeten dunnefilmelektrodes kunnen beschreven worden als een 2-laags structuur waarin de Pd- en $Mg_ySc_{(1-y)}$ lagen beide bijdragen aan de totale elektrochemische respons. Pure Pd dunnefilms, identiek aan de Pd toplaag van de $Mg_ySc_{(1-y)}$ dunnefilmelektrodes in dikte en oriëntatie, werden onderzocht om de respons van de Pd topcoat in het 2-laags systeem te kunnen identificeren. Elementaire thermodynamica en de evenwichtsgegevens van pure Pd en met Pd bedekte $Mg_ySc_{(1-y)}$ dunnefilms werden gebruikt om de exacte waterstofconcentratie in elke laag vast te stellen. Hieruit werd geconcludeerd dat de

compositie van de Pd toplaag, die de $Mg_ySc_{(1-y)}$ dunnefilm bedekt, dicht in de buurt komt van $PdH_{0.001}$ tijdens het grootste deel van het waterstofextractieproces. Impedantiemetingen op $Mg_ySc_{(1-y)}$ dunnefilms (y = 0,65 - 0,85) en pure Pd films tonen aan dat de oppervlaktekinetiek volledig gedomineerd wordt door de Pd toplaag. Bovendien is de ladingsoverdrachtsreactie en niet de absorptiereactie de snelheidsbepalende stap. De totale kinetische impedantie, wanneer de $Mg_ySc_{(1-y)}$ dunnefilmelektrodes in hun waterstofarme staat zijn, wordt gedomineerd door de overdracht van waterstof van de Pd naar de $Mg_ySc_{(1-y)}$ laag. Bovendien neemt de absolute impedantie die geassocieerd wordt met dit proces toe met een afnemend Sc gehalte.

Elektrochemisch onderzoek laat zien dat de dunnefilms een terugval laten zien in zowel het vermogen om met een hoge stroom alle waterstof te verwijderen als in de totale opslagcapaciteit bij dezelfde kritische compositie als het bulksysteem. Ondanks het ontbreken van ondubbelzinnige structurele gegevens, is het redelijk om aan te nemen dat de kristalstructuur van de dunnefilms hetzelfde is als die van de bulkmaterialen. Röntgendiffractiegegevens van MgSc bulk systemen laten duidelijk zien dat de volledig beladen $Mg_ySc_{(1-y)}$ hydrides een éénfasig fcc-gestructureerd hydride vormen en dat er geen fasenscheiding plaatsvindt. Tijdens waterstofextractie blijft deze fcc structuur behouden. Het elektrochemisch gemeten 2-fasengebied kan toegeschreven worden aan een fasetransformatie van een waterstofrijke (fluoriet) naar een waterstofarme fcc structuur (sphaleriet).

De MgSc materialen hebben een heel hoge waterstofopslagcapaciteit, die bijna zes keer hoger is als die van de commercieel gebruikte Mischmetal-gebaseerde materialen. Echter vanuit een commercieel oogpunt bezien, is het grootste nadeel van deze MgSc materialen het zeer kostbare Sc. Het is daarom wenselijk dat Sc (gedeeltelijk) wordt vervangen door een minder kostbaar materiaal zonder het introduceren van nadelige effecten. Eerder werd getoond dat de superieure waterstoftransporteigenschappen van het MgSc hydride toegeschreven konden worden aan de fcc structuur van het hydride. Een logisch substituut voor Sc zou een element moeten zijn dat ook een fcc-gestructureerd hydride vormt wanneer het met Mg gelegeerd wordt. Tevens zou het materiaal ongeveer even zwaar moeten zijn als Sc. Mogelijke kandidaten, gebaseerd op deze criteria zijn Ti, V en Cr. Helaas vormt geen van deze elementen een legering met Mg onder normale legeer-omstandigheden. Door gebruik te maken van extreme drukken en temperaturen zijn enkele onderzoekers erin geslaagd om MgTi, MgV en MgCr hydrides te prepareren met de zogenaamde ‘aambeeld-cel’ techniek (‘anvil-cell’ technique). Hoewel deze techniek erg ingewikkeld is, toont het aan dat kristallijne MgX hydrides (X = Ti, V, Cr) kunnen bestaan in bulk vorm. Tot nu toe hebben slechts enkele onderzoekers geprobeerd dezelfde materialen te maken via een dunnefilm benadering.

In Hoofdstuk 5 wordt de preparatie en karakterisering van MgX dunnefilms beschreven. XRD metingen tonen aan dat kristallijne $Mg_yX_{(1-y)}$ (X = Ti, V, Cr) dunnefilms kunnen worden vervaardigd d.m.v. hoog vacuum opdampen. Eénfasige verbindingen werden verkregen in alle gevallen, bestaande uit een Mg-structuur met daarin opgelost Ti, V of Cr. Het blijkt dus mogelijk te zijn om deze meta-stabiele verbindingen te prepareren zonder gebruik te hoeven maken van extreme drukken en temperaturen.

De waterstofopslageigenschappen van met Pd bedekte $Mg_yX_{(1-y)}$ dunnefilms (X = Ti), met y variërend van 0,50 tot 0,95, zijn elektrochemisch onderzocht. Pd bedekte Mg lagen zijn hierbij gebruikt als referentiemateriaal. De metingen tonen aan dat de reversibele opslagcapaciteit van deze MgTi materialen toeneemt met toenemend Mg gehalte en dat er zich een optimum bevindt bij $y \approx 0{,}80$. Galvanostatische metingen laten zien dat het Ti gehalte een behoorlijk effect heeft op het vermogen om de materialen met een hoge stroom te kunnen ontladen (tot y = 0,80). Echter, het vermogen om de materialen met een hoge stroom

te kunnen ontladen neemt drastisch af indien $y > 0{,}80$ is. Deze afhankelijkheid is nagenoeg gelijk aan die van de $Mg_ySc_{(1-y)}$ dunnefilms. Net zoals voor de $Mg_ySc_{(1-y)}$ materialen is dit effect toe te schrijven aan een verandering in hydride structuur (van fcc naar rutiel). Samenvattend, de elektrochemische metingen laten duidelijk zien dat het goedkope Ti een uitstekend substituut is voor het kostbare Sc in de $Mg_ySc_{(1-y)}$ materialen zonder dat het nadelige effecten introduceert.

Daar de optimale compositie van zowel de Ti- als Sc-bevattende materialen 80 at.% Mg bevatte (y = 0,80) werden V- en Cr-bevattende dunnefilms opgedampt met dezelfde compositie en hun elektrochemische waterstofopslagkenmerken vergeleken. De reversibele waterstofopslagcapaciteiten van de $Mg_{0.80}X_{0.20}$ (X = Ti, V, Cr) bedragen 1750 mAh/g voor $Mg_{0.80}Ti_{0.20}$ (6,5 gew.%), 1700 mAh/g voor $Mg_{0.80}V_{0.20}$ (6,4 gew.%) en 1270 mAh/g voor $Mg_{0.80}Cr_{0.20}$ (4,9 gew.%). Het vermogen van de $Mg_{0.80}X_{0.20}$ dunnefilms om deze met een hoge stroom te ontladen wordt interessant genoeg sterk beïnvloed door element X in MgX. Elektrochemische metingen laten zien dat het vermogen om de Ti-bevattende dunnefilms met een hoge stroom te ontladen ongeveer gelijk is aan dat van het Sc-bevattende legering ($Mg_{0.80}Sc_{0.20}$) en superieur aan dat van de V- en Cr-bevattende verbindingen. Dit resulteert in het feit dat, vergeleken met de V- en Cr-bevattende verbindingen, eenzelfde hoeveelheid waterstof bijna tien keer sneller kan worden vrijgegeven van de Ti- en Sc-bevattende verbindingen. Isothermen van de MgX systemen tonen aan dat de evenwichtspotentiaal van het laad/ontlaadplateau slechts marginaal beïnvloed wordt door element X in MgX. Vergeleken met de $Mg_{0.80}Sc_{0.20}$ verbinding zijn de evenwichtspotentialen van deze legeringen meer negatief.

De impedantiegegevens laten zien dat de oppervlaktekinetiek van de $Mg_{0.80}X_{0.20}$ (X = Ti, V, Cr) dunnefilms identiek is aan die van de $Mg_{0.80}Sc_{0.20}$ en pure Pd dunnefilms. Dit duidt erop dat de Pd toplaag de oppervlaktekinetiek dicteert. Naast de oppervlaktekinetiek zijn er twee andere processen die de gemeten impedantie kunnen domineren; de overdracht van waterstof van de Pd laag naar de $Mg_yX_{(1-y)}$ laag (bij tussenliggende frequenties) en vaste stof diffusie van waterstof in de bulk (bij de laagste frequenties). De absolute weerstand van deze processen is beduidend hoger voor de V- en Cr-bevattende dunnefilms, vergeleken met de Ti- en Sc-bevattende materialen. Dit heeft tot gevolg dat het vermogen om de V- en Cr-bevattende dunnefilms met een hoge stroom te ontladen erg laag is.

De potentie om waterstof op te slaan is ook elektrochemisch onderzocht voor veel verschillende CNT materialen. Dit is beschreven in Hoofdstuk 6. De materialen die onderzocht zijn bestaan uit ‘as-produced’ (a.p.), gezuiverde en goed-georienteerde SWNT, MWNT en CNF materialen. Ook werden enkele van deze materialen chemisch gezuiverd om specifieke fracties te verkrijgen. De elektrochemische respons van deze materialen is, tijdens het beladen en ontladen, zonder specifieke kenmerken en toont geen fasenovergangen of duidelijke redoxresponses. De maximale ontlaadcapaciteit van alle materialen die onderzocht zijn, is ongeveer 150 mAh/g (a.p. SWNT material). Metingen laten zien dat de elektrochemische activiteit van het matrixmateriaal, dat gebruikt wordt om composietelektrodes te vervaardigen, niet genegeerd mag worden. Vooral materialen die elektrochemisch actief zijn in het potentiaalgebied dat algemeen gebruikt wordt wanneer men de energieopslageigenschappen van CNT materialen onderzoekt, kunnen de redoxrespons domineren. Een duidelijk voorbeeld hiervan is nikkel (Ni). Elektrochemische metingen bevestigen dat dit soort reacties in het verleden abusievelijk zijn toegeschreven aan de waterstofopslageigenschappen van het CNT materiaal.

Door middel van experimenten wordt aangetoond dat de elektrochemische respons van commercieel gezuiverde CNTs veel lager is dan die van hun a.p. tegenhanger. Dit duidt erop dat de CNTs zelf slechts een zeer klein deel van de totale respons kunnen verklaren. Analyse

op een aantal specifieke CNT materialen laat zien dat de totale gemeten respons van a.p. materialen toe te wijzen is aan verschillende processen. Deze processen zijn; de irreversibele oxidatie van koolstofmateriaal, de reversibele oxidatie/reductie van achtergebleven metaalkatalysator of de koolstofhoudende onzuiverheden en een significante elektrostatische component. Impedantiemetingen gecombineerd met cyclovoltammetrische gegevens bewijzen ondubbelzinnig dat de elektrostatische opslag van energie rechtstreeks toe te wijzen is aan het beladen/ontladen van de elektrische dubbellaag. De karakterisering van zeer zuivere CNT materialen (commercieel gezuiverde SWNTs en MWNTs) toont aan dat tot 90 - 95 % van de totale lading op deze manier wordt opgeslagen. Voor a.p. materialen is dit slechts 20 - 30 %. Het overige deel wordt veroorzaakt door de andere processen die hierboven vermeld zijn.

De conclusie van het onderzoek beschreven in dit proefschrift is dat er geen waterstof in CNT materiaal opgeslagen kan worden en dat de gemeten responses toe te wijzen zijn aan elektrostatische belading van de dubbellaag en de reversibele oxidatie/reductie van (metaal) onzuiverheden. Deze conclusie staat haaks op het werk dat de laatste jaren door andere onderzoekers gedaan is waarin deze responses toegeschreven werden aan de opslag van waterstof in CNT materiaal. Dit leidde tot hoge opslagcapaciteiten van rond de 800 mAh/g of 3 gew.% waterstof. De huidige studie laat verder zien dat de totale hoeveelheid lading die reversibel in CNT materiaal opgeslagen kan worden in hoge mate afhankelijk is van de morfologie en de mate van zuiverheid.

Daar de CNT materialen gekarakteriseerd worden door een heel hoge dubbellaagcapaciteit (rond de 10 - 100 F/g) en alle energie die gebruikt is voor het beladen van deze dubbellaag vrijgegeven kan worden zonder veel verliezen, zijn zij veelbelovende kandidaten op het gebied van elektrochemische dubbellaagcondensatoren. Nochtans is deze energieopslag/vrijgave, hoewel beduidend, behoorlijk lager dan reeds bestaande elektrochemische dubbellaagcondensator-materialen gebaseerd op bijvoorbeeld RuO_2.

Ter afronding kan gezegd worden dat het onderzoek dat beschreven wordt in dit proefschrift laat zien dat Mg-gebaseerde legeringen bestaande uit MgSc en MgTi gekarakteriseerd worden door een uitstekende waterstofopslagkinetiek en een zeer hoge reversibele waterstofopslagcapaciteit (6,7 gew.%). Deze kenmerken laten zien dat deze materialen zeer veelbelovende kandidaten zijn voor toepassingen zoals batterijelektrodemateriaal of waterstofopslagmedium. CNTs daarentegen kunnen geen waterstof opslaan. De lading die opgeslagen kan worden in deze materialen wordt hoofdzakelijk elektrostatisch opgeslagen in de elektrische dubbellaag en is gedeeltelijk toe te wijzen aan de reversibele oxidatie/reductie van (metaal) onzuiverheden. De goede elektrostatische energieopslageigenschappen van deze materialen zouden benut kunnen worden in elektrochemische dubbellaagcondensator-toepassingen.

List of publications

Publications related to this thesis

1. R.A.H. Niessen, and P.H.L. Notten, *Electrochemical hydrogen storage characteristics of thin film MgX (X = Sc, Ti, V, Cr) compounds*, Electrochem. Solid St. Lett., 8, A534 (2005).

2. R.A.H. Niessen, P. Vermeulen, and P.H.L. Notten, *The electrochemistry of Pd-coated $Mg_ySc_{(1-y)}$ thin film electrodes; a thermodynamic and kinetic study*, in press Electrochim. Acta (2005).

3. R.A.H. Niessen, and P.H.L. Notten, *Reference electrode-induced surface poisoning of thin film electrodes*, J. Electrochem. Soc., 152, A2051 (2005).

4. R.A.H. Niessen, and P.H.L. Notten, *The influence of O_2 on the electrochemistry of thin film, hydrogen storage, electrodes*, Electrochim. Acta, 50, 2959 (2005).

5. R.A.H. Niessen, and P.H.L. Notten, *Hydrogen storage in thin film Magnesium-Scandium alloys*, in press J. Alloys Compd., (2005).

6. W.P. Kalisvaart, R.A.H. Niessen, and P.H.L. Notten, *Mg-Sc alloys for electrochemical hydrogen storage; a comparative study between thin films and bulk materials*, in press J. Alloys Compds. (2005).

7. P. Vermeulen, R.A.H. Niessen, and P.H.L. Notten, *Hydrogen storage in metastable $Mg_yTi_{(1-y)}$ thin films*, in press Electrochem. Comm. (2005).

8. R.A.H. Niessen, and P.H.L. Notten, *The electrochemistry of carbon nanotubes, part I: aqueous electrolyte*, in preparation (2005).

Other publications

1. A.R.M. Verschueren, R.A.H. Niessen, P.H.L. Notten, W. Oepts, and E.M.L. Alexander-Moonen, *Experiments and modeling of conduction and charge accumulation in liquid crystal cells*, Trans. Dielec. Electr. Insul., 10, 6, 963 (2003).

2. R.A.H. Niessen, and P.H.L. Notten, *The electrochemistry of carbon nanotubes, part II: organic electrolyte*, in preparation (2005).

Résumé

Rogier Adrianus Henrica Niessen was born in Weert, the Netherlands on December 23, 1975. In 1989 he finished his primary education at the Martin Luther King School. Secondary education (VWO) was at the Philips van Horne Scholengemeenschap in Weert. In 1994 he started studying Chemical Engineering at Eindhoven University of Technology (the Netherlands). During his studies he performed several traineeships, covering a wide range of topics ranging from organic synthesis of main-chain liquid crystal polymers (Polymer Technology group, Eindhoven University of Technology) to advanced process technology in a sugarcane processing plant (Usina Nova América, Tarumã, Brazil). He received his M.Sc. degree in 2001 on the topic of impedance spectroscopic investigations of liquid crystal displays. This study was performed at Philips Research Laboratories Eindhoven, the Netherlands (Flat Display Modules group). In the same year he started his Ph.D. research at Eindhoven University of Technology (Inorganic Chemistry and Catalysis group) under the supervision of prof.dr. P.H.L. Notten. This research was focused on the electrochemical energy storage characteristics of lightweight Mg-based alloys and nanostructured carbon materials. A large part of this work was performed in the System in Package Devices group at Philips Research Laboratories Eindhoven. During his Ph.D. research he attended various workshops and conferences, both in the Netherlands and abroad (Poland, Canada, Sweden), where he presented the work described in this thesis.

References

1. R. McAlister, *The solar hydrogen civilization: the future of energy is the future of our global economy*, (American Hydrogen Association, New York, 2003).

2. F. Barbir, *PEM fuel cells; theory and practice*, (Elsevier Academic Press, London, 2005).

3. S. Inman, M. El-Gindy, and D.C. Haworth, *Hybrid electric vehicles technology and simulation: literature review*, Int. J. Heavy Vehicle Systems, 10, 167 (2003).

4. U.S. Department of Energy, Multi-Year Research, Development and Demonstration Plan: Planned program activities for 2003 – 2010, http://www.eere.energy.gov/hydrogenandfuelcells/mypp/ (Aug. 2005).

5. T. Graham, *On the absorption and dialytic separation of gases by colloid septa*, Phil. Trans. R. Soc., 156, 415 (1866).

6. W.M. Müller, J.P. Blackledge, and J.J. Libowitz, *Metal hydrides*, (Academic Press, New York, 1968).

7. F. Stampfer, C.E. Holley, and J.F. Suttle, *The magnesium-hydrogen system*, J. Am. Chem. Soc., 82, 3504 (1960).

8. K.A.G. Amankwah, and J.A. Schwarz, *Storage on superactivated carbon at refrigeration temperatures*, Int. J. Hydrogen Energy, 14, 437 (1989).

9. J. Jagiello, T.J. Bandosz, K. Putyera, and J.A. Schwarz, *Micropore structure of template derived carbons using adsorption of gases with different molecular diameters*, J. Chem. Soc. Faraday Trans., 91, 2929 (1995).

10. C. Carpetis, and W. Peschka, *A study of hydrogen storage by use of cryoadsorbents*, Int. J. Hydrogen Energy, 5, 539 (1980).

11. J.L.C. Rowsell, and O.M. Yaghi, *Metal–organic frameworks: a new class of porous materials*, Micropor. Mesopor. Mat., 73, 3 (2004).

12. A. Chambers, C. Park, R. T. Baker, and N. Rodriguez, *Hydrogen storage in graphite nanofibers*, J. Phys. Chem. B, 102, 4253 (1998).

13. A.C. Dillon, and M.J. Heben, *Hydrogen storage using carbon adsorbents: past, present and future*, Appl. Phys. A, 72, 133 (2001).

14. P.H.L. Notten, in: *Interstitial intermetallic alloys, NATO ASI Series E*, vol. 281 (Kluwer Academic Publishers, London, 1995), p. 151.

15. D. Linden (Edt), *Handbook of batteries*, 2nd ed. (McGraw-Hill, New York, 1995), Chapter 28.

16. P.H.L. Notten, E. Verbitskiy, W.S. Kruijt, and H.J. Bergveld, *Oxygen evolution and recombination kinetics inside sealed rechargeable, Ni-based batteries*, J. Electrochem. Soc., 152, A1423 (2005).

17. T. Akari, M. Nakayama, K. Fukuda, and K. Onda, *Thermal behavior of small nickel/metal hydride battery during rapid charge and discharge cycles*, J. Electrochem. Soc., 152, A1128 (2005).

18. P.H.L. Notten, M. Ouwerkerk, H. van Hal, D. Beelen, W. Keur, J. Zhou, and H. Feil, *High energy density strategies: from hydride-forming materials research to battery integration*, J. Power Sources, 129, 45 (2004).

19. N. Rajalakshmi, K.S. Dhathatreyan, A. Govindaraj, and B.C. Satishkumar, *Electrochemical investigation of single-walled carbon nanotubes for hydrogen storage*, Electrochim. Acta, 45, 4511 (2000).

20. B. Bogdanovic, R.A. Brand, A. Marjanovic, M. Schwickardi, and J. Tölle, *Metal-doped sodium aluminium hydrides as potential new hydrogen storage materials*, J. Alloys Compd., 302, 36 (2000).

21. A. Zaluska, L. Zaluski, and J.O. Ström-Olsen, *Sodium alanates for reversible hydrogen storage*, J. Alloys Compd., 298, 125 (1999).

22. P. Chen, Z. Xiong, J. Luo, J. Lin, and K.L. Tan, *Interaction of hydrogen with metal nitrides and imides*, Nature, 420, 302 (2002).

23. K. Ohoyama, Y. Nakamori, S. Orimo, and K. Yamada, *Revised crystal structure model of Li_2NH by neutron powder diffraction*, J. Phys. Soc. Jpn., 74, 483 (2005).

24. T. Ichikawa, N. Hanada, S. Isobe, H.Y. Leng, and H. Fujii, *Hydrogen storage properties in Ti catalyzed Li–N–H system*, J. Alloys Compd., in press (2005).

25. Z. Xiong, J. Hu, G. Wu, P. Chen, W. Luo, K. Gross, and J. Wang, *Thermodynamic and kinetic investigations of the hydrogen storage in the Li–Mg–N–H system*, J. Alloys Compd., 398, 235 (2005).

26. W. Luo, *($LiNH_2$–MgH_2): a viable hydrogen storage system*, J. Alloys Compd., 381, 284 (2004).

27. B. Baranowski, H.D. Hochheimer, K. Strössner, and W. Hönle, *High pressure X-ray investigation of AlH3 and Al at room temperature*, J. Less-Common Met., 113, 341 (1985).

28. J.H.N. van Vught, F.A. Kuijpers, and H.C.A.M. Bruning, *Reversible room-temperature absorption of large quantities of hydrogen by intermetallic compounds*, Philips Res. Reports, 25, 133 (1970).

29. H.H. van Mal, K.H.J. Buschow, and F.A. Kuijpers, *Hydrogen absorption and magnetic properties of $LaCo5_xNi_{5-5x}$ compounds*, J. Less-Common Met., 32, 289 (1973).

30. H.H. van Mal, K.H.J. Buschow, and A.R. Miedema, *Hydrogen absorption in $LaNi_5$ and related compounds: Experimental observations and their explanation*, J. Less-Common Met., 35, 65 (1974).

31. M.H. Mendelsohn, D.M. Gruen, and A.E. Dwight, *$LaNi_{5-x}Al_x$ is a versatile alloy system for metal hydride applications*, Nature, 269, 45 (1977).

32. H. Uchida, M. Tada, and Y. Huang, *The influence of cerium, praseodymium, neodymium and samarium on hydrogen absorption in $LaNi_5$ alloys*, J. Less-Common Met., 88, 81 (1982).

33. F.G. Will, US Patent N° 3874928 (1975).

34. J.J.G. Willems, *Metal hydride electrodes stability of $LaNi_5$-related components*, Philips J. of Research, 39, Suppl. N°1 (1984).

35. A. Taniguchi, N. Fujioka, M. Ikoma, and A. Ohta, *Development of nickel/metal-hydride batteries for EVs and HEVs*, J. Power Sources, 100, 117 (2001).

36. M.H. Mendelsohn, and D.M. Gruen, *Intermetallic compounds as bulk getters*, J. Less-Common Met., 74, 449 (1980).

37. E. Glueckhauf, and G.P. Kitt, *"Chromatograpic separation of hydrogen isotopes" in Vapor phase chromatography* (Butterworths, London, 1957).

38. D.R. Rosseinsky, and R.J. Mortimer, *Electrochromic Systems and the Prospects for Devices*, Adv. Mater., 13, 783 (2001).

39. J.N. Huiberts, *On the road to dirty metallic atomic hydrogen*, Ph.D. thesis, Vrije Universiteit Amsterdam (1995).

40. J.N. Huiberts, R. Griessen, J.H. Rector, R.J. Wijngaarden, J.P. Dekker, D.G. de Groot, and N.J. Koeman, *Yttrium and lanthanum hydride films with switchable optical properties*, Nature, 380, 231 (1996).

41. M. Ouwerkerk, *Electrochemically induced optical switching of $Sm_{0.3}Mg_{0.7}H_x$ thin layers*, Sol. St. Ionics, 113-115, 431 (1998).

42. T.J. Richardson, J.L. Slack, R.D. Armitage, R. Kostecki, B. Farangis, and M.D. Rubin, *Switchable mirrors based on nickel-magnesium films*, Appl. Phys. Lett., 78, 3047 (2001).

43. P. Kumar, and L.K. Malhotra, *Palladium capped samarium thin films as potential hydrogen sensors*, Mat. Chem. Phys., 88, 106 (2004).

44. S. Iijima, *Helical microtubules of graphitic carbon*, Nature 354 (1991), 56

45. http://www.photon.t.u-tokyo.ac.jp/~maruyama/agallery/agallery.html (Aug. 2005).

46. C. Journet, and P. Bernier, *Production of carbon nanotubes*, Appl. Phys. A, 67, 1 (1998).

47. M.S. Dresselhaus, G. Dresselhaus, and R. Saito, *Physics of carbon nanotubes*, Carbon, 33, 883 (1995).

48. M.S. Dresselhaus, G. Dresselhaus, and P.C. Eklund, *Science of fullerenes and carbon nanotubes: their properties and applications* (Academic Press Inc., London, 1996).

49. G.S. Duesberg, W.J. Blau, H.J. Byrne, J. Muster, M. Burghard, and S. Roth, *Experimental observation of individual single-wall nanotube species by Raman microscopy*, Chem. Phys. Letters, 310, 8 (1999).

50. R.H. Baughman, A.A. Zakhidov, and W.A. de Heer, *Carbon nanotubes - the route toward applications*, Science, 297, 787 (2002).

51. P.M. Ajayan, and O.Z. Zhou, *Topics in applied physics - Carbon nanotubes: synthesis, structure, properties and applications* (Springer-Verlag, Berlin, 2001).

52. E. Frackowiak, S. Gautier, H. Gaucher, S. Bonnamy, and F. Beguin, *Electrochemical storage of lithium in multiwalled carbon nanotubes*, Carbon, 37, 61 (1999).

53. H. Shimoda, B. Gao, X.P. Tanga, A. Kleinhammes, L. Fleming, Y. Wu, and O. Zhou, *Lithium intercalation into etched single-wall carbon nanotubes*, Physica B, 323, 133 (2002).

54. Z. Yang, S. Sang, K. Huang, and H. Wu, *Lithium insertion into the raw multi-walled carbon nanotubes pre-doped with lithium - an electrochemical impedance study*, Diam. Relat. Mater., 13, 99 (2004).

55. E. Frackowiak, K. Jurewicz, K. Szostak, S. Delpeux, and F. Beguin, *Nanotubular materials as electrodes for supercapacitors*, Fuel Processing Techn., 77, 213 (2002).

56. E. Frackowiak, K. Jurewicz, K. Szostak, S. Delpeux, and F. Beguin, *Supercapacitors from nanotubes/polypyrrole composites*, Chem. Phys. Lett., 347, 36 (2001).

57. J.M. Bonard, H. Kind, T. Stöckli, and L.A. Nilsson, *Field emission from carbon nanotubes: the first five years*, Sol. St. Electronics, 45, 893 (2001).

58. L. Schlapbach, *Topics in applied physics – Hydrogen in intermetallic compounds II* (Springer, Berlin, 1992), p. 15.

59. K. Machida, M. Enyo, G. Adachi, and J. Shiokawa, *The hydrogen electrode reaction characteristics of thin film electrodes of Ni-based hydrogen storage alloys*, Electrochim. Acta, 29, 807 (1984).

60. P.W. Atkins, *Dynamic electrochemistry*, 6th ed. (Oxford University Press, Oxford, 1998), p. 878.

61. A.J. Bard, and L.R. Faulkner, *Electrochemical methods; fundamental and applications*, 2nd ed. (John Wiley & Sons, New York, 2001), p. 95.

62. R. Griessen, and T. Riesteter, *Topics in applied physics – Hydrogen in intermetallic compounds I* (Springer, Berlin, 1988), p. 219.

63. P.W. Atkins, *Physical chemistry* (Oxford University Press, Oxford, 1998), p. 258.

64. S. Licht, *pH Measurement in Concentrated Alkaline Solutions*, Anal. Chem., 57, 514 (1985).

65. A.J. Bard, and L.R. Faulkner, *Electrochemical methods; fundamental and applications*, 2nd ed. (John Wiley & Sons, New York, 2001), p. 156.

66. J. R. MacDonald, *Impedance spectroscopy* (John Wiley & Sons, New York, 1987), Chapter 1.

67. J. R. MacDonald, *Impedance spectroscopy* (John Wiley & Sons, New York, 1987), p. 60.

68. R.A.H. Niessen, and P.H.L. Notten, *The influence of O_2 on the electrochemistry of thin film, hydrogen storage, electrodes*, Electrochim. Acta, 50, 2959 (2005).

69. P.B. Sweetster, *Calorimetric determination of trace levels of oxygen in gases with the photochemically generate methyl viologen radical-cation*, Anal. Chem., 39, 979 (1967).

70. R.A.H. Niessen, and P.H.L. Notten, *Hydrogen storage in thin film magnesium–scandium alloys*, J. Alloys Compd., in press (2005).

71. R.A.H. Niessen, and P.H.L. Notten, *Reference electrode induced surface poisoning of thin film electrodes*, J. Electrochem. Soc., 152, A2051 (2005).

72. M. Pourbaix, *Atlas of electrochemical equilibria in aqueous Solutions*, 2nd ed. (National Association of Corrosion Engineers, Houston, 1974), p. 496.

73. P.H.L. Notten, M. Ouwerkerk, A. Ledovskikh, H. Senoh, and C. Iwakura, *Hydride-forming electrode materials seen from a kinetic perspective*, J. Alloys Compd., 356, 759 (2003).

74. P.H.L. Notten, and P. Hokkeling, *Double-phase hydride forming compounds: a new class of high electrocatalytic materials*, J. Electrochem. Soc., 138, 1877 (1991).

75. T. Erdey-Grúz, *Kinetics of electrode processes* (Adam Hilger Ltd., London, 1972), p. 174.

76. J. R. MacDonald, *Impedance spectroscopy* (John Wiley & Sons, New York, 1987), p. 74.

77. C. Gabrielli, P.P. Grand, A. Lasia, and H. Perrot, *Investigation of hydrogen adsorption-absorption into palladium thin films, I. Theory*, J. Electrochem. Soc., 151, A1925 (2004).

78. D.T. Sawyer, and J.L. Roberts, *Experimental electrochemistry for chemists* (John Wiley & Sons, New York, 1974), p. 48.

79. T.H. Yang, and S.I. Pyun, *Hydrogen absorption and diffusion into and in palladium: ac-impedance analysis under impermeable boundary conditions*, Electrochim. Acta, 41, 843 (1996).

80. C. Gabrielli, P.P. Grand, A. Lasia, and H. Perrot, *Investigation of hydrogen adsorption and absorption in palladium thin films, III. Impedance spectroscopy*, J. Electrochem. Soc., 151, A1943 (2004).

81. P. Selvam, B. Viswanathan, C.S. Swamy, and V. Srinivasan, *Magnesium and magnesium alloy hydrides*, Int. J. Hydrogen Energy, 11, 169 (1986).

82. K. Ogawa, H. Aoki, and T. Kobayashi, *Hydrogen absorption and electronic structure of magnesium-based yttrium and scandium dilute alloys*, J. Less-Common Met., 88, 283 (1982).

83. S. Morizumi, H. Saikawa, T. Minegishi, M. Matsuyama, K. Watanabe, M. Iijima, and M. Ohtushi, *Structure and mechanical properties of internally hydrided Mg-III$_a$ transition metal alloys*, J. Mat. Sci 31, 4647 (1996).

84. M. Ouwerkerk, *Scandium-magnesium hydride, a new electrode material of rechargeable batteries*, Phillips Research TN 2001/7207, Philips Research (2001).

85. I.A.M.E. Giebels, *Shining light on magnesium switchable mirrors*, Ph.D. thesis, Chapter 6, Vrije Universiteit Amsterdam (2004).

86. I.A.M.E. Giebels, R. Griessen, and M. Ouwerkerk, *Insulating cubic $MgSc_{3-\delta}$ in $Mg_ySc_{1-y}H_x$*, in preparation (2005).

87. B.J. Beaudry, and A.H. Daane, *A study of the scandium-magnesium system from 0 to 60 at.% scandium*, J. Less-Common Met., 18, 305 (1969).

88. M. Baldauf, and D.M. Kolb, *A hydrogen adsorption and absorption study with ultrathin Pd overlayers on Au(111) and Au(100)*, Electrochim. Acta, 38, 2145 (1993).

89. J. Horkans, *Film thickness effects on hydrogen sorption at palladium electrodes*, J. Electroanal. Chem., 106, 245 (1980).

90. R. Griessen, and T. Riesteter, *Topics in applied physics – Hydrogen in intermetallic compounds I* (Springer, Berlin, 1988), Chapter 6.

91. W.P. Kalisvaart, R.A.H. Niessen, and P.H.L. Notten, *Electrochemical hydrogen storage in MgSc alloys: a comparative study between thin films and bulk materials*, in press J. Alloys Compds. (2005).

92. D. Linden (Edt), *Handbook of batteries*, 2nd ed. (McGraw-Hill, New York, 1995), p. 29.4.

93. H. Senoh, K. Morimoto, H. Inoue, C. Iwakura, and P.H.L. Notten, *Relationship between equilibrium hydrogen pressure and exchange current for the hydrogen electrode reaction at $MnNi_{3.9-x}Mn_{0.4}Al_xCo_{0.7}$ alloy electrodes*, J. Electrochem. Soc., 147, 2451 (2000).

94. A. Krozer, and B. Kasemo, *Equilibrium hydrogen uptake and associated kinetics for the Mg-H_2 system at low pressures*, J. Phys.: Condens. Matter, 1, 1533 (1989).

95. A. Krozer, and B. Kasemo, *Hydrogen uptake by Pd-coated Mg: absorption-decomposition isotherms and uptake kinetics*, J. Less-Common Met., 160, 323 (1990).

96. P. Spatz, H.A. Aebischer, A. Krozer, and L. Schlapbach, *The diffusion of H in Mg and the nucleation and growth of MgH_2 in thin films*, Z. Phys. Chem., 181, 393 (1993).

97. Z. Luz, J. Genossar, and P.S. Rudman, *Identification of the diffusing atom in MgH_2*, J. Less-Common Met., 73, 113 (1980).

98. I.A.M.E. Giebels, *Shining light on magnesium switchable mirrors*, Ph.D. thesis, p. 67, Vrije Universiteit Amsterdam (2004).

99. A. Milchev, and M.I. Montenegro, *A galvanostatic study of electrochemical nucleation*, J. Electroanal. Chem., 333, 93 (1992).

100. F.A. Lewis, *The palladium hydrogen system* (Academic Press Inc., London, 1967), p. 4.

101. M. Nicolas, L. Dumoulin, J.P. Burger, *Thickness dependence of the critical solution temperature of hydrogen in Pd*, J. Appl. Phys., 60, 3125 (1986).

102. M. Pourbaix, *Atlas of electrochemical equilibria in aqueous Solutions*, 2nd ed. (National Association of Corrosion Engineers, Houston, 1974), p. 358.

103. R.A.H. Niessen, P. Vermeulen, and P.H.L. Notten, *The electrochemistry of Pd-coated $Mg_ySc_{(1-y)}$ thin film electrodes; a thermodynamic and kinetic study*, in press Electrochim. Acta (2005).

104. J. R. MacDonald, *Impedance spectroscopy* (John Wiley & Sons, New York, 1987), p. 75.

105. C. Montella, *EIS study of hydrogen insertion under restricted diffusion conditions: I. Two-step insertion reaction*, J. Electroanal. Chem., 497, 3 (2001).

106. A. Lasia, in: *Modern aspects of electrochemistry*, vol. 35 (Kluwer Academic/Plenum Publishers, New York, 2002), p. 29.

107. T.H. Yang, and S.I. Pyun, *An investigation of the hydrogen absorption reaction into, and the hydrogen evolution reaction from, a Pd foil electrode*, J. Electroanal. Chem., 414, 127 (1996).

108. S.E. Johnsen, G. Lindbergh, A. Lundqvist, R. Tunold, *A single particle investigation on the kinetics of metal hydride materials*, J. Electrochem Soc., 150, A629 (2003).

109. Y.G. Yoon, and S.I. Pyun, *Hydrogen transport through plasma enhanced chemical vapor-deposited TiO_2 film-palladium bilayer by ac-impedance spectroscopy*, Electrochim. Acta, 40, 999 (1995).

110. J.P. Diard, N. Glandut, C. Montella, and J.Y. Sanchez, *One layer, two layers, etc. An introduction to the EIS study of multilayer electrodes. Part 1: Theory*, J. Electroanal. Chem., 578, 247 (2005).

111. P. Villars (Edt), *Pearson's handbook desk edition*, vol. 2 (ASM International, Materials Park, 1997), p. 2101.

112. P.H.L. Notten, R.E.F. Einerhand, and J.L.C. Daams, *On the nature of the electrochemical cycling stability of non-stoichiometric $LaNi_5$-based hydride-forming compounds Part I. crystallography and electrochemistry*, J. Alloys Compd., 210, 233 (1994).

113. D.G. Westlake, *Site occupancies and stoichiometries in hydrides of intermetallic compounds: Geometric considerations*, J. Less-Common Met., 90, 251 (1983).

114. A.C. Switendick, *Electronic structure and total energy calculations for transition metal hydrides*, J. Less-Common Met., 130, 249 (1987).

115. L. Schlapbach (Edt), *Topics in applied physics,* vol. 63 (Springer, Berlin, 1988), Chapter 4.

116. I. O. Bashkin, E. G. Ponyatovski, and M. E. Kost, *Phase transformations in hydrides of rare-earth metals under pressure, II. The Sc-H and Yb-H systems under high hydrogen pressure*, Physica Status Solidi B, 87, 369 (1978).

117. I. O. Bashkin, E. G. Ponyatovski, and M. E. Kost, *p-T diagram of the system Sc-H at high hydrogen pressures*, Inorg. Mater. (USSR), 380, 1260 (1978).

118. P. Villars (Edt), *Pearson's handbook desk edition*, vol. 2 (ASM International, Materials Park, 1997), p. 2083.

119. J. Isidorsson, I. A. M. E. Giebels, E. S. Kooij, J. H. Rector, A. T. M. van Gogh, and R. Griessen, *Structural, optical and electronic properties of $LaMgH_x$ switchable mirrors*, Electrochim. Acta, 46, 2179 (2001).

120. I.A.M.E. Giebels, *Shining light on magnesium switchable mirrors*, Ph.D. thesis, p. 138, Vrije Universiteit Amsterdam (2004).

121. F. Gingl, K, Yvon, T, Vogt, and A. Hewat, *Synthesis and crystal structure of tetragonal $LnMg_2H_7$ (Ln = La, Ce), two Laves phase hydride derivatives having ordered hydrogen distribution*, J. Alloys Compd., 253-254, 313 (1997).

122. Y. Goto, H. Kakuta, A. Kamegawa, H. Takamura, and M. Okada, *Effect of synthesis pressure on hydride phases in Mg–M systems (M = Mn, Y)*, Sci. Technol. Adv. Mat., 4, 333 (2003).

123. P. Vajeeston, P. Ravindran, A. Kjekshus, and H. Fjellvåg, *Pressure-induced structural transitions in MgH_2*, Phys. Rev. Letters, 89, 175506 (2002).

124. B. Vigeholm, K. Jensen, B. Larsen, and A. Schrøder Pedersen, *Elements of hydride formation mechanisms in nearly spherical magnesium powder particles*, J. Less-Common Met., 131, 133 (1987).

125. D. Kyoi, T. Sato, E. Rönnebro, N. Kitamura, A. Ueda, M. Ito, S. Katsuyama, S. Hara, D. Noreus, and T. Sakai, *A new ternary magnesium–titanium hydride Mg_7TiH_x with hydrogen desorption properties better than both binary magnesium and titanium hydrides*, J. Alloys Compd., 372, 213 (2004).

126. D. Kyoi, T. Sato, E. Rönnebro, Y. Tsuji, N. Kitamura, A. Ueda, M. Ito, S. Katsuyama, S. Hara, D. Noreus, and T. Sakai, *A novel magnesium–vanadium hydride synthesized by a gigapascal-high-pressure technique*, J. Alloys Compd., 375, 253 (2004).

127. D. Kyoi, E. Rönnebro, N. Kitamura, A. Ueda, M. Ito, S. Katsuyama, and T. Sakai, *The first magnesium–chromium hydride synthesized by the gigapascal high-pressure technique*, J. Alloys Compd., 361, 252 (2003).

128. E. Rönnebro, D. Kyoi, H. Blomqvist, D. Noreus, and T. Sakai, *Structural characterization of Mg_3CrH_6-a new high-pressure phase synthesized in a multi-anvil cell at 8 GPa*, J. Alloys Compd., 368, 279 (2004).

129. T.J. Richardson, B. Farangis, J.L. Slack, P. Nachimuthu, R. Perera, N. Tamura, and M. Rubin, *X-Ray absorption spectroscopy of transition metal–magnesium hydride thin films*, J. Alloys Compd., 356-357, 204 (2003).

130. P. Villars (Edt), *Pearson's handbook desk edition*, vol. 2 (ASM International, Materials Park, 1997), p. 2336.

131. A.R. West, *Solid state chemistry and its applications*, 1st ed. (John Wiley & Sons, New York, 1984), p. 367.

132. P. Vermeulen, R.A.H. Niessen, and P.H.L. Notten, *Hydrogen storage in metastable $Mg_yTi_{(1-y)}$ thin films*, in press Electrochem. Comm. (2005).

133. U. Kaess, G. Majer, M. Stoll, D.T. Peterson, and R.G. Barnes, *Hydrogen and deuterium diffusion in titanium dihydrides/dideuterides*, J. Alloys Compd, 259, 74 (1997).

134. R.J. Elias, H.L. Corso, and J.L. Gervasoni, *Fundamental aspects of the Ti–H system: theoretical and experimental behavior*, Int. J. Hydrogen Energy, 27, 91 (2002).

135. V. Bhosle, E.G. Baburaj, M. Miranova, and K. Salama, *Dehydrogenation of TiH_2*, Mat. Sc. Eng., A356, 190 (2003).

136. D.V. Schur, S.Yu. Zaginaichenko, V.M. Adejev, V.B. Voitovich, A.A. Lyashenko, and V.I. Trefilov, *Phase transformations in titanium hydrides*, Int. J. Hydrogen Energy, 21, 1121 (1996).

137. R.A.H. Niessen, and P.H.L. Notten, *Electrochemical hydrogen storage characteristics of thin film MgX (X = Sc, Ti, V, Cr) compounds*, Electrochem. Sol. St. Lett., 8, A534 (2005).

138. J.J. Reilly, and R.H. Wiswall, *Formation and properties of iron titanium hydride*, Inorg. Chem., 9, 1678 (1970).

139. A.T.M. van Gogh, D.G. Nagengast, E.S. Kooij, N.J. Koeman, and R. Griessen, *Quenching of giant hysteresis effects in $La_{1-z}Y_zH_x$ switchable mirrors*, Phys. Rev. Lett., 85, 2156-2159 (2000).

140. A.C. Dillon, K.M. Jones, T.A. Bekkedahl, C.H. Kiang, D.S. Bethune, M.J. Heben, *Storage of hydrogen in single-walled carbon nanotubes*, Nature, 386, 377 (1997).

141. C. Nützenadel, *Wasserstoffspeicherung in nanostrukturen*, Ph.D. thesis, Chapter 8-10, University of Fribourg (1999).

142. C. Nützenadel, A. Züttel, D. Chartouni, and L. Schlapbach, *Electrochemical storage of hydrogen in nanotube materials*, Electrochem. Sol. St. Lett., 2, 30 (1999).

143. S.M. Lee, K.S. Park, Y.C. Choi, Y.S. Park, J.M. Bok, D.J. Bae, K.S. Nahm, Y.G. Choi, S.C. Yu, N. Kim, T. Frauenheim, and Y.H. Lee, *Hydrogen adsorption and storage in carbon nanotubes*, Synth. Met., 113, 209 (2000).

144. X. P. Gao, Y. Lan, G. L. Pan, F. Wu, J.Q. Qu, D.Y. Song, and P.W. Shena, *Electrochemical hydrogen storage by carbon nanotubes decorated with metallic nickel*, Electrochem. Sol. St. Lett., 4, A173 (2001).

145. A. Züttel, Ch. Nützenadel, P. Sudan, Ph. Mauron, Ch. Emmenegger, S. Rentsch, L. Schlapbach, A. Weidenkaff, and T. Kiyobayashi, *Hydrogen sorption by carbon nanotubes and other carbon nanostructures*, J. Alloys Compd., 330-332, 676 (2002).

146. H. Zhang, X. Fu, Y. Chen, S. Yi, S. Li, Y. Zhu, and L. Wang, *The electrochemical hydrogen storage of multi-walled carbon nanotubes synthesized by chemical vapor deposition using a lanthanum nickel hydrogen storage alloy as catalyst*, Physica B, 352, 66 (2004).

147. A.K.M. Fazle Kibria, Y.H. Mo, K.S. Park, K.S. Nahm, and M.H. Yun, *Electrochemical hydrogen storage behaviors of CVD, AD and LA grown carbon nanotubes in KOH medium*, Int. J. of Hydrogen Energy, 26, 823 (2001).

148. A. Züttel, P. Sudan, Ph. Mauron, T. Kiyobayashi, Ch. Emmenegger, and L. Schlapbach, *Hydrogen storage in carbon nanostructures*, Int. J. Hydrogen Energy, 27, 203 (2002).

149. http://www.iljinnanotech.co.kr/en/home.html (Aug. 2005).

150. J. de Jonge, R.A.H. Niessen, and P.H.L. Notten, *Electrochemical storage of energy in single-wall carbon nanotubes*, Phillips Research TN 2005/00159, Philips Research (2005).

151. X. Qin, X.P. Gao, H. Liu, H.T. Yuan, D.Y. Yan, W.L. Gong, and D.Y. Song, *Electrochemical hydrogen storage of multiwalled carbon nanotubes*, Electrochem. Sol. St. Lett., 3, 532 (2000).

152. M. Pourbaix, *Atlas of electrochemical equilibria in aqueous Solutions*, 2nd ed. (National Association of Corrosion Engineers, Houston, 1974), p. 333.

153. A.J. Bard, and L.R. Faulkner, *Electrochemical methods; fundamentals and applications*, 2nd ed. (John Wiley & Sons, New York, 2001), p. 103.

154. K. Jurewicz, E. Frackowiak, and F. Béguin, *Enchancement of reversible hydrogen capacity into activated carbon through water electrolysis*, Electrochem. Sol. St. Lett., 4, A27 (2001).

155. A.J. Bard, and L.R. Faulkner, *Electrochemical methods; fundamentals and applications*, 2nd ed. (John Wiley & Sons, New York, 2001), p. 18.

156. E. Karden, *Using low-frequency impedance spectroscopy for characterization, monitoring, and modeling of industrial batteries*, Ph.D. thesis, Chapter 2, Aachen University of Technology (2001).

157. Ch. Emmenegger, Ph. Mauron, P. Sudan, P. Wenger, V. Hermann, R. Gallay, and A. Züttel, *Investigation of electrochemical double-layer (ECDL) capacitors electrodes based on carbon nanotubes and activated carbon materials*, J. Power Sources, 124, 321 (2003).

158. B.E. Conway, *Electrochemical supercapacitors*, (Kluwer Academic/Plenum Publishers, New York, 1999).